Karlsruher Institut für Technologie

Laboratorium für Elektronenmikroskopie

Material Contrast by Scanning Electron Microscopy and Low-Energy Scanning Transmission Electron Microscopy

Zur Erlangung des akademischen Grades eines
Doktors der Naturwissenschaften (Dr. rer. nat.)

von der KIT-Fakultät für Physik des
Karlsruher Instituts für Technologie (KIT)
angenommene

DISSERTATION

Von

M. Eng. Martin Čalkovský

Tag der mündlichen Prüfung: 29. April 2022
Referentin: Prof. Dr. Dagmar Gerthsen
Korreferent: Prof. Dr. Christian Kübel

Contents

List of variables

a	screening length
a_0	Bohr radius
A	atomic mass number
b	beam broadening
c	speed of light
c_g	geometrical correction factor
d	distance between the sample and the CBS detector
$\frac{d\sigma}{d\Omega}$	elastic differential scattering cross-section
$\frac{d\sigma_{inel}}{d\Omega}$	inelastic differential scattering cross-section
e	electron charge
E	energy
E_0	primary electron energy
E_{th}	threshold energy
E_τ	screening energy parameter
E_i	energy of the individual electron
$\overline{E_\iota}$	mean energy for electron-hole pair excitation
f	scattering function
$F_{s,g}$	structure factor
g	impact parameter
$\hbar$	reduced Planck constant
I	intensity
I_0	intensity of the primary electrons
I_b	black intensity
I_w	white intensity
$I_{Si\ bulk}$	silicon bulk BSE intensity
I_{HAADF}	high-angle annular dark-field intensity
I_t	unfiltered intensity
I_{ZL}	zero-loss intensity

I_{cc}	charge collection current
I_{cc0}	charge collection current of the incident electrons
I_p	incident electron current
J	mean ionization potential
$\vec{k}$	wave vector
m_e	mass of an electron
$\bar{n}$	mean number of electron-hole pairs
n_0	number of incident electrons
N	number of atoms per unit volume
p	number of scattering events
P	electron range
Q	random number in (0,1) interval
r	radius
$\vec{r}$	position vector
R	screening radius
s	free path length
S	single-scattering function
t	sample thickness
t_0	wedge offset
t_{SE}	exit depth of secondary electrons
v	velocity
V	electrostatic potential
V_e	volume of the unit cell
W	energy loss
x	distance along a line scan
Z	atomic number
$\bar{Z}$	average atomic number
α	wedge angle
γ	fine structure constant
δ	secondary electron yield

ε_0	vacuum permittivity
ε_c	charge collection efficiency
ζ	backscattering coefficient
ζ_g	extinction length
η	screening parameter
θ	scattering angle
θ_B	Bragg angle
θ_0	Characteristic angle
λ	wavelength
λ_p	mean-free path for plasmon scattering
Λ	mean-free-path length
ρ	material density
σ	total scattering cross-section
σ_{el}	elastic scattering cross-section
σ_{inel}	inelastic scattering cross-section
τ	low-keV correction factor
φ	incident angle of an electron with respect to the surface normal
$\Phi(r)$	screening function
Ω	solid angle

List of acronyms

2D	two-dimensional
3D	three-dimensional
ADF	annular dark-field
ALD	atomic layer deposition
BF	bright field
BSE	backscattered electron
CBS	circular backscattered detector
DF	dark field
DLC	diamond-like carbon
DPSO	Darwin particle swarm optimization algorithm
DSCS	differential scattering cross-section
EDXS	energy-dispersive X-ray spectroscopy
EFTEM	energy-filtered transmission electron microscopy
EMO	electromagnetism optimization algorithm
ETD	Everhart-Thornley detector
FIB	focused ion beam
HAADF	high-angle annular dark field
HSO	harmony search optimization algorithm
ICD	in-column detector
ITO	indium tin oxide
MC	Monte Carlo
MD	mirror detector
ML	machine learning
$PC_{71}BM$	[6,6]-phenyl-C_{71}-butyric acid methyl ester
PEDOT:PSS	poly(3,4-ethylenedioxythiophene):polystyrenesulfonate
PETA	2,2-Bis{[(prop-2-enoyl)oxy]methyl}propane-1,3-diyl di(prop-2-enoate)
PTB7	poly[[4,8-bis[(2-ethylhexyl)oxy]benzo[1,2-b:4,5-b']dithiophene-2,6-

diyl][3-uoro-2-[(2-ethylhexyl)carbonyl]thieno[3,4-b]thiophenediyl]]

ROI	region of interest
SE	secondary electron
SEM	scanning electron microscopy
SNR	signal-to-noise ratio
STEM	scanning transmission electron microscopy
TE	transmitted electron
TED	transmitted electron diffraction
TEM	transmission electron microscopy
TLD	through-lens detector
TWS	trainable WEKA segmentation
UI	user interface
WD	working distance

1. Introduction

The first electron microscope was designed by Ruska and Knoll [Kno1932] in the 1930s and since then electron microscopy has become an indispensable technique in numerous scientific fields. The traditional subdivision of electron microscopy into (scanning) transmission electron microscopy ((S)TEM) performed at high electron energies and scanning electron microscopy (SEM) performed at lower electron energies, is nowadays bridged by implementing a STEM detector below the specimen in a conventional scanning electron microscope. This enables STEM at low electron energies, which is denoted as low-keV STEM or STEM-in-SEM [Mer2005, Mor2007, Pfa2011, Pfa2012, Vol2014, Li2020]. A scanning electron microscope with a STEM detector is a very versatile tool that is capable of topography imaging of bulk specimens and the investigation of thin, electron-transparent specimens in the STEM mode within one instrument. Moreover, the STEM detector is often installed in a dual-beam instrument, where thin samples can be prepared from bulk specimens using a focused-ion beam (FIB) that can be subsequently analyzed by STEM in the same instrument without exposure to ambient conditions. Low electron energies (5 – 30 keV) used in low-keV STEM is beneficial for weakly scattering materials, like life-science samples and polymers, because the contrast is enhanced due to the improved signal-to-noise ratio in the images [Sas2014]. Furthermore, materials susceptible to knock-on damage can be studied at these low electron energies without inducing electron-beam damage. Another advantage is the availability of different detectors enabling correlative SEM and STEM imaging, where the topography and interior of the same specimen region are simultaneously imaged and thus provide comprehensive information on the sample properties [Sun2018]. In addition to imaging, several analytical techniques are available in a conventional scanning electron microscope. Energy-dispersive X-ray spectroscopy (EDXS) is the most common technique and provides chemical information on the analyzed specimen. Overall, the potential of the imaging capabilities of scanning electron microscopes is up to now not developed to their full extent and deserves further methodological developments.

Traditionally, SEM or low-keV STEM images provide only qualitative information on the sample morphology, chemical composition, or distribution of different phases. It is not straightforward to derive quantitative information because the measured intensity is determined by a complex interplay of several different factors, such as imaging parameters, detection-system settings, sample thickness, and material properties. More recently, the interest in extracting quantitative information from SEM and low-keV STEM images has significantly increased, which requires adequate approaches for the simulation of SEM and STEM intensities [Vol2010, Wal2018, Xia2018, Gua2020, Kim2010, Cid2018, Mül2017]. Image simulations also provide insight into the image-contrast formation and enable the optimization of imaging conditions. The quantification of material contrast is of particular interest because it can provide information on the chemical (in)homogeneity of the sample directly from high-angle annular dark-field (HAADF-)STEM or backscattered-electron (BSE-) SEM images. Even

quantitative chemical analyses can be performed if some pre-knowledge on the material system is available.

Quantification of information from low-keV HAADF-STEM and BSE-SEM images requires the comparison of experimental and simulated image intensities performed for well-known simulation parameters. Monte Carlo (MC) simulations are well suited and often applied to calculate low-keV STEM and BSE intensities and can be utilized for quantitative analysis. However, the comparison of measured and simulated image intensities is not straightforward. All data must be normalized with respect to a suitable reference intensity and the properties of the electron-detection system must be well known. Moreover, MC-simulation results strongly depend on the differential scattering cross-sections (DSCSs), that describe the interaction between electrons and the sample. The use of screened Rutherford DSCSs in MC simulations is convenient because the screening parameter in the DSCSs can be utilized as a calibration parameter to achieve agreement between measured and simulated data. In previous work, MC simulations have been demonstrated to be well suited to quantitatively describe experimental low-keV HAADF-STEM intensities [Hol2018, Wal2018, Xia2018, Li2020]. However, a consistent description for different materials and electron-energy intervals was not achieved, which is attributed to inadequately chosen DSCSs. Up to now, no general agreement regarding the applicability of different DSCSs or screening radii in Rutherford DSCSs for a wide range of materials and electron energies is available in the literature, which motivates the study of screening parameters in screened Rutherford DSCSs performed in this work.

BSE-SEM imaging is a valuable technique for materials characterization because it provides important information about the mean atomic number of the analyzed specimen. The main challenge of quantitative BSE-SEM imaging is to relate the measured BSE intensity to the backscattering coefficient η and the (average) atomic number Z to derive chemical information from the BSE-SEM image. Several successful attempts of using quantitative BSE-SEM are found in the literature, e.g. [Gua2020, Ros1995, Kim2010, Mül2017], where MC simulations were used as an essential addition to the measured data to reveal quantitative information from the BSE intensities. However, a detailed study addressing measures for precise comparison of the measured and simulated data is missing. The measures are analogical to low-keV HAADF STEM, where the selection of proper DSCS and the detection-system geometry and properties must be determined and considered in the calculations. Moreover, a method for normalization of the measured data is needed to enable direct comparison with MC simulations. These challenges are addressed in the new quantitative BSE method proposed in this work.

The exploitation of MC simulations for the interpretation and understanding of contrast formation in SEM images is essential for FIB-SEM tomography where reliable segmentation of different phases in SEM images is required. A challenging task for FIB-SEM tomography is the 3D reconstruction of porous polymer structures that were analyzed in this work because of the weak contrast between the pore and polymer phases. It is even more challenging to quantitatively determine the pore-size

distribution within these structures because precise SEM-image segmentation is the biggest obstacle in deriving trustworthy 3D material properties. Due to the non-zero interaction volume of the primary electrons, the measured intensity contains information not only from the sample surface (as is desired) but also from the region below the sample surface. As a result, a single pixel in the SEM image contains an intermediate intensity that cannot be assigned to the pure pore (or material) phase. Therefore, a grey-value itself is not sufficient as a segmentation criterium leading to a large number of incorrectly classified pixels by the traditional thresholding algorithms [Ots1978, Bez1981, Kim2019, Sal2014]. The application of MC simulations to study the intensity variation at the pore/material interface enables to derive segmentation criteria that could be applied to the segmentation of SEM images using machine-learning segmentation algorithms. This motivates the 3D quantitative study of material properties of porous polymer structures that were fabricated within the excellence cluster 3D Matter Made to Order (3DMM2O) at KIT.

The three research topics contained in this thesis are all concerned with the quantification of image intensity and are organized in three Chapters. Beforehand Chapter 2 provides the fundamentals of the experimental techniques, together with the physical background of electron-matter interactions, and gives details on MC simulations. The first research topic on the quantification of low-keV HAADF-STEM image intensities is presented in Chapter 3. It presents a method for the experimental determination of screening parameters in screened Rutherford DSCS, which enables the agreement between measured and simulated data. The second research topic is covered in Chapter 4. It deals with the quantitative analysis of BSE contrast in SEM. In this chapter, a method for quantitative BSE analysis is proposed and tested on two differently challenging multilayer systems. Chapter 5 is not a purely methodological study but addresses the quantification of the pore-size distribution in porous polymers. The focus of this chapter is on the reliable segmentation of the pore and polymer phase of SEM images in FIB-SEM data stacks by using a machine-learning segmentation algorithm and insights from MC simulations on the experimental BSE-SEM images. Finally, Chapter 6 summarizes the results of this thesis and provides an outlook.

2. Fundamentals

Within this chapter, we introduce the basic principles of methods used in this thesis. In the first part, the interaction of an electron with a solid material is described, including the elastic and inelastic scattering. Further, multiple electron scattering, beam broadening, and electron interaction volume are introduced, as these phenomena are essential to understand the origin of different signals in scanning electron microscopy (SEM) and low-keV scanning transmission electron microscopy (STEM). The latter technique is also often referred to as STEM-in-SEM. Section 2.2 describes the experimental techniques in more detail. First, the SEM setup is presented together with an overview of the individual components. Additionally, the two most common detectors in SEM are introduced. Next, the focused ion beam (FIB) technique is presented. FIB and SEM are often combined in one FIB/SEM instrument. The advantages of FIB/SEM and possible limitations are discussed. Finally, the low-keV STEM and the high-angle annular dark-field (HAADF) imaging modes are presented. Section 2.3 covers the analytical techniques used within this thesis. Energy-filtered transmission electron microscopy (EFTEM) technique is introduced, which was mainly used to determine the local sample thickness of a wedge-shaped specimen. The second technique is energy dispersive X-ray spectroscopy (EDXS), which yields the chemical composition of the specimen. The last section of this chapter deals with Monte-Carlo (MC) simulations that are an essential part of quantitative analyses of STEM image intensities. The MC simulation principle is introduced and necessary aspects for comparison of MC-simulated and measured data are discussed.

2.1. Introduction in electron – material interactions

The interaction between an electron beam and a sample material is a fundamental source of contrast and several different signals that are used for imaging in electron microscopy. Based on the electron energy and sample thickness, the electrons can pass through the sample without any interaction, undergo only one scattering event, or, most likely, undergo multiple scattering events. In general, we can distinguish between two scattering processes. Elastic scattering occurs due to the interaction of the impinging electron with the atom core of the sample material, where the impinging electron only changes its trajectory without losing energy. Contrary, inelastic scattering occurs due to the interaction of the impinging electron with electrons of the sample material and involves energy transfer from the impinging electron to the target atom. The transferred energy is often released via photon/electron emission that can be exploited to investigate the studied sample material.

Elastic/inelastic scattering processes are mathematically described by differential electron scattering cross-sections (DSCS). The DSCS $\frac{d\sigma}{d\Omega}$ describes the probability of an electron to be scattered into the differential solid angle $d\Omega$ after impinging on an atom with its potential $V(\vec{r})$. In general, the DSCS is calculated using Eq. 2.1, where $f(\theta)$ is a scattering function.

$$\frac{d\sigma}{d\Omega} = |f(\theta)|^2 \tag{2.1}$$

Under the first Born approximation [Lew1956] the scattering function is related to the Fourier transform [Bra1999] of the potential $V(\vec{r})$, as described in Eq. 2.2. The m_e denotes the mass of an electron, $\vec{k}$ and $\overrightarrow{k'}$ denote the wave vector of the impinging and scattered electron, respectively.

$$f(\theta) = -\frac{m_e}{2\pi\hbar^2}\int e^{-i\left(\overrightarrow{k'}-\vec{k}\right)\vec{r}}V(\vec{r})\,d^3\vec{r} \tag{2.2}$$

As Eq. 2.1 and Eq. 2.2 reveal, in non-relativistic quantum mechanics the potential of an atom defines the DSCS. The validity of Eq. 2.2 is restricted by the first Born approximation to high electron energies and low atomic-number materials.

2.1.1 Elastic electron scattering

The first elastic DSCS was derived in 1911 by Rutherford [Rut1911] by considering an electron with an impact parameter g scattering in the Coulomb potential of a positively charged atomic core without electron cloud (Figure 2.1a). The DSCSs for carbon and gold are plotted in Figure 2.1b (dashed line) and show a divergence for small scattering angles θ. The divergence for the small scattering angles can be eliminated by introducing a dimensionless screening function $\Phi(r)$ to the Coulomb potential (Eq. 2.3) [Joy1995]. The screening function reduces the Coulomb potential with increasing distance from the nucleus and describes the screening of the nucleus by the electron cloud.

$$V(r) = -\frac{Ze^2}{4\pi\varepsilon_0 r}\Phi(r) \tag{2.3}$$

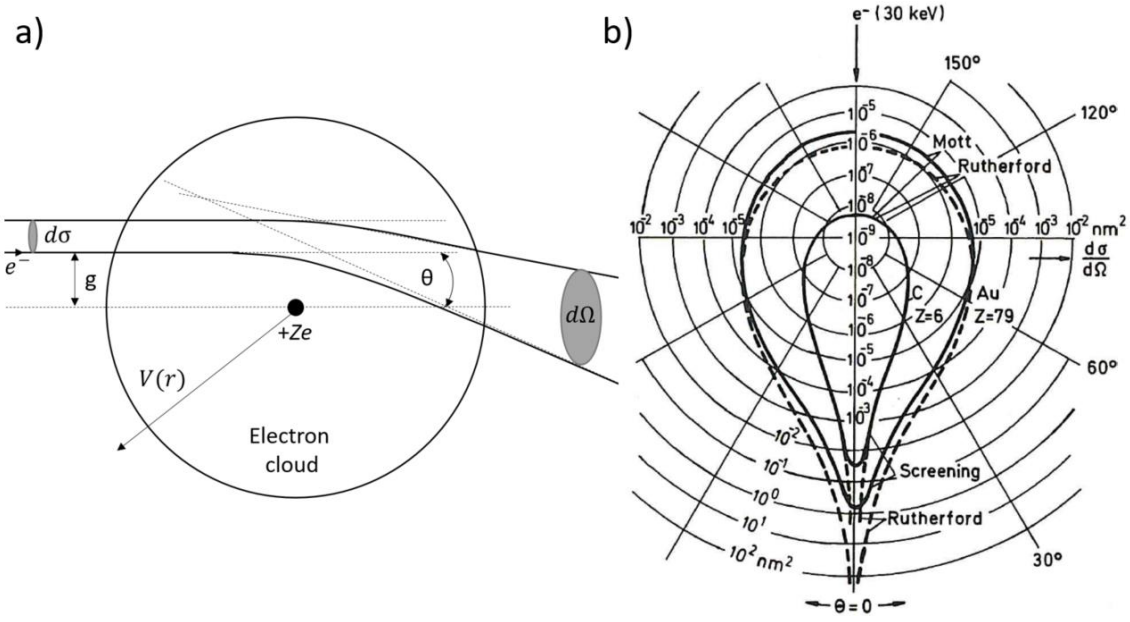

Figure 2.1 Elastic electron scattering. a) Classical model of elastic electron scattering at a charged nucleus (with impact parameter g) scattering at a nucleus in the Coulomb potential $V(r)$. Electrons that hit the area $d\sigma$ are scattered through an angle θ into a

solid angle $d\Omega$. b) Logarithmic polar diagram of the screened (full line) and unscreened (dashed line) Rutherford differential scattering cross-sections of carbon and gold. Taken from [Rei1998].

Several expressions for the function $\Phi(r)$ are available in the literature. In the Bohr potential [Boh1948] the screening effect is described through an exponential function, resulting in a potential shown in Eq. 2.4. The constant a is the screening length.

$$V(r) = -\frac{Ze^2}{4\pi\varepsilon_0 r} e^{-r/a} \tag{2.4}$$

More accurately, the screening effect can be approximated by a series of exponentials (Eq. 2.5), where the coefficients a_j and b_j are calculated using the Hartree-Fock-Slater functions [Cox1967].

$$V(r) = -\frac{Ze^2}{4\pi\varepsilon_0 r} \sum_j b_j exp(-a_j r) \tag{2.5}$$

The most common screening function is derived from the Wenzel model with only one exponential term (Eq. 2.6), where the parameter R is the screening radius (defined by Eq. 3.3) [Len1954].

$$V(r) = -\frac{Ze^2}{4\pi\varepsilon_0 r} e^{-r/R} \tag{2.6}$$

Despite its implemented approximation, the Coulomb potential with the Wenzel screening function is widely used in elastic electron-scattering calculations and is also used in the following text, particularly in chapter 3.

Substituting the Wenzel potential (Eq. 2.6) in Eq. 2.2 and further calculating $\frac{d\sigma}{d\Omega}$ according to Eq. 2.1 leads to the screened Rutherford DSCS in Eq. 2.7. E_0 denotes the primary electron energy and η is the screening parameter (defined by Eq. 3.2) that is a function of E_0 and Z [Kyr2013]. Consideration of the screening parameter results in a finite value of $\frac{d\sigma}{d\Omega}$ at $\theta = 0$ (see Figure 2.1b full line) and leads to more accurate calculations, especially for small θ [Rei1998].

$$\frac{d\sigma_{el}}{d\Omega} = \left(\frac{eZ}{4\pi\varepsilon_0}\right)^2 \frac{1}{4{E_0}^2} \frac{1}{(1-\cos(\theta)+2\eta)^2} \tag{2.7}$$

Another widely used elastic DSCS is the Mott cross-section [Mott1987], which is obtained by substituting the screened Coulomb potential (Eq. 2.3) in the relativistic Pauli-Dirac equations. Contrary to the screened Rutherford DSCS, the Mott DSCS considers relativistic effects, a spin of the electrons and thus is believed to be more accurate, particularly for heavy target atoms. However, the suitability of the Mott or the screened Rutherford DSCS has to be tested for a particular experiment because contradictory findings have been reported in the literature. According to Reimer [Rei1998], the difference between the screened Rutherford and Mott DSCS is small for

light target atoms and low electron energies (3-30 keV). Contrary, Browning *et al.* [Bro1994] reported that the screened Rutherford DSCS is suitable for low Z materials at high electron energies, whereas the Mott DSCS gives reliable results only at low electron energies. Shimizu and Ze-Jun [Shi1992] recommend using screened Rutherford DSCS for elements with $Z < 13$ and electron energies in the 1-20 keV range. Since the exact form of the Mott DSCS can be expressed only as an infinite series of Legendre polynomials, no analytical formula can be derived. Using the Mott DSCS in simulations requires the determination of the scattering amplitudes numerically or from tabulated values [Rei1998].

2.1.2 Inelastic electron scattering

In an inelastic scattering process, the kinetic energy of the impinging electron is not conserved but is partially transferred to the target atom [Wil2009]. The energy loss of the electron is a continuous process due to several processes including bremsstrahlung (i.e. electrons are decelerated by the Coulomb force and the energy is released as an X-ray), generation of SE electrons, and phonon excitations (i.e. collective vibrational motion of a lattice of atoms). Moreover, the transferred energy excites electrons in the target atom and can be subsequently released in some other form (plasmon, secondary electron emission, photon emission,…). The transferred energy has only discrete values, which is characteristic for a particular atom, and thus the energy loss W is valuable analytical information. The most important excitation processes are [Wil2009, Rei1998, Ful2008]:

- The most frequent inelastic excitation is a phonon and molecular oscillation excitation. The energy loss W in this process is < 1 eV. The consequence of phonon and molecular oscillations is heating of the specimen.
- Plasmons (i.e. collective longitudinal oscillations of the valance or conduction band electrons) can be excited by the incident electrons. The transferred energy is related to the plasmon frequency ω_{pl} and is in the 5-30 eV range.
- Inter- and intraband electronic transitions with energy loss $0 < W < 50$ eV. The plasmon excitation and inter/intraband transitions lead to scattering angles below 10 mrad.
- Excitation of inner-shell electrons: In the ionization process, the impinging electron transfers some energy to the inner-shell electron, which is excited to a vacant level at higher energies, or it can be released into a vacuum. Subsequently, the created vacancy can be filled by an electron from a higher energy level. The energy difference between both energy levels is released by the emission of an X-ray photon. The X-ray energy is characteristic for the particular atom and can be used for qualitative and quantitative chemical composition analysis. This technique is denoted as energy-dispersive X-ray spectroscopy (EDXS) which is introduced later in section 2.3.2).

In analogy to elastic scattering, inelastic scattering can be mathematically described by a DSCS $\frac{d\sigma_{inel}}{d\Omega}$. The inelastic DSCS of inner-shell ionization [Rei1998] is shown in Eq. 2.8,

where J is the mean ionization potential, E_0 is the primary electron energy, θ_0 is the characteristic angle and λ is the wavelength.

$$\frac{d\sigma_{inel}}{d\Omega} = \frac{4e^2Z}{(4\pi\varepsilon_0)^2 {m_e}^2 v^4} \frac{1-\left(\frac{1}{1+(\theta^2+\theta_E^2)/\theta_0^2}\right)^2}{(\theta^2+\theta_E^2)^2}, \theta_E = \frac{J}{4E_0}, \theta_0 = \frac{\lambda}{2\pi R} \quad (2.8)$$

To reduce inelastic scattering (and radiolysis damage), high electron energies are preferred. Moreover, inelastic interactions (apart from phonon scattering) typically scatter electrons into small angles compared to elastic scattering [Wil2009]. Considering the probability of scattering through large angles $\theta > 10\,°$, the contribution of the inelastic DSCS can be included in the elastic DSCS by replacing the factor Z^2 in Eq. 2.7 with $Z(Z+1)$ [Rei1998]. In the MC simulations performed within this work, the inelastic electron scattering was considered in the $Z(Z+1)$ form.

Considering elastic and inelastic scattering the total cross-section is given by integration of the elastic and inelastic DSCS over the scattering angle range as shown in Eq. 2.9.

$$\sigma \quad = \sigma_{el} + \sigma_{inel} = 2\pi \int_0^\pi \left(\frac{d\sigma_{el}}{d\Omega} + \frac{d\sigma_{inel}}{d\Omega}\right) \sin(\theta)\, d\theta \quad (2.9)$$

2.1.3 Multiple electron scattering

In electron-microscopic analyses of real samples, the primary electrons usually experience several scattering events. Therefore, the mathematical description of single scattering discussed in sections 2.1.1 and 2.1.2 has to be adapted. The approach outlined in the following neglects the effects of Bragg diffraction, which is adequate for amorphous materials or kinematical imaging conditions, where Bragg reflections are only weakly excited. In this case, the number of scattering events p depends on the local sample thickness t and on the mean-free-path length Λ according to $p = t/\Lambda$. Λ describes the distance that an electron travels between scattering events and is expressed by $\Lambda = 1/(N\sigma)$, where N denotes the number of atoms per unit volume. Calculated values of Λ are listed elsewhere [Rei1998] and are in the nm range. For example, the mean-free-path length of a 30 keV electron beam in C and Au is 14 and 3.8 nm, respectively. As a consequence, even for very thin samples (thickness of 100 nm), multiple electron scattering theories have to be employed.

The angular intensity distribution of scattered electrons into the solid angle $d\Omega$ after one scattering event can be described using the normalized single-scattering function $S_1(\theta) = (1/\sigma)\, d\sigma/d\Omega$ by

$$I_1(\theta)d\Omega = I_0 N\sigma t \left(\frac{1}{\sigma}\frac{d\sigma}{d\Omega}\right) d\Omega = I_0 \frac{t}{\Lambda} S_1(\theta) d\Omega \quad (2.10)$$

where I_0 denotes the intensity of the primary electrons. Expanding Eq. 2.10 to consider two scattering events means replacing the function S_1 with function $S_2(\theta) = S_1(\theta) \otimes$

$S_1(\theta)$, where $S_2(\theta)$ is given by self-convolution of the function $S_1(\theta)$. Considering p scattering events, the m-fold scattering function $S_m(\theta)$ is given by the m-fold self convolution of $S_1(\theta)$. Using the function $S_m(\theta)$, the angular intensity distribution of p-times scattered electrons is given by Eq. 2.11.

$$I(\theta)d\Omega = I_0 d\Omega \sum_{m=0}^{\infty} \frac{p^m}{m!} e^{-p} S_m(\theta) \tag{2.11}$$

Eq. 2.11 is exact only with two approximations that are considered for the multiple electron scattering [Rei1998]. First, the energy loss is negligible and $d\sigma/d\Omega$ does not change with scattering at different sample depths. Second, the decrease of the mean-free path length of the scattered electrons can be neglected. To calculate Eq. 2.11 analytically, Goudsmit and Saunderson [Gou1940] expanded the function $S_1(\theta)$ into a series of Legendre polynomials. Rewriting Eq. 2.11 using the series of the Legendre polynomials $P_n(\cos\theta)$ leads to the final expression (Eq. 2.12) for the angular intensity distribution after multiple electron scattering, normalized to the primary electron intensity. The integration variable s denotes the path length inside the sample.

$$\begin{aligned}\frac{1}{I_0} I(\theta)d\Omega = \frac{d\Omega}{4\pi} \sum_{n=0}^{\infty} (2n & \\ + 1)\exp\left[-N \int_0^s \left\{ \int_0^{\pi} \frac{d\sigma}{d\Omega} [1 \right.\right. & \\ \left.\left. - P_n(\cos\theta)] 2\pi \sin\theta \, d\theta \right\} ds \right] & P_n(\cos\theta)\end{aligned} \tag{2.12}$$

Even with today's computation power, solving Eq. 2.12 is very challenging and requires several approximations [Neg2005]. For this reason, the scattered intensities are often calculated based on other approaches (Monte Carlo simulations, electron transport equation, semi-empirical equations assuming Gaussian angular distribution,…) [Rei1998].

2.1.4 Beam broadening

Due to the multiple scattering of the primary electrons, the diameter of the electron beam broadens as the electrons propagate through the sample. Particularly for low electron energies and large specimen thicknesses the lateral resolution strongly degrades and beam broadening has to be considered in image interpretation [Dre2017].

A simple model of beam broadening developed by Goldstein *et al.* [Gol1977] is schematically shown in Figure 2.2. In this model, the scattering of the electron beam is assumed to take place in the middle of the sample at thickness $t/2$. The effective scattering angle θ then defines the beam broadening b. Based on this model a mathematical formula (Eq. 2.13) for the beam broadening was derived. The variable Z is the average atomic number of the sample with thickness t in cm units, ρ is mass density in g/cm^3, A is average atomic weight in g/mol and E_0 is the primary electron energy in keV.

$$b = 625 \frac{Z}{E_0} \sqrt{\frac{\rho}{A}} t^{3/2}, (\mathrm{cm}) \tag{2.13}$$

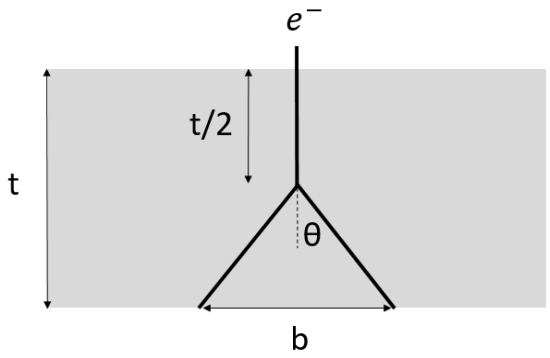

Figure 2.2 Scheme of beam broadening. In the scattering model of Goldstein *et al.* [Gol1977], the electrons are assumed to be scattered only once in the middle of the sample. The resulting beam broadening b is then given by the effective scattering angle θ.

Even though the Goldstein *et al.* model is very simple, according to other studies [Koh2008, Mic1987] the $t^{3/2}$ dependence of the beam broadening is confirmed. Recently, a more elaborated model of beam broadening was established [Gau2016], introducing a Hurst exponent that takes into account different scattering regimes depending on the sample thickness. An experimental study by Hugenschmidt *et al.* [Hug2019] confirmed the suitability of this model and revealed a $t^{1.75}$ dependence of the beam broadening on the sample thickness in STEM measurements for sample materials in $10 < Z < 32$ range, sample thicknesses up to 900 nm, and electron energies between 15 and 30 keV.

Another possibility of calculating beam broadening is from the trajectory image obtained from Monte Carlo simulations [Kys1976].

2.1.5 Electron-specimen interactions

In SEM, the impinging electron beam interacts with the sample material and produces numerous additional signals. In the case of thin electron-transparent samples (Figure 2.3a), a fraction of the primary electrons remain unscattered and are transmitted through the specimen without being deflected. The transmitted electrons (TE) can undergo elastic (Section 2.1.1) or inelastic (Section 2.1.2) scattering events and are deflected from the unscattered electron beam. Electrons that leave the sample via the upper surface, are by definition separated mainly into two categories. Electrons with a kinetic energy of less than 50 eV are denoted as secondary electrons (SE) and electrons with an energy ≥ 50 eV are denoted as backscattered electrons (BSE). Besides electrons, X-rays can be also emitted as a result of electron-sample interaction. All produced signals are a valuable source of information about the analyzed sample and can be collected with various detection systems.

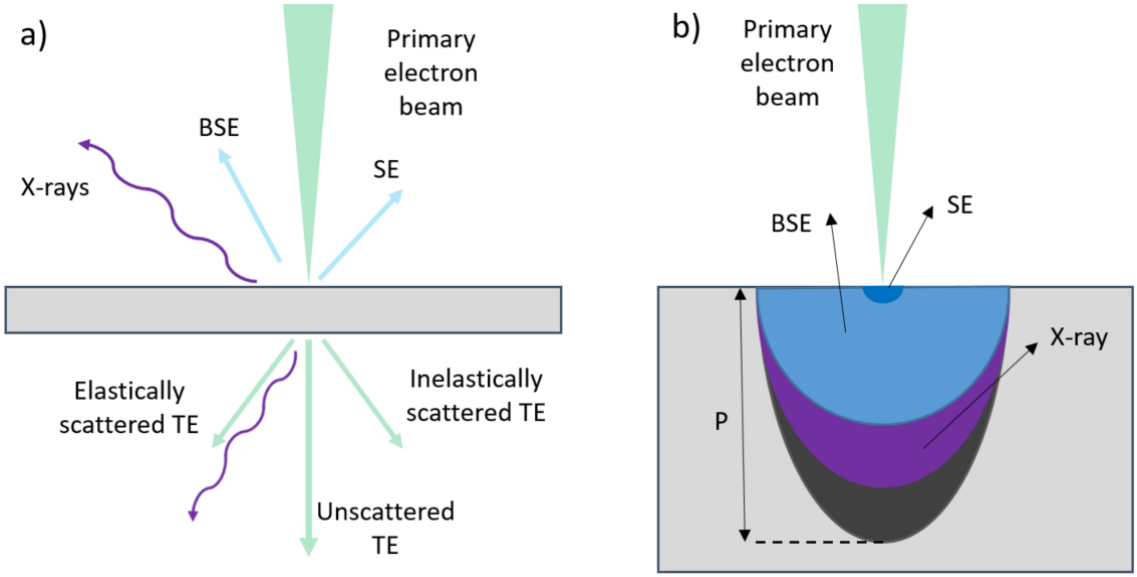

Figure 2.3 Electron beam – sample interactions. a) Scheme of electron-sample interactions in SEM with possible emitted signals. b) Scheme of interaction volumes of the SEs in dark blue, BSEs in light blue, and X-rays in purple. The electron range P is shown in black.

In the case of bulk samples (Figure 2.3b), it is important to consider the interaction volumes of the different signals. SEs can only be emitted from regions close to the sample surface (medium blue regions in Figure 2.3b) due to their low energy. As a result, the SEs are used for topography imaging with high spatial resolution. However, the spatial resolution of the SEs is not given by the small diameter of the primary electron beam because BSEs can generate SEs on their way back through the specimen surface and thus can deteriorate the spatial resolution. The information volume of the BSEs (light blue regions in Figure 2.3b) is generally much larger than the information volume of the SEs, resulting in worse spatial resolution. The primary electrons penetrate even deeper into the sample and, based on inelastic interactions, lose their energy until they are absorbed. Most of the energy lost by the electrons is converted to phonons and heat the sample. Concurrently, X-rays with characteristic energies of the sample material can be emitted. The information volume of the X-rays is represented by the purple region in Figure 2.3b. The total range of the electrons P is given by Eq. 2.14 [Kan1972] and depends on the primary electron energy E_0 and material parameters, i.e., material density ρ, (average) atomic weight A, and (average) atomic number Z. The validity of Eq. 2.14 was experimentally verified for SEM electron energies [Kur2007]. In literature [Rei1998] several expressions for the electron range exist depending on their definition. For SEM samples P is usually in the range 10 nm – 10 µm. According to Reimer [Rei1998], the escape depth of BSEs is in the order of half of the range P.

$$P = 27.6 \frac{A E_0^{\,1.67}}{\rho Z^{0.89}}, (\mathrm{nm}) \tag{2.14}$$

The generation of BSEs is described by the backscattering coefficient ζ, which gives the number of BSEs per single primary electron. ζ is given by Eq. 2.15 [Rei1998], where Z is the atomic number and φ is the incident angle of the electron with respect to the surface normal.

$$\zeta = (1 + \cos\varphi)^{\frac{-9}{\sqrt{Z}}} \tag{2.15}$$

We note that Eq. 2.15 was derived from fitting experimental data, does not apply to low electron energies (below approximately 5 keV) and other approaches exist for calculating ζ [Rei1998]. However, Eq. 2.15 nicely visualizes the dependence of ζ on Z, which is the prerequisite for material contrast for samples with flat-polished surfaces.

Eq. 2.15 does not describe the dependence of ζ as a function of E_0, which is shown for several materials in Figure 2.4a. We see that ζ is almost constant for all materials for $E_0 > 5\ \mathrm{keV}$. The value of the ζ increases with increasing Z for $E_0 \geq 5\ \mathrm{keV}$. This is well visible in Figure 2.4b, where the Z dependence of ζ is shown for several primary electron energies. For 5 and 20 keV, the curves monotonically increase with Z. This yields material contrast, where an increasing BSE intensity can be attributed to phases with increasing (average) atomic number. However, this is not true for $E_0 < 5\ \mathrm{keV}$ because ζ for low-Z materials increases and goes through a maximum with increasing atomic number. This introduces an ambiguity for the assignment of ζ to one particular Z value. The ζ dependence on Z at low electron energy range (0.4 – 5 keV) for materials ranging from Be to Au expressed in an analytical formula was obtained by Cazaux [Caz2012].

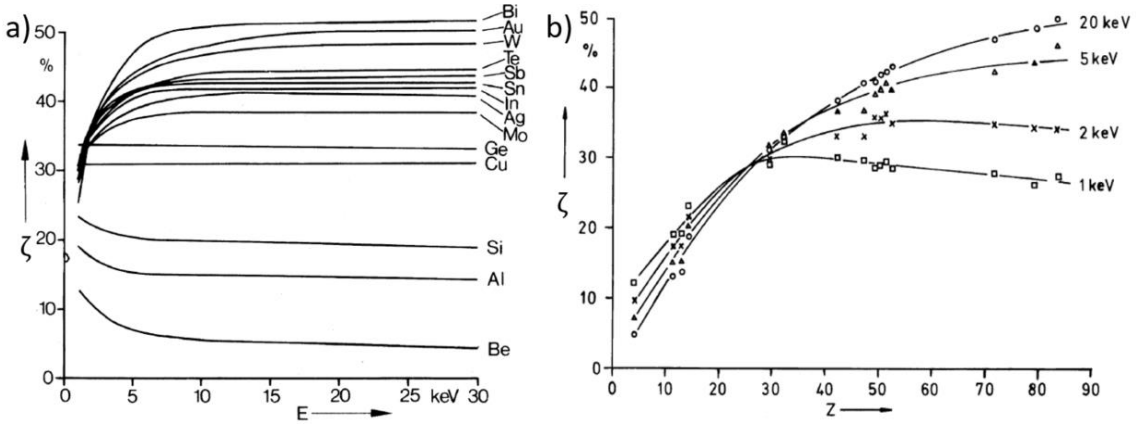

Figure 2.4 Backscattering coefficient ζ. a) Backscattering coefficient ζ as a function of electron energy. b) Measured backscattering coefficient ζ as a function of atomic number Z for different electron energies in range 0.5 – 5 keV. Taken from [Rei1998]

The emission of SE is described by SE yield δ that gives the number of SEs per primary electron. δ strongly depends on the primary electron energy E_0, on the exit depth for SEs t_{SE} and on the incident angle of the primary electrons φ. Because of these strong dependencies, SEs are mainly used for topography imaging. A simplified

expression for δ is shown in Eq. 2.16 [Rei1998], where J denotes the mean ionization energy.

$$\delta \propto {E_0}^{-1} \ln\left(\frac{E_0}{J}\right) \frac{1}{\cos\varphi} \int_0^\infty exp\left(-\frac{z}{t_{\mathrm{SE}}}\right) dz \tag{2.16}$$

2.2 Experimental techniques

In this section, we briefly introduce the experimental techniques used in this thesis. Section 2.2.1 describes the working principle of the scanning electron microscope (SEM) and describes the two most common detection systems. Section 2.2.2 introduces the focused ion beam (FIB) and its combination with the SEM instrument. The FIB/SEM instrument was used in all experimental chapters of this thesis. Section 2.2.3 discusses the low-keV scanning transmission electron microscopy (STEM) that could be performed in the FIB/SEM instrument. Low-keV STEM is further discussed in more detail in Chapter 3.

2.2.1 Scanning electron microscopy

Scanning electron microscopy (SEM) is a technique that is widely used to image and analyze near-surface properties of bulk samples at the nanoscale. In a scanning electron microscope (see scheme in Figure 2.5a), the electrons are produced at the top of the column and accelerated towards the specimen. The electron beam is focused to a small diameter in the order of 1 nm or even below on the sample surface by a combination of lenses and apertures. The beam position on the sample surface is controlled by scan coils, which are used to scan over the sample surface. The beam position in the raster-scan pattern is combined with the intensity of the detected signal to produce an SEM image [Rei1998]. Depending on the detected signal (Section 2.1.5), different information on the specimen is retrieved. The best possible spatial resolution in SEM depends on the diameter of the electron beam, which is determined by the electron energy and the electron-optical system of the instrument [Ham2018]. However, in most cases, the resolution is limited by the interaction volume, as already discussed above. Modern scanning electron microscopes can achieve a spatial resolution better than 1 nm in the SE-imaging mode [Kaz2004].

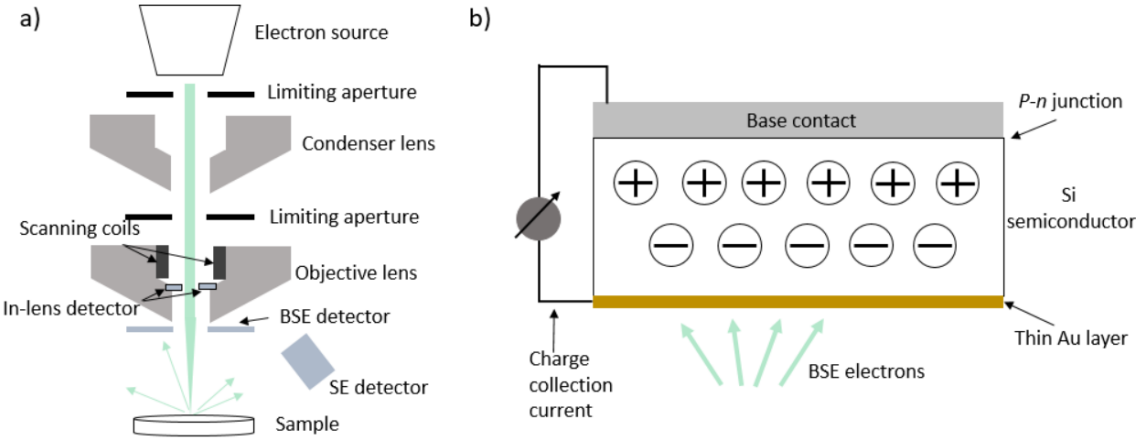

Figure 2.5 Scanning electron microscope. a) Scheme of the scanning electron microscope (SEM). b) Scheme of a semiconductor BSE detector, where BSEs reaching the silicon detector with implemented p/n junction create electron-hole pairs that lead to a formation of charge collection current. This current leads to a detected BSE signal.

For electron detection, two types of detectors are usually used. The first type uses a scintillator-photomultiplier combination and is referred to as Everhart-Thornley detector (ETD) [Eve1960]. This type of detector is located in the SEM chamber and is usually used for the collection of SE electrons. The SEs are collected by a biased grid and accelerated towards the scintillator. Within the scintillator, the detected electrons generate light quanta that are further guided to a photomultiplier [Sch1992]. In the photomultiplier, the light quantum creates a photoelectron that is further multiplied by successive acceleration to a series of dynodes, where on each dynode 2-10 secondary electrons are generated [Rei1998]. In this way, a signal from the detected electron is multiplied. The Everhart-Thornley detector shows low noise and is therefore widely used for SE detection. In modern SEM the specimen is often immersed into a magnetic field of the objective lens, which hinders the SE detection with the ETD. For this case detectors inside the objective lens or inside of the column are used for electron detection. Especially for SEs, in-lens detectors are convenient because they collect mostly SEs generated by direct interaction with the incident beam and thus carry the highest spatial resolution information. The BSEs are often detected using the second type of detector, i.e., a semiconductor detector (see scheme in Figure 2.5b). The BSE detector is positioned below the pole piece of the objective lens directly above the specimen. BSEs first penetrate through the thin Au electrical contact (serving also as a protection layer) and are inelastically scattered within the semiconductor material. The inelastic interaction results in the generation of electron-hole pairs. For silicon, the average energy that is necessary to create such an electron-hole pair is $\overline{E}_\iota = 3.6$ eV. The mean number of electron-hole pairs $\bar{n}$ created by an electron with energy E_0 is $\bar{n} = E_0/\overline{E}_\iota$. The *p-n* junction in the detector acts as an internal field and separates electrons and holes before recombination, which leads to an external charge collection current. The current is fed into an amplifier to generate a signal with corresponding intensity at the image position that is synchronized with the position of the electron beam [Gol1992]. A semiconductor detector is sensitive to both the number and energy of detected electrons. Semiconductor detectors detect only BSEs because SEs are

adsorbed in the Au-protection layer due to their low kinetic energy and, hence, cannot be detected by the detector. Likewise, BSEs lose part of their energy while penetrating through the protection layer. For quantitative BSE analysis, this effect must be considered in MC simulations.

2.2.2 Focused-ion-beam/scanning-electron microscopy

The combination of a scanning electron microscope with a focused-ion beam (FIB) column is denoted as a combined FIB/SEM instrument. The FIB column generates Ga^+ ions and focuses them on the specimen surface. The scanned Ga^+ beam (FIB) can be used for imaging (in analogy to SEM) because the interaction of an ion beam with the specimen results in the generation of SEs, secondary ions and neutral atoms [Ham2018]. More importantly, ions carry a larger momentum compared to electrons, and can easier remove material from the specimen surface. Utilizing this, FIB is used for sputtering, milling, etching, or micromachining of materials. The FIB can be also equipped with gas injectors to introduce precursor gases in the vicinity of the sample surface. The gas molecules are split by the ion beam and materials such as Pt, C, or W are deposited on the surface during ion-beam-assisted deposition. Alternatively, etching processes can be induced [Ham2018]. FIB-based material deposition and material removal can be controlled with a nanometre precision resulting in milled/deposited features as small as 10-15 nm [Gia1999]. An advantage of FIB, compared to SEM, is the possibility to characterize nonconducting materials by neutralizing the accumulated positive charge on the sample surface by a source of low-energy electrons [Rey2001].

A FIB/SEM instrument is especially convenient because specimens can be prepared with FIB and subsequently analyzed by SEM. Moreover, combined FIB/SEM instruments enable FIB/SEM tomography, where FIB milling is alternated with SEM imaging of a region of interest and in this manner, an SEM image data stack is obtained. Segmenting the images of the data stack regarding different phases enables then 3D visualization of the analyzed volume and calculation of 3D material properties [Utk2012]. The FIB/SEM method is described in more detail in Chapter 4. In Chapter 3 and Chapter 5, FIB was used to prepare wedge-shaped specimens from bulk materials to enable low-energy STEM analysis. The preparation of wedge-shaped specimens follows the FIB preparation of conventional lamellae for TEM analysis [Giu2020]. After milling a lamella and lift-out of the lamella from the bulk material, it is attached to a prefabricated TEM grid. The lamella is then milled on one side in a wedge-shaped manner. The drawback of FIB preparation is ion implantation and possible amorphization of the crystalline structure close to the sample surface. Both ion implantation and amorphization can be reduced by milling with low ion energies, low ion currents, and grazing incidence of the ion beam. According to a recent study [Kel2013, Raj2002], the amorphization damage in crystalline Si by a Ga^+ FIB with 30, 5 and 2 keV ions is 22, 7, and 3 nm, respectively. Using instead Xe^+ ions instead of Ga^+ dramatically reduces the amorphization damage to 13, 4, and 2 nm for 30, 5, and 2 keV, respectively [Kel2013]. More details on FIB-based sample preparation are given in section 3.3.2.

2.2.3 Low-energy scanning transmission electron microscopy

Low-energy scanning transmission electron microscopy (low-keV STEM) is a technique that is gaining importance for imaging and analysis of soft and beam-sensitive materials. The advantages of using lower electron energies were illustrated for TEM in the work of Kaiser et al. [Kai2014]. Unlike in high-energy (S)TEM, where energies between 80-300 keV are used, low-keV STEM uses electron energies of 30 keV and below. At these smaller energies, knock-on-damage is reduced. Furthermore, the contrast is enhanced due to the improved signal-to-noise ratio [Sas2014]. The practical advantages of low-keV STEM apply in particular to weakly scattering materials including polymers, 2D materials, biological samples, etc. [Bel2014, Dru2014, Pfa2011, Sun2018]. Conveniently, low-keV STEM is possible in a scanning electron microscope if it is equipped with a STEM detector position below the sample. The working principle of low-keV STEM is schematically shown in Figure 2.6a. A focused electron beam scans an electron-transparent sample. The transmitted electrons are detected with a STEM detector that is positioned below the sample. There is no image-forming lens system in low-keV STEM, as compared to TEM. A STEM detector is usually subdivided into three segments. The bright-field (BF) segment is positioned on the optical axis and collects the unscattered or only weakly scattered electrons. The annular dark-field (ADF) segment is positioned concentrically around the BF segment. It collects electrons with intermediate scattering angles. Transmitted electrons scattered into large angles are detected by the high-angle annular dark-field (HAADF) segment of the STEM detector. The semiconductor STEM detector implemented in the Helios G4 FX microscope is schematically shown in Figure 2.6b. The ADF segment of this particular detector is further subdivided into three segments (DF1, DF2, and DF3).

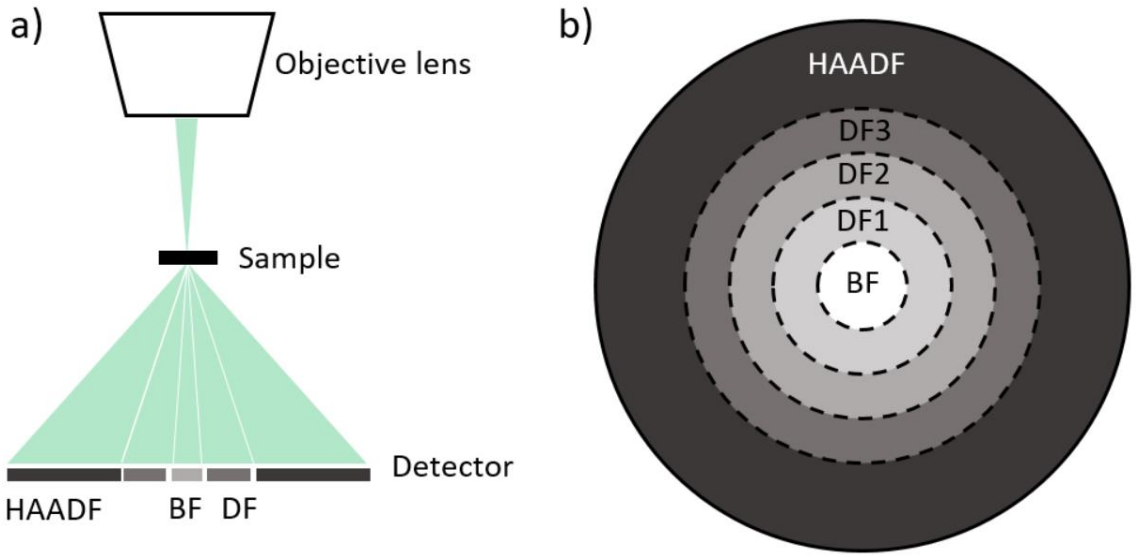

Figure 2.6 Low-keV STEM in a scanning electron microscope. a) Scheme of low-keV STEM setup: A focused electron beam scans an electron-transparent specimen. The transmitted electrons are detected with a STEM detector positioned below the specimen. b) Scheme of the STEM-detector design in the Helios G4 FX microscope.

The HAADF segment is widely used for the detection of the transmitted electrons because only incoherently scattered electrons into large scattering angles are collected. The coherent interferences of the electron waves do not contribute to the image formation in this case. The HAADF signal is therefore intuitively interpretable. Large-angle scattering is related to electron interaction with the nuclei of the target atoms [Pen1988]. The HAADF-STEM intensity strongly depends on the (average) atomic number Z of the sample material and is therefore often called Z-contrast imaging. However, several other parameters such as material density, (average) atomic weight, local sample thickness, etc. determine the HAADF-STEM intensity. Therefore, the contrast in HAADF-STEM images has to be interpreted with care.

The resolution of low-keV STEM is determined by the diameter of the primary electron beam, denoted as spot size, and the electron interaction volume. For very thin electron-transparent samples, the electron interaction volume is small, and spatial resolution in HAADF-STEM is mainly limited by the spot size that is given by the spherical aberration of the objective lens [Vys2017]. However, the spatial resolution of modern low-keV STEM instruments in the BF-imaging mode is ≈ 0.3 nm at 30 keV electron energy. This resolution exceeds the spot size as a result of coherent interference of the electron waves, which allows to resolve lattice planes in some materials (carbon nanotubes 0.34 nm, silicon 0.31, tungsten disulphide 0.27 nm, etc.) [Sun2016, Vys2017]. The drawbacks of using low-energy electrons are mainly increased contamination and increased ionization-radiation damage in materials with low electrical conductivity [Ege2004]. Ionization damage arises from inelastic scattering of the incident electrons and can be reduced by cooling the specimen to low temperatures [Ege2012]. Mitigation of the sample contamination is possible by special treatments (heating, plasma cleaning, …) before the low-keV STEM analysis [Ege2019].

2.3 Analytical techniques

Among the analytical techniques, energy-filtered transmission electron microscopy (EFTEM) was utilized to characterize the FIB-prepared wedge-shaped specimen. The chemical composition of the sample materials was verified by energy-dispersive X-ray spectroscopy (EDXS). This was particularly important for the determination of the Os content in the OsO_4-stained PETA structures (Chapter 4).

2.3.1 Energy-filtered transmission electron microscopy (EFTEM)

EFTEM is a technique that is used in transmission electron microscopy (TEM), where only transmitted electrons of particular kinetic energy contribute to the image formation. In EFTEM images, chemical information is present and can be used to locate specific elements in the sample. When a thin specimen is illuminated by a high-energy electron beam, most electrons are not at all or only elastically scattered and only part of the electrons undergo inelastic scattering. The latter results in a change of momentum and energy loss, which in the case of inner-shell ionisation is characteristic of the element in the sample. By placing a magnetic prism on the optical axis below the sample, the trajectory of the transmitted electrons is changed depending on their energy. An adjustable slit placed in front of the detector allows only electrons with a

certain range of energies to form an energy-filtered image [Wil2009]. The working principle of EFTEM is schematically shown in Figure 2.7. With EFTEM, it is possible to visualize also light elements in the sample [Ver2004]. Therefore, it is popular in the analysis of soft materials and biological samples, although beam damage needs to be considered [Rhi2011].

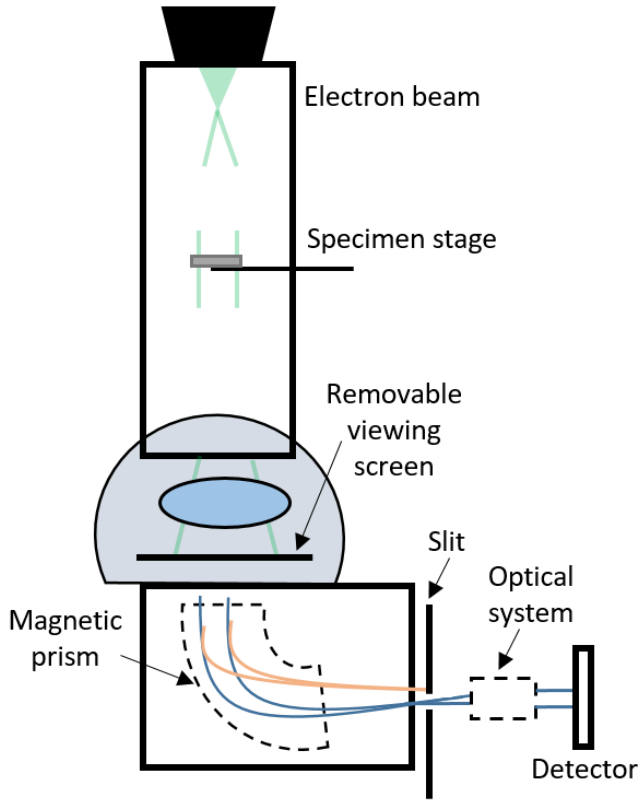

Figure 2.7 Energy-filtered transmission electron microscopy (EFTEM). Simplified scheme of the EFTEM setup, where the electron beam passes through a thin specimen, while some electrons are inelastically scattered. The magnetic prism changes the electron path depending on its energy. The adjustable slit admits only electrons within a certain range of energies to form the image on the detector.

In this thesis, EFTEM was mainly used to characterize wedge-shaped specimens prepared by FIB milling. EFTEM can be also utilized to reveal the local specimen thickness [Aro2007, Lea1984]. In this approach, an unfiltered image is acquired, and subsequently another image of the same sample region is taken, where only the zero-loss electrons contribute to image intensity. With knowledge of the mean-free path for plasmon scattering of the analyzed material, the local sample thickness can be calculated. This approach is discussed in more detail in Section 3.3.3.

2.3.2 Energy-dispersive X-ray spectroscopy (EDXS)

EDXS is an analytical technique used for the qualitative and quantitative chemical analysis of the studied material. The EDXS technique relies on a fact that each element has a unique electronic structure and therefore a unique set of peaks in the X-ray emission spectrum [Rus1984]. In SEM, a variety of signals arise from the interaction

between electron beam and sample. Among others, X-rays are generated (Figure 2.8). Inelastic interaction between beam electrons and inner-shell electrons can lead to the excitation of inner-shell electrons while leaving a hole in the inner shell. Subsequently, an electron from an outer shell fills the vacancy. As the electron moves from the outer (higher-energy state) to the inner (lower-energy state) shell of the atom, the energy difference is released in form of an X-ray. This characteristic X-ray is specific for a particular element and transition within an atom.

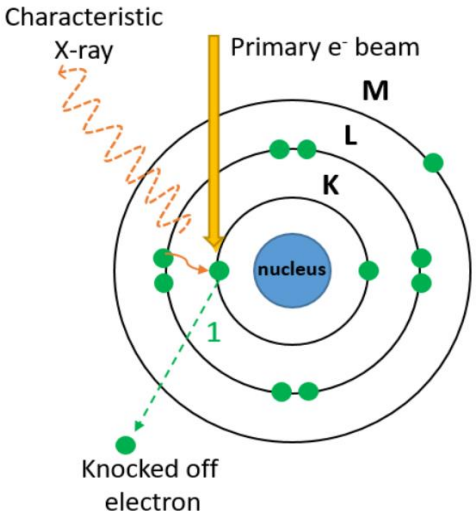

Figure 2.8. Energy dispersive X-Ray spectroscopy (EDXS). Scheme of characteristic X-ray generation used for EDXS. First, the incident electron excites an inner-shell electron. Subsequently, this position is filled by another electron from a higher-energy shell. As a result, an X-ray photon is emitted with an energy corresponding to the energy difference between the two shells.

The emitted X-rays are detected by a detector, which measures the number of X-rays over the chosen energy interval and interprets it using software (for Bruker Quantax 400 EDXS system in the Helios G4 FX microscope the XFlash 6T detector was used). In this manner, the chemical composition of the sample can be qualitatively and quantitatively analyzed. EDXS is widely used for its ease of application and rapid qualitative insight into chemical composition. The drawback of this technique is its low precision, especially when trying to quantify low-Z materials [Shi2002].

2.4. Monte-Carlo (MC) simulations

MC simulations are a class of computational algorithms that rely on repeated random sampling to obtain numerical results. MC simulations are widely used in electron microscopy to calculate electron-material interactions [Mül2017, Mur1971, Kuh1999, Tia2018]. A correct interpretation of images and spectra in electron microscopy is not simple because the interaction of an electron beam with a solid is highly complex. Before losing its energy or escaping from the sample, each primary electron may undergo hundreds of separate scattering events, which can be elastic or inelastic with a variety of different inelastic scattering processes. The MC technique aims to describe the trajectory, which each primary electron takes through the solid specimen [Joy1991]. Even though a simulated trajectory does not represent the trajectory of a

''real'' electron, simulated predictions based on a large number of trajectories can accurately describe experimental data. The MC simulation process is schematically illustrated in Figure 2.9a. Each electron position $\vec{r}_{n+1}$ is calculated from the previous electron position $\vec{r}_n$ according to Eq. 2.17.

$$\vec{r}_{n+1} = \vec{r}_n + s_{n+1} \sin\theta_n \cos\chi_n \tag{2.17}$$

The values for the free path length (distance between two scattering processes) s_n and the azimuthal angle χ are derived using a random number Q in an interval $(0,1)$ according to Eq. 2.18 and Eq. 2.19, respectively. Λ denotes the mean-free path length of the electron.

$$s = -\Lambda ln(1 - Q) \tag{2.18}$$

$$\theta = 2\pi Q \tag{2.19}$$

The scattering-angle probability of an electron being scattered in the interval $\theta, \theta + d\theta$ is given by Eq. 2.20 using the differential scattering cross-section $d\sigma/d\Omega$ [Rei1998]. The selection of the scattering cross-section has a major impact on the result of MC simulations.

$$p(\theta)d\theta = \frac{d\sigma}{d\Omega} 2\pi \sin\theta \, d\theta \tag{2.20}$$

In MC simulations, each electron is traced until it leaves the sample as a transmitted electron, backscattered electron, or completely loses its energy and is absorbed within the specimen. A result of MC calculations of 30 keV electrons interacting with a 700 nm thick Si film is shown in Figure 2.9b. The electron trajectories within the Si film are shown in blue. Trajectories above the sample represent the BSEs, whereas the red trajectories below the sample represent the transmitted electrons.

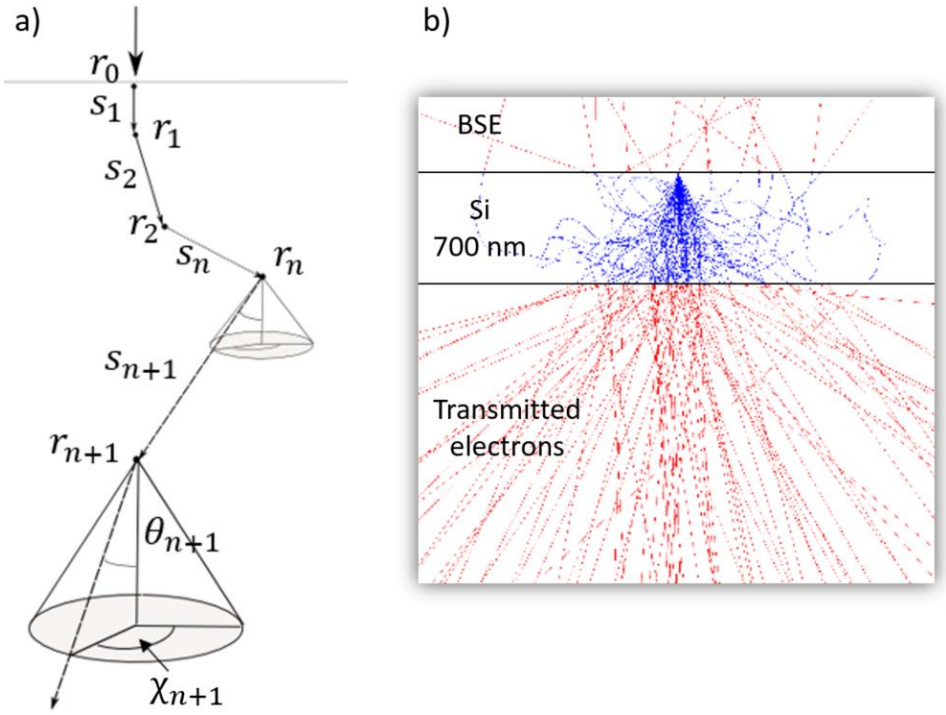

Figure 2.9 Monte-Carlo simulations. a) Scheme of a sequence of single scattering events in MC simulations, wherein each step all coordinates are recalculated using random number (adopted from [Rei1998]) b) A trajectory image as a result of MC simulations of 30 keV electrons interacting with a 700 nm thick Si film. The blue trajectories represent the electron path within the sample. Red trajectories mark backscattered and transmitted electrons.

The energy loss in MC simulations is assumed to be continuous, rather than a result of discrete inelastic events [Joy1989]. This assumption dramatically simplifies the calculation because the exact details of each inelastic scattering event do not have to be considered. For MC simulations at low electron energies, the continuous slowing down approximation by Joy and Luo [Joy1989] is widely used. It semi-empirically modifies the Bethe stopping power [Bet1930] by introducing an energy dependence to the mean ionization potential J in Eq. 2.21, where s denotes the path length along the electron trajectory in Å, ρ is material density in g/cm^3, A is the (average) atomic weight, and Z the (average) atomic number of the target material.

$$\frac{dE_0}{ds} = -785\frac{\rho Z}{AE_0}\ln\left[\frac{1.166E_0}{J(E_0)}\right] \text{ eV/Å} \tag{2.21}$$

The result of the MC simulations yields the angular and energy distribution of the electrons leaving the sample. To calculate, for example, the transmitted STEM intensity, all transmitted electrons into the angular range of the STEM detector are summed up. Normalizing the summed-up number of electrons with respect to the number of incident electrons and consideration of the detector characteristics enable the comparison of the simulations with the measured STEM intensity. Considering a semiconductor STEM detector, the measured intensity does not only depend on the number of electrons but also on their energy E_i. The detected charge collection current

I_{cc} of the silicon STEM detector is given by Eq. 2.22 [Rei1998], where I_p denotes the incident electron current, ε_c describes the charge collection efficiency and $\overline{E_\iota}$ is the mean energy for electron-hole pair excitation ($\overline{E_\iota} = 3.6\ \mathrm{eV}$ in case of silicon). Moreover, the ζ_c takes into account the loss of electron-hole pair generation by electron backscattering.

$$I_{cc} = I_p(1 - \zeta_c)\left(\frac{E_i - E_{th}}{\overline{E_\iota}}\right)\varepsilon_c \tag{2.22}$$

The threshold energy E_{th} denotes the minimum electron energy that can be detected by the STEM detector and needs to be taken into account for the simulated STEM intensity. The threshold energy of the STEM detector is influenced by the metal protection layer (see Figure 2.5b), which leads to an estimated value for E_{th} of 500 eV. Electrons with lower energies are partially adsorbed in the protection layer and contribute to the calculated STEM intensity with linearly decreasing detection efficiency. Normalizing Eq. 2.22 to the collection current of the incident electrons (I_{cc}/I_{cc0}) simplifies Eq. 2.22 and yields Eq. 2.23, which is used to calculate the STEM and BSE intensities. The n_0 denotes the number of incident electrons with energy E_0. The STEM (or BSE) intensity is given by the number of transmitted (or backscattered) electrons n_i with energy E_i.

$$\frac{I_{cc}}{I_{cc0}} = \frac{\sum_i n_i(E_i - E_{th})}{n_0(E_0 - E_{th})} \tag{2.23}$$

3. Screened Rutherford differential electron scattering cross-sections at low electron energies

This chapter describes the calibration of the Monte Carlo (MC) simulations for calculations of high-angle annular dark-field scanning transmission electron microscopy intensities (HAADF STEM) at low electron energies (10-30 keV). The MC simulations are calibrated by means of the screening parameter in the screened Rutherford differential scattering cross-section (DSCS). Section 3.1 explains the necessity to readjust the MC simulations and gives motivation to this work. In section 3.2 the screened Rutherford DSCS is introduced. Moreover, equations for different screening parameters are shown and described. Section 3.4 presents the experimental procedures that were used to derive measured HAADF STEM intensity –thickness curves ($I_{\mathrm{HAADF}}(t)$ curves). First of all, wedge shaped specimens were prepared from bulk materials. Secondly, the wedge specimens were characterized and measured in HAADF STEM mode. Lastly, the measure $I_{\mathrm{HAADF}}(t)$ curves were extracted from the HAADF STEM images and compared to MC simulations using different screening parameters, as shown in Section 3.5 for all 9 studied materials (PTB7, DLC, MgO, Si, $SrTiO_3$, ZnO, Ge, Pd, and W). In section 3.6 the screening radius in the MC simulations was treated as a fit parameter in order to obtain the best possible agreement between the measured and simulated data. Moreover, a new expression for the screening radius was derived. In Section 3.7 the Z dependence of the HAADF STEM intensity is calculated. Section 3.8 validates the applicability of the newly derived screening radius expression for a larger detection angle range at different electron microscope. Finally, Section 3.9 summarizes Chapter 3.

3.1. Introduction

Quantitative evaluation of electron microscopy images requires the comparison of measured and simulated data. Image simulations are therefore a valuable addition to the experimental images enabling a deeper understanding of image formation as a function of imaging and material parameters. Monte Carlo (MC) simulations are well established for this purpose under experimental conditions, where Bragg contrast is absent (amorphous materials, crystalline materials under kinematic imaging conditions, and for large sample thickness). Under these conditions, MC simulations are frequently used in electron microscopy and provide insight into electron scattering. In the MC simulations, the electrons are traced by a sequence of single scattering events. Each scattering event is described by a differential scattering cross-section (DSCS). Calibration of the DSCS to particular experimental conditions is essential for reliable simulations of the measured data.

High-energy electrons (80 – 300 keV) propagating through a thin specimen experience only one or few scattering event(s). For such a case several simulations models are well established and yield reliable results [Rei1984, Gen1976, Del2013]. In the case of scanning transmission electron microscopy (STEM) at low electron energy (≤ 30 keV) multiple electron scattering occurs. For low energy STEM, MC simulations are predominantly used to simulate HAADF STEM intensities. In this chapter, we calibrate the screened Rutherford DSCS by comparison of measured and simulated HAADF STEM

intensities at low electron energies. The calibration parameter in the MC simulations is the screening parameter that needs to be calibrated to the particular experimental conditions.

Low energy STEM has gained increasing interest in the more recent past because high contrast and good signal-to-noise ratio are obtained especially for weakly scattering materials. Moreover, knock-on damage can be avoided [Kai2011, Bel2014]. At electron energies ≤ 30 keV the mean free path length is in the 1 – 20 nm range [Rei1998]. As a consequence, single-electron scattering is not valid anymore and even for sample thicknesses of a few 10 nm, multiple electron scattering has to be considered [Xu1989]. In MC simulations multiple electron scattering is modeled as a sequence of single scattering events defined by the scattering cross-section. Up to now, there is no general scattering cross-section that would yield reliable MC results for any arbitrary sample material, electron energy, or detection-angle range [Dil1974, Jac1973, Mic2003].

MC simulations are well suited for the calculation of low-keV STEM intensities and can be, hence, utilized for the quantification of low-keV STEM images. However, only a few examples are found in the literature, which deal with the quantification of STEM images at low electron energies. For example, Volkenandt *et al.* [Vol2010] used low-keV STEM and MC simulations to quantify the In concentration of InGaAs quantum wells. Holm [Hol2018] compared measured and simulated STEM intensities as a function of the collection angle in annular dark-field STEM images. Walker *et al.* [Wal2018] compared measured and simulated STEM intensity for 100 nm Si and Au film as a function of the detector offset. Xiao *et al.* [Xia2018] used MC simulations to enable quantitative low-keV STEM in a liquid cell. Morandi and Merli [Mor2007] studied quantitatively the contrast of GaAs/AlAs multilayer in low-keV STEM. For quantification of image information, e.g. chemical composition, the local sample thickness is a decisive parameter. A method for sample-thickness determination based on comparison of MC simulations with measured low-keV STEM intensities has been previously established in our group [Vol2014, Pfa2011]. Moreover, MC simulations are essential in low-keV STEM images for the assignment of material contrast for materials with only slightly different scattering properties, e.g., P3HT:PCBM-based absorber layers of organic solar cells [Pfa2012, Li2020].

The examples listed above show the necessity for a reliable model of electron scattering in MC simulations at electron energies at 30 keV and below. Considerable deviations between experimental and MC-simulated STEM intensities were observed in some cases (e.g. for Si at 15 keV [Vol2014], polymers PTB7 and PCBM at 30 keV [Li2020]) and the origin of these deviations are not clear up to now. To investigate the origin of these discrepancies, this work is concerned with the comparison of different DSCSs and the importance of the screening parameter in DSCSs in the MC simulations. To get access to DSCSs we have acquired low-keV HAADF STEM images to obtain high-angle annular dark-field intensities I_{HAADF} from materials with well-known composition using specimens with a known thickness profile. In addition, by comparison of experimental and simulated I_{HAADF} the effect of different screening parameters on the Z dependence of I_{HAADF} is evaluated.

3.2 Screening parameter

The selection of DCSC is decisive for reliable results of MC simulations. DSCSs can be subdivided into two groups. The first group is based on the Rutherford formula and the first Born approximation [Kyr2013]. The second group of DSCSs is Mott cross-sections [Mot1987], which are derived from partial wave calculations and are thus more precise. The inconvenience of the numerical form of the Mott DSCSs led to several attempts to represent the Mott DSCSs as a semi-analytical function [Kyr2013, Bro1994, Czy1990, Fit1985, Rei1998], usually based on the screened Rutherford model. Kyriakou *et al.* [Kyr2013] and Fitting and Reihardt [Fit1985] derived DSCSs that are particularly suitable for low electron energies by introducing an energy-dependent screening radius for the Thomas-Fermi screening parameter in the screened Rutherford DSCS. The latter DSCS is known as NISTelaFit because it was obtained by fitting to calculated NIST data of the Mott DSCS [Jab2004]. Currently, the NISTelaFit is considered to be the state-of-the-art elastic DSCS for low-electron energy scattering with a precision better than ± 3% [Kyr2013].

$$\frac{d\sigma}{d\Omega} = \left(\frac{eZ}{4\pi\varepsilon_0}\right)^2 \frac{1}{4{E_0}^2} \frac{1}{(1-\cos(\theta)+2\eta)^2} \tag{3.1}$$

$$\eta = \frac{\hbar^2}{8m_e E_0 e R^2} = const\frac{Z^{2/3}}{E_0} \tag{3.2}$$

The screening parameter (Eq. 3.2) in the screened Rutherford DSCS (Eq. 3.1) is given by the reduced Planck constant ħ, electron mass m_e, electron energy E_0, electron charge e, and screening radius R. The screening radius is a function of the average atomic number of the sample material Z and is usually described by Eq. 3.3, where a_0 denotes the Bohr radius and τ is the low-keV correction factor.

$$R = \frac{0.885 a_0 Z^{-1/3}}{\tau} \tag{3.3}$$

The physical meaning of the screening radius expresses the effect of the electron cloud of an atom on the scattering process of a charged particle and it decreases the electrostatic potential with increasing distance from the nucleus [Eve1955].

Substituting R in Eq. 3.2 by Eq. 3.3 reveals the dependence of η on Z and E_0, multiplied by a constant value. Several expressions for η exist in the literature. The basic screening parameters differ only by a constant which depends on the choice of the low-keV correction factor τ. Setting $\tau = 1$ yields the Thomas-Fermi screening parameter with $const = 4.34$ J [Kyr2013]

$$\eta_{\mathrm{TF}} = 4.34\frac{Z^{2/3}}{E_0} \tag{3.4}$$

For $\tau = 0.885$ the Bishop screening parameter [Joy1995] with $const = 3.4$ J is obtained (Eq. 3.4). A slightly higher prefactor $const = 5.44$ J is given by $\tau = 1.12$, which corresponds to the Nigam [Nig1959] screening parameter. Eq. 3.5 gives the more advanced Moliere screening parameter [Mol1947] that was obtained from the Thomas-Fermi screening parameter by introducing an additional *Z*-dependent term representing the deviation from the 1. Born approximation. Because Moliere's screening parameter was derived by exploiting the small-angle approximation, its use is restricted to electron energies above about $0.1\,Z^{4/3}$ keV. The parameter γ in Eq. 3.5 denotes the fine structure constant $(1/137)$ and $\beta = v/c$, where v is the electron velocity and c is the speed of light.

$$\eta_M = \frac{Z^{2/3}}{4}\left(\frac{\gamma}{0.885}\right)^2 \frac{1-\beta^2}{\beta^2}\left[1.13 + 3.76\left(\frac{\gamma Z}{\beta}\right)^2\right] \tag{3.5}$$

Seltzer [Sel1991] modified Moliere's screening parameter to achieve better results at low electron energies for high-Z materials by adding the term $\tau = E_0/m_e c^2$. The screening parameter suggested by Seltzer has a form of Eq. 3.6.

$$\eta_S = \frac{Z^{2/3}}{4}\left(\frac{\gamma}{0.885}\right)^2 \frac{1-\beta^2}{\beta^2}\left[1.13 + 3.76\left(\frac{\gamma Z}{\beta}\right)^2 \left(\frac{\tau}{\tau+1}\right)^{1/2}\right] \tag{3.6}$$

The screening parameter obtained by Fitting and Reinhardt [Fit1984] (Eq. 3.7) introduces an energy dependence to the Thomas-Fermi screening parameter in order to better describe scattering at lower electron energies ($E > 0.1$ keV). In Eq. 3.7 q_0 represents the wave vector of the incident electron and E the electron energy in eV. E_τ denotes a screening energy parameter, which is unique for each material. Values of E_τ for some materials can be found in [Fit1984].

$$\eta_{\mathrm{Fitt}} = \frac{1}{4}\frac{\hbar^2}{q_0^2}\left[\frac{0.9 + \exp\left(-\frac{E}{E_\tau}\right)}{a_0 Z^{-1/3} 0.885}\right]^2 = \eta_{\mathrm{TF}}\left[0.9 + \exp\left(-\frac{E}{E_\tau}\right)\right]^2 \tag{3.7}$$

The NISTelaFit screening parameter [Kyr2013] given by Eq. 3.8 is believed to be the state-of-the-art screening parameter for low electron energies with an applicability range of 50 eV – 30 keV. For energies $E > 1$ keV, η_{TF} (Eq. 3.4) is used, whereas for $E \leq 1$ keV an additional energy-dependent term in η_{TF} is included.

$$\eta_{\mathrm{NIST}} = \begin{cases} \eta_{\mathrm{TF}}, & E > 1\ \mathrm{keV} \\ \eta_{\mathrm{TF}}\left[1 + \exp\left(-\frac{E\ (\mathrm{eV})}{200} - 2.15\right)\right]^2, & E \leq 1\ \mathrm{keV} \end{cases} \tag{3.8}$$

All screening parameters listed above were implemented in the MC simulations and tested to fit the measured I_{HAADF}.

3.3 Experimental procedures

The experimental procedures comprise three steps. In the first step, a wedge-shaped specimen is milled from a bulk material with well-known chemical composition and material density ρ (cf. section 3.3.1). The wedge-shaped specimens allow to determine the local specimen thickness with high accuracy, which can be correlated with the local STEM intensity. Despite careful FIB milling, the prepared wedges are not ideally sharp but rounded at the wedge edge. In the following, the minimal thickness at the wedge edge is denoted as the wedge offset. In the second step, the prepared wedges were characterised. The wedge angle and wedge offset were determined from the top view SEM image. Additionally, the wedge thickness profile was measured by the energy-filtered transmission electron microscopy (EFTEM). In the third step, the I_{HAADF} is measured as a function of the local sample thickness and compared with the MC-simulated data.

3.3.1 Microscopes

The STEM measurements and sample preparation were performed in Helios G4 FX dual-beam instrument (Thermo Fisher Scientific, USA). This instrument is equipped with a field-emission gun and a focused Ga^+-ion beam system. In addition to the bulk stage, the Helios G4 FX is equipped with a compustage with a double-tilt sample holder for electron-transparent specimens that enable precise control of the orientation of crystalline materials. A semiconductor detector (STEM detector) positioned 40 mm below the pole piece detects the electrons that are transmitted through the specimen. The STEM detector is subdivided into 5 segments where the outermost is the HAADF segment. The detection-angle range of the HAADF segment depends on the working distance (WD) between the objective pole piece and the specimen. For WD = 4 mm, as used in all measurements, the detection-angle range of the HAADF segment is 65 – 272 mrad. Furthermore, the Helios G4 FX is equipped with an e-Flash^{HR} CCD camera (Bruker, Germany) implemented in a Bruker OPTIMUS^{TM} camera head enabling the acquisition of on-axis transmission electron diffraction (TED) patterns. TED patterns reveal information about the crystal orientation and crystal structure of the sample. The Helios instrument was also used for the two-beam measurements. Firstly, precise two-beam sample orientation was obtained using the double-tilt sample holder and checked with the TED pattern. Secondly, the dark field image under the two-beam condition was acquired.

The energy-filtered transmission electron microscopy (EFTEM) measurements were performed on a Titan3 80-300 (Thermo Fisher Scientific, USA) transmission electron microscope operated at 300 keV and equipped with a Gatan Tridiem 655 HR imaging filter. Measured thickness maps were obtained using a log-ratio routine implemented in the software suite Gatan DigitalMicrograph (version 1.85.1535).

3.3.2 Preparation of wedge samples

Wedge-shaped samples were prepared from 9 different materials with well-known compositions. The chosen materials cover a large range of atomic numbers Z. Low-Z materials comprise of PTB7 ($C_{41}H_{53}FO_4S_4$), diamond-like amorphous carbon (DLC),

MgO, and Si. Among intermediate-Z materials comprise $SrTiO_3$, ZnO, Ge, and Pd. Tungsten (W) was chosen as a representative of the high-Z materials. Among those materials, PTB7 and DLC have a disordered/amorphous atomic structure. Material densities ρ and (average) atomic numbers are compiled in Table 3.1. The average atomic numbers of compounds were calculated according to Eq. 3.9, where c_i and Z_i are concentrations in at.% and the atomic number of the particular element in the compound. The power $a = 2$ is related to the Rutherford model where Z has a quadratic dependence.

$$\bar{Z} = \sqrt[a]{\sum_i c_i Z_i^a} \tag{3.9}$$

Table 3.1 Sample materials and wedge sample properties. The top-view wedge angles and offsets were estimated by SEM from top-view secondary-electrons SEM images. The EFTEM wedge offset was determined by EFTEM.

Material	Average atomic number *Z*	Density ρ (g/cm^3)	Top-view wedge angle	Top-view wedge offset (nm)	Thickness contours wedge angle	EFTEM wedge offset (nm)
PTB7	5.3	1.12	20°±0.5°	30±10	-	35±10
DLC	6	1.9	25°±0.5°	12±5	-	15±4
MgO	10.2	3.58	24.8°±0.5°	10±5	-	-
Si	14	2.33	29.7±0.5°	22±10	28.2°±1.3°	35±5
$SrTiO_3$	20.6	5.11	24.7°±0.5°	20±10	23.7°±0.2°	35±10
ZnO	21.95	5.6	24.9°±0.5°	35±10	-	23±8
Ge	32	5.3	29.7°±0.5°	20±10	29.1°±0.4°	23±4
Pd	46	11.99	24.2°±0.5°	24±10	-	30±10
W	74	19.25	25°±0.5°	20±10	-	50±20

The FIB-milling procedure of wedge preparation was the same for all materials. First, a Pt-protection layer was deposited to protect the material from damage by the Ga^+ ions. Second, a lamella with a thickness of about 1.5 µm was prepared. Lamella preparation is a common procedure and details can be found elsewhere [May2007]. The prepared lamella was further thinned in a wedge-like shape with a wedge angle α. The milling parameters have to be chosen carefully in order to prepare a smooth and sharp wedge edge. The best results were obtained for a 5 keV and 63 pA ion beam for final polishing.

Even though the final wedge polishing was performed with rather low-energy ions, implantation of Ga ions into the milled material is unavoidable [Bas2011]. To estimate Ga^+-ion implantation, simulations were performed using the stopping and range of ions in matter (SRIM) formalism [Zie2010] to determine the penetration depth of 5 keV Ga^+ ions into polymer PTB7. In order to investigate the worst case, the PTB7 material was chosen because the Ga^+-ion implantation is more pronounced for light materials. The average penetration depth at a grazing angle of 1° was found to be only

a few nm. The influence of Ga^+ implantation on the HAADF-STEM intensity measurements is most severe at the thin wedge edge. Considering a wedge-edge thickness of 20 nm and a Ga^+-implantation concentration into PTB7 of 7 %, the error in HAADF-STEM intensity is only 5 %. For larger sample thicknesses, the influence of the Ga^+ implantation is even lower. Already at 100 nm, the error for sample-thickness determination is reduced to 1.3 %, and it further decreases with even larger sample thicknesses. As a consequence, Ga^+ implantation was not considered in the evaluation of the HAADF-STEM intensities.

3.3.3 Wedge characterization

After wedge preparation, the wedge angle and the wedge offset were characterised to enable precise determination of the local wedge thickness. Especially for materials with high Z and ρ, the local thickness at the wedge tip has to be known with high accuracy. Moreover, the surface of the polished wedge has to be verified to be as smooth as possible.

The wedge properties can be determined by the acquisition of top-view secondary electron (SE)-SEM images. Figure 3.1 shows as an example SE-SEM images of the $SrTiO_3$ wedge. The wedge angle can be measured from the top-view SE-SEM image in Figure 3.1a. Enlarging the image in the region of the wedge edge, the wedge offset can be obtained. The wedge angle for the shown $SrTiO_3$ wedge is $\alpha = 24.7° \pm 0.5°$ and the wedge offset is $t_0 = 20 \pm 10$ nm. The determined wedge angles and wedge offsets from the top-view SE-SEM image of all prepared wedges are summarized in Table 3.1. This simple characterisation method has one disadvantage. In the top-view SE-SEM image the Pt protection layer is imaged and not the wedge of the material to be analysed below. Due to different sputtering properties of the Pt layer and the material below, the wedge angle and wedge offset of the material below could differ from the values determined from the Pt layer. The smoothness of the milled surfaces can be checked by tilting the wedge in both directions with respect to the top-view position. Figure 3.1b and c show SE-SEM images of the $SrTiO_3$ wedge tilted to -8° and +17° and reveal smooth wedge surfaces. The error for the wedge-angle determination was estimated to be $\pm 0.5°$. The uncertainty of the wedge offset is related to the shape of the wedge tip and was estimated between ± 5 nm and ± 10 nm. The uncertainties of the wedge angles and wedge offsets represent the ability to deduce the correct values of the wedge angles and wedge offsets from the top view SE SEM image. The relatively large uncertainty of the wedge offset comprises also possible small effects of Ga^+ implantation during FIB milling.

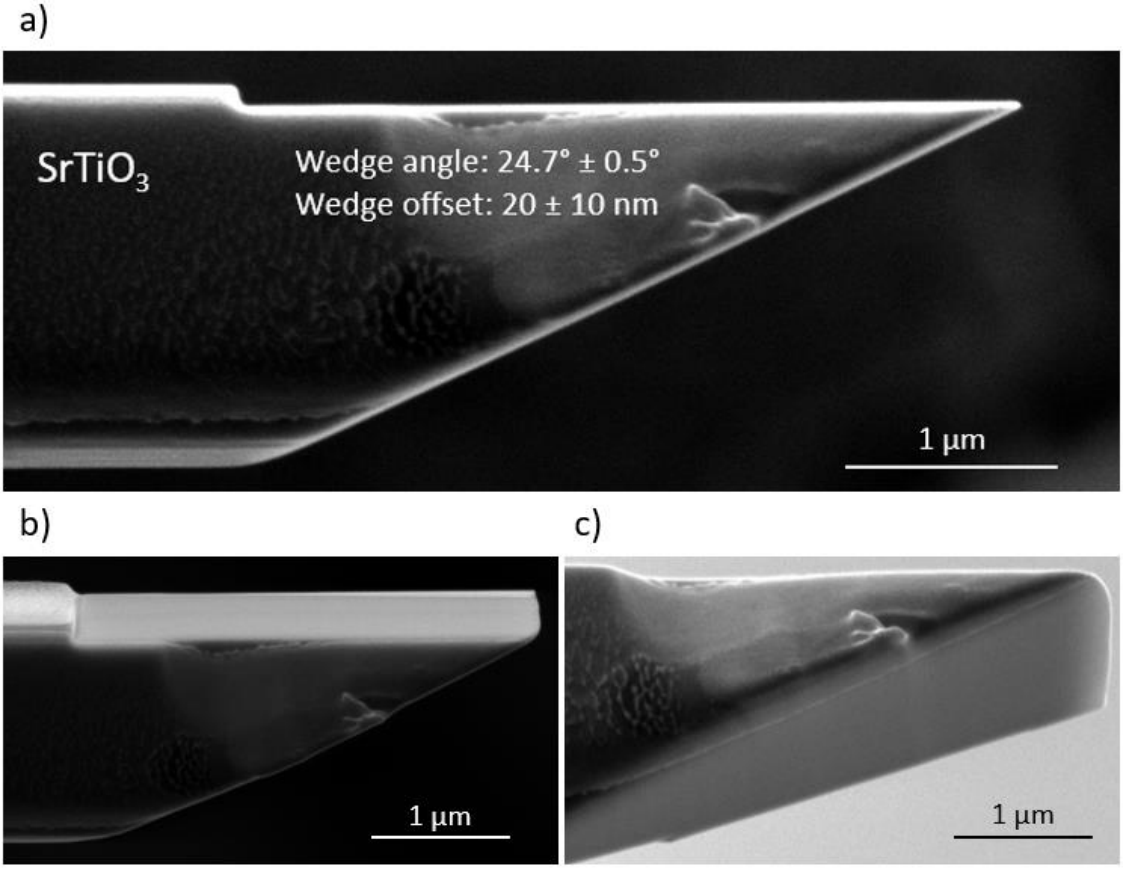

Figure 3.1 Top-view SEM image wedge characterization. a) 5 keV SE-SEM top-view image of the FIB-prepared $SrTiO_3$ wedge, enabling the determination of wedge angle and wedge offset. Adapted from a publication [Čal2019]. The smoothness of the milled surfaces is verified by 5 keV SE-SEM images acquired at b) -8° and c) +17° tilt with respect to the top-view orientation.

Another technique for sample-thickness and wedge-angle determination is the acquisition of STEM images acquired under two-beam conditions, where only one reflection together with the zero-order beam is strongly excited while other Bragg reflections show only weak intensities. In such a case, the bright-field or dark-field STEM intensity oscillates as a function of the specimen thickness. Local intensity minima appear in dark-field STEM images for thicknesses t_n given by Eq. 3.10 where n is an integer number and ζ_g is the extinction length for the Bragg reflection excited in a two-beam condition. The extinction length for particular Bragg reflection is given by Eq. 3.11, where λ is the electron beam wavelength, V_e is the volume of the unit cell, θ_B denotes the Bragg angle for the particular Bragg reflection, and $F_{s,g}$ denotes the structure factor of the unit cell for the particular Bragg reflection g.

$$t_n = n\,\zeta_g \tag{3.10}$$

$$\zeta_g = \frac{\pi V_e \cos\theta_B}{\lambda F_{s,g}} \tag{3.11}$$

The position of the intensity minima can be used to determine the local thickness by the following procedure. First, the wedge has to be tilted into a two-beam condition. Figure 3.2a shows a diffraction pattern of the $SrTiO_3$ wedge with the (200) Bragg reflection and zero-order beam strongly excited while other Bragg reflections show only weak intensities. Second, a DF-STEM image is taken that shows thickness contours at the thin wedge region (Figure 3.2b). An intensity-line profile along the red dashed line in Figure 3.2b was extracted, where the thickness increases from right to left. By converting the spatial coordinate x into a local wedge thickness t according to $t = x\tan(\alpha)$, an oscillating intensity-thickness line profile (Figure 3.2c) is obtained. The wedge-thickness change between intensity minima in the intensity profile is constant and 25.4 nm for $SrTiO_3$. The wedge angle α was treated as a parameter and was modified until the spacing of the intensity minima was 25.4 nm. Using the thickness-contour method, the wedge angle of the $SrTiO_3$ wedge was determined to be $\alpha = 23.7° \pm 0.2°$. The wedge offset can be also deduced from the curve in Figure 3.2c. For the $SrTiO_3$ wedge, the offset based on the thickness-contour method is $t_0 = 12 \pm 10$ nm. The drawback of this method is that it is only applicable to crystalline materials. It is also less accurate due to the effect of a non-zero excitation error on the extinction distance.

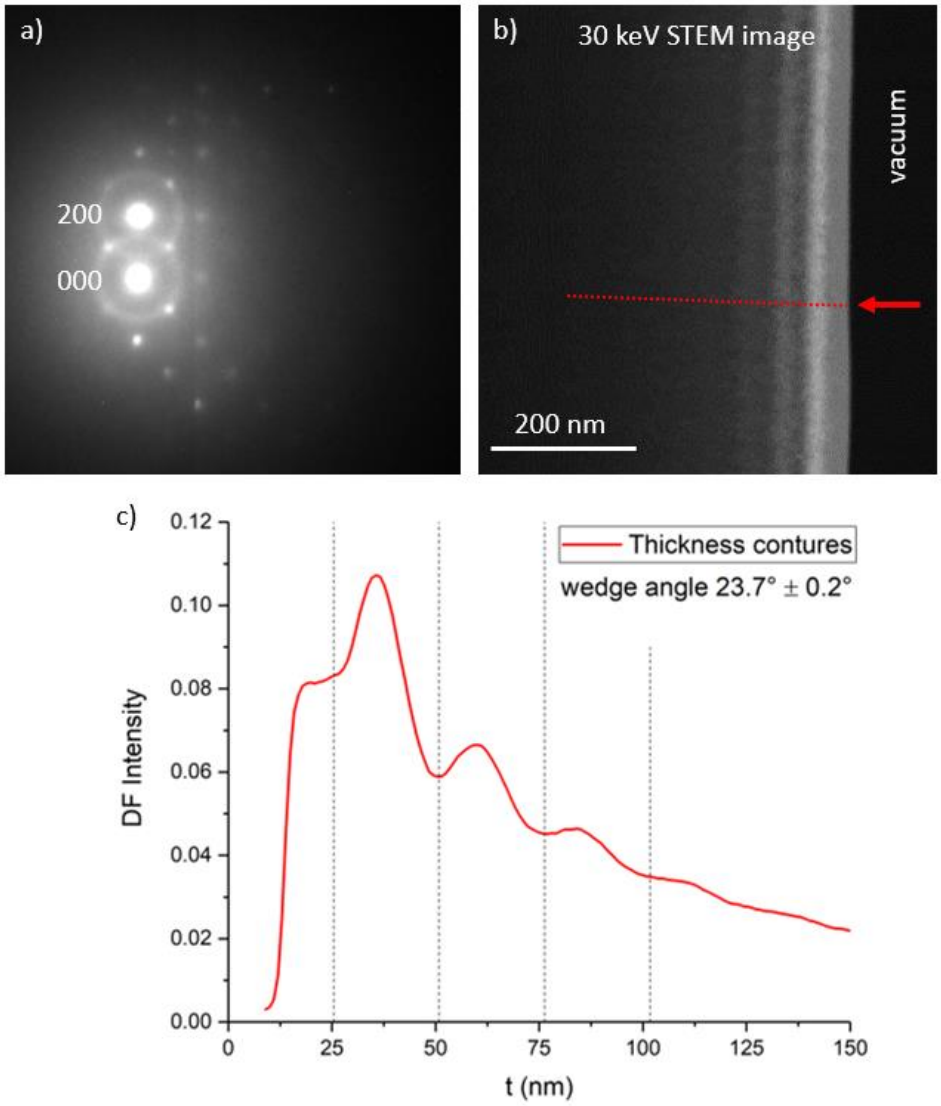

Figure 3.2 Wedge characterisation using thickness contours. a) Diffraction pattern of a $SrTiO_3$ wedge tilted into a (200) two-beam condition. b) Two-beam dark-field STEM image of the $SrTiO_3$ wedge edge where thickness contours are visible. c) Intensity line profile along the red-dashed line in b) as a function of the sample thickness. The vertical dashed lines indicate the position of the intensity minima. Fitting the minima in the thickness-contour curve to the vertical lines enable the determination of the wedge angle.

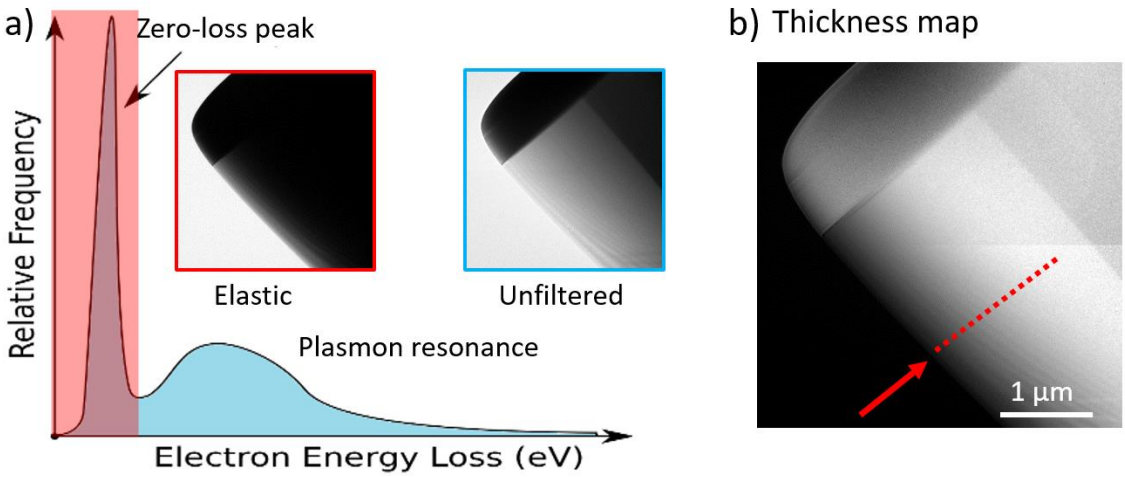

Figure 3.3 Energy-filtered transmission electron microscopy (EFTEM) measurement. a) Electron energy loss spectra of the transmitted electrons. The unfiltered image in the blue frame was acquired using all transmitted electrons. Only the electrons in the zero-loss peak of the spectrum were selected for the elastic image in the red frame. b) Thickness map obtained by EFTEM at 300 keV from the $SrTiO_3$ wedge based on the elastic and unfiltered images in a). The red arrow indicates the direction of the thickness-line profile that is shown in Figure 3.4.

Alternatively, the wedge offset can be determined from a thickness map obtained by energy-filtered transmission electron microscopy (EFTEM). The thickness map can be deduced from the log-ratio routine in the software suite Gatan DigitalMicrograph (version 1.85.1535). In this routine, an unfiltered and a zero-loss filtered image from the same sample region are acquired. Figure 3.3a shows an electron energy loss spectrum (EELS) of the transmitted electrons, where the first peak is the zero-loss peak. Using EFTEM the electrons in the zero-loss peak can be filtered and only the zero-loss electrons (the red-highlighted region in the EELS) contribute to the image formation. By considering the logarithm of the intensity ratio between unfiltered I_t and zero-loss I_{ZL} images according to Eq. 3.12, a relative thickness map is obtained.

$$t = \lambda_p \ln\left(\frac{I_t}{I_{ZL}}\right) \tag{3.12}$$

A thickness map corresponding to the unfiltered and zero-loss images of the $SrTiO_3$ wedge in Figure 3.3a is shown in Figure 3.3b. Each pixel in the thickness map contains the information on the local wedge thickness in units of the mean free path for plasmon scattering λ_p. For wedge-shaped specimen λ_p can be obtained from geometry considerations according to Eq. 3.13, where α is the wedge angle and f is the fitted slope of the wedge.

$$\lambda_p = \frac{\tan(\alpha)}{f} \tag{3.13}$$

Figure 3.4 shows the thickness profile of the $SrTiO_3$ wedge as a function of the distance x that was extracted along the red dashed line in the thickness map in Figure 3.3b. By fitting the thickness profile with a linear function (black curve in Figure 3.4) the slope

$f = 0.004556$ is determined. Considering the wedge angle $\alpha = 24.7°$ obtained by the top-view image yields $\lambda_p = 100.9 \pm 1.2$ nm at 300 keV for the $SrTiO_3$ wedge. Calibrating the thickness map with λ_p rescales the y axis in Figure 3.4. The smoothness of the wedge surfaces can be also assessed from the thickness profile. The wedge profile shown in Figure 3.4 reveals only light surface roughness. The wedge beginning is indicated by the steep increase of the thickness profile and is not ideally sharp, rather rounded with an offset value of $t_0' = 35 \pm 10$ nm. The EFTEM results for the wedge offsets of other wedge-shaped specimens are summarized in Table 3.1.

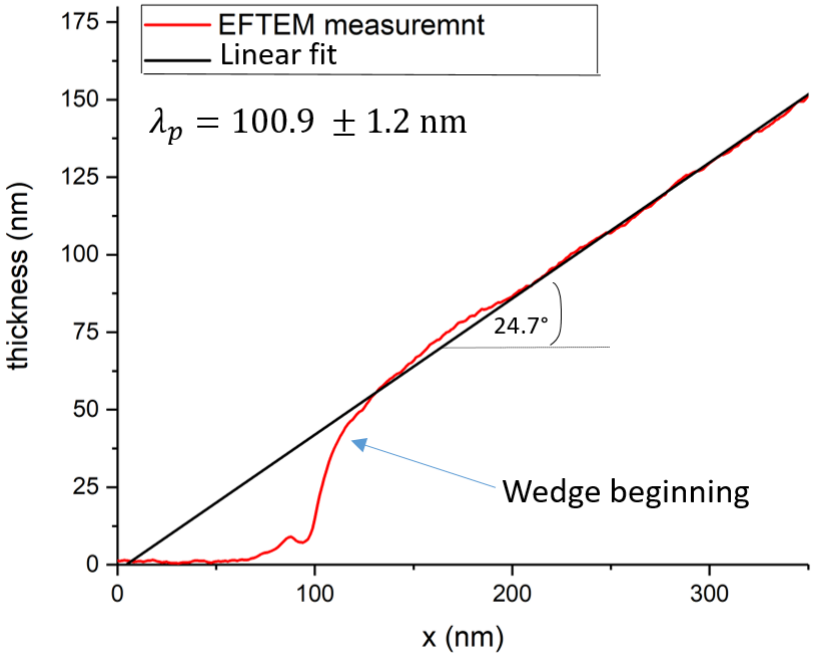

Figure 3.4 EFTEM $SrTiO_3$-thickness profile. The thickness profile of the $SrTiO_3$ wedge as a function of the spatial coordinate x is shown in red. The linear fit (black curve) is necessary for the determination of the mean free path for plasmon scattering λ_p that is used to rescale the y axis of the plot. With knowledge of the wedge angle and λ_p, the wedge offset can be evaluated. Adapted from a publication [Čal2019].

Among the wedge characterisation methods presented above, the wedge angle and wedge offset results determined from the top-view SE-SEM image (cf. Table 3.1) are considered to be the most reliable and will be used in further evaluations. The EFTEM measurements of crystalline materials are affected by diffraction contrast. The thickness contours of two-beam STEM images are strongly dependent on the accuracy with which the two-beam condition can be set up. However, for amorphous materials (DLC and PTB7), the determined wedge offsets determined from the top-view SEM image and EFTEM agree well.

3.3.4 Measurement of I_{HAADF}-thickness line profiles

I_{HAADF}-thickness line profiles are measured on the prepared wedge samples in HAADF-STEM mode. Figure 3.5a shows a 30 keV HAADF-STEM cross-section image of the $SrTiO_3$ wedge where the black region represents vacuum. The dark layer in the upper part of the image is the Pt-protection layer. Below is the studied $SrTiO_3$ wedge, where

the wedge thickness increases from left to right. The HAADF-STEM intensity was extracted by an intensity-line scan averaged over a width of 20 pixels along the red dashed line in Figure 3.5a. The line-scan distance x from the wedge edge can be converted to the local wedge thickness t according to $t = t_0 + x\tan(\alpha)$ where t_0 and α are the previously determined wedge offset and wedge angle (cf. Table 3.1). The obtained measured I_{HAADF}-thickness dependence is shown in Figure 3.5b. In general, the I_{HAADF}-thickness profiles first increase as expected with increasing sample thickness. A maximum is then reached before I_{HAADF} decreases for larger wedge thicknesses. The origin of the I_{HAADF} reduction is electron scattering in very large angles beyond the scattering-angle range of the HAADF segment of the STEM detector. The sample thickness at the I_{HAADF} maximum depends strongly depends on the material properties and primary electron energy. The error of the measured data originates from the errors of the wedge angle and thickness-offset (Table 3.1) and is further carried through the data evaluation calculations.

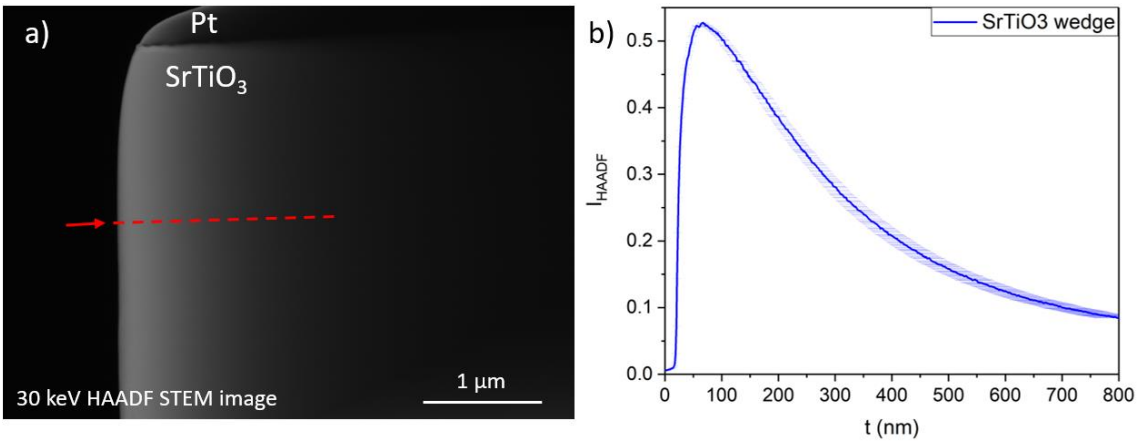

Figure 3.5 HAADF-STEM intensity as a function of sample thickness. a) 30 keV HAADF-STEM image of the $SrTiO_3$ wedge, where the thickness of the wedge increases from left to right. b) HAADF-STEM intensity-line profile as a function of the local wedge thickness taken along the red dashed line in a). Adapted from a publication [Čal2019].

To enable the comparison of the measured $I_{\mathrm{HAADF}}(t)$ with simulations, normalization of the measured I_{HAADF} data is necessary. Moreover, special attention has to be paid to the contrast and brightness settings for the correct quantification of the measured I_{HAADF}. The contrast/brightness settings have to be adjusted to detect the full range of the HAADF intensity, whereas over- and undersaturation of the STEM detector must be strictly avoided. The contrast/brightness settings have to be kept constant during the measurements. Normalization of the HAADF-STEM intensity with respect to the primary electron beam is carried out according to Eq. 3.14

$$I_{\mathrm{HAADF}} = \frac{I_m - I_b}{I_w c_g - I_b} \tag{3.14}$$

where I_m is the measured HAADF-STEM intensity, I_b is a reference black intensity, and I_w is a reference white intensity. I_w and I_b are obtained from a reference image where the STEM detector is directly illuminated by the primary beam without a sample. The

reference image has to be acquired before every $I_{\mathrm{HAADF}}(t)$ measurement with unchanged imaging conditions. A reference image corresponding to the HAADF-STEM image in Figure 3.5a is shown in Figure 3.6. I_b is determined by averaging intensity values of the pixels in the inactive area of the STEM detector appearing dark (pixels circumscribed by the white dashed line). In analogy, I_w is determined from the active regions of the STEM detector (here HAADF segment) that are exemplarily marked by black dashed squares. We note that only a small fraction of the HAADF segment is visible in Figure 3.6 because the field of view is limited by the pole piece and apertures. Figure 3.6 also shows that parts of the HAADF segment of the STEM detector are covered by bars and inactive narrow line-like regions occur between the active regions. For this reason I_w has to be corrected by a geometrical correction factor c_g. For our system c_g is 0.84 because 8.5 % of the HAADF segment are completely blocked by bars and 7.5% are inactive due to the line-like regions. All measured HAADF-STEM intensities were normalized using Eq. 3.14.

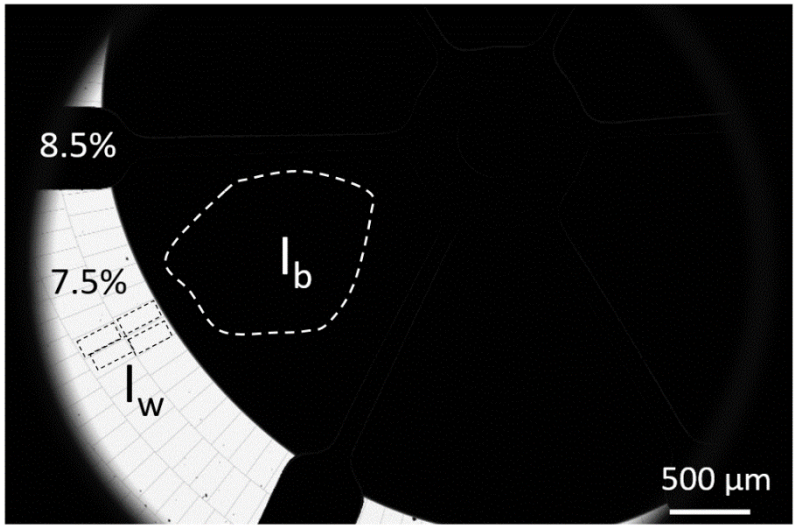

Figure 3.6 Reference image obtained by directly scanning a part of the STEM detector. A reference image is obtained by direct illumination of the STEM detector. The bright region corresponds to a small section of the activated HAADF segment of the STEM detector, from which I_w is obtained. The black value I_b is determined from the inactive regions (the region in the white dashed line). About 8.5% of the HAADF STEM detector is shielded by bars and 7.5% of the HAADF-STEM segment is inactive. Adapted from a publication [Čal2019].

3.3.5 Influence of sample orientation on the HAADF-STEM intensity

The HAADF-STEM intensity of crystalline materials depends on the sample orientation. However, MC simulations do not take into account crystal structures and, hence, Bragg-diffraction effects cannot be taken into account. Nevertheless, MC simulations can be used to simulate the STEM intensity of crystalline materials under incoherent imaging conditions (i.e. in the absence of Bragg reflections contributing to the image intensity). To examine the influence of sample orientation on the HAADF-STEM intensity, we have compared $I_{\mathrm{HAADF}}(t)$ curves derived from HAADF-STEM images

of a Si-wedge specimen under zone-axis and off-zone-axis sample orientation. The sample orientations were examined by taking transmission electron diffraction (TED) patterns. Figure 3.7a and b show TED patterns of the Si wedge tilted to zone-axis and off-zone-axis conditions, respectively. The white circle represents the inner radius of the HAADF-detector segment. For the Si wedge oriented in zone-axis, the TED pattern reveals several Bragg reflections within the HAADF-detector segment. To avoid the contributions of these Bragg reflections, the wedge was tilted to off-zone-axis orientation. However, for materials with strong Bragg reflections (including Si) even at off-zone-axis orientation, the Bragg reflections cannot be completely avoided and still contribute to the measured HAADF-STEM intensity. Figure 3.7c shows $I_{\mathrm{HAADF}}(t)$ derived from the HAADF-STEM images acquired under zone-axis (green curve) and off-zone-axis (blue curve) sample orientations. For comparison, an MC simulated curve is plotted in red. The difference between the plotted $I_{\mathrm{HAADF}}(t)$ curves are at the maximum of the curve. Relating the curves to the particular TED patterns and considering, that the MC-simulated curve corresponds to ideal incoherent imaging, reveals that the presence of Bragg reflections lowers the $I_{\mathrm{HAADF}}(t)$ curve at the curve maximum.

Before the acquisition of HAADF-STEM images, the sample orientation was checked by taking TED patterns and if needed, the sample was tilted to minimize the excitation of Bragg reflections on the HAADF-detector segment. $I_{\mathrm{HAADF}}(t)$ curves obtained from HAADF STEM images under off-zone-axis sample orientations are comparable with the MC-simulated data.

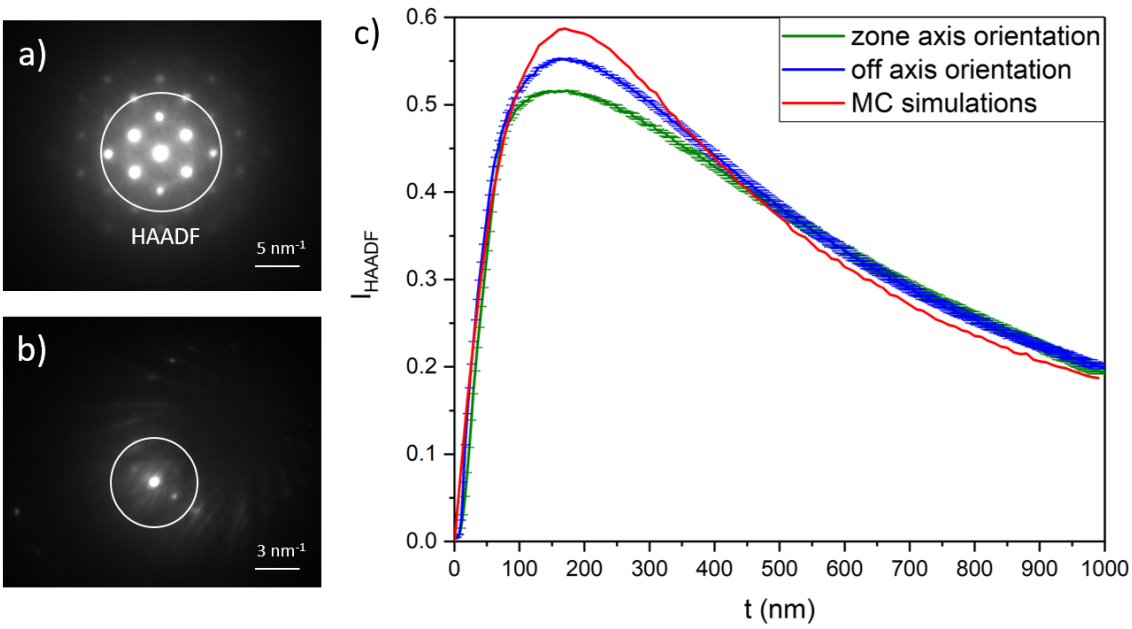

Figure 3.7 Influence of sample orientation on the HAADF-STEM intensity. Transmission electron diffraction patterns of the Si wedge specimen tilted in (a) zone-axis, (b) off-zone-axis orientation. The white circle represents the inner radius of the HAADF detector segment. c) Comparison of the measured $I_{HAADF}(t)$ curves for different sample orientations (zone-axis – green, off-zone-axis – blue) and MC simulations (red). Adapted from a publication [Čal2019].

3.4 MC-simulated I_{HAADF}-thickness profiles

Along with the measured $I_{\mathrm{HAADF}}(t)$ curves, MC simulations with different screening parameters were carried out to test their applicability to correctly predict the $I_{\mathrm{HAADF}}(t)$ curves for various sample materials (material properties in Table 3.1) and electron energies. In this work, we have adopted the NISTMonte simulation package [Rit2005] and implemented the screening parameters mentioned in section 3.2 into the screened Rutherford scattering cross-section. The energy loss of the scattered electrons is described by the Joy and Luo [Joy1989] continuous slowing down approximation. To obtain simulated $I_{\mathrm{HAADF}}(t)$ curves, the MC simulations were performed in the thickness range of 1 – 1000 nm with 2 nm thickness intervals. By integrating the angular distribution of the transmitted electrons over the detection-angle range of the HAADF detector segment (65 – 272 mrad), $I_{\mathrm{HAADF}}(t)$ is calculated at each sample thickness.

In order to achieve a more precise comparison between measured and simulated data, the properties of the semiconductor STEM detector have to be considered in the simulated intensity. The intensity detected by the semiconductor STEM detector is the sum of contributions of all transmitted electrons that are traced in the MC simulations with energy E_i [Rei1998]. The detected intensity is given by the detected charge which depends on the number of electrons n_i with energies E_i impinging on the semiconductor STEM detector. Normalization of the detected intensity I to the primary electron intensity I_0 is given by Eq. 3.15

$$\frac{I}{I_0} = \frac{\sum_i n_i (E_i - E_{th})}{n_0 (E_0 - E_{th})} \tag{3.15}$$

where E_0 is the incident electron energy, n_0 denotes the number of incident electrons, and E_{th} represents the cut-off energy of the STEM detector caused by a metal protection layer. The cut-off energy of the STEM detector was experimentally determined by measuring the grey-value dependence on the primary electron energy while keeping the contrast/brightness settings unchanged. The measured dependence is linear with an intersection of the energy axes at $E_{th} = 500\ \mathrm{V}$, which is the cut-off energy of the STEM detector. Electrons with lower electron energy, that reach the STEM detector, are partially adsorbed in the protection layer and contribute to the calculated HAADF-STEM intensity with linearly decreasing detection efficiency.

MC-simulated $I_{\mathrm{HAADF}}(t)$ curves with different screening parameters (introduced in section 3.2) are plotted in Figure 3.8. In the first column (Figure 3.8a, c, and e), MC-simulated data for Si at 30, 20, and 10 keV electron energies are presented. The second column (Figure 3.8b, d, and f) contain results for Ge using the same conditions. The MC-simulated $I_{\mathrm{HAADF}}(t)$ curves for different screening parameters in the differential Rutherford cross-section are colour-coded in the following manner: Bishop – red, Moliere – orange, Nigam – green, NISTelaFit – light green, Seltzer – black, and Thomas Fermi – purple. In addition, MC simulations using Mott scattering cross-sections derived by Czyzewski [Czy1990] are plotted in blue for comparison. The plots in Figure 3.8 reveal that, with the used experimental conditions (electron energy and detection-angle range), several of the screening parameters lead to similar results. This applies in

particular to the Bishop and the NISTelaFit screening parameters, which yield similar $I_{\mathrm{HAADF}}(t)$ curves for both studied materials (Si and Ge) at 30 and 20 keV. Similarly, the $I_{\mathrm{HAADF}}(t)$ curves derived from the Thomas-Fermi, Moliere, and Seltzer screening parameters are identical. An explanation for this behaviour is that Moliere and Seltzer screening parameters are derived from the Thomas-Fermi screening parameter. For Ge at 10 keV (Figure 3.8f) the situation is the same, the Bishop and NISTelaFit curves are identical. Furthermore, the Thomas-Fermi result is only slightly shifted from the identical Moliere and Seltzer $I_{\mathrm{HAADF}}(t)$ curves. In Figure 3.8e, where the results for Si at 10 keV are displayed, only the $I_{\mathrm{HAADF}}(t)$ curves calculated using the Moliere and Seltzer screening parameters overlap. Interestingly, the $I_{\mathrm{HAADF}}(t)$ curves calculated using the Mott scattering cross-section yield the same result as the Bishop and NISTelaFit screening parameters for Si at 30 and 20 keV and for Ge at 10 keV. For Si at 10 keV the Mott scattering cross-section result is identical with the NISTelaFit screening parameter.

The results in Figure 3.8 indicate that for our experimental conditions screening parameters derived from the Thomas-Fermi screening parameter (Moliere and Seltzer) give similar results. The same applies to Bishop and NISTelaFit screening parameters. Therefore, only Bishop, Nigam, and Thomas-Fermi screening parameters are compared in the following $I_{\mathrm{HAADF}}(t)$ plots. The Mott scattering cross-section is not shown in the following $I_{\mathrm{HAADF}}(t)$ plots because it does not represent the measured data consistently and is not easily adaptable as compared to the Screened Rutherford scattering cross-section.

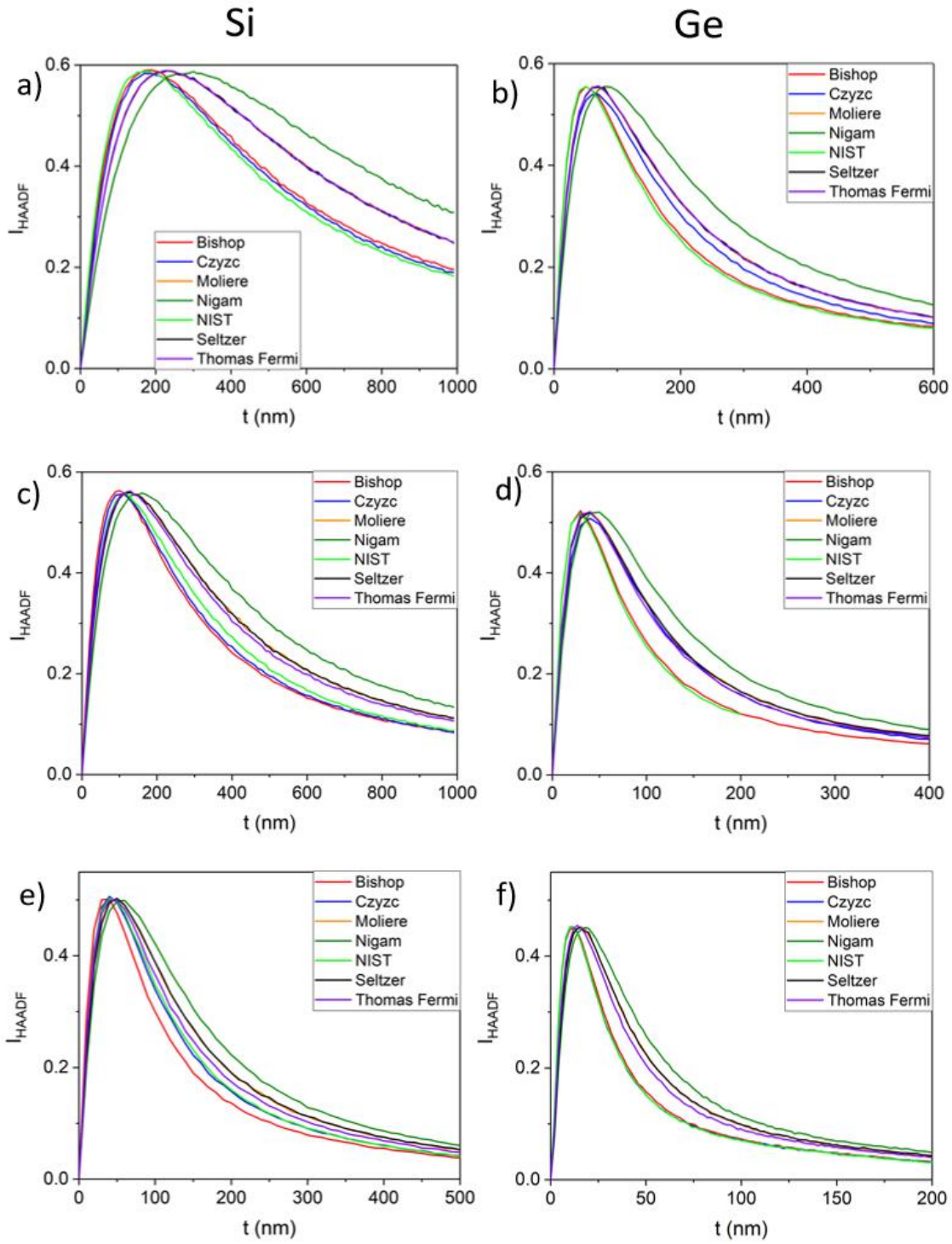

Figure 3.8 Comparison of MC-simulated $I_{HAADF}(t)$ curves with different screening parameters. a), c) and e) show results for Si at 30, 20, and 10 keV respectively. In the same way, results for Ge are shown in b), d), and f). Calculated $I_{HAADF}(t)$ curves using different screening parameters (Bishop – red, Moliere – orange, Nigam – green, NISTelaFit – light green, Seltzer – black, and Thomas-Fermi – purple). In addition, calculated $I_{HAADF}(t)$ curves using Mott differential scattering cross-sections are displayed in blue.

3.5. Experimental results

In this section, the experimental results are presented and compared with MC-simulated $I_{\mathrm{HAADF}}(t)$ curves for all studied materials listed in Table 3.1. Figures 3.9 – 3.17 show in (a) the top-view SE-SEM image of the wedge with a TED pattern revealing the wedge crystal orientation for the crystalline materials (PTB7 and DLC have disordered atomic structures), in (b) a 30 keV HAADF-STEM image with indicated position of the line scan (white dashed line). Plots in (c), (d), and (e) show the measured $I_{\mathrm{HAADF}}(t)$ curves (in blue) acquired at 30, 20, and 10 keV, respectively, with corresponding simulated $I_{\mathrm{HAADF}}(t)$ curves using the Bishop (red), Thomas-Fermi (purple), and Nigam (green) screening parameters. The error bars of the measured data indicate the uncertainties of the determined wedge angles and wedge offsets. The wedge offset error is constant at all sample thicknesses, whereas the wedge angle error increases with increasing sample thickness. The Sum of these errors for all measured data is shown in the following plots.

3.5.1 PTB7 ($C_{41}H_{53}FO_4S_4$)

The preparation of a wedge-shaped sample from polymer materials is challenging and requires low-voltage (5 keV) milling. The PTB7 wedge is shown in the top-view SE SEM image in Figure 3.9a. The black regions represent the Si support material that is not fully milled. The 30 keV HAADF-STEM image in Figure 3.9b shows the wedge cross-section with indicated line scan (dashed line) in the PTB7 layer. The PTB7 is deposited on a Si support. On top of the PTB7 layer is the Pt-protection layer. Comparison of measured and simulated $I_{\mathrm{HAADF}}(t)$ curves in Figure 3.9c-e reveal that none of the screening parameters describes the measured data well. However, the closest result is obtained with the Bishop screening parameter.

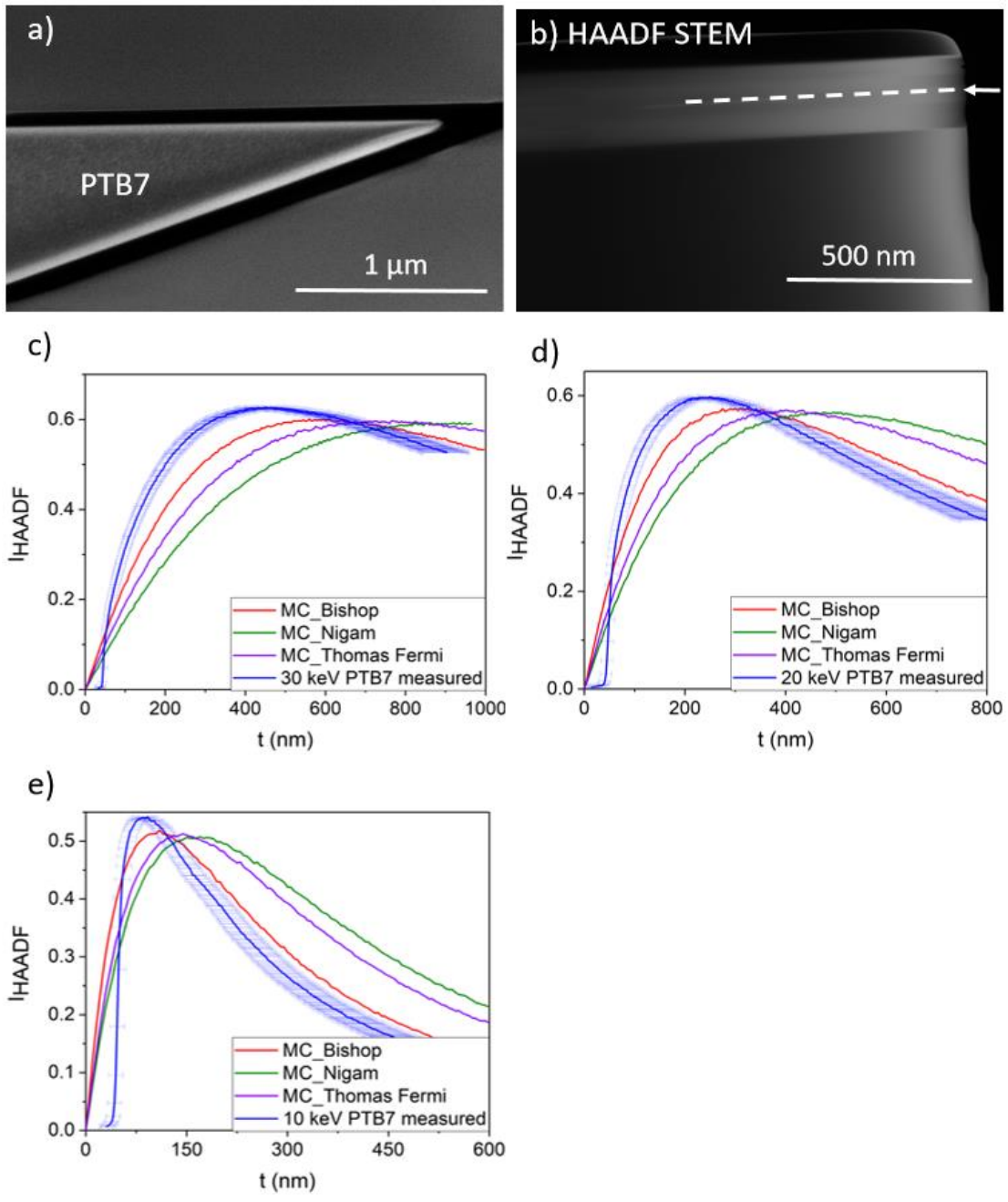

Figure 3.9 Experimental results and MC simulations for PTB7. a) Top-view SE-SEM image and b) HAADF-STEM image of the PTB7 wedge-shaped specimen. c)-e)

Comparison of measured and MC-simulated $I_{HAADF}(t)$ curves with Bishop (red), Thomas-Fermi (purple), and Nigam (green) screening parameters at 30, 20, and 10 keV electron energy.

3.5.2 Diamond-like-carbon (DLC)

The DLC wedge was cut with a sharp wedge edge with only 12 ± 5 nm wedge offset, as visualized in Figure 3.10a. The 30 keV HAADF STEM image (Figure 3.10b) shows a smooth grey-scale transition throughout the whole DLC layer that is confirmed by smooth measured $I_{\mathrm{HAADF}}(t)$ curves (blue) in Figure 3.10c-e. The plots in Figure 3.10c-e resemble the results for PTB7, where none of the simulated curves represents the measured data sufficiently well. The closest conformity is given by the Bishop screening parameter. However, for all studied electron energies the maximum of the measured curves is shifted to lower thicknesses as predicted by the simulations.

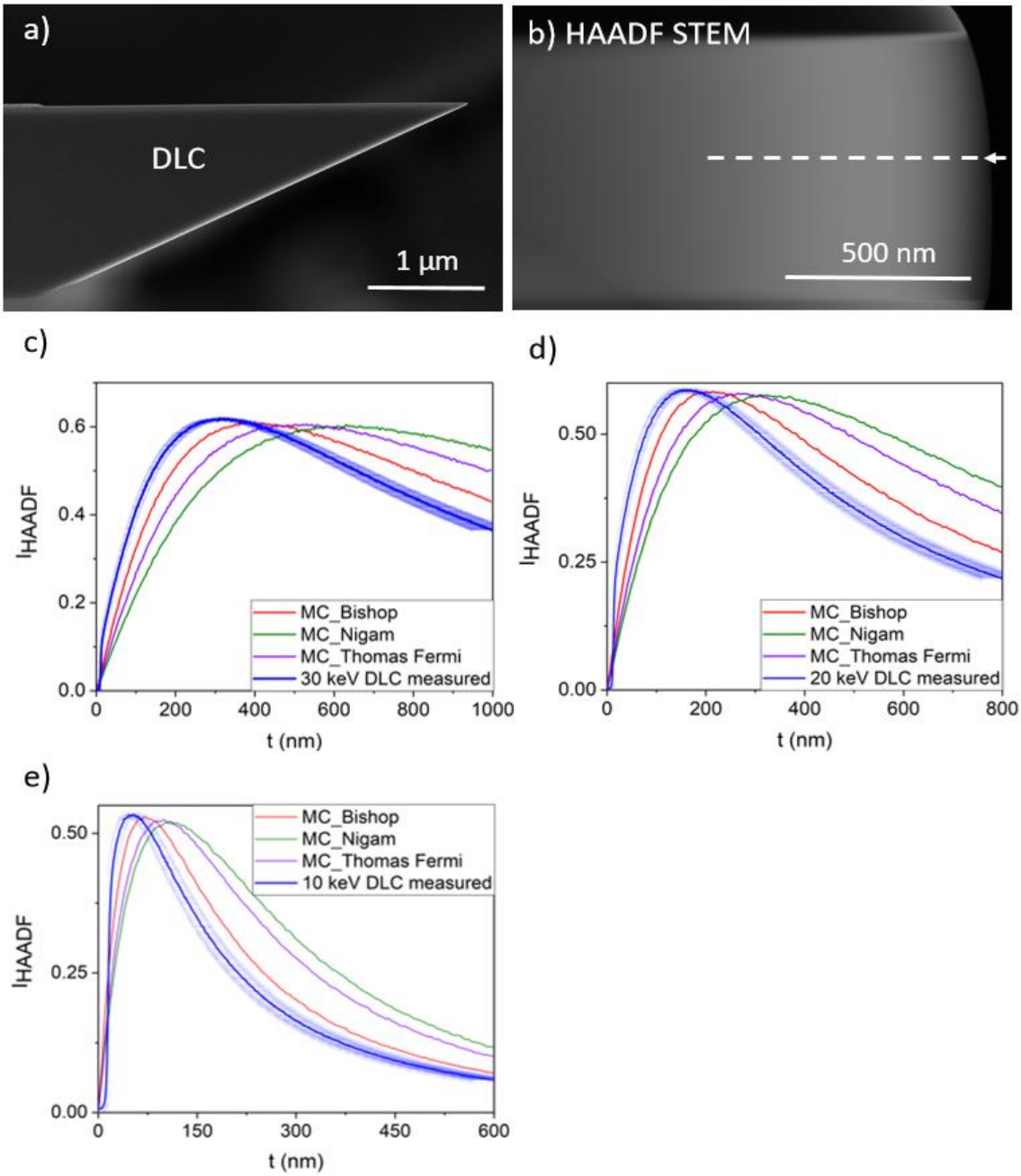

Figure 3.10 Experimental results and MC simulations for DLC. a) Top-view SE-SEM image and b) HAADF-STEM image of the DLC wedge-shaped specimen. c)-e) Comparison of measured and MC-simulated $I_{HAADF}(t)$ curves with Bishop (red), Thomas-Fermi (purple), and Nigam (green) screening parameters at 30, 20, and 10 keV electron energy.

3.5.3 MgO

The preparation of a sharp and smooth MgO-wedge sample (Figure 3.11a) was challenging. While FIB milling, either the MgO structure becomes amorphous at a certain sample thickness, or the milled surface suffers from redeposition. As a result, the wedge tip (up to a wedge thickness of about 100 nm) in the 30 keV HAADF STEM image (Figure 3.11b) looks rough and not homogeneous. Moreover, the TED pattern (inserted in Figure 3.11a) reveals some excited Bragg reflections that are situated on the HAADF-detector segment (outside of the white circle, pointed out by arrows). Due to these

imperfections, the measured $I_{\mathrm{HAADF}}(t)$ curves do not reach the simulated intensity at the maximum of the curve at all electron energies. At larger wedge thicknesses, MC simulations with the Bishop screening parameter describe the measured curves well.

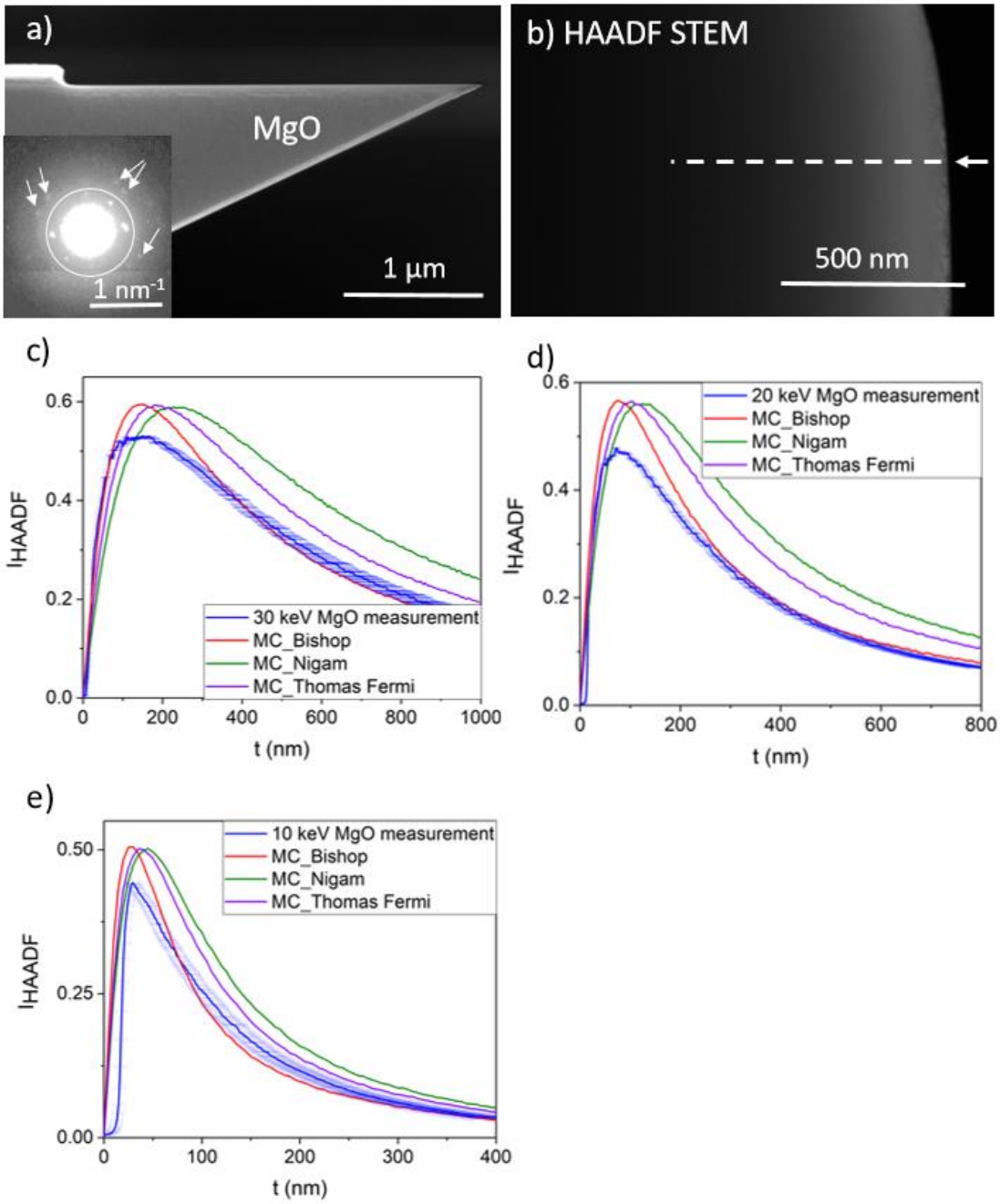

Figure 3.11 Experimental results and MC simulations for MgO. a) Top-view SE-SEM image with inserted TED pattern and b) HAADF-STEM image of the MgO wedge-shaped specimen. c)-e) Comparison of measured and MC-simulated $I_{HAADF}(t)$ curves with Bishop (red), Thomas-Fermi (purple), and Nigam (green) screening parameters at 30, 20, and 10 keV electron energy.

3.5.4. Si

The Si-wedge specimen was milled with an angle of 30°. The smoothness of the prepared wedge seen in the top-view SE-SEM image (Figure 3.12a) is confirmed by the

smooth grey-scale transition in the HAADF-STEM image (Figure 3.12b). The TED pattern reveals only a few weak reflections outside of the white circle indicating the inner radius of the HAADF-STEM detector. Comparison of the measured and simulated data in Figures 3.12c-d shows good agreement between the measured and MC-simulated $I_{\mathrm{HAADF}}(t)$ curves with the Bishop screening parameter for all studied electron energies.

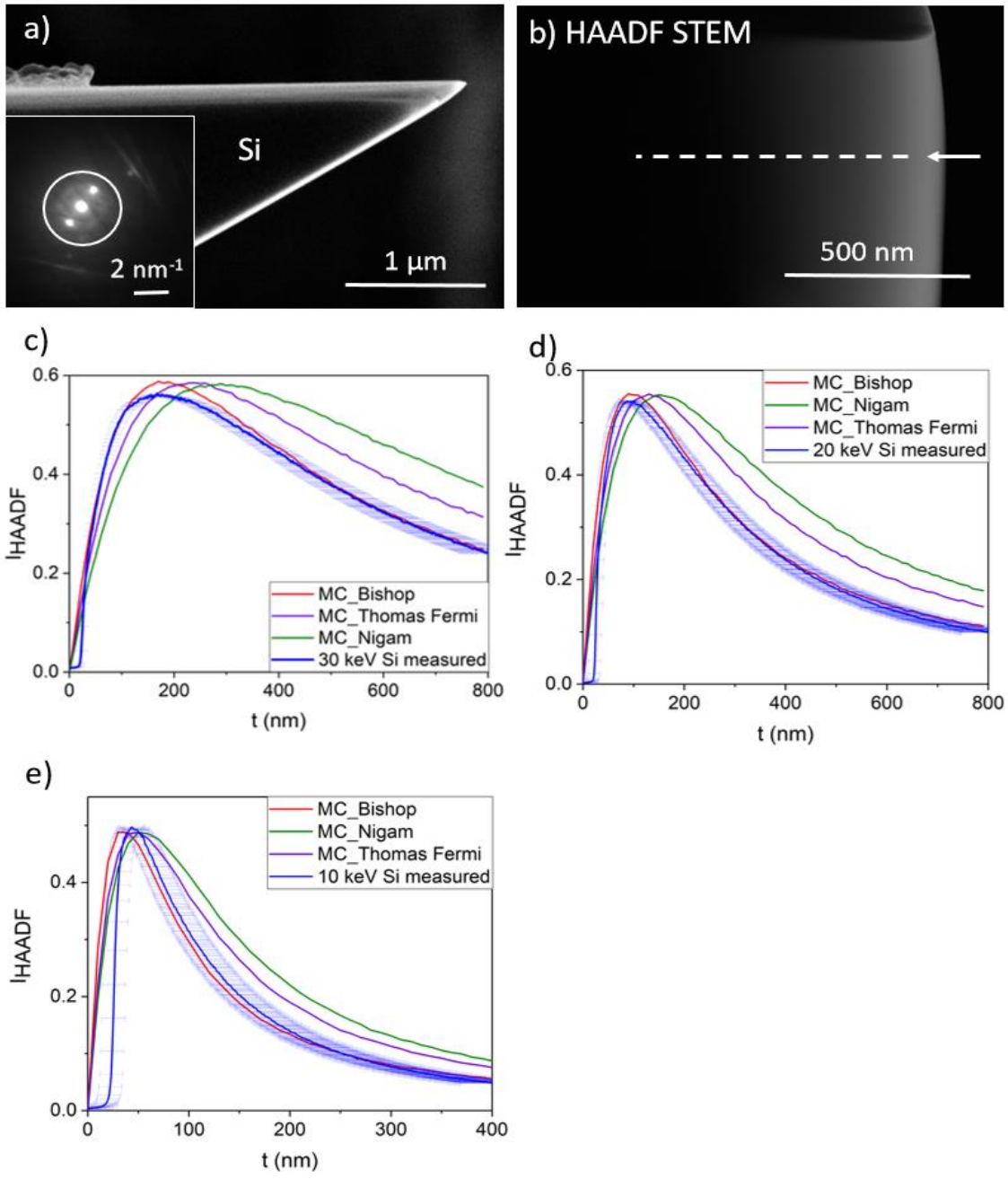

Figure 3.12 Experimental results and MC simulations for Si. a) Top-view SE-SEM image with inserted TED pattern and b) HAADF-STEM image of the Si wedge-shaped specimen. c)-e) Comparison of measured and MC-simulated $I_{HAADF}(t)$ curves with Bishop (red), Thomas-Fermi (purple), and Nigam (green) screening parameters at 30, 20, and 10 keV electron energy.

3.5.5 $SrTiO_3$

The top-view SE-SEM image in Figure 3.13a and the HAADF-STEM image in Figure 3.13b shows a well-prepared $SrTiO_3$ wedge. The best off-zone-axis crystal orientation of the wedge is shown in the TED pattern in Figure 3.13a. For results obtained at 30 and 20 keV (Figure 3.13c and d), the best agreement between measured and simulated data is obtained for the Thomas-Fermi screening parameter. At 10 keV (Figure 3.13e) the Nigam screening parameter more accurately describes the measured data.

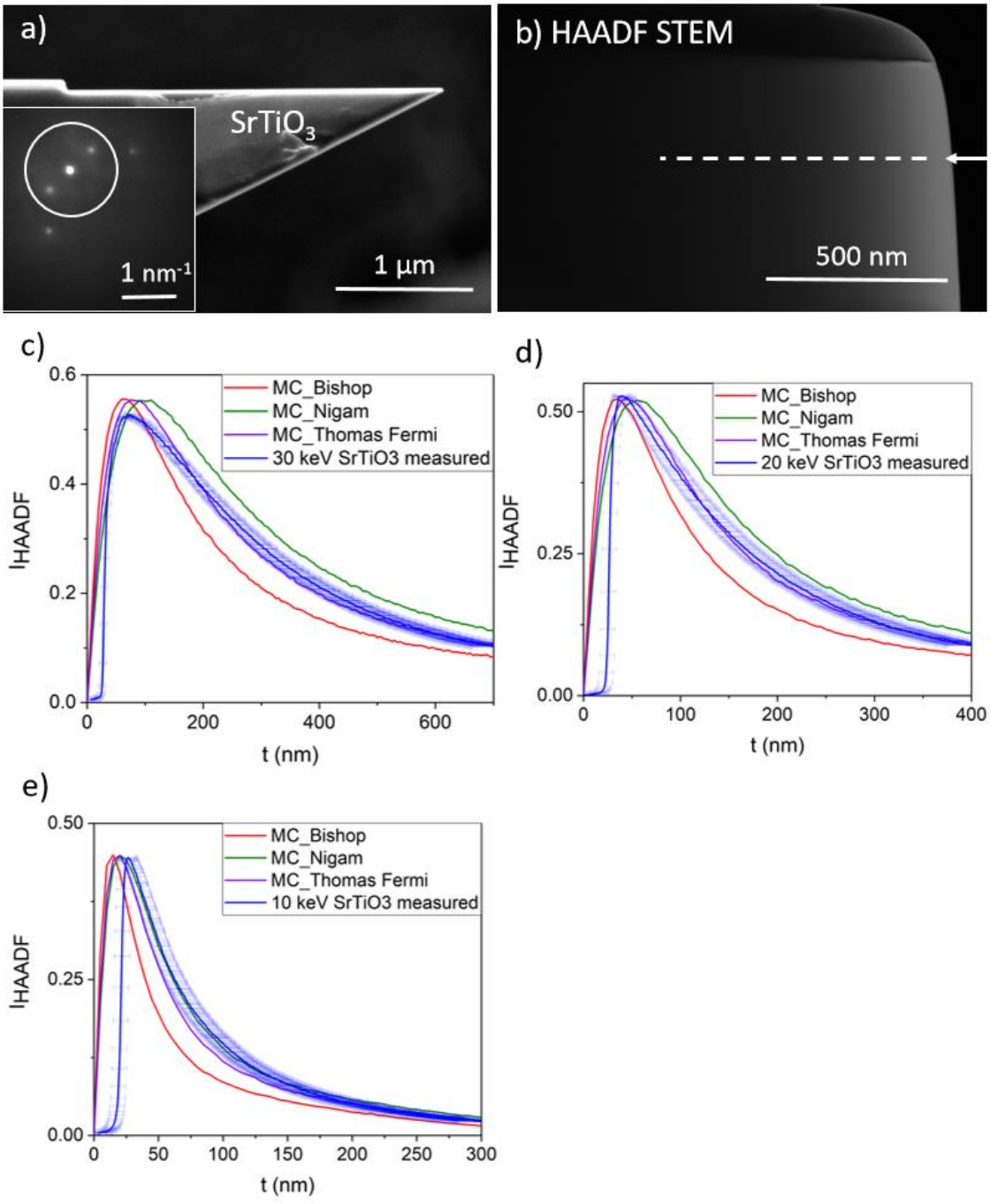

Figure 3.13 Experimental results and MC simulations for $SrTiO_3$. a) Top-view SE-SEM image with a TED pattern and b) HAADF-STEM image of the $SrTiO_3$ wedge-shaped specimen. c)-e) Comparison of measured and MC-simulated $I_{HAADF}(t)$ curves with

Bishop (red), Thomas-Fermi (purple), and Nigam (green) screening parameters at 30, 20, and 10 keV electron energy.

3.5.6. ZnO

The top-view SE SEM image in Figure 3.14a shows a not ideally sharp ZnO wedge with a wedge offset of 35 ±10 nm. Extracting a line scan along the white dashed line in the HAADF-STEM image in Figure 3.14b yields a smooth $I_{\mathrm{HAADF}}(t)$ curve, shown in blue in Figure 3.14c. Figures 3.14c and d reveal that the MC simulations with the Thomas-Fermi screening parameter describe the measured $I_{\mathrm{HAADF}}(t)$ curves well at 30 and 20 keV. At 10 keV (Figure 3.14e) the Thomas-Fermi screening parameter gives good agreement only at higher wedge thicknesses.

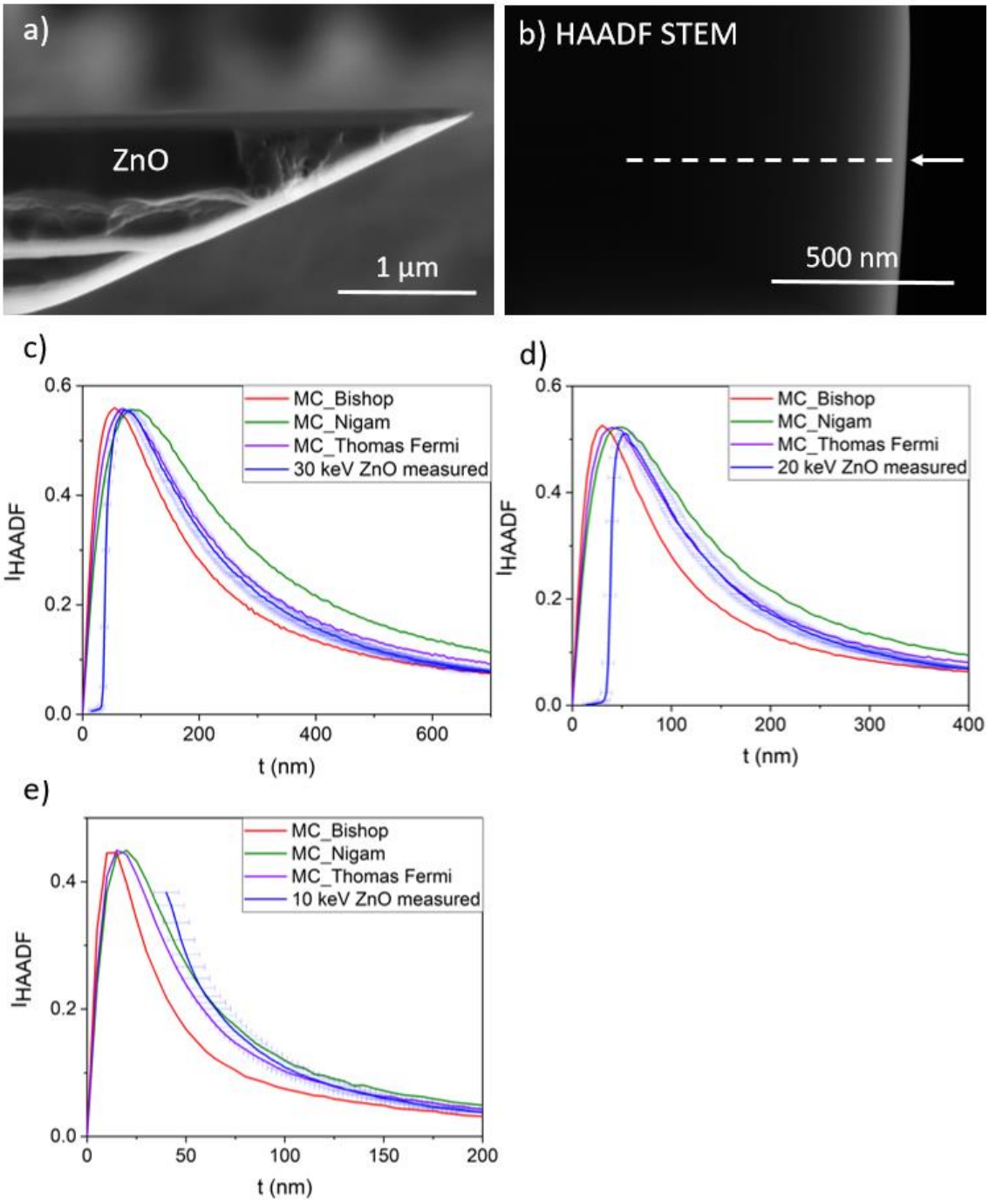

Figure 3.14 Experimental results and MC simulations for ZnO. a) Top-view SE-SEM image and b) HAADF-STEM image of the ZnO wedge-shaped specimen. c)-e) Comparison of measured and MC-simulated $I_{HAADF}(t)$ curves with Bishop (red), Thomas-Fermi (purple), and Nigam (green) screening parameters at 30, 20, and 10 keV electron energy.

3.5.7 Ge

Figure 3.15a shows the Ge wedge with a small hump at the wedge edge (marked by a white arrow) that could not be removed by FIB milling. However, this hump can serve as a marker because it is visible in the measured $I_{\mathrm{HAADF}}(t)$ curves (marked by black arrows in Figure 3.15c-e). Determining wedge thickness directly next to the hump (20 ± 10 nm) and subsequently positioning the visible hump in the $I_{\mathrm{HAADF}}(t)$ curve to

this determined thickness enables precise comparison with MC simulations. For 30 and 20 keV (Figure 3.15c and d), the best fitting MC results are obtained for the Thomas-Fermi screening parameter with a decent agreement with the measured data. At 10 keV (Figure 3.15e) the situation is similar as for the 10 keV ZnO wedge. For larger thicknesses, the Thomas-Fermi screening yields good results, but at smaller thicknesses, none of the screening parameters represents the measured data well.

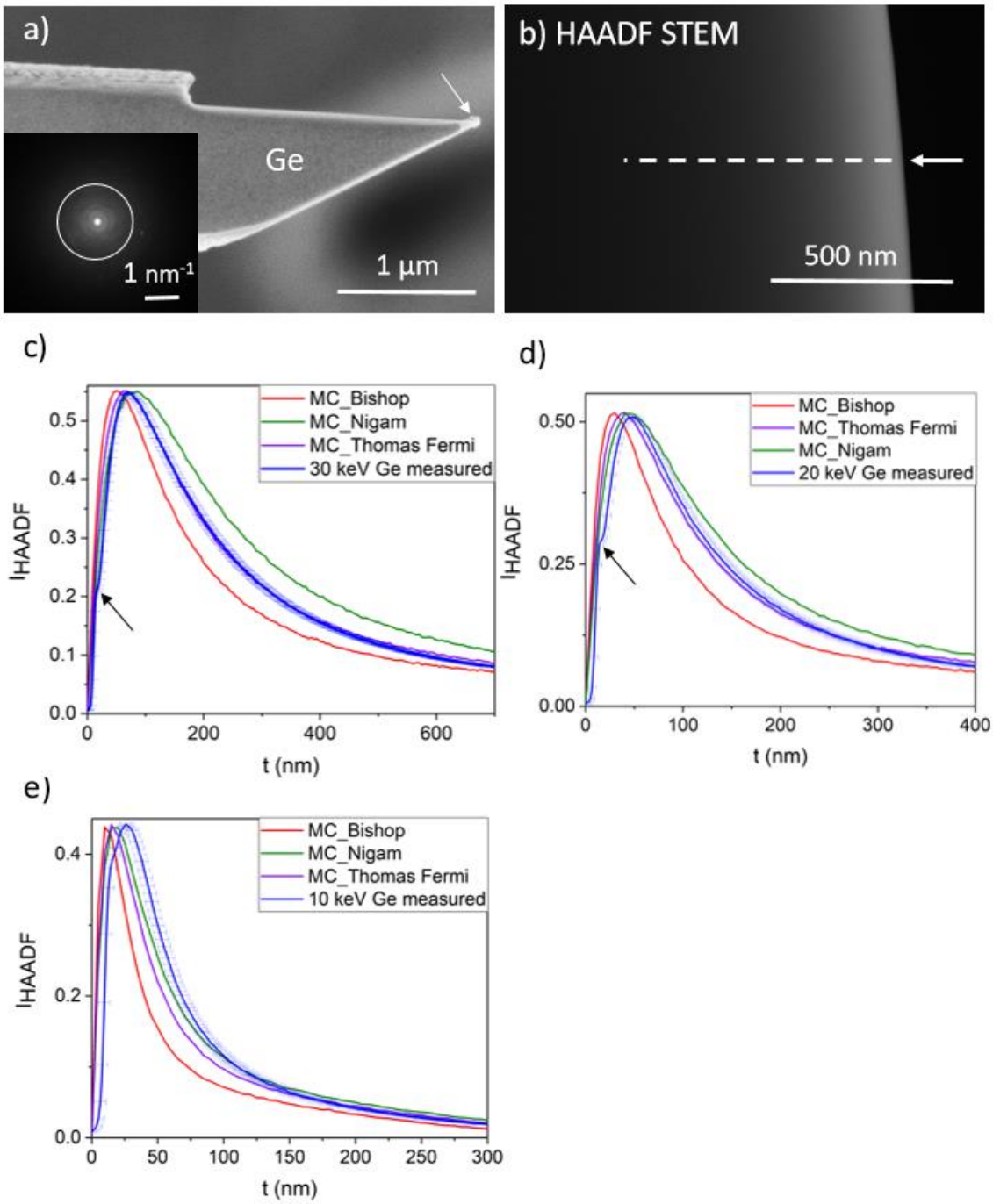

Figure 3.15 Experimental results and MC simulations for Ge. a) Top-view SE-SEM image with a TED pattern and b) HAADF-STEM image of the Ge wedge-shaped specimen. c)-e) Comparison of measured and MC-simulated $I_{HAADF}(t)$ curves with Bishop (red), Thomas-Fermi (purple), and Nigam (green) screening parameters at 30, 20, and 10 keV electron energy.

3.5.8 Pd

Figure 3.16a shows the prepared Pd wedge, where the wedge offset was determined to be 24 ± 10 nm. The TED pattern in Figure 3.16a shows the best possible off-zone-axis crystal orientation of the wedge that was achieved. Pd (and also W) represent high-Z materials. For these materials, the HAADF-STEM image (Figure 3.16b) typically shows only a decline of the intensity with increasing wedge thickness because the intensity maximum appears already at small wedge thicknesses. The wedge tip is never ideally sharp and is always rounded. As a result, the measured $I_{\mathrm{HAADF}}(t)$ curves in Figures 3.16c – e (in blue) are displayed from thicknesses, where the comparison with simulations is relevant. Comparison of the measured and simulated $I_{\mathrm{HAADF}}(t)$ curves in Figures 3.16c – e indicate that the Thomas-Fermi screening parameter is suitable for the MC simulations for larger sample thicknesses. The Nigam screening reaches better agreement with the measurements at smaller sample thicknesses, although substantial deviations are observed between simulated and experimental data at 20 and 10 keV.

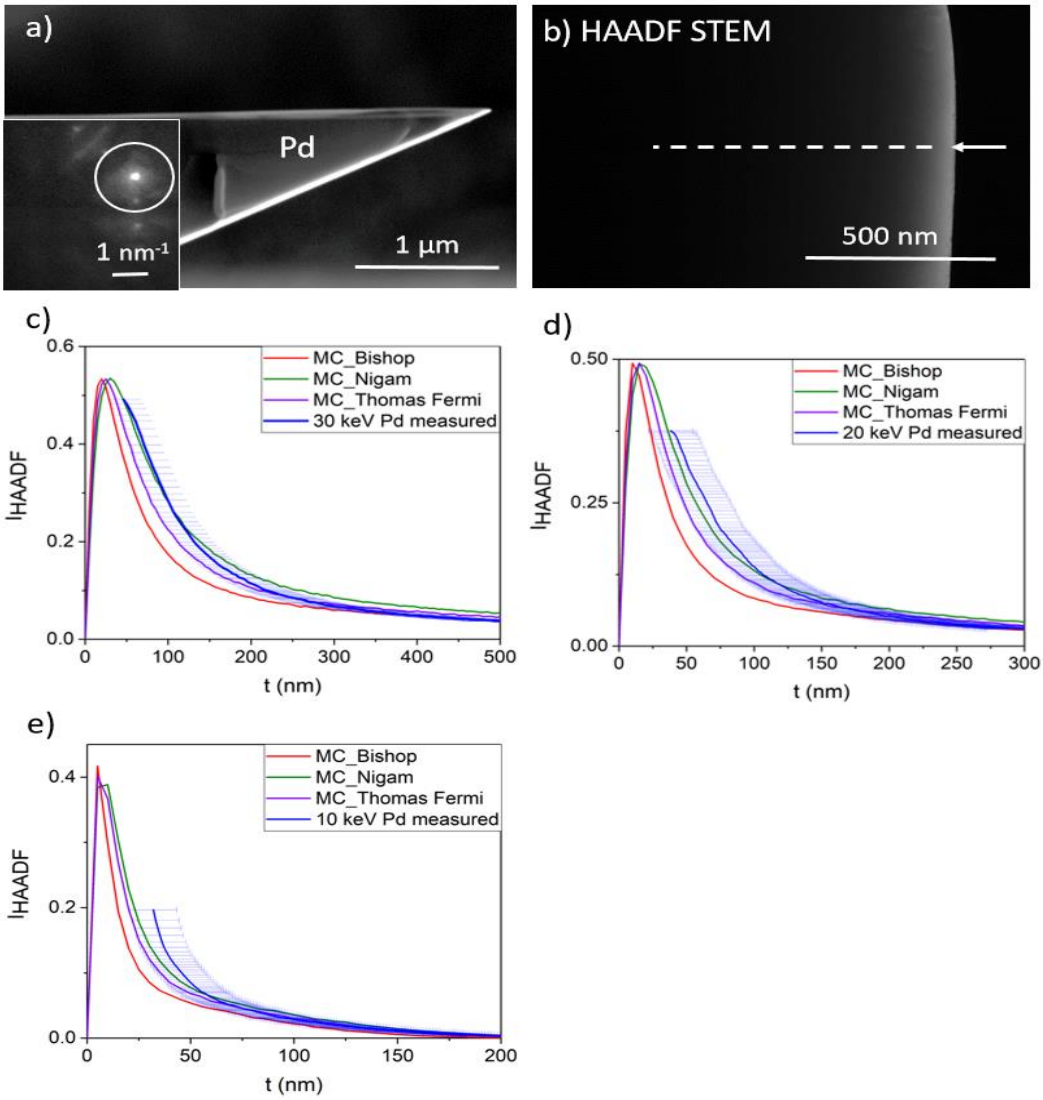

Figure 3.16 Experimental results and MC simulations for Pd. a) Top-view SE-SEM image with a TED pattern and b) HAADF-STEM image of the Pd wedge-shaped specimen. c)-e) Comparison of measured and MC-simulated $I_{HAADF}(t)$ curves with Bishop (red),

Thomas-Fermi (purple), and Nigam (green) screening parameters at 30, 20, and 10 keV electron energy.

3.5.9. W

The preparation of the W wedge-shaped specimen turned out to be challenging because tungsten is in general difficult to mill with Ga^+ ions. The milled wedge is seen in the SE-SEM image (Figure 3.17a) and the cross-section in the HAADF-STEM image (Figure 3.17b). Several grains are visible in Figure 3.17b leading to different image intensities due to Bragg contrast. This is expected from the TED pattern in Figure 3.17a which shows a polycrystalline structure. The intensity line scan was performed along the white dashed line in a grain that is sufficiently large to contain the full $I_{\mathrm{HAADF}}(t)$ curve. Comparison of the measured and MC-simulated $I_{\mathrm{HAADF}}(t)$ curves at 30 and 20 keV reveals that Thomas-Fermi and Nigam screening parameters can predict the measured intensities reasonably well. Figure 3.17 does not show data for 10 keV electron energy because the HAADF STEM intensities are too low. We note that the measured curves for W might be inaccurate because the orientation of the grain is not clear and the peak in the measured $I_{\mathrm{HAADF}}(t)$ curve is located at small thicknesses even below the thickness of the wedge edge.

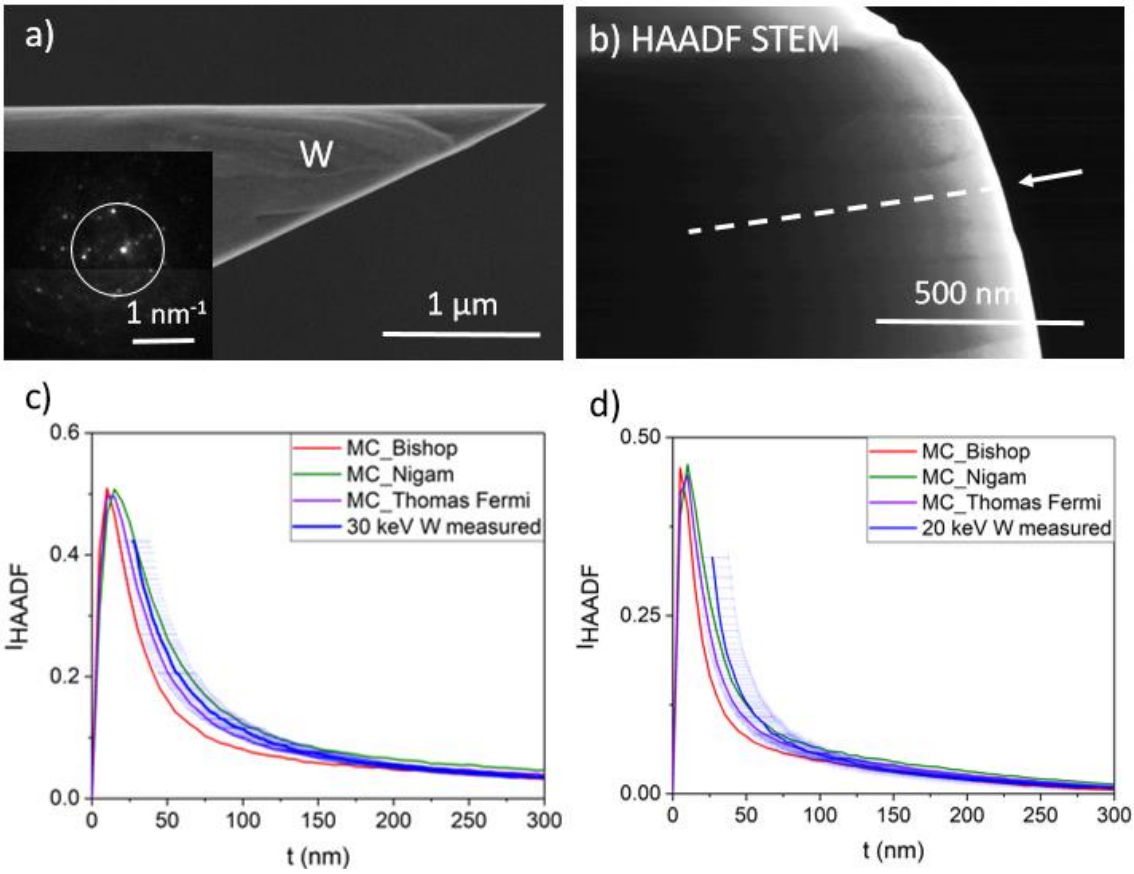

Figure 3.17 Experimental results and MC simulations for W. a) Top-view SE SEM image with a TED pattern and b) HAADF-STEM image of the W wedge-shaped specimen. c) and d) Comparison of measured and MC-simulated $I_{HAADF}(t)$ curves with Bishop (red), Thomas-Fermi (purple), and Nigam (green) screening parameters at 30 and 20 keV electron energy.

3.5.10 Summary of the comparison between experimental and simulated HAADF-STEM intensities

For each material, the most suitable screening parameter was determined. It was shown that the Bishop screening parameter is most adequate for the description of the HAADF-STEM intensities in low-Z materials (Figure 3.9 – 3.12; PTB7, DLC, MgO and Si). However, for materials with very low Z (PTB7 or DLC) the discrepancy between measured and simulated $I_{\mathrm{HAADF}}(t)$ is significant and thus not satisfactory. For the intermediate-Z range (Figure 3.13 – 3.15; $SrTiO_3$, ZnO and Ge), the measured $I_{\mathrm{HAADF}}(t)$ curves can be well described by using the Thomas-Fermi screening parameter. For high-Z materials (Figure 3.16 and 3.17; Pd and W), the simulated $I_{\mathrm{HAADF}}(t)$ curves yield the best fit of the measured data using the Nigam screening parameter.

The origin of the deviations between the measured and simulated $I_{\mathrm{HAADF}}(t)$ curves particularly at low sample thicknesses are not clear. A possible source of these deviations might be a change of material composition by FIB milling. As discussed in Section 3.3.2 Ga^+ implantation is present, however, the effect on the I_{HAADF} is rather small. Another possible source of inaccuracy could be the incorrectly determined wedge angle or wedge offset. The wedge angles and wedge offsets were determined from the SE SEM images (Section 3.3.3), where only the Pt protection is visible. The wedge shape of the material underneath can possible have slightly different. The difference between the real values for wedge angle and wedge offset compared to the values determined from the SE SEM images are expected to be small, as suggested by other wedge characterisation techniques (EFTEM and two-beam thickness contours) discussed in Section 3.3.3.

In summary, this section reveals that none of the tested screening parameters is suitable to describe all the studied materials at all electron energies studied. The results in Section 3.5 indicate incorrect Z dependence of the screening parameter. Possible readjustment of the Z dependence of the screening radius could improve the MC simulation fit to the measured data.

3.6 Adjustment of the screening radius

The previous section reveals that none of the screening parameters can generally describe the measured data (all studied materials and electron energies) sufficiently well. Moreover, the results show that a transition from the Bishop to the Nigam (through the Thomas-Fermi) screening parameter is required to obtain reliable MC-simulated data for different materials with different Z. This indicates an incorrect Z dependence in the screening parameter formula (Eq. 3.2). The $Z^{2/3}$ dependence is derived from the screening radius (Eq. 3.3) where the Bishop, Thomas-Fermi, and Nigam screening parameters differ only by the constant τ maintaining the $Z^{-1/3}$ dependence for all screening radii.

Figure 3.18 compares measured and MC-simulated $I_{\mathrm{HAADF}}(t)$ curves for single-element materials (DLC, Si, Ge, Pd and W) at different electron energies. In the presented MC-simulated data, the value of the screening radius was treated as a fit

parameter to achieve the best fit between experimental data and simulations with the Bishop screening parameter. For DLC (Figure 3.18a), the best fit was achieved for a screening radius $R_{\mathrm{DLC}} = 0.58\ a_0$. MC-simulated $I_{\mathrm{HAADF}}(t)$ curves (in red) with this value of the screening radius yield good agreement with the measured data for all investigated electron energies. Good agreement with the measured data for all electron energies for Si (Figure 3.18b) and Ge (Figure 3.18c) was obtained for screening radii $R_{\mathrm{Si}} = 0.41\ a_0$ and $R_{\mathrm{Ge}} = 0.27\ a_0$. For studied single-element high Z materials the determined screening radii were $R_{\mathrm{Pd}} = 0.22\ a_0$ for Pd and $R_{\mathrm{W}} = 0.2\ a_0$ for W. For both these materials small discrepancy between the measured and simulated data at lower electron energies is probably caused by analyzing a not well-focused HAADF-STEM image.

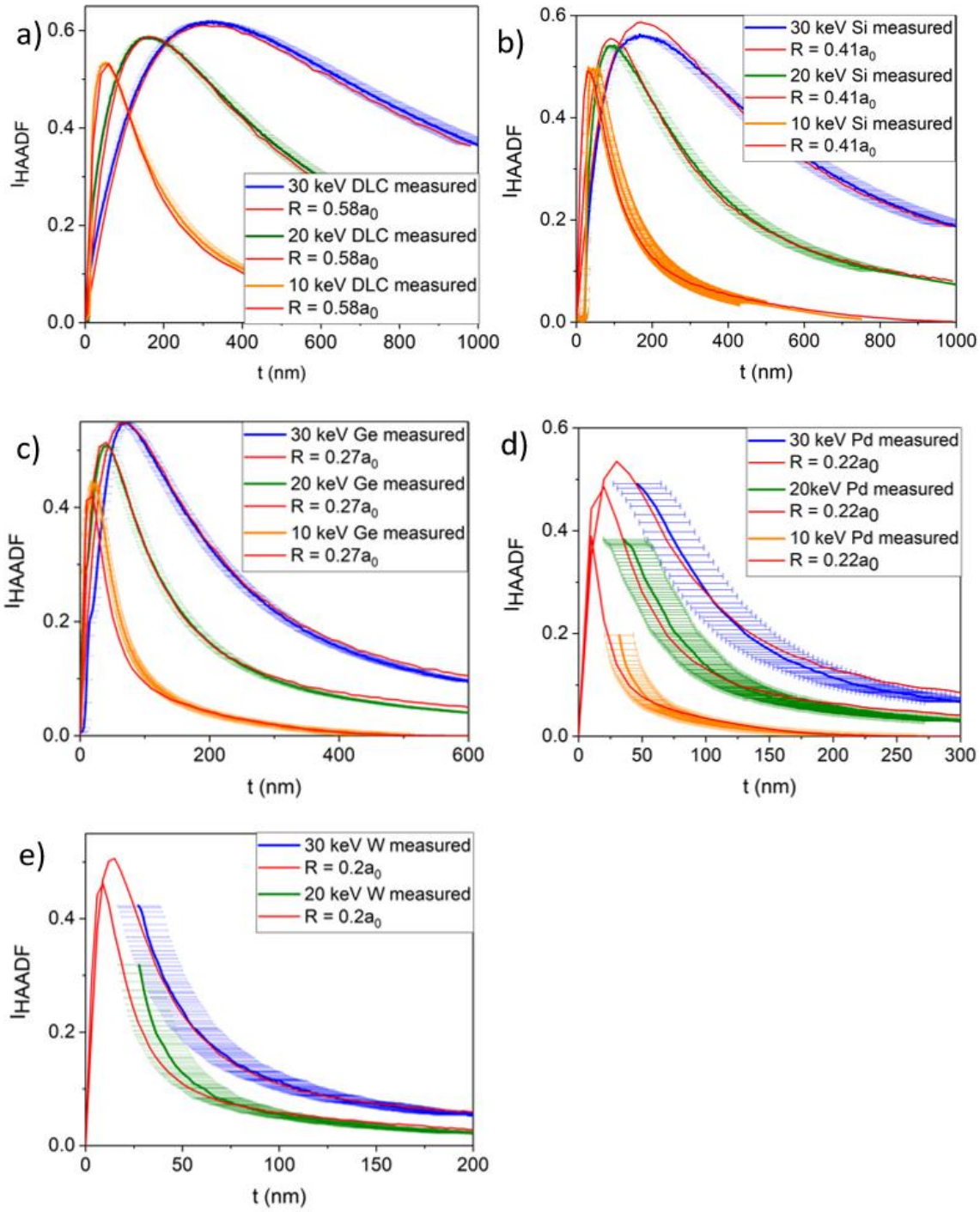

Figure 3.18 Comparison of measured and MC-simulated (red curves) HAADF-STEM intensities for different electron energies as a function of the local specimen thickness by treating the screening radius *R* as a fit parameter. The screening radius *R* was manually adjusted in the simulations to obtain the best fit of the measured data for (a) DLC, (b) Si, (c) Ge, (d) Pd, and (e) W. Adapted from a publication [Čal2019].

The screening radii determined from single-element materials from the best fit between the experimental and simulated $I_{\mathrm{HAADF}}(t)$ curves were plotted as a function of the atomic number Z, as shown by black squares in Figure 3.19. Fitting these data points by a power-law function yields a new expression (Eq. 3.16) for the screening radius in units of the Bohr radius a_0.

$$R = 1.28Z^{-0.44}\ [a_0] \tag{3.16}$$

Besides the new expression for the screening radius (red curve), the screening radius used in the Bishop screening parameter is displayed in blue In Figure 3.19. An intersection of these two curves appears at $Z = 10$ and with further decreasing and increasing Z the difference increases. For very low Z, e.g. $Z = 1$, Eq. 3.16 yields $R = 1.28a_0$, as compared to the Bishop screening radius $R = a_0$.

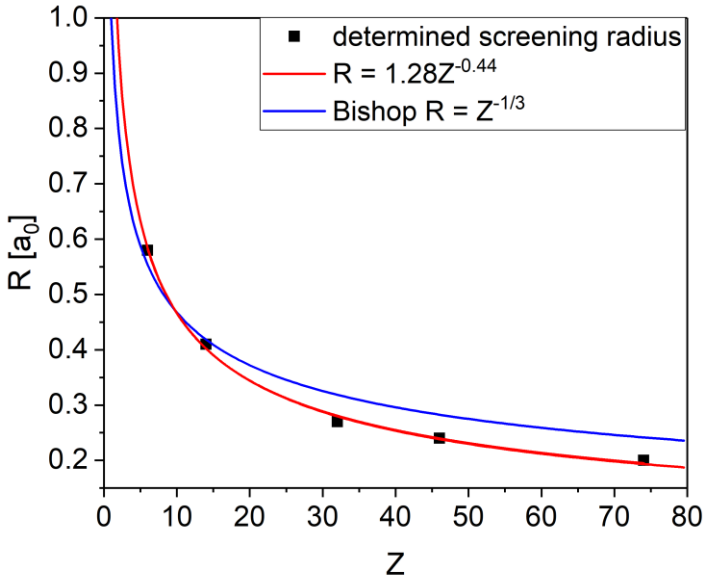

Figure 3.19 Screening radii in units of Bohr radius plotted as a function of the atomic number Z. The screening radii were determined from single-element materials (DLC, Si, Ge, Pd, and W) from the best fit between experimental and simulated $I_{HAADF}(t)$ curves and fitted by a power-law function (red curve). For comparison, the Z dependence of the screening radius used in the Bishop screening parameter is plotted in blue. Adapted from a publication [Čal2019].

The newly determined expression for the screening radius can be validated by comparing experimental and simulated (using the new screening parameter) $I_{\mathrm{HAADF}}(t)$ curves for all investigated compounds (PTB7, MgO, $SrTiO_3$, and ZnO). Figure 3.20 shows the same measured $I_{\mathrm{HAADF}}(t)$ curves as previously shown (Figures 3.9-3.14) for 30 keV in blue and 20 keV in green. The corresponding MC-calculated $I_{\mathrm{HAADF}}(t)$ curves using the screening radius in Eq. 3.16 are plotted in red. For PTB7 (Figure 3.20a) and ZnO (Figure 3.20d), the simulated curves agree well with the measured data. In the case of MgO (Figure 3.20b) and $SrTiO_3$ (Figure 3.20c), a discrepancy is observed at the maximum of the $I_{\mathrm{HAADF}}(t)$ curves similarly to Figure 3.11 and Figure 3.13, respectively. As discussed in section 3.2.4, this discrepancy originates from Bragg reflections with a non-negligible intensity that could not be sufficiently suppressed on the HAADF-STEM detector segment.

The MC-simulated $I_{\mathrm{HAADF}}(t)$ curves using the new expression for the screening radius represent well the measured $I_{\mathrm{HAADF}}(t)$ curves for single elements (Figure 3.18)

and even for compounds (Figure 3.20). This validates the newly derived screening radius. Moreover, Eq. 3.16 is valid even for very low *Z*-materials since PTB7 (Figure 3.20a) contains a considerable amount of hydrogen, and the discrepancy between the measured and simulated data is small.

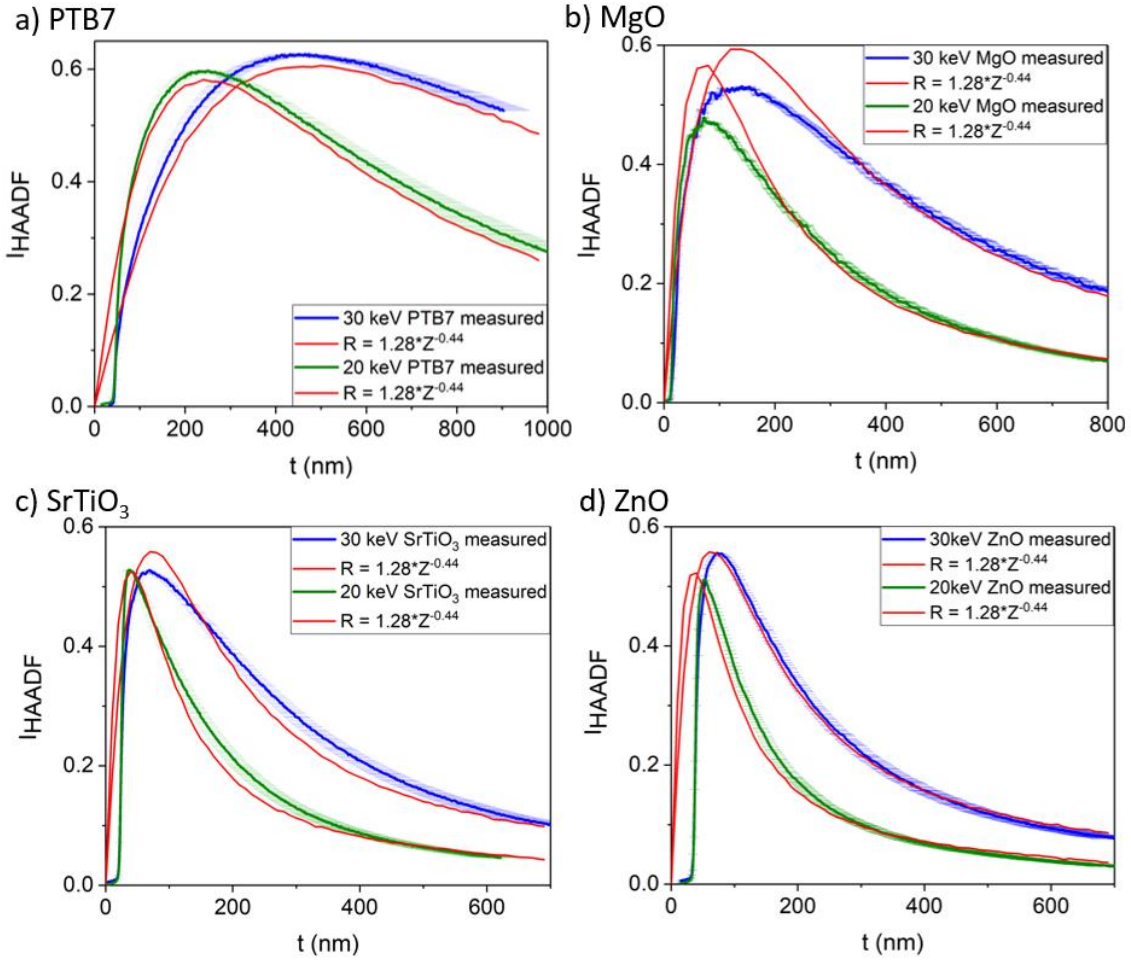

Figure 3.20 Comparison of experimental and simulated HAADF STEM intensities as a function of the local specimen thickness for 30 keV (blue curves) and 20 keV (green curves) for (a) PTB7, (b) MgO, (c) SrTiO3, and (d) ZnO. The new expression for the screening radius $R = 1.28a_0Z^{-0.44}$ was used for the MC simulations of the $I_{HAADF}(t)$ (red curves). Adapted from a publication [Čal2019].

3.7 Z dependence of the $I_{\mathrm{HAADF}}(t)$

The overall Z dependence of the HAADF intensity is particularly interesting because it is monotonic and thus could be used for direct interpretation of HAADF STEM images with respect to material composition [Lak1997, Liu2001, Tak2004, Voy2003, Pen2000]. The overall HAADF intensity follows the Z^b dependence and is proportional to the scattering cross-section σ_e (for single scattering case). The scattering cross-section is obtained by integration of the DSCS $\frac{d\sigma}{d\Omega}$ over the detection angle range of the STEM detector. Substituting the Screened Rutherford DSCS (Eq. 3.1) for $\frac{d\sigma}{d\Omega}$ leads to a formula shown in Eq. 3.17. In the presented formula, there is a Z^2 term in the first

nominator and another Z dependence in screening radius R (Eq. 3.3), which is contained in the screening parameter η (Eq. 3.2.)

$$I \sim \sigma_e = \int_0^{2\pi} \int_{\theta_1}^{\theta_2} \frac{d\sigma}{d\Omega} \sin\theta \, d\theta d\varphi = \left(\frac{e^2 Z}{4\pi\varepsilon_0}\right)^2 \frac{2\pi}{{E_0}^2} \left(\frac{1}{1+2\eta-\cos\theta_1} - \frac{1}{1+2\eta-\cos\theta_2}\right) \tag{3.17}$$

The overall *Z* dependence of the HAADF intensity can be derived from Eq. 3.17 by fitting the logarithm of the Eq. 3.17 with the $b \ln Z + c$ function, as suggested by Hartel *et al.* [Har1996]. The coefficient b then represents the power of the overall Z dependence of the HAADF intensity. According to different studies [Har1996, Hil1995, Kir1987], predictions of the exponent b in Z^b vary between 1.5 and 2, depending on the detection-angle range. For single scattering, an electron is scattered into an angle based on the impact parameter. For low impact parameters, the electron trajectory is more modified towards higher scattering angles as compared to an electron with a larger impact parameter because the charge of the atom nucleus is screened by the surrounding electrons. As a result, for low-angle electron scattering the exponent b in the Z dependence of the HAADF intensity will be lowered by the Z dependence of the screening parameter towards $b = 1.5$. Contrary, for high-angle electron scattering, the electrons are scattered at the unscreened atom nucleus leading to $b = 2$. An experimental approach to determine the Z dependence of the I_{HAADF} for the single-scattering case was performed by Krivanek *et al.* [Kri2012] by analyzing a monolayer of BN with 60 keV electrons. In their experiment the I_{HAADF} was governed by pure Z contrast and the exponent of the Z dependence was found to be $b = 1.64$.

To qualitatively estimate the Z dependence of I_{HAADF} that was measured and simulated in the presented work, the newly derived screening radius (Eq. 3.16) was considered in the screening parameter η in Eq. 3.17. Additionally, the detection-angle range θ_1 and θ_2 of the HAADF segment of the STEM detector was taken into account as the integration limits in Eq. 3.17. By fitting the logarithm of Eq. 3.17 with the $b \ln Z + c$ function yields $I_{\mathrm{HAADF}} \sim Z^{1.58}$, i.e. $b = 1.58$. This derived Z dependence is obtained for electrons that undergo multiple scattering events and under conditions where coherent scattering contributions to the intensity are avoided. It is noted, that the detection angle range (65 – 272 mrad) of the Helios G4 FX microscope is rather small for HAADF STEM at 30 keV. Testing the Z dependence of I_{HAADF} by considering the detection angle range of the FEI DualBeam Strata 400S microscope (58 – 610 mrad) in Eq. 3.17 yields $b = 1.57$. This small change of b suggests only weak dependence of the Z dependence of the I_{HAADF} on the HAADF scattering-angle range. The Z dependence of I_{HAADF} for the traditional Bishop screening parameter (Eq. 3.3) can be also calculated, yielding $b = 1.66$. This value is slightly higher as compared with the result obtained for the new screening radius ($b = 1.58$).

3.8 Applicability of the new screening radius for a larger detection-angle range

The new screening radius (Eq. 3.16) was derived for a detection-angle range between 65 and 272 mrad, and the calculated Z dependence of the I_{HAADF} suggests only weak dependence on the detection-angle range. To study the applicability of the new screening radius for different detection-angle ranges, the same measurements as in section 3.5 were performed by using another instrument (FEI DualBeam Strata 400S). This microscope contains a HAADF-STEM detector with a 58 – 610 mrad detection-angle range while positioning the specimen 5 mm below the pole piece. By comparing the measured data with MC simulations using the new screening radius, the suitability of the new screening radius for the description of I_{HAADF} for larger detection angles can be verified. This work was carried out by Alisa Sinigalia within her Bachelor thesis [Sin2020].

The wedge-shaped specimens from the measurements presented in section 3.4 were re-shaped to obtain fresh sample surfaces without contamination. The wedge angles and wedge offsets were determined from the top-view SE-SEM image. The determined wedge properties are summarized in Table 3.2.

Table 3.2 Materials and shape characteristics of the wedge-shaped specimens. The wedge angles and offsets were estimated from top-view SE-SEM images.

Material	Average atomic number Z	Density ρ ($\mathrm{g/cm^3}$)	Top-view wedge angle	Top-view wedge offset (nm)
PTB7	5.3	1.12	26.0°±0.5°	23±10
DLC	6	1.9	24.4°±0.5°	19±5
ZnO	21.95	5.6	25.7°±0.5°	33±10
Pd	46	11.99	24.5°±0.5°	27±10
W	74	19.25	24.5°±0.5°	18±10

To compare MC-simulated $I_{\mathrm{HAADF}}(t)$ and measured data acquired with the STEM detector in the FEI DualBeam Strata 400S microscope, the data evaluation was performed as discussed in Section 3.3.4 and Section 3.4. Figure 3.21 shows a reference image of the STEM detector of the DualBeam Strata 400S microscope that was obtained by directly scanning the detector (see Figure 3.6 for comparison). From the reference image, I_w and I_b were determined and further used in the normalization of the measured HAADF intensity with respect to the primary electron beam in Eq. 3.14. More importantly, the correction factor c_g in Eq. 3.14 has to be changed. For the STEM detector in Figure 3.21 $c_g = 0.98.$ was determined. The threshold energy E_{th} of the STEM detector in Eq. 3.15 is another parameter that needs to be adapted. It is $3\ \mathrm{keV}$ for the STEM detector in the FEI DualBeam Strata 400S microscope

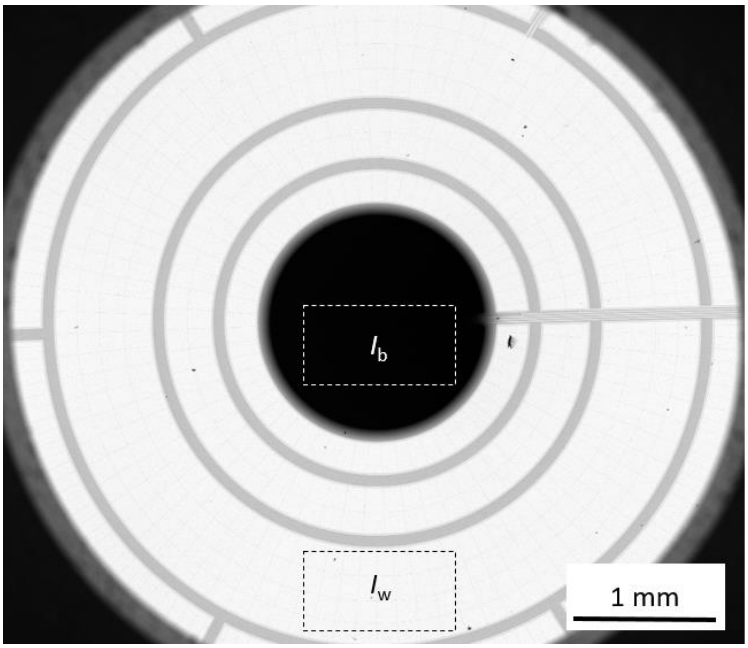

Figure 3.21 Reference image of the STEM detector implemented in the FEI DualBeam Strata 400S microscope. A reference image is obtained by direct illumination of the STEM detector. The bright region is a section of the STEM detector, from where I_w is obtained. The black value I_b is determined from the inactive regions. About 2% of the active region of the STEM detector is inactive due to the segmentation of the STEM detector.

In contrast to the Helios G4 FX microscope, the DualBeam Strata 400S microscope is not equipped with a CCD camera below the specimen that would enable the acquisition of the TED patterns. For this reason, the crystal orientation of the wedge-shaped specimens could not be directly examined. As already discussed (Section 3.3.5), the sample orientation influences the HAADF-STEM intensity. To identify sample orientations close to the off-zone-axis orientation, $I_{HAADF}(t)$ curves obtained from HAADF-STEM images acquired at different sample tilts were compared. Such a comparison is presented in Figure 3.22, where the Pd wedge-shaped specimen was tilted from -6° to 6° in 2° steps. According to the information obtained in Figure 3.7, the sample orientation with the highest intensity at the maximum of the $I_{HAADF}(t)$ curve is the closest to an off-zone-axis orientation. For the Pd specimen (Figure 3.22) the closest off-zone-axis orientation is obtained for 4° and -4° sample tilt. The closest off-zone-axis orientation based on the tilt series was determined for all studied crystalline materials (ZnO, Pd, and W). Corresponding $I_{HAADF}(t)$ curves were then compared with the MC simulations with different screening parameters.

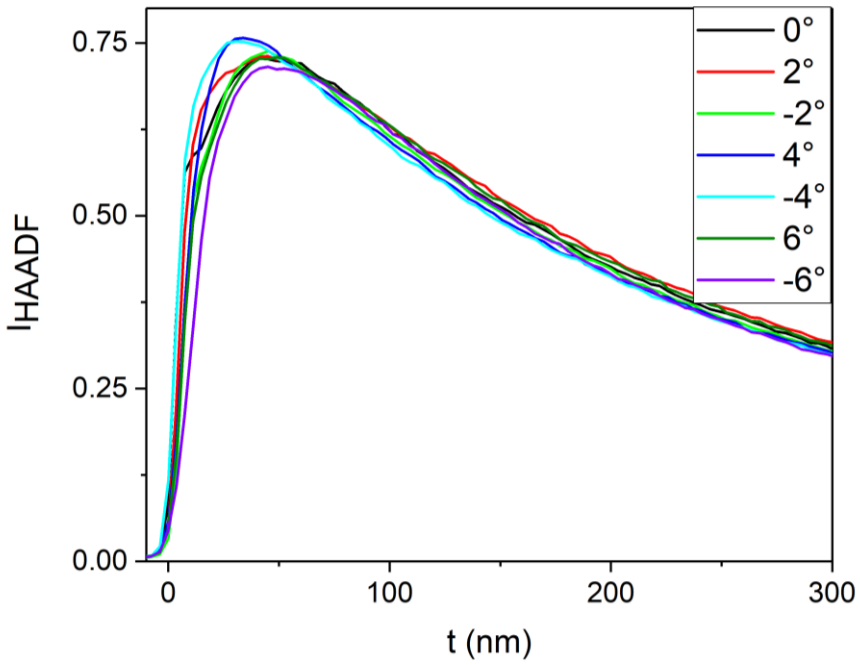

Figure 3.22 Tilt series to determine off-zone-axis sample orientations. Colour-coded $I_{HAADF}(t)$ curves of a Pd wedge tilted to different angles. The sample tilt, for which the $I_{HAADF}(t)$ curves reach the highest intensity at the curve maximum (light blue -4° and dark blue 4°) is closest to an off-zone-axis orientation.

Figure 3.23a to c compares the measured (blue) and MC-simulated $I_{\mathrm{HAADF}}(t)$ curves for the PTB7 wedge acquired with the DualBeam Strata 400S microscope at 30 keV, 20 keV, and 15 keV electron energy. The MC-simulated $I_{\mathrm{HAADF}}(t)$ curves were calculated using the Bishop (red), Nigam (green), and Thomas-Fermi (purple) screening parameters. The orange $I_{\mathrm{HAADF}}(t)$ curve represents the MC-simulated data where the newly derived screening radius (Eq. 3.16) was used in the Bishop screening parameter. The comparison reveals that the closest MC-simulated curve is obtained for the new screening radius. However, the discrepancy between the measured and simulated data is significant at all studied electron energies. The measured intensities are in general higher and reach higher intensity values already at smaller sample thicknesses as compared to the MC simulations. This behaviour was observed previously for the traditional screening parameters, in Section 3.5.1, where the data were obtained for the former detection angle range. By considering the new screening parameter in the MC simulations (Figure 3.20a), the discrepancy between the measured and simulated data for the former detection angle range was minimized. However, in the case of the larger detection angle range (Figure 3.23) even the MC simulations using the new screening parameter do not give satisfactory results. A possible explanation for this discrepancy could be a lack of precise knowledge of the material density and chemical composition for PTB7. Especially the differences in the real and simulated chemical composition could cause large discrepancies in the HAADF intensities because the scattering properties of different elements could significantly vary with respect to the detection-angle range.

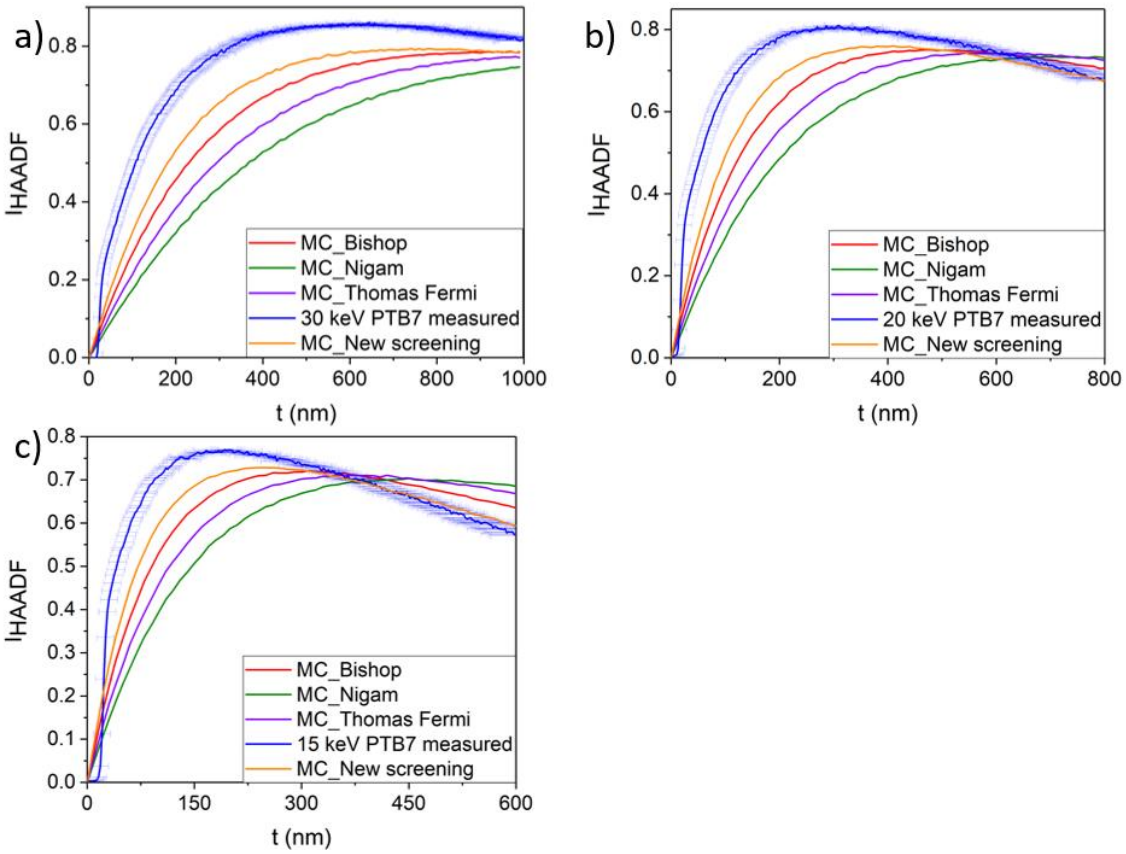

Figure 3.23 Experimental results and MC simulations for PTB7. Comparison of measured and MC-simulated $I_{HAADF}(t)$ curves with Bishop (red), Nigam (green), Thomas-Fermi (purple), and the new (orange) screening parameter at a) 30, b) 20 and c) 15 keV electron energy. The experimental data corresponds to a 58 – 610 mrad detection-angle range.

DLC is the second low-Z material that was investigated with the DualBeam Strata 400S. The measured and simulated data are compared in Figure 3.24a to c for 30, 20, and 15 keV electron energies. The colour-coding of the MC-simulated $I_{\mathrm{HAADF}}(t)$ curves with different screening parameters are the same as in Figure 3.23. Figure 3.24 reveals that the measured $I_{\mathrm{HAADF}}(t)$ curve (in blue) reach higher intensities at the maximum of the $I_{\mathrm{HAADF}}(t)$ curve, as compared to the MC simulations for all electron energies. Interestingly, the shape of the $I_{\mathrm{HAADF}}(t)$ curves obtained for MC simulations using the new screening parameter (in orange) agrees well with the measured curves, which is not the case for the other screening parameters. Moreover, the measured data at small sample thicknesses are well represented by the MC simulations using the new screening parameter. At larger sample thicknesses, especially for 20 keV (Figure 3.24b) and 15 keV (Figure 3.24c), the Bishop screening parameter provides reasonable agreement with the measured data.

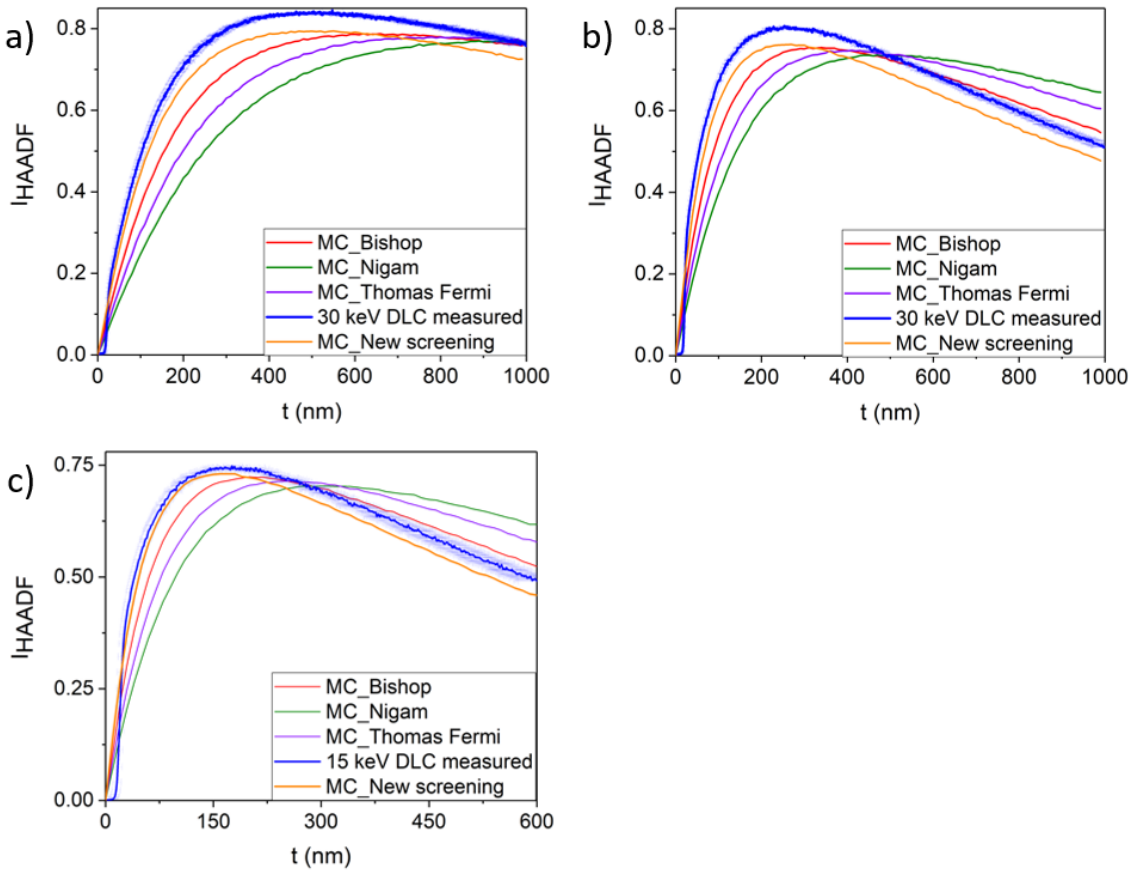

Figure 3.24 Experimental results and MC simulations for DLC. Comparison of measured and MC-simulated $I_{HAADF}(t)$ curves with Bishop (red), Nigam (green), Thomas-Fermi (purple), and the new (orange) screening parameter at a) 30, b) 20 and c) 15 keV electron energy. The experimental data corresponds to a 58 – 610 mrad detection-angle range.

ZnO was analyzed as a representative of the mid-Z group of materials. Comparing the measured curves with the MC simulations in Figure 3.25 reveals, that at 30 keV (Figure 3.25a) the measured curve lies in between the Thomas-Fermi (purple) and Nigam (green) curves. For 20 keV (Figure 3.25b), MC simulations with the Thomas-Fermi screening parameter fit the measured data the best. At 15 keV (Figure 3.25c) none of the simulated curves describe the measured data sufficiently well. Moreover, the shape of the measured curve differs from the MC-simulated curves. The shape of the measured curve depends on the position of the line scan in the HAADF STEM image. Taking the line scan not exactly perpendicular to the wedge edge leads to incorrect calculations of the local thickness and thus "deform" the real shape of the $I_{\mathrm{HAADF}}(t)$ curve. The HAADF-STEM images at lower electron energies are rather noisy, causing difficulty in data evaluation. The MC-simulated curves using the new screening parameter describe the measured data with a significant discrepancy, however, the new screening parameter leads to better-simulated results than other screening parameters, considering all electron energies studied.

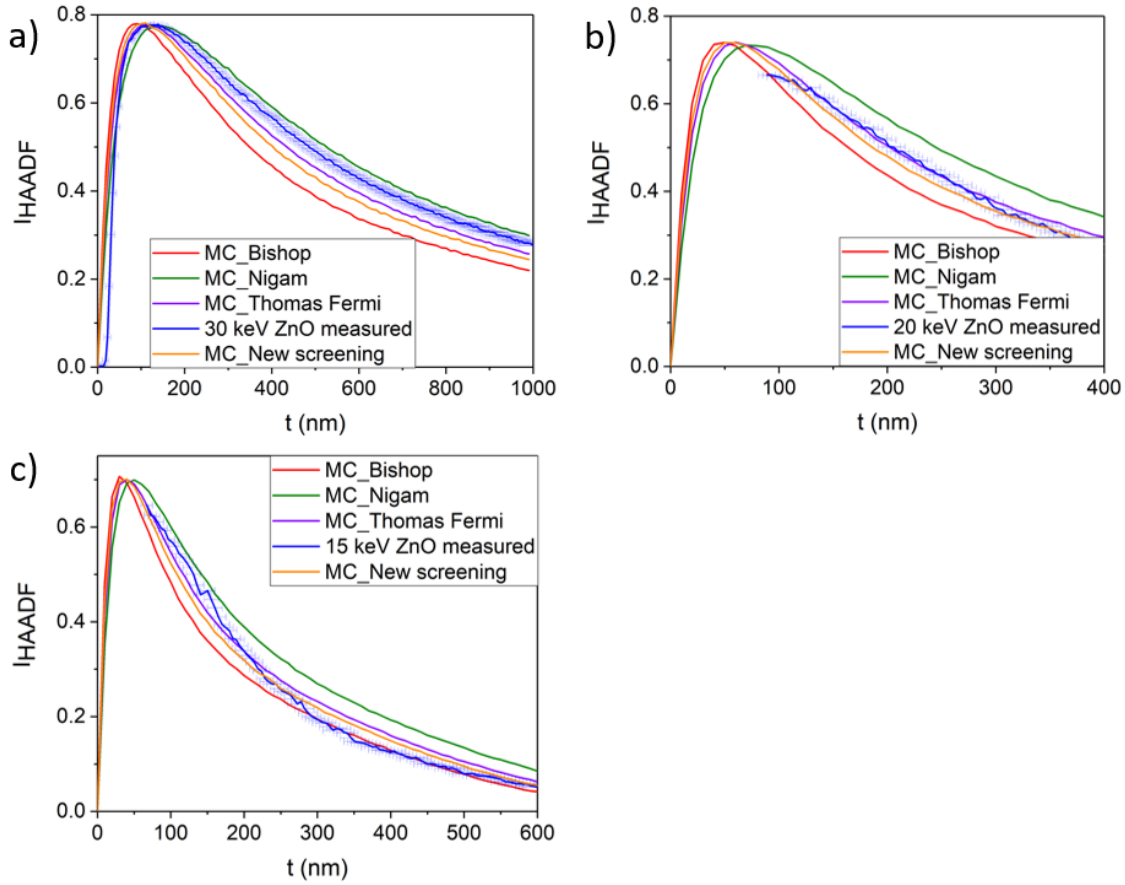

Figure 3.25 Experimental results and MC simulations for ZnO. Comparison of measured and MC-simulated $I_{HAADF}(t)$ curves with Bishop (red), Nigam (green), Thomas-Fermi (purple), and the new (orange) screening parameter at a) 30, b) 20 and c) 15 keV electron energy. The experimental data corresponds to a 58 – 610-mrad detection-angle range.

Figure 3.26 shows the comparison of measured and simulated $I_{\mathrm{HAADF}}(t)$ curves for the Pd wedge. In the case of Pd, the MC-simulated $I_{\mathrm{HAADF}}(t)$ curves obtained for the new and the Thomas-Fermi screening parameter are identical at all studied electron energies. More importantly, the Thomas-Fermi/new screening-parameter simulations fit the measured Pd data at larger sample thicknesses. At smaller sample thicknesses, the measured data is best fitted by the Nigam screening parameter. We note that the HAADF-STEM image taken at 15 keV was not well focused due to the low overall image intensity. Hence, the measured Pd $I_{\mathrm{HAADF}}(t)$ curve at 15 keV might not be reliable, especially at small sample thicknesses.

W was analyzed as a representative of the high-Z materials. The comparison of the measured and MC-simulated $I_{\mathrm{HAADF}}(t)$ curves is presented in Figure 3.27a,b for 30 keV and 20 keV. The data for 15 keV electron energy is not shown because the image intensities are already too low. Figure 3.27 reveals that for high-Z materials the MC simulations using the new screening parameter yield the same results as the Nigam screening parameter. Moreover, the new/Nigam screening parameter describe the experimental data well at both (30 and 20 keV) electron energies.

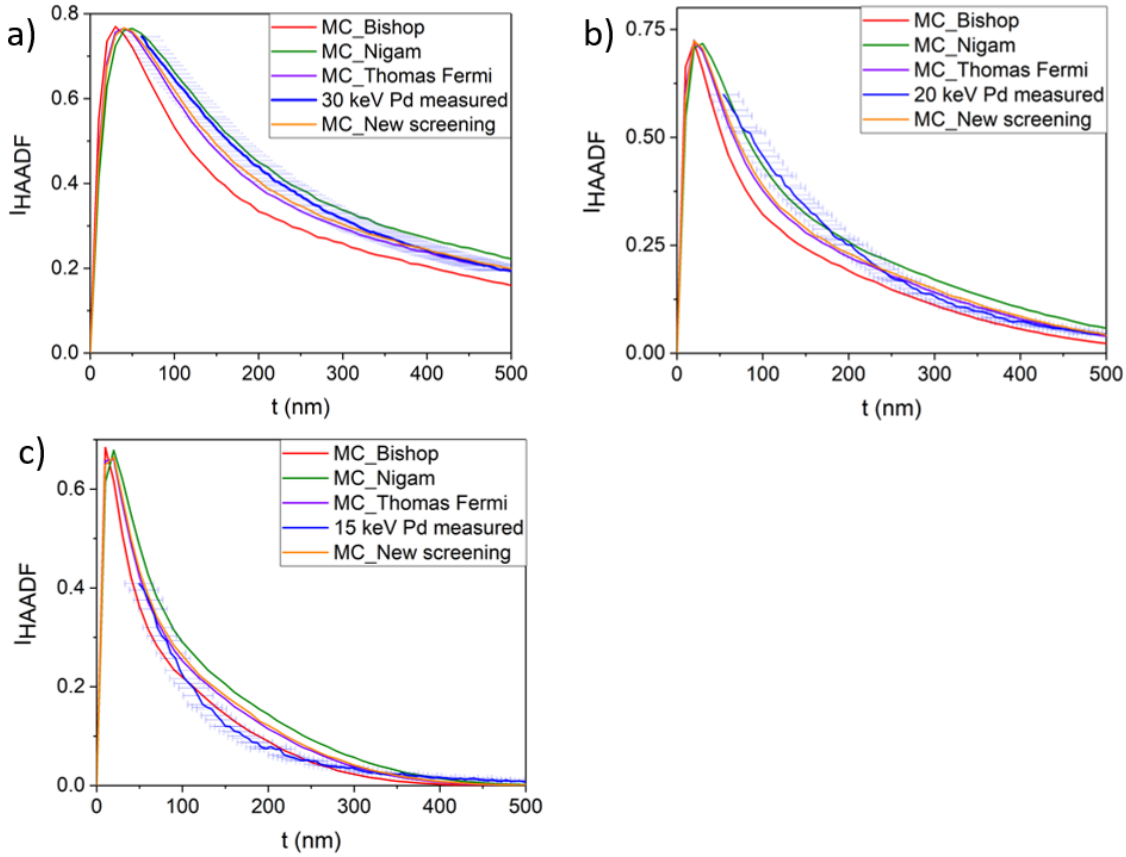

Figure 3.26 Experimental results and MC simulations for Pd. Comparison of measured and MC-simulated $I_{HAADF}(t)$ curves with Bishop (red), Nigam (green), Thomas-Fermi (purple), and the new (orange) screening parameter at a) 30, b) 20 and c) 15 keV electron energy. The experimental data corresponds to a 58 – 610 mrad detection-angle range.

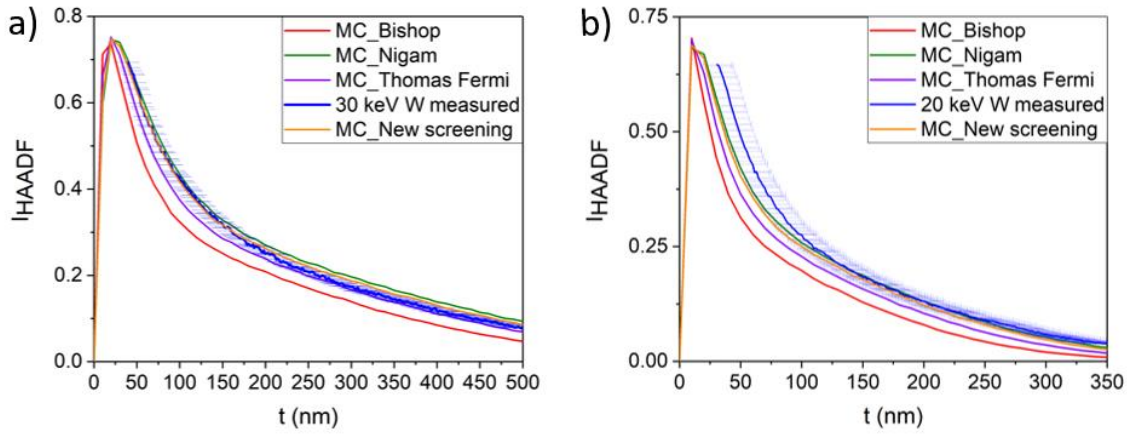

Figure 3.27 Experimental results and MC simulations for W. Comparison of measured and MC-simulated $I_{HAADF}(t)$ curves with Bishop (red), Nigam (green), Thomas-Fermi (purple), and the new (orange) screening parameter at a) 30, b) 20 and c) 15 keV electron energy. The experimental data corresponds to a 58 – 610 mrad detection-angle range.

In summary, the comparison of the measured and simulated data with the new screening parameter shows reasonable agreement even for the larger detection angle

range. The already discussed possible uncertainty of the wedge angle and offset determination, as well as the Ga^+ implantation, also apply to the data comparison at the larger detection angle range. Moreover, the new screening parameter was derived for the detection angle range of the Helios G4 FX instrument. In order to obtain better agreement between the measured and MC simulated data at the FEI DualBeam Strata 400S instrument, the screening radius should be again readjusted to the particular detection angle range in the same way as presented in Section 3.6.

3.9 Summary

In this chapter, we examined the importance of the screening parameter in the MC simulations. Several screening parameters from the literature were implemented into the NISTMonte simulation package and tested to describe the I_{HAADF} intensities as a function of the local sample thickness for materials varying in the average atomic Z number. The measured $I_{\mathrm{HAADF}}(t)$ curves were obtained from HAADF-STEM images of wedge-shaped specimens. To compare the measurements with MC simulations, precise wedge characterization (determination of wedge angle and wedge offset), STEM detector characteristics, as well as normalization of the measured intensities with respect to the primary electron beam have to be considered. Comparison of the measured and simulated $I_{\mathrm{HAADF}}(t)$ curves in Figures 3.9-3.17 reveal that none of the tested screening parameters allows to consistently describe the measured data at 10-30 keV electron energy and for the 65-272 mrad detection-angle range. To overcome this problem, the screening radius was considered as a fit parameter in the MC simulations. For each single-element material studied (DLC, Si, Ge, Pd, W) a particular value of the screening radius was determined, for which the best fit between the measured and simulated data was achieved (Figure 3.18). The adjusted screening radii could be represented by a power-law function (Figure 3.19) yielding a new expression for the screening radius $R = 1.28\, a_0 Z^{-0.44}$. The validity of this new expression was tested by comparing measured and simulated HAADF-STEM intensities of compounds (PTB7, ZnO, MgO, $SrTiO_3$). MC simulations using the new expression for the screening radius in the Bishop screening parameter yield good agreement with the measured HAADF-STEM intensities of compounds, i.e. PTB7, ZnO, MgO, and $SrTiO_3$ (Figure 3.20), demonstrating the validity of the new screening radius. Moreover, the Z dependence of the I_{HAADF} in the low-energy HAADF STEM regime was estimated by integrating the DSCS over the HAADF scattering-angle range. For the newly derived screening parameter, the Z dependence was found to be proportional to $Z^{1.58}$ and only weakly dependent on the detection-angle range. Comparison of measurements (Figures 3.23-3.27) performed with a different microscope with a larger HAADF-STEM detection-angle range (58-610 mrad) with MC simulations using the newly derived screening parameter shows good agreement.

The new expression for the screening radius was derived based on experimental data obtained on the Helios G4 FX instrument. It was shown that for this particular experimental setup the measured data can be well simulated using the new screening radius, however, in the case of the large detection angles, more discrepancies between the measured and simulated data are visible. Thereby we do not claim that the new

screening radius is valid for all experimental setups, but rather recommend the introduced procedure to determine screening radii for other microscopes with different experimental setups. Possible improvements of the presented method could include a better wedge characterization method and the use of more materials with precisely known material composition and density. This particularly applies to low Z materials, where the observed discrepancy was the greatest.

4. Quantitative analysis of backscattered-electron contrast in SEM

This chapter proposes a method for quantitative analysis of backscattered-electron (BSE) contrast in SEM. The method is based on the comparison of measured and Monte-Carlo (MC) simulated BSE intensities. With the use of MC simulations, it is possible to relate the grey values in BSE-SEM images with the mean atomic number of the sample and quantify the chemical composition of the studied material phases if pre-information on the material system is available. Another motivation for this work is that the BSE-SEM imaging conditions can be determined for optimum material contrast by MC simulations – provided that MC simulations are demonstrated to reliably describe BSE-SEM contrast.

Section 4.1 gives a literature overview on quantitative BSE-SEM measurements and discusses recent improvements of this method. In section 4.2, the experimental procedure of our proposed approach is presented. This includes the determination of detector-collection angles (section 4.2.1), determination of detector-threshold energy (section 4.2.2), and normalization of the measured BSE-SEM intensities with respect to the Si-bulk intensity (section 4.2.3). Section 4.3 discusses the application of MC simulations for the calculation of BSE intensities and shows the influence of different screening parameters on the MC-simulation results. The proposed quantitative BSE-SEM method was tested on two different challenging multilayer-sample systems. Section 4.4 discusses the quantitative BSE analysis of the first sample, a Si/ZnO/Zn(O_xS_{1-x})/ZnS-multilayer system. The results for the second test sample, a PTB7/$PC_{71}BM$-multilayer system, are presented in section 4.5.

4.1 Introduction

BSE-SEM imaging is a valuable technique for materials characterization because it provides important information about the mean atomic number of the analyzed specimen [Gol1992]. BSE-image intensities depend on the backscattered-electron coefficient ζ, which is defined by the number of BSEs per primary electron. A considerable amount of work has been already devoted to measurements and calculations of the atomic number (Z) dependence of ζ, as already discussed in section 2.1.5.

The main challenge of quantitative BSE-SEM imaging is to relate the measured BSE intensity to ζ and the (average) atomic number Z to derive chemical information from the BSE-SEM image. For quantitative BSE analysis, comparison of the measured data with MC simulations is essential. Quantitative BSE-SEM analysis has already been successfully used to identify strategic metals in minerals [Gua2020], evaluate the mineral distribution in bones [Ros1995], quantify Au, Ag, Ge, Cu, and Fe films on a Si substrate at 3 – 30 keV energies [Kim2010], quantify an $Al_{0.22}Ga_{0.78}N$/GaN-layer system [Cid2018], or for composition quantification of $In_xGa_{1-x}As$ layers embedded in a GaAs matrix [Mül2017]. Furthermore, quantitative BSE analysis could be utilized for layer thickness determination, by comparing the measured BSE intensities with MC

simulations. In this way, Dapor *et al.* [Dap2013] measured 20 – 250 nm thick Au films on Si-bulk substrates with 20 % accuracy. Haimovich *et al.* [Hai1996] proposed a method for the layer-thickness measurement of Au and Pd layers with 3 to 1000 nm thickness on a Ni substrate at 10, 20, and 30 keV.

Optimization of the BSE-imaging parameters by MC simulations is often carried out to understand the image contrast and distinguish the features of interest in a BSE image. Aoyama *et al.* [Aoy2015] studied the BSE contrast of heat-treated steel by controlling the primary electron energy and the detection-angle range. Sato *et al.* [Sat2015] used the BSE-intensity dependence on the detection-angle range to distinguish different phases in steel. Kowoll *et al.* [Kow2017] used MC simulations to understand the BSE contrast of complex nanoscale samples such as SiO_2 NPs deposited on indium-tin-oxide-covered glassy carbon substrates. Moreover, MC simulations were used to derive conditions for the separation of material and topography contrast. Wan *et al.* [Wan2015] distinguished topographical and material contrast of polymer samples using BSE analysis based on different angular distributions of BSEs, which were calculated using MC simulations. This angular selectivity method was later expanded also to BSE-SEM imaging under deceleration fields [Wan2016]. MC simulations have been also applied to study the influence of carbon contamination on the BSE-energy distribution [Ass2019]. It was found that surface contamination reduces the number of BSEs emerging with energies close to E_0 and increases the number of BSE with lower energies.

All examples of quantitative BSE-SEM mentioned above include MC simulations as an important addition to the measured data to reveal quantitative information from the BSE images. However, MC-simulated results depend on the used differential scattering cross-section (DSCS) (respectively on the screening parameter in the screened Rutherford cross-section) [Ass2018]. Suitable DSCSs for MC simulations depend on the material and the experimental conditions [Han2014]. To achieve reliable MC-simulation data, the MC-simulation package must be first calibrated to the particular sample material and experimental setup. Comparing MC-simulation results with measurements validates the calibration and enables reliable prediction of BSE contrast as well as optimization of the imaging parameters. To compare MC simulations with BSE measurements, normalization of the data is necessary. Contrary to quantitative HAADF STEM (Chapter 2), where the intensity of the primary electron beam is used for normalization, direct normalization of the measured BSE-SEM intensity with respect to the incident electron beam is not possible. Therefore, other normalization methods have been developed. For example, the measured BSE intensities of thin specimens can be normalized to their bulk-BSE intensity values [Mül2017] or another reference material. Another possibility of normalizing measured BSE grey values is to use an analytical formula that was previously calibrated to particular imaging conditions [San2012].

In this work, we propose a quantitative BSE method that includes MC simulations to understand BSE-SEM intensities. In this method, a wedge-shaped specimen is FIB milled from the studied bulk sample, where the sample thickness gradually increases

from 0 to approximately 2 µm. Acquiring a BSE-SEM image of the wedge-shaped specimen enables to follow the BSE-intensity increase with increasing sample thickness until the bulk intensity value is reached. Such BSE intensity-thickness profiles are suitable for comparison with simulated data because sample thickness is an additional parameter for comparison. Direct comparison is possible by normalizing the BSE intensities to the intensity of bulk Si. The Si-bulk material can be either present in the studied specimen (e.g. as a substrate) or a Si wafer is utilized for the normalization. Moreover, we consider the BSE-detector properties in the simulations to reach a better agreement with the measured data. The proposed method is tested on two different challenging multilayer-sample systems. The first is a Si/ZnO/Zn(O_xS_{1-x})/ZnS-multilayer system, where the chemical composition between individual layers varies only slightly and thus probes the sensitivity of the method. The second studied sample is a PTB7/$PC_{71}BM$-multilayer system, which was chosen as a representative of weakly-scattering materials with similar electron-scattering properties. The quantitative analysis of both sample systems demonstrates the validity of the proposed method and emphasizes the importance of reliable MC simulations for quantitative BSE-SEM analysis.

4.2 Experimental procedure

All experiments presented in this chapter were performed with a Helios G4 FX dual-beam instrument (Thermo Fisher Scientific, USA). This instrument is equipped with an annular semiconductor backscattered-electron (CBS) detector positioned below the pole piece (see Figure 2.5). Utilizing the CBS detector for quantitative BSE analysis is convenient because this detector does not require any fields to collect BSEs, and thus the comparison with simulations is feasible. To compare measured data with simulations, all experimental parameters (primary electron energy and current, detector-collection angles, detector properties, etc.) have to be known. The determination of the detector-collection angles of the CBS detector is described in section 4.2.1 and the detector properties are outlined in section 4.2.2. Moreover, for comparison with simulations, the normalization of the measured data is essential. Contrary to STEM-data normalization (section 3.3.4), the direct illumination of the CBS detector is not possible in BSE-SEM experiments, and an alternative normalization procedure for measured BSE-SEM data is presented in section 4.2.3.

4.2.1 Determination of the collection-angle range of the CBS detector

To determine the collection-angle range of the CBS detector, the detector geometry and the distance between the detector and the sample surface must be known. The CBS detector can be imaged by utilizing the electron-mirror phenomenon [Cro2008] in SEM, which enables imaging of the upper hemisphere of the SEM chamber together with the CBS detector. In this method, an insulating sample, polypropylene in this case, is charged by scanning the sample at a slow rate with 20 keV electrons for about 4 minutes. Subsequently, the electron energy is reduced to 2 keV and a mirror image of the SEM interior is obtained with the CBS detector. The image can be focused

to show the SEM components of interest. Figure 4.1a presents the electron-mirror image of the CBS detector in the Helios G4 FX. The mirrored image (Figure 4.1a) is not scaled, however, calibration with the known size of the bore of the pole piece (1.5 mm, Figure 4.1a) is possible. From the calibrated image, the inner and outer radii of the CBS-detector segments can be determined. The detector consists of four segments labelled A-D in Figure 4.1a. The inner and outer detector radii of the detector segments derived from the image in Figure 4.1a are given in Table 4.1.

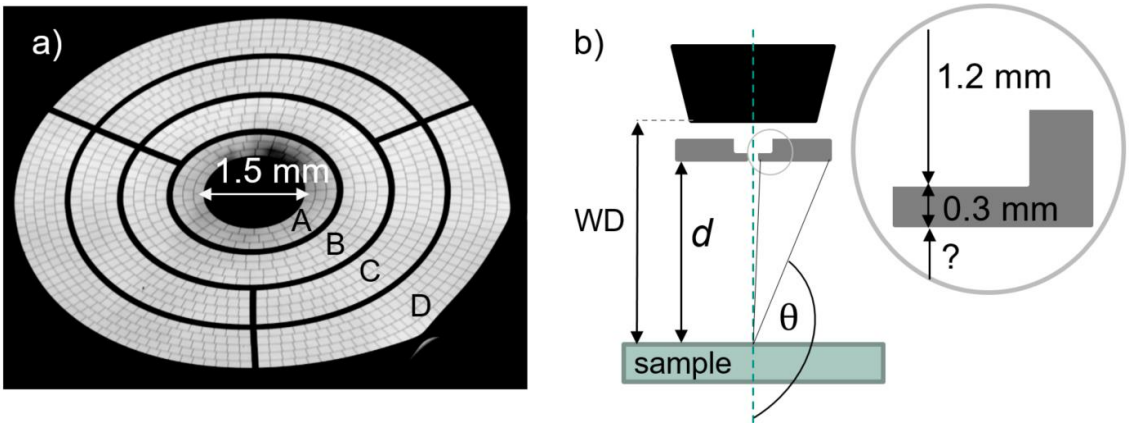

Figure 4.1 Annular backscattered-electron (CBS) detector. a) An electron-mirror image of the CBS detector in the Helios G4 FX microscope. The image scale can be calibrated with the known size of the bore of the pole piece, which is 1.5 mm. b) A scheme of the CBS-detector position in the microscope. The distance between the bottom surface of the detector and the sample surface d is essential for the determination of the collection-angle range of the CBS detector.

To determine the detector-collection angles θ, the distance between the sample and the CBS detector d must be known. Figure 4.1b shows the geometry inside the SEM chamber. The distance between the pole piece and the sample surface is known, it is the working distance (WD). The distance between the pole piece and the surface of the CBS detector was determined by focusing the electron beam on the upper side of the CBS detector. The WD in this situation is 1.2 mm. The last necessary distance is the thickness of the active semiconductor layer. This thickness was estimated to be 0.3 mm [Nan2013]. The resulting distance between detector and sample d for a particular WD is $d = \mathrm{WD} - 1.5$ mm. Moreover, the collection angles θ for the detector segments A-D result from geometry (inner and outer radii of the corresponding segment) and is given by Eq. 4.1. The collection angles for WD = 8 mm are given in Table 4.1.

$$\theta = \pi - \operatorname{atan}\left(\frac{r}{d}\right) \ [\mathrm{rad}] \tag{4.1}$$

Table 4.1 CBS-detector properties. The inner and outer radii of the CBS detector segments A-D were determined from a mirror-electron image. The derived collection angles correspond to WD = 8 mm.

Segment		Radius r [mm]	collection angle θ [rad]
A	Inner	2.4	2.79
	Outer	4	2.59
B	Inner	4.2	2.57
	Outer	6.4	2.36
C	Inner	6.7	2.34
	Outer	9.2	2.19
D	Inner	9.4	2.18
	Outer	12	2.07

Figure 4.1a also reveals, that similar to the STEM detector (section 3.3.4), some parts of the CBS detector are inactive (dark regions) and therefore a geometrical correction factor c_g has to be introduced for the normalization of the measured data. Moreover, inactive areas are also present in between the concentric detector segments. The presented BSE-SEM images taken with the CBS detector in this chapter were always acquired using all CBS detector segments together. That means that the collection-angle range was 2.07 - 2.79 rad and that the geometrical correction factor must also consider the inactive regions between the concentric detector segments. Here $c_g = 0.07$ was determined, which means that 7 % of the detector is inactive.

4.2.2 Determination of the detector-threshold energy

As a result of the metal-protection layer, that protects the semiconductor detector, a threshold energy E_{th} is introduced. Impinging electrons need to penetrate this layer and lose part of their energy. Electrons with lower electron energy than the E_{th}, that reach the detector, are partially adsorbed in the protection layer and contribute to the calculated BSE intensity with linearly decreasing detection efficiency. It is important to consider E_{th} in MC simulations (as discussed in section 2.4) to enable the comparison with measured data. The simulated normalized intensity considering the E_{th} is given by Eq. 2.23. E_{th} can be determined by measuring the detector-response curve. The response curve describes the dependence of the measured grey values as a function of the primary electron energy. Importantly, the contrast/brightness settings must stay unchanged throughout the whole measurement. For each electron energy, an SEM image of a Si-wafer sample and a corresponding blanked beam image was acquired. Averaging the image intensity in each of the acquired images and subtracting the averaged values from the corresponding blanked images lead to the grey values plotted in Figure 4.2 as a function of primary electron energy. Figure 4.2a shows the measured detector response curve for contrast (electronic gain of the detector) of 80 %. For this contrast setting, the detector is oversaturated at energies > 1000 eV. The response curve in Figure 4.2a is not linear and shows a local maximum at $E = 500$ eV. Similar

behaviour is observed in Figure 4.2b, where the response curve was measured for a contrast setting of 60 %. Local maxima are also observed at 1, 2 and 3.5 keV in Figure 4.2b. For higher electron energies, the local maxima are less pronounced, and the response curve becomes linear. The origin of these local maxima is not clear, however, most probably they originate from the detector-amplifier system. Fitting a linear curve to the data shown in Figure 4.2b reveals an intersection with the energy axis at $E_{th} = 500$ eV, which is the detector threshold energy. The determined E_{th} was taken into account in all MC-simulated BSE data in this chapter.

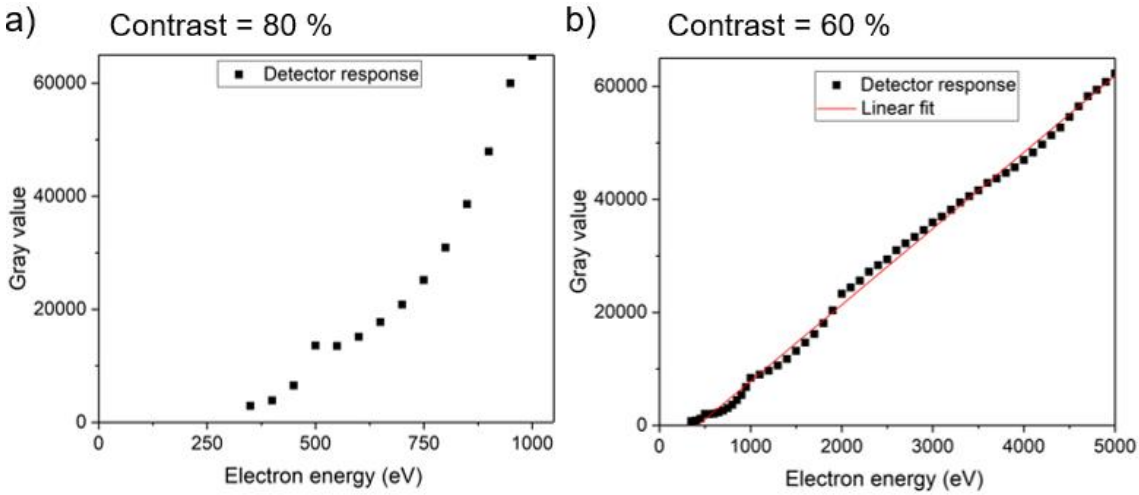

Figure 4.2 CBS-detector response curve. The measured response curve of the CBS detector for a) a contrast setting of 80 % and b) contrast setting of 60 %. The linear fit to measured data in b) reveals the detector threshold energy $E_{th} = 500$ eV.

4.2.3 Normalization of measured BSE data

Normalization of the measured data is essential for comparison with simulations and quantitative analysis of BSE intensities. In STEM (section 3.3.4), the data normalization was straightforward by acquiring a reference image of the STEM detector with unchanged imaging parameters. In the experimental setup for BSE imaging, direct illumination of the CBS detector is not possible, requiring a different approach to data normalization. Measured data normalization by the bulk intensity value of a suitable material yields relative intensity values that can be compared with simulated data normalized to the same bulk intensity. In this thesis silicon (Si) was chosen as reference material because Si is widely used and often serves as a support material for different samples.

Figure 4.3 compares two Si-bulk intensity values obtained from a Si wafer and a Si wedge-shaped specimen under the same experimental conditions. In Figure 4.3a, a wedge-shaped sample consisting of a Si substrate, diamond-like carbon (DLC) and a deposited Pt-protection layer was imaged in a cross-section perspective. The sample was prepared by FIB milling from a bulk specimen. The preparation of wedge-shaped specimens was already described in section 3.3.2. The BSE image of the wedge sample in Figure 4.3a was acquired using 30 keV electrons, a 0.2 nA electron current, and an 8 mm working distance. The BSEs were collected with the CBS detector using all detector

segments. Subsequently, the same imaging parameters, particularly the contrast/brightness settings, were used to acquire a BSE-SEM image of the Si wafer, serving as a reference sample. Such a reference image is shown in Figure 4.3b. Averaging the image intensity gives a grey value of 12012 that corresponds to the Si-bulk intensity for the chosen imaging parameters. Figure 4.3c shows an intensity-line profile obtained from the BSE image in Figure 4.3a by averaging over a line width of 20 pixels along the green line. The starting point of the line scan is denoted by an arrow. The line profile in Figure 4.3c shows a grey-value dependence on the local sample thickness of the Si wedge. Knowing the wedge angle ($\alpha = 25°$), the distance along the line scan x can be converted to the local sample thickness $t = x \tan \alpha$. Figure 4.3c shows the typical shape of the BSE intensity for a wedge-shaped sample. The intensity (grey value) increases with increasing wedge thickness because more electrons are backscattered within the sample. The BSE intensity saturates when the thickness of the sample reaches the electron range and becomes constant even for larger sample thicknesses. The constant intensity value is the BSE-bulk intensity, which is related to a particular material, electron energy, detection-angle range and sample tilt. Moreover, the bulk intensity is influenced by the surface topography and surface contamination, which is undesired. FIB-milled wedge-shaped specimens are well suited for BSE analysis because contributions from topography and surface contamination are minimized. Moreover, observing the thickness dependence of the BSE intensity precisely reveals the desired bulk intensity. A Si-bulk grey value of 12407 was obtained from the wedge-shaped sample (Figure 4.3a and c), which is very similar to the Si-wafer bulk value (12012). One possible origin of the discrepancy between the Si-bulk BSE intensities could originate from the native SiO_x layer, which is present on the Si wafer surface. However, the native oxide layer is only a few nm thick and does not significantly influence the measured BSE intensities. Agreement between the Si-bulk grey values measured on Si wedge and Si wafer was obtained also for 15, 10 and 5 keV. We note that the Si-bulk grey values are similar throughout the whole wafer and that the electron-beam induced contamination does not have a significant influence on the BSE intensity at primary electron energies between 5 and 30 keV. Therefore, it is possible to use a Si wafer as a reference sample for normalization of the measured BSE intensities with respect to the Si-bulk intensity. In the case of quantitative BSE analysis of DLC in Figure 4.3 or the two samples in sections 4.4 and 4.5, the Si-bulk intensity can be determined directly from the BSE image of the specimen because the layer systems are deposited on Si wafers and no other reference sample is needed.

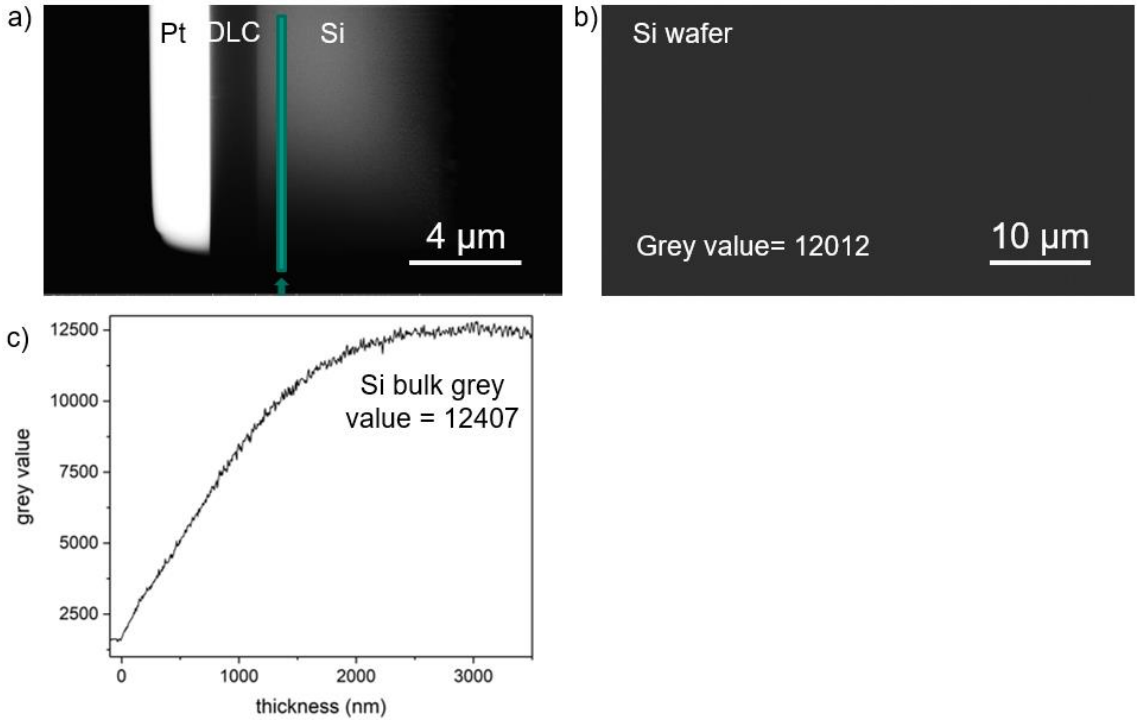

Figure 4.3 Si-bulk intensity for normalization of measured data. a) 30 keV BSE-SEM image of a FIB-milled wedge-shaped cross-section specimen containing a diamond-like carbon (DLC) layer covered with a Pt-protection layer on a Si substrate. The BSE-SEM image was acquired with the CBS detector using all segments. b) 30 keV BSE-SEM image of a Si wafer taken with the same imaging parameters as in a). The averaged Si-bulk grey value from the Si wafer is 12012. c) An intensity-line profile along the green line in a) reveals the grey-value dependence on the local sample thickness of Si wedge. The saturated Si-bulk grey value 12407 is comparable to the grey value obtained from the image in b).

The normalized BSE intensity is given by Eq. 4.2, where I_m denotes the measured intensity, c_g is the geometrical correction factor, $I_{Si\ bulk}$ is the Si bulk intensity and I_b is the black intensity obtained by averaging the grey values in an image acquired with a blanked beam. The normalized Si curve in Figure 4.3c according to Eq. 4.2 is shown in Figure 4.4. Additionally, a normalized BSE-intensity thickness curve for DLC is plotted in red. Such normalized BSE-intensity thickness curves can be compared with data obtained by MC simulations.

$$I_{Norm} = \frac{I_m(1 + c_g) - I_b}{I_{Si\ bulk}(1 + c_g) - I_b} \tag{4.2}$$

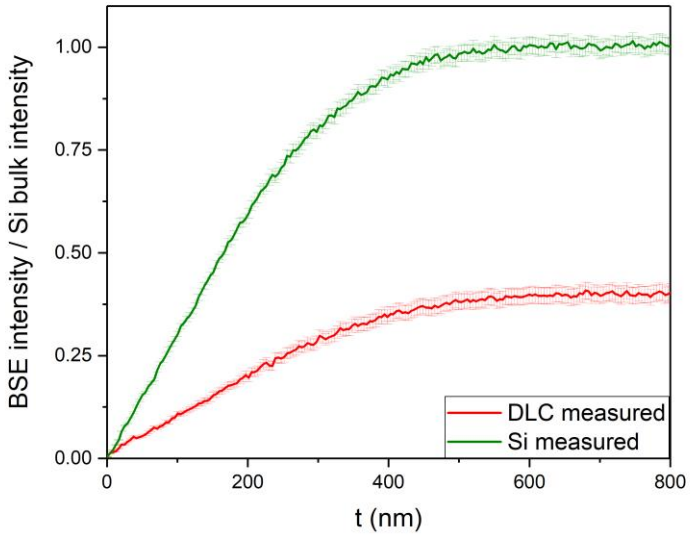

Figure 4.4 Normalization of measured data. The plot shows the dependence of the BSE intensity as a function of the local sample thickness for Si (green) and DLC (red) normalized with the bulk BSE intensity of Si (Eq. 4.2). The measured data was obtained from intensity-line scans in Figure 4.3a along the green line for Si and analogously for DLC.

When normalizing the measured data with the bulk value of Si or any other crystalline material, electron channelling [Zau1992] has to be considered, as it can influence the measured bulk intensity. The electron-channelling phenomenon occurs in crystals under specific incidence angles, where the electron paths are constrained to atomic columns, which influences the scattering properties. In other words, the BSE coefficient ζ is dependent on the crystal orientation. However, ζ depends also on sample tilt according to Eq. 2.15.

The influence of the sample tilt on the BSE intensity for a Si(111) wafer was investigated, and the measured data is shown in Figure 4.5. Unfortunately, the CBS detector cannot be used when the stage in the Helios G4 FX microscope is tilted. Therefore, the measurements were performed with two other BSE detectors, the through-lens detector (TLD) (Figure 4.5a) and the mirror detector (MD) (Figure 4.5b). Both detectors are positioned inside the electron column. The shape of the two curves is similar and shows a peak at -1° tilt and minima around -7° and 6°. The measured data are a result of the superposition of channelling and the sample-tilt dependence of ζ within the detection-angle range. The sample-orientation dependence causes the intensity decrease from the -1° sample tilt as expected from Eq. 2.15. The channelling effect then modulates the intensity decrease and causes an intensity increase at larger tilt angles in Figure 4.5. The intensity minima correspond to the Bragg angles for the Si (022) planes, which is plausible for a Si(111) substrate. Considering the grey-value intensity modulations in Figure 4.5, we can conclude that the sample orientation does not strongly affect the measured BSE intensity. The use of the CBS detector for BSE

imaging further reduces the channelling effect because it has a much larger detection-angle range compared to the MD and TLD detector.

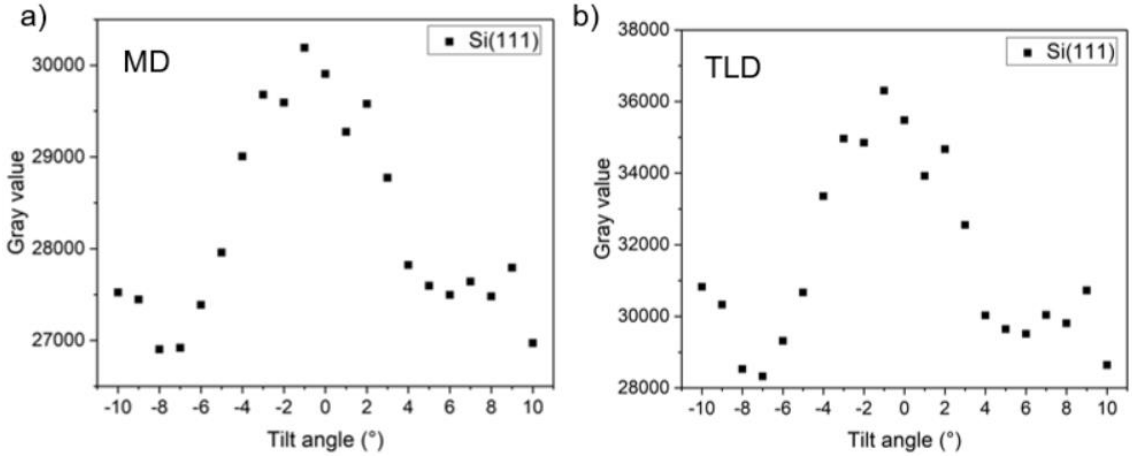

Figure 4.5 BSE-SEM intensity as a function of the sample orientation. The data were measured on a Si(111) wafer with 2 keV electrons. The BSEs were detected with a) a mirror detector (MD) and b) a through-lens detector (TLD).

4.3 Monte-Carlo simulations of BSE intensity

MC simulations are utilized in this work to quantify the contrast of the studied materials and optimize the experimental parameters, i.e. electron energy and detection-angle range. Moreover, MC simulations can be used to understand the contrast in experimental BSE images and explain unexpected contrast features of the measured data. In this work, we have adopted the NISTMonte simulation package [Rit2005] with implemented screened Rutherford scattering cross-sections. Possible choices of the screening parameters in the cross-section are listed in section 3.2. The energy loss of the scattered electrons is described by the Joy and Luo [Joy1995] continuous-slowing-down approximation. To obtain the dependence of the simulated BSE intensity on the sample thickness, the MC simulations were performed in a thickness range of 1 – 3000 nm with 10 nm thickness intervals. By integrating the angular distribution of the backscattered electrons over the detection-angle range of the CBS detector (see Table 4.1), the simulated BSE intensity is calculated at each sample thickness. To achieve a more precise comparison between measured and simulated data, the properties of the BSE detector must be considered in the simulated BSE intensities according to Eq. 2.22 and Eq. 2.23. The threshold energy of the CBS detector was measured and has a value of $E_{th} = 500\ \mathrm{V}$ (section 4.2.2).

Figure 4.6 shows the angular distribution of the scattered electrons obtained by MC simulations for 15 keV electrons interacting with a 1.5 µm thick Si film. The x-axis gives the scattering angle and the y-axis the number of electrons. The total number of simulated electrons was 10^5. The forward-scattering direction covers the $0 - \pi/2$ range and back-scattering directions are $\pi/2 - \pi$. The typical shape of the scattering-angle curve for a thin-film sample is shown in Figure 4.6. The counts increase with increasing scattering angle, reach a maximum and then decrease towards the scattering angle $\pi/2$, where all electrons are absorbed, because this is the scattering direction parallel to the

film surface. On the further increase of the scattering angle, the counts again increase as the electrons are backscattered. Finally, the counts decrease towards scattering angle π. The green curve corresponds to MC simulations with the Nigam screening parameter, whereas the red curve was calculated with the Bishop screening parameter. Comparing these two curves reveals that the screening parameter significantly influences the angular distribution of the scattered electrons and has to be carefully chosen to match the measured data.

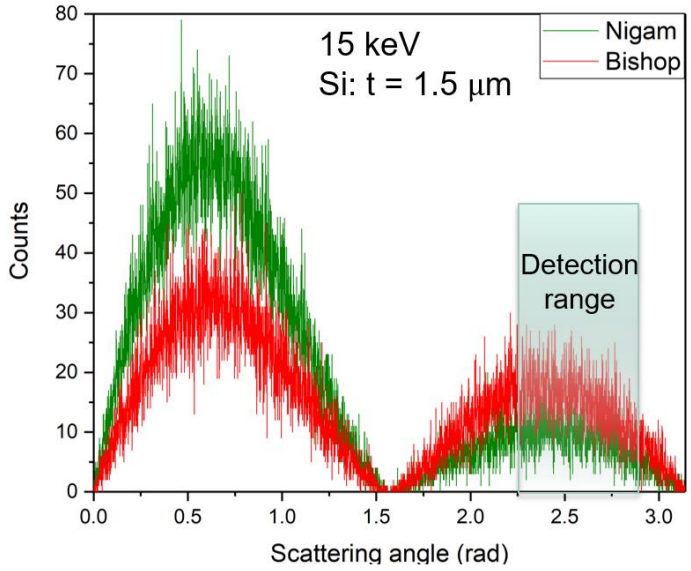

Figure 4.6 Angular distribution of scattered electrons. MC-simulated angular distributions of 15 keV scattered electrons interacting with a 1.5 µm-thick Si film are plotted in red for the Bishop and in green for the Nigam screening parameter. The detection-angle range of the CBS detector is indicated by the blue-green box.

To understand the BSE-intensity dependence on the different screening parameters, the dependence of the MC-simulated BSE intensity on the sample thickness was calculated for Si using different screening parameters listed in Section 3.2. The simulation results are plotted in Figure 4.7 for 20 keV in a) and 10 keV in b). The simulated data are normalized to the total number of electrons and not to the counts corresponding to Si-bulk intensity because we want to compare the performance of the different screening parameters also in the Si-bulk region. An increase of the BSE intensity with the sample thickness is observed for all curves and the corresponding bulk-intensity values vary. The lowest bulk value is obtained with the Nigam screening parameter (green curve), whereas the highest value yields the NIST screening parameter (dark blue). The Thomas-Fermi (yellow curve), Moliere (purple curve) and Seltzer (brown curve) screening parameters give similar results. Additionally, results for the Mott scattering-cross-section are plotted in light blue. These results agree well with the Bishop screening parameter (red curve).

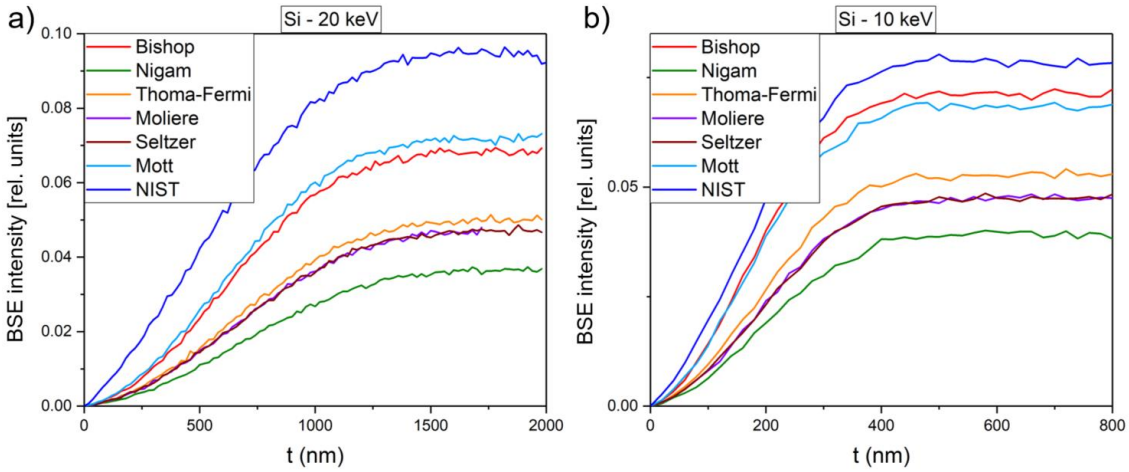

Figure 4.7 Dependence of the MC-simulated BSE intensity on the sample thickness using different screening parameters. a) MC-simulated BSE intensity as a function of the sample thickness *t* for 20 keV electrons for Si normalized to the total number of simulated electrons. Different curves were calculated with different screening parameters: Bishop (red), Nigam (green), Thomas-Fermi (yellow), Moliere (purple), Seltzer (brown) and NIST (dark blue). MC simulations based on the Mott cross-section are indicated in light blue. b) The same calculations as in a) for 10 keV electron energy.

Comparison of the simulated curves in Figure 4.7 reveals that the screening parameter significantly influences the simulated result. To achieve a reliable representation of the measured BSE data, the suitability of a particular screening parameter for particular sample material and experimental conditions (electron energy, detection angle range) must be verified. Choosing the suitable screening parameter based on comparison of the measured (obtained from a wedge-shaped specimen) and MC simulated BSE intensity vs. thickness curves is convenient because the thickness serves as an additional parameter for the comparison. In the following, suitable screening parameters for the two studied test samples are determined, i.e. Bishop screening parameter for the Si/ZnO/Zn(O_xS_{1-x})/ZnS-multilayer system and NIST screening parameter for the PTB7/$PC_{71}BM$-multilayer system. We note that the Bishop screening parameter with the new expression for the screening radius (Eq. 3.16) derived in Chapter 3 is not suited for simulation of BSE intensities as it was derived for HAADF-STEM simulations with completely different detection angle ranges.

4.4 Quantitative analysis of a Si/ZnO/Zn(O_xS_{1-x})/ZnS-multilayer system by BSE-SEM

As the first test sample for quantitative BSE analysis, a multilayer system consisting of 100 nm thick layers of ZnO, Zn($O_{0.7}S_{0.3}$), Zn($O_{0.5}S_{0.5}$), Zn($O_{0.4}S_{0.6}$) and ZnS was studied. The multilayer system was deposited on a Si substrate, as shown in the cross-section scheme in Figure 4.8a. This multilayer system was fabricated as a test sample in the study of a buffer-layer system for Cu(In,Ga)Se_2-based solar cells [Jin2019]. In this thesis, the sample was chosen because the rather small composition variations between the layers probe the limits of the suggested quantitative BSE method. Moreover, the material parameters of ZnO and ZnS are well known and yield precise MC-simulated

data. The average atomic number of the compounds was calculated using Eq. 4.3, where c_i and Z_i are concentrations in at.% and atomic numbers of the particular element in the compound. The power $a = 2$ is related to the Rutherford model where Z has a quadratic dependence. Eq. 4.3 was adopted for the calculation of the average atomic mass A by substituting A for Z and for $a = 1$.

$$\bar{Z} = \sqrt[a]{\sum_i c_i Z_i^a} \tag{4.3}$$

The material densities for ZnO (5.61 g/cm^3, [Hay2011]) and for ZnS (4.09 g/cm^3, [Lid1998]) are known. The material densities for $Zn(O_xS_{1-x})$ were interpolated and all material parameters are shown in Table 4.2.

Table 4.2 Material parameters of the Si/ZnO $Zn(O_xS_{1-x})$/ZnS multilayer system.

Material	Average atomic number Z	Density ρ (g/cm^3)	Average atomic mass (atomic mass units)
ZnO	21.95	5.61	40.69
$Zn(O_{0.7}S_{0.3})$	22.6	5.15	43.1
$Zn(O_{0.5}S_{0.5})$	23	4.85	44.71
$Zn(O_{0.4}S_{0.6})$	23.23	4.7	45.51
ZnS	24	4.09	48.72
Si	14	2.33	28.09

From the material parameters, the BSE-image contrast can be qualitatively determined. The BSE intensity is proportional to $Z^2\rho t/A$. If the TEM-sample thickness is the same for all material layers, the presumed BSE intensity for ZnO is higher as compared to ZnS based on the $Z^2\rho t/A$ dependence. The qualitatively presumed BSE intensity of the layers is shown in Figure 4.8b. The Si substrate should appear even darker compared to the ZnS layer.

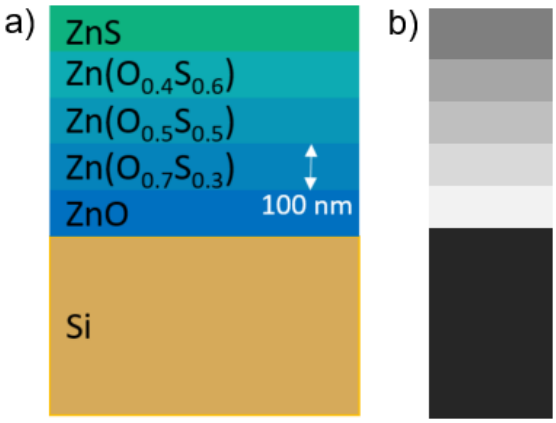

Figure 4.8 Scheme of the Si/ZnO/$Zn(O_xS_{1-x})$/ZnS-multilayer system. a) The scheme of the Si/ZnO/$Zn(O_xS_{1-x})$/ZnS-multilayer system in a cross-section shows 100 nm-thick layers with the respective chemical composition. b) Corresponding qualitatively

presumed BSE intensities based on the material parameters of the different layers. The BSE image of ZnO appears brighter than ZnS.

4.4.1 Monte-Carlo simulations for BSE-SEM parameter optimization

Before BSE measurements, MC simulations were used to obtain insights into the BSE-SEM contrast of the Si/ZnO/Zn(O_xS_{1-x})/ZnS-multilayer system and to determine the imaging parameters for optimum contrast. Among the imaging parameters, the primary electron energy is the most significant. Moreover, the wedge-shaped specimen enables to study the multilayer system at a certain sample thickness, which means that the sample thickness is an additional parameter that needs to be investigated. For distinguishing the thin (100 nm) layers within the Si/ZnO/Zn(O_xS_{1-x})/ZnS-multilayer system, the primary electron energy should be as high as possible to reduce beam broadening. We note, that the opposite would apply to a bulk sample, where the interaction volume is minimized at small electron energies. The largest wedge thickness is approximately 2 µm, which restricts the primary electron energy to 15 keV. At this electron energy, the measured BSE data can be directly normalized with the bulk intensity of the Si substrate.

MC simulations were performed for 15 keV electrons with the Bishop screening parameter (Eq. 3.2) implemented into the screened Rutherford differential scattering cross-section (Eq. 3.1) and BSEs were collected in the 2.07 – 2.79 rad detection-angle range. The normalized BSE-intensity dependence on the sample thickness was calculated for each layer of the Si/ZnO/Zn(O_xS_{1-x})/ZnS-multilayer system and is plotted in Figure 4.9a. The data were normalized to the Si-bulk intensity, as the black dashed curve for Si reaches the value 1 for sample thicknesses above 1000 nm. The ZnO/Zn(O_xS_{1-x})/ZnS curves are very similar and reach bulk values at $t \approx 400\ \mathrm{nm}$. The bulk value of the BSE intensity of all Zn(O_xS_{1-x}) layers is about 1.5 times higher than the Si-bulk value and is most likely indistinguishable between the different layers considering noise in real measurements. Figure 4.9b shows an enlarged part of Figure 4.9a for thicknesses between 100 and 500 nm. At these sample thicknesses, where the bulk BSE intensity is not yet reached, the intensity of the layers is sufficiently different to reveal a contrast in a BSE-SEM image. Considering the MC simulations, the most suitable sample-thickness range for BSE imaging of the studied multilayer system is at thicknesses between 150 and 300 nm (blue-green shaded region in Figure 4.9b). Moreover, the MC simulations confirm the qualitatively presumed contrast, i.e. ZnO appears brighter than ZnS in a BSE image.

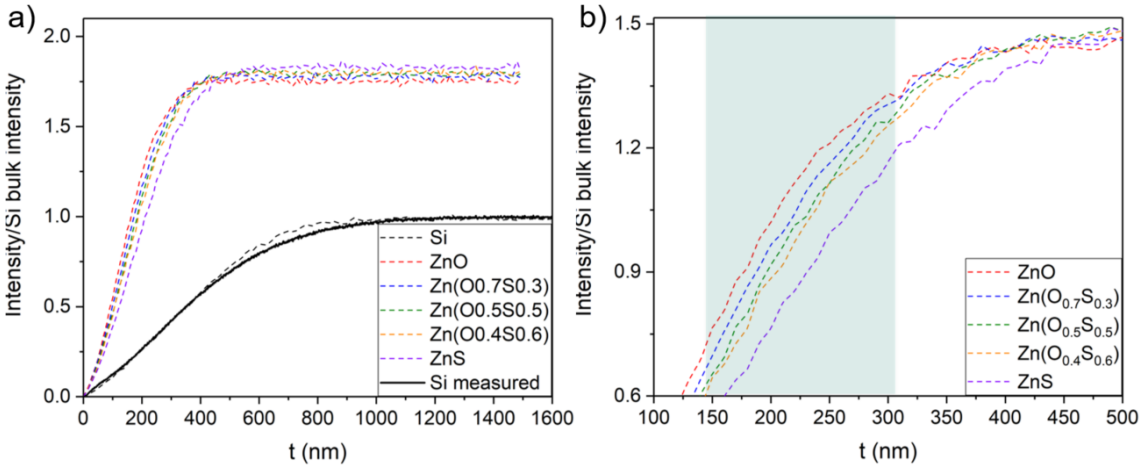

Figure 4.9 MC simulations of the Si/ZnO/Zn(O_xS_{1-x})/ZnS-multilayer system. a) 15 keV BSE intensity of the different layers in the Si/ZnO/Zn(O_xS_{1-x})/ZnS-multilayer system normalized to the Si-bulk intensity as a function of the sample thickness. b) Enlarged selection of a) showing the most suitable thickness range (150 – 300 nm) for BSE measurements.

4.4.2 Experimental results

From the bulk Si/ZnO/Zn(O_xS_{1-x})/ZnS-multilayer system, a lamella was prepared and further trimmed in a wedge shape using FIB. The final FIB milling was performed using a 5 keV ion beam to prepare smooth wedge surfaces with negligible Ga^+ implantation. The wedge sample preparation was already discussed in more detail in section 3.3.2. The FIB-prepared wedge of the Si/ZnO/Zn(O_xS_{1-x})/ZnS-multilayer system was imaged in a top view orientation with the SEs (Figure 4.10a). From the top-view SE-SEM image, the wedge angle was measured to be $\alpha = 25° \pm 0.5°$. In the top-view image, the Pt-protection layer is visible and the material of interest is located underneath. The wedge angle for the multilayer system could therefore slightly differ from the wedge angle measured on the Pt-protection layer. A possible difference might be induced by different sputter rates of the materials and, hence, a wedge angle error of $\pm 0.5°$ was introduced. A cross-section view is obtained by tilting the sample by 90° from the top-view orientation. Figure 4.10b shows a 15 keV BSE-SEM cross-section image acquired with the CBS detector at 8 mm WD. The bright contrast represents the Pt-protection layer. Underneath, the ZnO/Zn(O_xS_{1-x})/ZnS layers are present. The dark contrast below represents the Si substrate. In Figure 4.10b, the thickness of the wedge increases from left to right, and the black contrast on left is from the vacuum region. Performing a 20-pixel-wide line scan along the white line in direction of the white arrow, the measured BSE-intensity/thickness profile is obtained. The distance along the line scan x can be converted to the local sample thickness $t = x \tan(25°)$, and the measured intensities can be normalized to the Si-bulk intensity according to Eq. 4.2. The normalized measured curve for Si is shown in Figure 4.9a by the black full line. The measured curve can be directly compared with MC simulations (black dashed line). The comparison reveals that the MC simulations using the Bishop screening parameters represent the measured BSE data for Si well. A small discrepancy is observed at sample thicknesses, where the BSE intensity starts to saturate. The reason for the discrepancy

might be caused by the wedge angle of the prepared wedge sample, which may slightly differ from the real wedge angle.

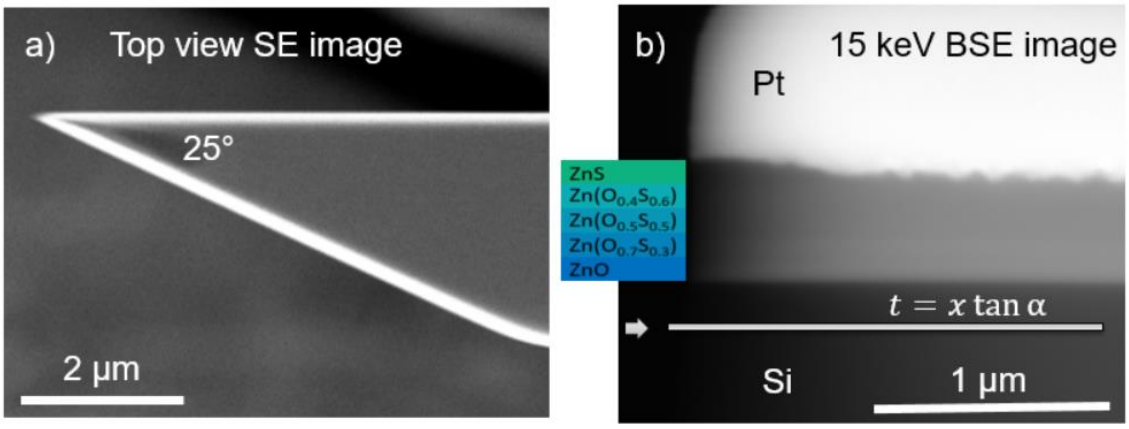

Figure 4.10 BSE-SEM imaging of the Si/ZnO/Zn(O_xS_{1-x})/ZnS-multilayer system. a) 5 keV top-view SE-SEM image of the FIB-milled wedge, from which the wedge angle is measured. b) 15 keV BSE-SEM cross-section image of the wedge, which was acquired by using all segments of the CBS detector at 8 mm WD. The thickness increases from left to right and the ZnO/Zn(O_xS_{1-x})/ZnS-multilayer system is between the Pt-protection layer and the Si substrate as indicated by the scheme.

The individual layers of the ZnO/Zn(O_xS_{1-x})/ZnS-multilayer system can be hardly distinguished in the BSE image shown in Figure 4.10b. Figure 4.11a shows an enlarged selection of the image in Figure 4.10b with 20 % enhanced contrast, where the individual layers can be recognised. Importantly, the predicted contrast (from qualitative analysis and also from MC simulations) is confirmed, showing bright contrast for ZnO and dark contrast for ZnS. The MC simulations suggest the highest contrast between the individual layers at a thickness $t = 150\,\mathrm{nm}$. A line scan perpendicular to the ZnO/Zn(O_xS_{1-x})/ZnS layers at a wedge thickness of $110\,\mathrm{nm}$ is plotted in Figure 4.11b (black line). The measured BSE intensities in Figure 4.11b are normalized according to Eq. 4.2. In the line scan, the different layers can be clearly distinguished apart from the Zn($O_{0.5}S_{0.5}$) and Zn($O_{0.4}S_{0.6}$) layers, where the chemical composition is not different enough. Due to beam broadening, the interfaces between the layers are not sharp but blurred. Considering material parameters of ZnS, 15 keV electron energy and sample thickness of 110 nm in Eq 2.13, the beam broadening at the bottom surface of the sample is estimated to be 105 nm. The influence of the beam broadening is not negligible and is discussed in more detail later. For comparison with MC simulations, the precise wedge thickness at the position of the line scan is important to know. The exact thickness at the position of the line scan can be determined from the Si intensity by comparison with MC simulations. The normalized BSE intensity at the beginning of the line scan (black curve in Figure 4.11b) corresponds to Si and has a value of 0.13. Assuming that the MC-simulated data represent the measured data sufficiently well (compare black lines in Figure 4.9a), the intensity value of 0.13 corresponds to the BSE intensity of Si with a thickness of $110 \pm 10\,\mathrm{nm}$. The uncertainty represents the discrepancy between the measured and simulated data in Figure 4.9a. For comparison, another line scan at a higher wedge thickness (700 nm) is plotted in Figure 4.11b (red

line). At this larger wedge thickness, the individual layers are not distinguishable anymore because beam broadening is more pronounced. Moreover, MC simulations also reveal a lower contrast between the layers at these larger wedge thicknesses. The main error in the measured data in Figure 4.11b originates from performing the line scans. The line scan should be acquired exactly perpendicular to the wedge thickness gradient. In practise, this is challenging, and therefore an error bar is introduced to the measured data in Figure 4.11b obtained by performing five line scans in a similar sample position and calculating the standard deviation for the average value.

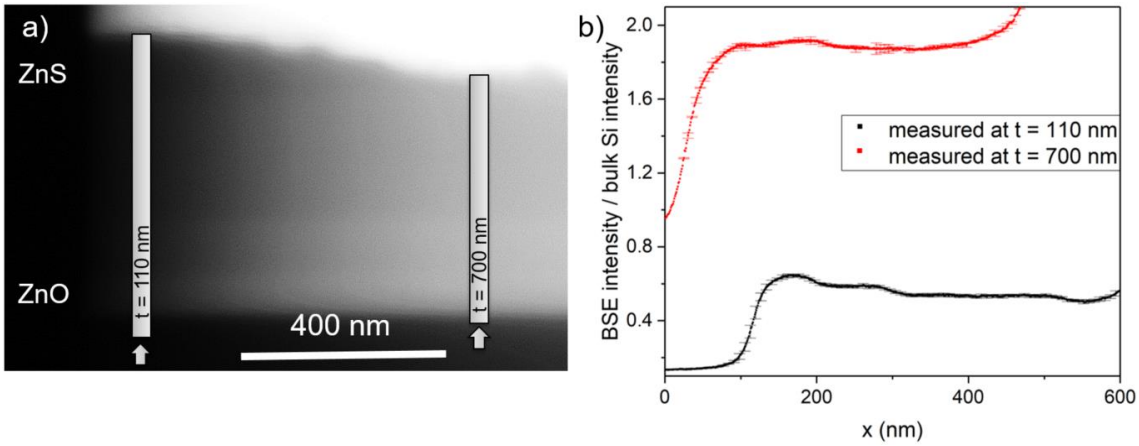

Figure 4.11 Intensity-line scans perpendicular to the Si/ZnO/Zn(O_xS_{1-x})/ZnS-multilayer system. a) Enlarged section of the BSE image in Figure 4.10b with enhanced contrast to reveal the ZnO/Zn(O_xS_{1-x})/ZnS layers. b) Measured intensity-line scans along the indicated lines in a). The black line scan was acquired at wedge thickness $t = 110\ nm$ and the red line scan at wedge thickness $t = 700\ nm$.

4.4.3 Comparison of measured and simulated data

Measured BSE intensities normalized according to Eq. 4.2 can be directly compared with MC-simulated data normalized to the simulated Si-bulk value. The MC-simulated intensities are calculated according to Eq. 2.23. Figure 4.12 shows the line scan from Figure 4.11b obtained at 110 nm wedge thickness. Additionally, MC-simulated BSE intensities with the Bishop screening parameter for each layer of the ZnO/Zn(O_xS_{1-x})/ZnS-multilayer system at a thickness of 110 nm are plotted (dashed red line). The uncertainty of the simulated data is estimated from the Poisson noise in the MC simulations. The measured and simulated data fit very well for all materials in the ZnO/Zn(O_xS_{1-x})/ZnS-multilayer system except for ZnS. In general, the measured intensity is slightly higher compared to the MC-simulated data. This small discrepancy is in the uncertainty range of the plotted data. A possible explanation for the discrepancy might be Ga^+ implantation, which would increase the measured BSE intensities compared to the ideal case without Ga^+ ions in the studied material. Even though measures to minimize the Ga^+ implantation during the wedge preparation procedure were applied, a small amount of Ga^+ might be present in the surface region of the sample and can cause the small discrepancy in Figure 4.12. The effect of the Ga^+ implantation on the measured BSE intensities can be estimated by comparing the measured and MC-

simulated curves for Si in Figure 4.9a. The measured and MC-simulated curves fit very well (particularly at small sample thicknesses where the effect of Ga^+ implantation should be most pronounced). Therefore, it can be concluded that Ga^+ implantation is not strongly present in the studied wedge specimen and does not significantly influence the measured BSE intensities. In the case of the ZnS layer, the simulations do not agree well with the measured data. The discrepancy can be explained by considering beam broadening in the experimental data. The ZnS layer is located next to the Pt-protection layer on right in the plot in Figure 4.12. Calculating the beam broadening within the ZnS layer according to Eq. 2.13 leads to a value $b = 105\ \mathrm{nm}$, which is comparable with the ZnS layer thickness. Therefore, the Pt layer (as a heavy scatterer) significantly contributes to measured intensities for ZnS and thus increases the measured intensity with respect to the MC simulations. The influence of beam broadening is also visible in the measured data for ZnO, where the ZnO intensity decreases towards the intensity of Si. Due to beam broadening the measured intensity for the ZnO layer is not constant over the whole ZnO layer thickness, as it is expected according to the MC simulations (red-dashed line in Figure 4.12). The measured intensity decreases from the constant ZnO value already at about half of the ZnO-layer thickness towards the BSE intensity of the Si substrate. To reduce the beam-broadening effect, higher primary electron energies or smaller sample thicknesses are required.

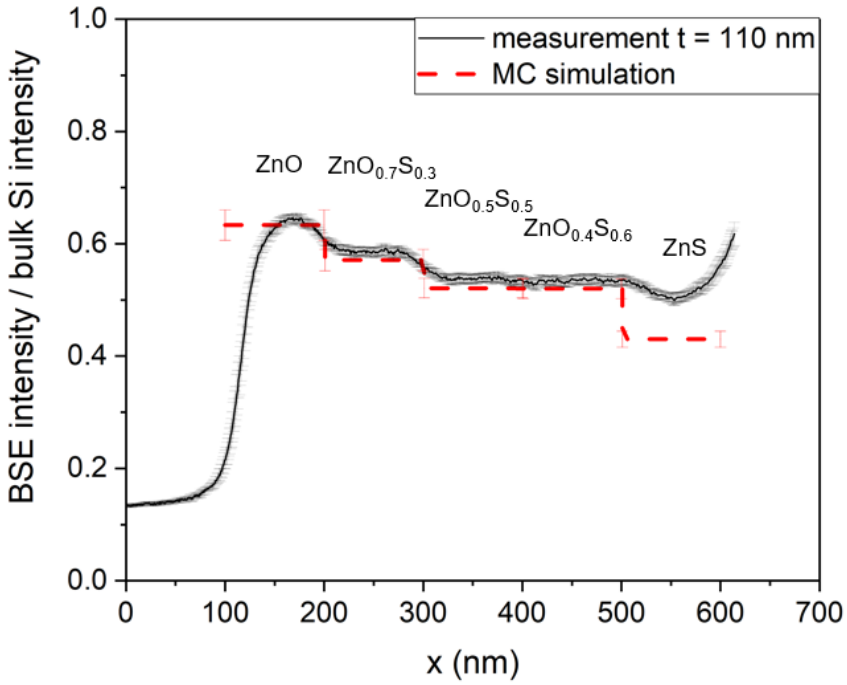

Figure 4.12 Comparison of measured and simulated normalized BSE intensities for the Si/ZnO/Zn(O_xS_{1-x})/ZnS-multilayer system. The black curve represents the measured 15 keV BSE intensity-line profile perpendicular to the Si/ZnO/Zn(O_xS_{1-x})/ZnS-multilayer system from Figure 4.11b at 110 nm wedge thickness. The red-dashed curve shows the MC-simulated data using the Bishop screening parameter for the layers of the sample.

To visualize the (dis)agreement between simulated and experimental BSE intensities more clearly, Table 4.3 shows the calculated intensity ratios between the MC-simulated and measured intensities for all layers of the ZnO/Zn(O_xS_{1-x})/ZnS-multilayer

system and the MC-simulated or measured intensities of the ZnO layer. The calculated intensity ratios for simulated and measured data agree very well for all layers except the ZnS layer. The measured ratio for ZnS gives a value of 0.77, whereas the MC simulations give 0.68. This discrepancy is caused by beam broadening, as discussed already above. In the absence of beam broadening, the simulated value is expected to approach the experimental data because the MC simulations do not consider beam broadening, and agree well with the measurements for the other layers of the ZnO/Zn(O_xS_{1-x})/ZnS-multilayer system.

Table 4.3 Intensity ratios of the measured and MC-simulated data of the Si/ZnO/Zn(O_xS_{1-x})/ZnS-multilayer system with respect to the ZnO intensity.

	ZnO	**Zn($O_{0.7}S_{0.3}$)**	**Zn($O_{0.5}S_{0.5}$)**	**Zn($O_{0.4}S_{0.6}$)**	**ZnS**
Intensity ratio MC simulation	1	0.90	0.83	0.83	0.68
Intensity ratio exper. data	1	0.89	0.83	0.82	0.77

Figure 4.12 and Table 4.3 reveal that the proposed approach of the quantitative BSE analysis is feasible and can be used for the determination of the O/S content in ZnO/Zn(O_xS_{1-x})/ZnS-multilayer system. The MC-simulated BSE intensity vs. thickness curves calculated using the Bishop screening parameter describes the measured data well and can be used for reliable optimization of the imaging parameters. It has been shown that materials varying only slightly in chemical composition, e.g. Zn($O_{0.7}S_{0.3}$) and Zn($O_{0.5}S_{0.5}$), can be distinguished in a BSE image if the interaction volume is not relevant at small sample thicknesses. However, the materials with chemical composition as close as Zn($O_{0.5}S_{0.5}$) and Zn($O_{0.4}S_{0.6}$) cannot be distinguished in a BSE image because the scattering properties of both materials are almost identical.

4.5 Quantitative analysis of a PTB7/$PC_{71}BM$-multilayer system by BSE-SEM

The second test sample, that was used to demonstrate the applicability of the proposed quantitative BSE-SEM analysis technique, is a PTB7/$PC_{71}BM$-multilayer system. PTB7 ($C_{41}H_{53}FO_4S_4$) and $PC_{71}BM$ ($C_{82}H_{14}O_2$) are materials that have attracted a lot of research interest because they are used in bulk-heterojunction absorber layers of polymer solar cells [Lia2012]. The bulk-heterojunction consists of an interpenetrating network of domains of PTB7 and $PC_{71}BM$ molecules with domain sizes as small as 10 nm. The size and morphology of these domains determine the properties of the solar cells. Studying the morphology of the PTB7 and $PC_{71}BM$ domains in bulk-heterojunction absorber layers on the nanoscale is of high relevance because it can be correlated with the solar-cell performance and contributes to the optimization of the next generation of polymer solar cells [Hee2014]. The challenge of imaging the phase morphology of the

PTB7/$PC_{71}BM$-absorber layers with electron microscopy is related to the weak contrast between the two materials because $PC_{71}BM$ and PTB7 materials scatter electrons only weakly [Li2021]. Moreover, the material parameters and thus the scattering properties of PTB7 and $PC_{71}BM$ are very similar. The PTB7/$PC_{71}BM$-multilayer system was chosen as a test sample to demonstrate the applicability of our proposed quantitative BSE analysis to soft weakly scattering materials with similar material parameters. The material parameters of both materials are summarized in Table 4.4.

MC simulations are applied to optimize the BSE-imaging parameters to obtain the best possible contrast between $PC_{71}BM$ and PTB7 and to verify the MC-simulated results by comparison with BSE measurements. A sample consisting of alternating pure PTB7 and pure $PC_{71}BM$ layers stacked on a Si substrate was fabricated as a test sample. In the sample fabrication process, approximately 90 nm thick PTB7 or $PC_{71}BM$ planar layers were deposited on a PEDOT:PSS-coated ITO substrate by spin coating. Subsequently, the deposited PTB7 or $PC_{71}BM$ layers were cut into pieces by scalpel. As the PEDOT:PSS is water-soluble, the small pieces were floated off the ITO substrate by dissolving the PEDOT:PSS in a water bath. Picking up the floated layers by a Si substrate leads to a stack of pure PTB7 and $PC_{71}BM$ layers. More information on the sample fabrication can be found in a publication by Li *et al.* [Li2020]. The structure of the fabricated test sample is schematically shown in Figure 4.13a. In the test sample, several few-nm thin layers of the PEDOT:PSS polymer are present (marked by red lines in Figure 4.13a) that are an artefact from the fabrication process when the PEDOT:PSS is not completely dissolved. Next, a Pt-protection layer was deposited and a cross-section specimen of the PTB7/$PC_{71}BM$-multilayer system was prepared by FIB milling. The specimen was trimmed in a wedge shape (wedge angle of 25°) to obtain a sample with an a priori known sample thickness. The final FIB milling was performed with low keV (5 keV) and low current (41 pA) to obtain a smooth sample surface and minimize sample damage (Ga^+ implantation).

Table 4.4 Material parameters of the PTB7/$PC_{71}BM$-multilayer system.

Material	Chemical formula	Average atomic number Z	Density ρ (g/cm^3)	Average atomic mass in atomic mass units
PTB7 [Dyc2015]	$C_{49}H_{57}FO_4S_4$	5.26	1.17	2.73
$PC_{71}BM$ [Mat2015]	$C_{82}H_{14}O_2$	5.62	1.63	3.24
PEDOT:PSS [Len2011, Kar2016]	$(C_6H_4O_2S)$: $(C_8H_8O_3S)$	6.39	1.18	9.82

In Figure 4.13b a cross-section 30 keV HAADF STEM image of the FIB-prepared PTB7/$PC_{71}BM$ wedge is shown. HAADF-STEM imaging was used to verify the order of the PTB7 and $PC_{71}BM$ layers in the sample because the HAADF-STEM contrast of PTB7 and $PC_{71}BM$ is already well understood [Li2020]. In Figure 4.13b, the wedge thickness

increases from left to right. In the thin sample regions, $PC_{71}BM$ shows brighter contrast compared to PTB7. The thin PEDOT:PSS layers (marked by red arrows in Figure 4.13b), retained from sample fabrication, shows the brightest contrast because PEDOT:PSS contains a comparatively large S content. At a thickness $t \approx 475\ \mathrm{nm}$, a contrast inversion (marked by the white dashed line in Figure 4.13b) occurs and above this thickness, $PC_{71}BM$ shows darker contrast compared to PTB7. The HAADF-STEM image in Figure 4.13b confirms the sequence of PTB7 and $PC_{71}BM$ layers shown in Figure 4.13a. The layer thicknesses of PTB7 and $PC_{71}BM$ was measured from the HAADF STEM image and are displayed in Figure 4.13b.

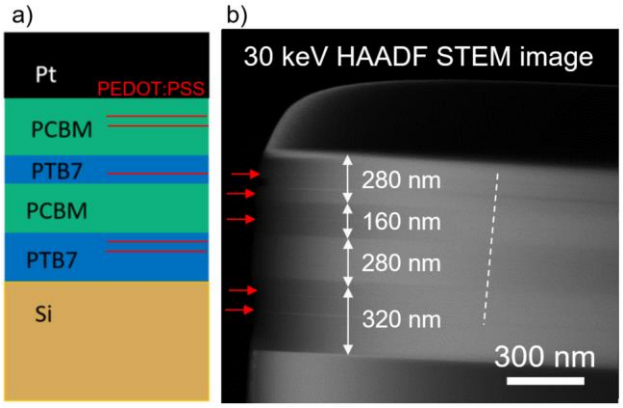

Figure 4.13 Scheme and HAADF-STEM image of the PTB7/$PC_{71}BM$-multilayer system. a) The scheme of the PTB7/$PC_{71}BM$-multilayer system in a cross-section perspective shows the arrangement of the layers. b) 30 keV HAADF-STEM image of the FIB-prepared wedge-shaped specimen with the same layer sequence as in a). The typical contrast inversion between the PTB7 and $PC_{71}BM$ layers with increasing specimen thickness is marked by the white dashed line. Additional thin PEDOT:PSS-polymer layers are present, marked by red arrows in b) and by red lines in a), which were not dissolved during the fabrication process.

4.5.1 Monte-Carlo simulations for BSE-SEM parameter optimization

MC simulations were used to find the best imaging parameters to obtain the highest contrast between PTB7 and $PC_{71}BM$. MC simulations were performed for these materials with the parameters from Table 4.4. Furthermore, the Bishop screening parameter (Eq. 3.2) in the screened Rutherford DSCS (Eq. 3.1) was chosen because it was successfully used for the $Zn(O_xS_{1-x})$-multilayer system (section 4.4). However, the suitability of the screening parameter for the PTB7/$PC_{71}BM$-multilayer system must be verified. Nevertheless, the choice of the screening parameter is not relevant for the determination of the imaging parameters.

The first important imaging parameter that can be adjusted in the BSE measurements is the detection-angle range of the CBS detector. MC simulations yield the angular distribution of the scattered electrons. Such angular distributions for 15 keV electrons interacting with 1000 nm thick $PC_{71}BM$ (red curve) and PTB7 (green curve) are plotted in Figure 4.14a. The *x*-axis describes the scattering angle of the exiting electrons

from the lower specimen surface and the *y*-axis reveals the number of electrons (counts) for each scattering angle. The scattering angles from $0 - \pi/2$ represent the forward scattering (related to the transmission mode), whereas the scattering angle range $\pi/2 - \pi$ is related to BSE imaging. From Figure 4.14a we can conclude that PTB7 will show brighter contrast compared to $PC_{71}BM$ not only in BSE but also in the HAADF STEM because it yields more counts in all scattering angles than $PC_{71}BM$. The plot in Figure 4.14b shows the count difference between PTB7 and $PC_{71}BM$ from Figure 4.14a to reveal that the distinction of the two materials by BSE-SEM is challenging since the count difference is only several electrons (based on 10^5 simulated trajectories). The detection-angle range of the CBS detector corresponding to 8 mm WD is visualised by the light green box. Further simulations showed that changing the detection-angle range will not improve the detected contrast and therefore WD = 8 mm was used in the BSE measurements.

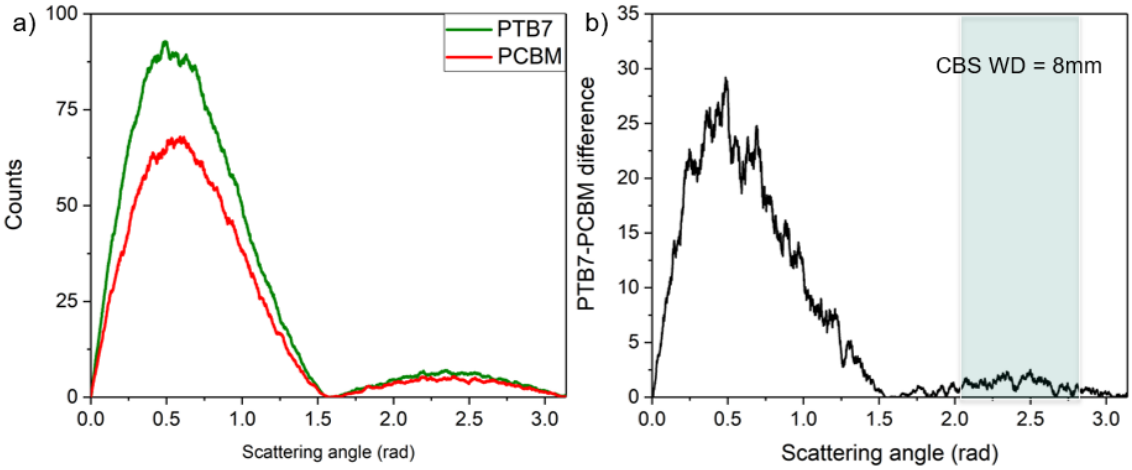

Figure 4.14 MC-simulated angular distribution of scattered electrons for PTB7 and $PC_{71}BM$. a) Angular distribution of scattered electrons for PTB7 (green curve) and $PC_{71}BM$ (red curve) as a function of the scattering angle. b) Count difference between the PTB7 and $PC_{71}BM$ curves from a). The detection-angle range of the CBS detector corresponding to WD = 8 mm is visualised by the light green box.

The second important imaging parameter that can be adjusted in the BSE measurements is primary electron energy. Integrating the simulated scattered intensity for the detection angle range of 2.07-2.79 rad (corresponding to WD = 8 mm) and normalizing it to the Si-bulk BSE intensity yields the simulated intensities shown in Figure 4.15. Figure 4.15 compares the MC-simulated BSE intensities as a function of sample thickness for PTB7 and $PC_{71}BM$ at 2 and 5 keV in Figure 4.15a and 10 and 15 keV in Figure 4.15b. The simulated data for $PC_{71}BM$ is displayed in dashed lines and for PTB7 in full lines. The expected contrast in the BSE image is then obtained by comparing the colour-coded dashed and full lines. The shape of all curves is typical, i.e. with increasing specimen thickness the BSE intensity increases until it reaches the bulk-intensity value. For all studied electron energies, the bulk intensity of PTB7 is higher than the bulk intensity of $PC_{71}BM$, meaning that the PTB7 should appear brighter compared to $PC_{71}BM$ at larger sample thicknesses. MC simulations suggest for each energy a contrast inversion point (similar to HAADF-STEM measurements) at the thickness, where the

colour-coded dashed and full lines intersect. At sample thicknesses below the contrast inversion point, the BSE intensities for PTB7 and $PC_{71}BM$ are similar and therefore hardly any contrast is expected.

Overall, the MC simulations in Figure 4.15 suggest that at higher sample thicknesses PTB7 will appear brighter compared to $PC_{71}BM$ in BSE-SEM images for all studied electron energies. In the case of imaging the wedge-shaped test sample in Figure 4.13, the lower electron energies are preferred because higher contrast is obtained already at smaller thicknesses. Moreover, the signal-to-noise ratio will be better for lower electron energies.

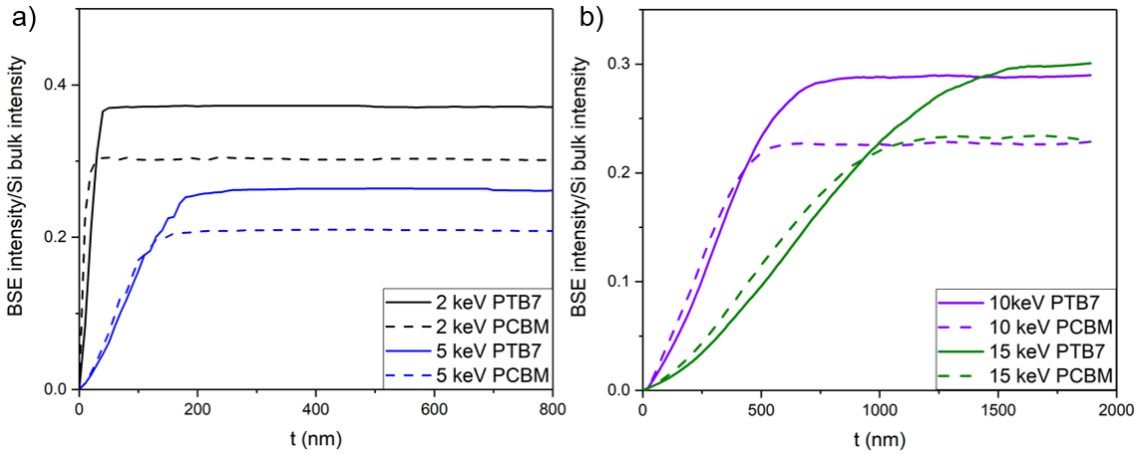

Figure 4.15 MC-simulated BSE intensity for PTB7 and $PC_{71}BM$ as a function of the sample thickness. The BSE intensities normalised to the Si-bulk intensity are plotted as a function of the sample thickness for both $PC_{71}BM$ (dashed curves) and PTB7 (full curves) at a) 2 and 5 keV, b) 10 and 15 keV.

The curves in Figure 4.15 are simulated for isolated PTB7 and $PC_{71}BM$ materials without considering the layer arrangement in the PTB7/$PC_{71}BM$-multilayer system (Figure 4.13). The layer thicknesses of PTB7 and $PC_{71}BM$ in the PTB7/$PC_{71}BM$-multilayer system are between 180 and 320 nm (see Figure 4.13b) and therefore contributions to the measured BSE intensity from the surrounding layers due to beam broadening are expected. It is noted, that the interaction volume and beam broadening are connected. For small electron energies and/or large sample thicknesses (bulk case), the interaction volume will be completely contained in the specimen and the size of the interaction volume needs to be considered. For thin specimens and comparatively large electron energies, the interaction volume is not completely contained in the specimen and beam broadening is relevant.

To understand the effect of the neighbouring layers within the PTB7/$PC_{71}BM$-multilayer system, the PTB7/$PC_{71}BM$-multilayer system as shown in Figure 4.13a was modelled by the MC simulations. MC simulations were performed for two different beam positions (Figure 4.16a), one position in the middle of the PTB7 layer and the other position in the middle of the $PC_{71}BM$ layer. Figure 4.16b shows a trajectory image for the PTB7/$PC_{71}BM$-multilayer system at a sample thickness of 500 nm interacting with 10 keV electrons positioned at position 1. The different colours of the trajectories describe

the electron paths through different materials, i.e. PTB7 – blue, $PC_{71}BM$ – yellow, PEDOT:PSS – turquoise, Pt – grey, Si – purple. The electron trajectories leaving the sample are displayed in red. From the trajectory image is obvious, that the measured PTB7 intensity contains signals from the surrounding layers at 500 nm sample thickness and 10 keV electron energy. According to the trajectory image (Figure 4.16b) electrons are absorbed that reach a heavy-scattering material (Pt and Si). This points out that the escape probability of the scattered electrons is an important parameter to consider, particularly if a heavy-scattering material is in the vicinity of the studied soft material.

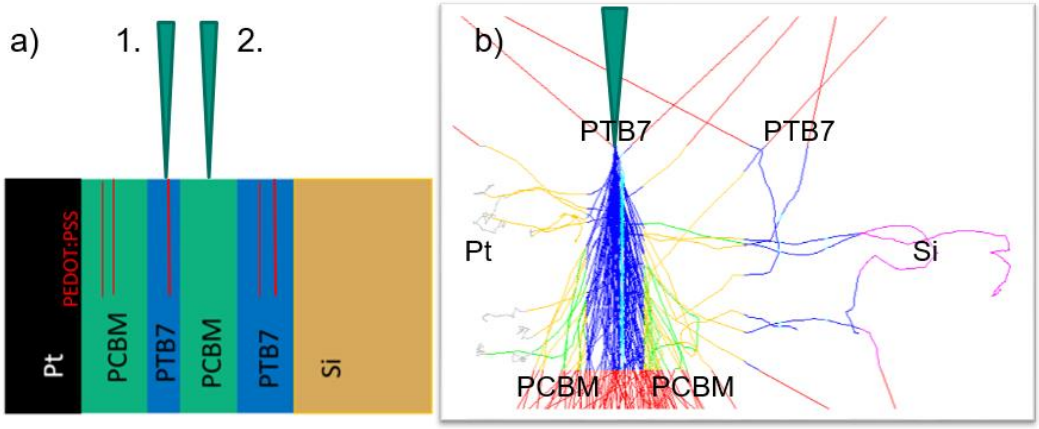

Figure 4.16 MC simulations of the PTB7/$PC_{71}BM$-multilayer system. a) The two beam positions are marked, for which the MC simulations were calculated. b) A trajectory image for the PTB7/$PC_{71}BM$-multilayer system with 500 nm sample thickness interacting with a 10 keV electron beam positioned at position 1.

MC-simulated BSE intensity vs. thickness curves for the PTB7 layer (beam position 1) and $PC_{71}BM$ layer (beam position 2) in the PTB7/$PC_{71}BM$-multilayer system (dashed curves in Figure 4.17) were compared with the simulated BSE intensity vs. thickness curves for the isolated PTB7 and $PC_{71}BM$ materials (full line curves in Figure 4.17). The MC simulations were performed using the NIST screening parameter (Eq. 3.8) to visualize the difference to the plots in Figure 4.15, where the Bishop screening parameter was used. Comparing the full lines in Figure 4.17 with the corresponding curves in Figure 4.15 reveals that the curves calculated using the NIST screening parameter show higher BSE-intensity bulk values as compared to the bulk values obtained from the Bishop screening parameter at all studied electron energies. This is consistent with the results shown in Figure 4.7 for Si. More importantly, by comparison of the full and dashed curves in Figure 4.17 the contribution of the neighbouring layers in the PTB7/$PC_{71}BM$-multilayer system to the calculated PTB7 (Figure 4.17a) and $PC_{71}BM$ (Figure 4.17b) BSE intensity can be studied. At 2 keV electron energy (black curves) the full and dashed curves are identical, indicating that the interaction volume does not exceed the thickness of the PTB7 (or $PC_{71}BM$) layer and that the surrounding layers of the PTB7/$PC_{71}BM$-multilayer system do not contribute to the simulated PTB7 (or $PC_{71}BM$) BSE intensity. At 5, 10 and 15 keV the full and dashed curves in Figure 4.17 disagree under bulk conditions, revealing a contribution of the surrounding layers to the simulated BSE intensity as a consequence of the comparably large interaction volumes at these energies. For thin-specimen regions, the curves for the isolated materials and

for the "layer" case agree even at higher electron energies, because the specimen thickness is smaller than the local beam diameter and the total size of the interaction volume is not relevant. In the case of PTB7 (Figure 4.17a), the bulk intensities of PTB7 in the layer structure (dashed lines) are lower at 5, 10 and 15 keV compared to the bulk intensity of isolated PTB7 (full lines) because the PTB7 layer in the PTB7/$PC_{71}BM$-multilayer system is surrounded by $PC_{71}BM$ layers. Since the interaction volume in the bulk case exceeds the PTB7-layer thickness, the $PC_{71}BM$ layers contribute to the calculated PTB7 intensity and lower the bulk intensity. In analogy, the PTB7 layers next to the $PC_{71}BM$ layer in the PTB7/$PC_{71}BM$-multilayer system increase the calculated $PC_{71}BM$ bulk intensity, which is visible in Figure 4.17b. The simulations suggest that the electron energy of 2 keV is favourable for the bulk case because a good contrast is achieved as suggested by Figure 4.15a and the effect of neighbouring layers can be neglected.

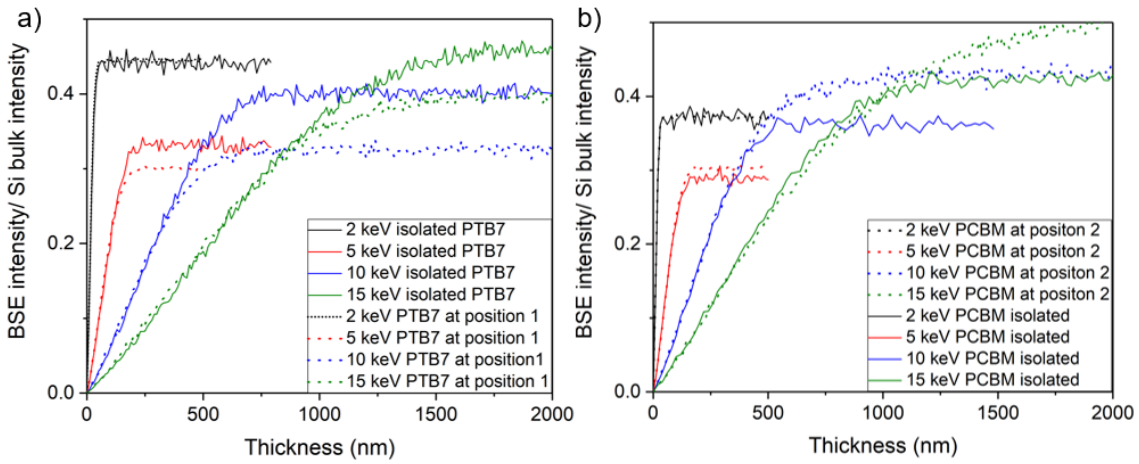

Figure 4.17 MC-simulated BSE intensity for the PTB7/$PC_{71}BM$-multilayer system as a function of the sample thickness. a) MC-simulated BSE intensity vs. thickness curves for an isolated PTB7 (full lines) and a PTB7 layer positioned at position 1 in the PTB7/$PC_{71}BM$-multilayer system (Figure 4.16a) in dashed lines for 2, 5, 10 and 15 keV electron energies. b) Same simulated curves as in a) only for isolated PCBM (full lines) and a PCBM layer in position 2 of the PTB7/$PC_{71}BM$-multilayer system (dashed lines). The MC simulations were calculated using the NIST screening parameter.

To consider the effect of neighbouring layers in more detail for electron energies between 5 keV and 15 keV, Figure 4.18 compares the BSE-SEM intensities of isolated PTB7 and $PC_{71}BM$ (black and red full lines as already plotted in Figure 4.15) and PTB7 and $PC_{71}BM$ layers in the PTB7/$PC_{71}BM$-multilayer system (black and dashed lines as already plotted in Figure 4.17). The considered electron energies are limited to 15 keV because the bulk case is not achieved at a maximum specimen thickness of 2 μm, which is the maximum thickness of the wedge samples. In addition, the behaviour of the simulated curves at small sample thicknesses will not be further considered because the experimental results in section 4.5.3 do not yield a BSE-SEM contrast at small specimen thicknesses for the reasons, which are also discussed below.

For the bulk case, no contrast is predicted at 5 keV (Figure 4.18a), as the dashed curves coincide. For 10 and 15 keV, the $PC_{71}BM$ layer in the PTB7/$PC_{71}BM$-multilayer

system is predicted to appear brighter compared to the PTB7 layer. This is unexpected because the contrast is inverted compared to the isolated materials, i.e. PTB7 is brighter compared to $PC_{71}BM$. The reason for the contrast inversion is the large interaction volume together with the escape probability of the scattered electrons from the individual materials in the PTB7/$PC_{71}BM$-multilayer system. For 15 keV, the interaction volume is so large that all layers within the PTB7/$PC_{71}BM$-multilayer system (together with the Pt protection layer and Si substrate) contribute to the simulated/measured PTB7 (or $PC_{71}BM$) intensity. It is important to note that the contribution to the simulated/measured intensity is limited by the escape probability of the BSEs in the particular material. As a result, the weakly scattering materials (PTB7 and $PC_{71}BM$) contribute more to the simulated/measured BSE intensity compared to Pt, because the escape probability for these materials is higher compared to Pt [Rei1998]. Evidence of this effect can be seen in the simulated trajectory image in Figure 4.16b, where most of the electrons scattered in Pt are absorbed, whereas in the case of PTB7 (or $PC_{71}BM$) a larger fraction of the scattered electrons leave the sample and are backscattered. Considering the escape probability of the scattered electrons enables us to explain why the $PC_{71}BM$ bulk intensity in Figure 4.18b and Figure 4.18c is higher compared to the bulk intensity of PTB7. The simulated BSE intensity for $PC_{71}BM$ (position 2 in Figure 4.16a) contains scattered electrons from the surrounding PTB7 layers, which increase the BSE intensity compared to the bulk case. Moreover, the Si substrate also contributes to the $PC_{71}BM$-bulk intensity. On the other hand, in the case of PTB7 (position 1 in Figure 4.16a), the surrounding $PC_{71}BM$ layers decrease the simulated PTB7-bulk intensity. However, in Figure 4.18b and Figure 4.18c, the simulated PTB7 bulk intensity (black dashed line) is even lower than the isolated $PC_{71}BM$ bulk intensity (full red line). This indicates that a significant number of electrons are scattered into the Pt-protection layer, are absorbed due to the low escape probability and therefore do not contribute to the simulated PTB7 intensity. This effect is particularly pronounced for the PTB7 layer (position 1 in Figure 4.16a) as the Pt-protection layer is in the vicinity.

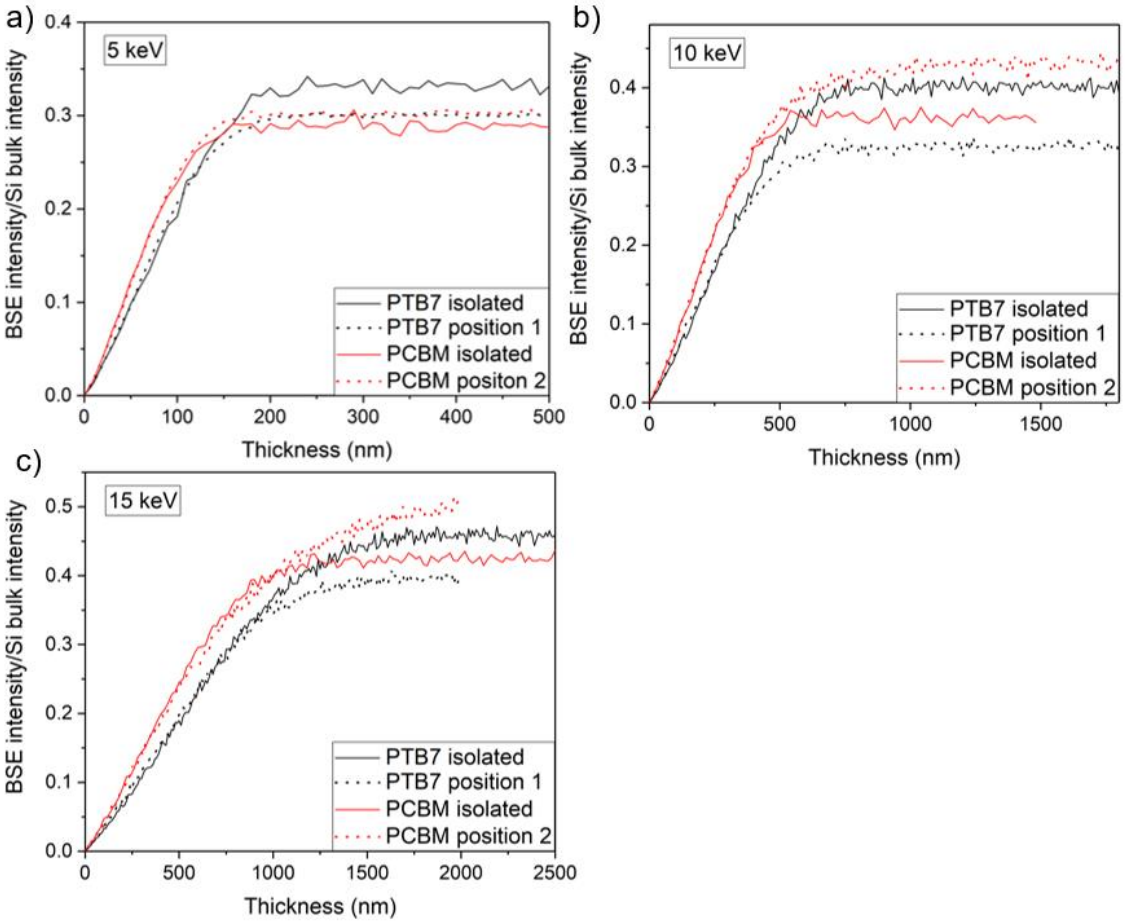

Figure 4.18 Comparison of MC-simulated BSE intensity vs. thickness curves for isolated PTB7 and $PC_{71}BM$ and PTB7 and $PC_{71}BM$ layers in the PTB7/$PC_{71}BM$-multilayer system. The isolated PTB7 and $PC_{71}BM$ curves are displayed in full black and red lines, respectively. The corresponding dashed colour-coded PTB7 and $PC_{71}B$ curves represent the BSE intensities for the incident electron beam positioned on the PTB7 and $PC_{71}B$ layers in the PTB7/$PC_{71}BM$-multilayer system. The curves are compared at a) 5 keV, b) 10 keV and c) 15 keV primary electron energies.

The MC simulations show that the interaction volume and escape probability must be considered when analysing sample systems similar to the PTB7/$PC_{71}BM$-multilayer system. Particularly the presence of a heavy scattering material (Pt) in the vicinity of a weakly scattering material can result in unexpected contrast inversions based on the different electron-escape probabilities. Moreover, the MC simulations reveal that in the bulk case the lateral width of the PTB7 and $PC_{71}BM$ layers in the PTB7/$PC_{71}BM$-multilayer system limits the beam energy that can be used for the analysis. The most suitable electron energies for the analysis of the PTB7/$PC_{71}BM$-multilayer system presented in this work is 2 and 5 keV, where the interaction volume is in a range not exceeding the PTB7 (or $PC_{71}BM$) layer thickness. As revealed by MC simulations, at higher electron energies (10 and 15 keV) the interaction volume exceeds the PTB7 (or $PC_{71}BM$) layer thickness and significantly influences the simulated/measured BSE intensities and the situation is much more complicated.

4.5.2 Experimental procedures and determination of the optimum screening parameter

First, the wedge angle of the FIB-prepared wedge-shaped specimen was measured from a top-view SE-SEM image. Figure 4.19a shows a 30 keV top-view SE-SEM image of the wedge, where the uppermost layer, i.e. the Pt-protection layer, is visible. Measuring the wedge angle yields $\alpha = 25° \pm 0.5°$. The uncertainty was introduced for the same reason as in section 4.4.2, i.e., the actual wedge angle of the PTB7/$PC_{71}BM$ layer system might be slightly different from the determined value for the Pt-protection layer that is visible in the top-view image. Figure 4.19a also reveals that the wedge surfaces are not ideally smooth. We note that milling polymer samples is challenging because the polymer layers slightly bend during FIB milling. However, the HAADF-STEM image in Figure 4.13b shows only minor obvious damage at the wedge edge for the PTB7 and $PC_{71}BM$ layers. At larger sample thicknesses, the specimen seems unharmed considering the contrast in the HAADF-STEM image.

An example of a 5 keV BSE-SEM image of the prepared PTB7/$PC_{71}BM$ wedge is presented in Figure 4.19b. The image was acquired with the typical detection-angle range 2.07 to 2.79 rad, corresponding to all segments of the CBS detector and WD = 8 mm. Figure 4.19b reveals, that the PTB7 layers show brighter contrast as compared to the $PC_{71}BM$, as predicted by the MC simulations for the bulk intensities. The intensity in all layers (including Si substrate and Pt-protection layer) is almost constant with increasing wedge thickness from right to left. The reason for this is that at 5 keV electron energy, the bulk intensity is reached already at 200 nm sample thickness for PTB7 and $PC_{71}BM$. For Si and Pt, this occurs at even lower thicknesses. In the BSE image, the PEDOT:PSS layers are visible (mainly in the $PC_{71}BM$ layers) and show bright contrast. The positions of the thin PEDOT:PSS layers are marked by the red lines in the scheme in Figure 4.19b.

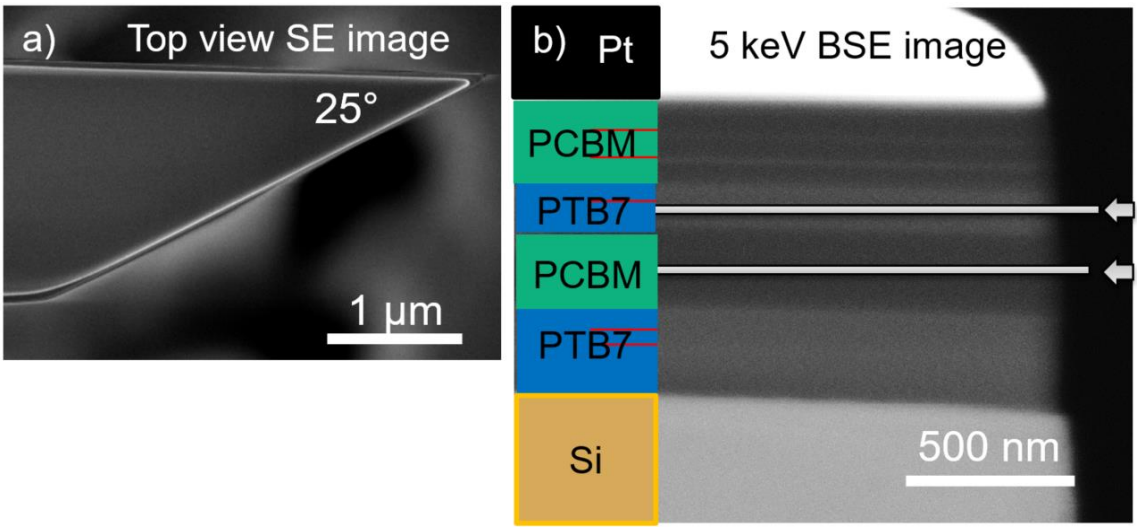

Figure 4.19 Wedge angle and layer sequence of the PTB7/$PC_{71}BM$-multilayer system. a) Top view SE-SEM image of the FIB-prepared PTB7/$PC_{71}BM$ wedge with a wedge angle $\alpha = 25° \pm 0.5°$. b) 5 keV BSE-SEM cross-section image of the PTB7/$PC_{71}BM$ wedge

acquired with the CBS detector at WD = 8 mm. PTB7 shows brighter contrast as compared to $PC_{71}BM$.

Performing 20-pixel-wide intensity-line scans along the white lines in the direction of the arrows in Figure 4.19b in the PTB7 and $PC_{71}BM$ layers yield the BSE intensity as a function of the sample thickness. The intensity-line scans were performed in the middle of the PTB7 (or $PC_{71}BM$) layers to minimize the effect of the neighbouring layers. The distance along the line scan x can be converted into the local sample thickness according to $t = x\tan(25°)$. The measured intensities are normalized with respect to the Si-bulk intensity according to Eq. 4.2. The normalized experimental intensity curves can be directly compared with MC simulations. Each line scan was measured 5 times (at slightly different positions), and the average value together with the uncertainty was calculated. The measured BSE-intensity vs. specimen-thickness curves from Figure 4.19b are plotted in Figure 4.20 in black for PTB7 and in red for $PC_{71}BM$. Additionally, the MC-simulated curves using the Bishop (dashed lines) and NIST (full lines) screening parameters are plotted in green and purple. The MC simulations were performed for the two primary beam positions shown in Figure 4.16a.The MC-simulated data predict no contrast in the bulk region because the bulk intensities are similar for PTB7 and $PC_{71}BM$. Contrary, the measured data show a significant difference in the bulk intensities of the PTB7 and $PC_{71}BM$ layers. For $PC_{71}BM$, the MC simulations using the NIST screening parameter agree well with the measurement. The considerable discrepancies between the experimental and simulated data for PTB7 are discussed in the following section.

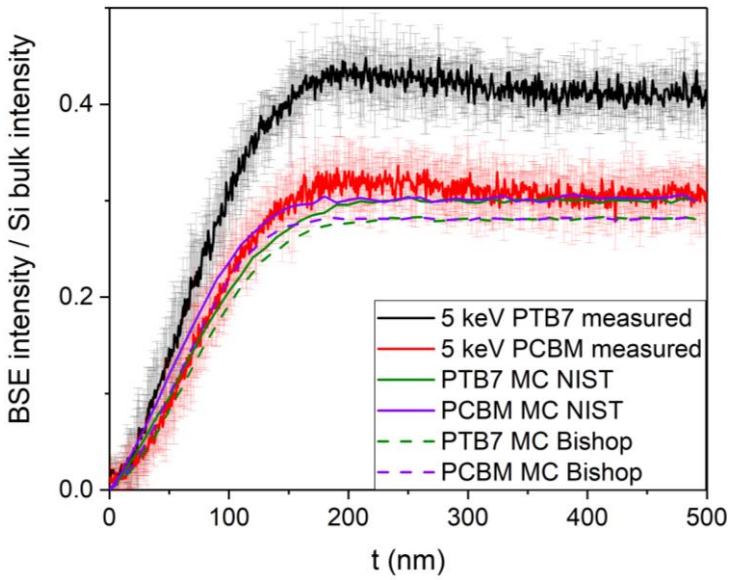

Figure 4.20 Measured BSE intensity for PTB7 and $PC_{71}BM$ as a function of the specimen thickness. The measured BSE intensity normalized to the Si-bulk BSE intensity vs. specimen thickness at 5 keV from Figure 4.19b for PTB7 (black) and $PC_{71}BM$ (red) (WD = 8 mm). MC-simulated curves normalized to the Si-bulk BSE intensity with Bishop (dashed green and purple curves) and NIST (full green and purple curves) screening parameters are plotted for comparison.

4.5.3 Comparison of measured and simulated data

The PTB7/$PC_{71}BM$ wedge was investigated at 2, 3, 5, 10 and 15 keV electron energies and the measured data were normalised in the same manner as discussed above leading to normalised curves as in Figure 4.20. The NIST screening parameter yields higher simulated BSE intensities for the PTB7 and $PC_{71}BM$ compared to the Bishop screening parameter for all studied electron energies and therefore results in a better fit of the measured data. For this reason, only simulated data using the NIST screening parameter are presented in the following.

Figure 4.21 compares the measured and simulated data for a) 15 keV, b) 10 keV, c) 5 keV, d) 3 keV and e) 2 keV electron energies. Focusing first on the thin sample regions, the experimental data (black and red curves) do only show weak or even no contrast. In addition, the bulk case for 2, 3 and 5 keV is reached already at small sample thicknesses. Hence, only the bulk case will be considered in the following. Figure 4.21 reveals that at all electron energies the measured PTB7-bulk intensity (black curve) is higher compared to the measured $PC_{71}BM$-bulk intensity (red curve). Analysing the MC-simulated curves (green for PTB7 and purple for $PC_{71}BM$) is more complex. At 2 and 5 keV, the MC-simulated curves for $PC_{71}BM$ (purple curves) agree reasonably well (within the data uncertainties) with the measured $PC_{71}BM$ curves. It is noted that the interaction volume at these small energies is small enough to avoid significant contributions from the neighbouring layers if the BSE-intensity line profile is acquired in the middle of the layers. However, the MC-simulated PTB7-bulk intensities at these small electron energies are approximately 25 % lower compared to the measurements. The possible origins of this discrepancy will be discussed below. At higher electron energies (Figure 4.21a and b), the situation is different because the interaction volume increases and exceeds the layer thicknesses (cf. section 4.5.1). At 15 keV (Figure 4.21a), the agreement between the measured and simulated BSE intensities is rather good. At 10 keV (Figure 4.21b), the measured and simulated PTB7 curves (black and green curves) agree reasonably well, whereas the discrepancy is large for $PC_{71}BM$ (red and purple curves). Moreover, the bulk intensity for both measured curves is not constant but slightly decreases with increasing sample thickness. For the higher electron energies, the situation is quite complex because the interaction volume entends over the whole layer system and (dis)agreement may depend very much on the specific sample region that is analysed. The largest discrepancies between simulations and experimental data are observed for 3 keV (Figure 4.21d). The MC simulations show a much lower bulk intensity for both materials compared to the measurement. At 3 keV, contributions from the surrounding layers to the measured and simulated PTB7 (or $PC_{71}BM$) are expected to be negligible because the interaction volume is confined within the individual layers and only the PTB7 (or $PC_{71}BM$) layer contributes to the measured and simulated PTB7 (or $PC_{71}BM$) curves. Comparing the plots in Figure 4.21c to e reveal that the MC simulations represent the measured $PC_{71}BM$ curve well at 2 and 5 keV. Only at 3 keV, the MC simulations substantially underestimate the $PC_{71}BM$-bulk intensity. The reason for the discrepancy is not clear, however, a possible explanation could be that the NIST screening parameter is not accurate, particularly at 3 keV electron energy. As discussed in context with Figure 2.4, the behaviour of the backscatter coefficient changes at $E_0 <$

$5\ \mathrm{keV}$ and therefore it is possible that the NIST screening parameter within the screened Rutherford DSCS does not adequately describe the BSE measurements at certain (low) electron energies.

As already discussed in context with Figure 4.17 and Figure 4.18, the quantitative analysis of the presented PTB7/$PC_{71}BM$-multilayer system should be performed at low electron energies, where the contributions of the surrounding layers in the multilayer system are minimized due to the small size of the interaction volume. At higher electron energies, the influence of the large interaction volume and escape probability of the BSEs must be considered and complicate the insight into the measured BSE intensities. Considering the layer thicknesses of the PTB7 and $PC_{71}BM$ layers in the studied PTB7/$PC_{71}BM$-multilayer system, quantitative BSE analysis is feasible at $E_0 \leq 5\ \mathrm{keV}$ (except for 3 keV), where the contribution of the surrounding layers to the measured PTB7 (or $PC_{71}BM$) BSE intensity is minimized if the intensities are measured with sufficient distance to the interfaces. For this reason, the most reliable quantitative analysis of the PTB7/$PC_{71}BM$-multilayer system is possible at 2 keV (Figure 4.21e).

Figure 4.22a shows a 2 keV BSE image of the PTB7/$PC_{71}BM$-multilayer system. Performing a line scan perpendicular to the layer system (white line) in the direction of the arrow and normalizing the BSE intensities according to Eq. 4.2 leads to the BSE-intensity profile shown in Figure 4.22b (black line). The line scan was performed in a sample region with sufficiently large thickness where the measured BSE intensity corresponds to the bulk intensity value. Figure 4.22b demonstrates that PTB7 and $PC_{71}BM$ can be clearly distinguished by BSE imaging. The MC-simulated BSE-bulk intensities at 2 keV for PTB7 and $PC_{71}BM$ are also included in Figure 4.22b (red-dashed line). The bright PTB7 and dark $PC_{71}BM$ layers are in qualitative agreement with the simulations. However, the simulated intensities are lower than the experimental data, which is particularly obvious for PTB7. A gradual intensity transition is observed between the layers, which is due to the finite size of the interaction volume that leads to BSEs from neighbouring layers if the interfaces are approached.

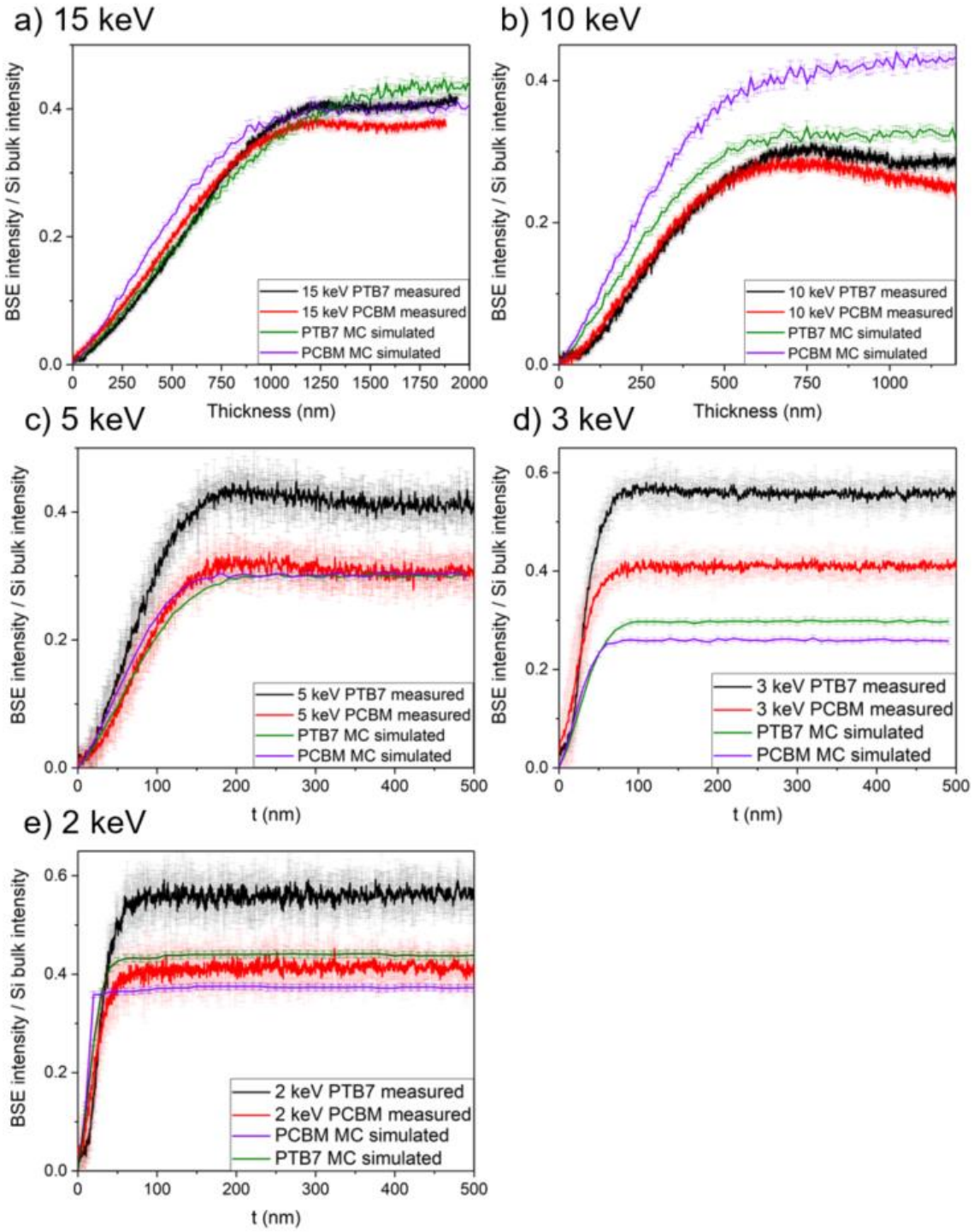

Figure 4.21 Comparison of measured and MC-simulated BSE intensities as a function of the specimen thickness. Comparison of measured and MC-simulated BSE intensities normalized to the Si-bulk intensity as a function of the specimen thickness (WD = 8 mm) for a) 15 keV, b) 10 keV, c) 5 keV, d) 3 keV, and e) 2 keV. The black and red curves represent the measured data for PTB7 and $PC_{71}BM$, whereas the green and purple curves represent the MC simulations for PTB7 and $PC_{71}BM$ using the NIST screening parameter.

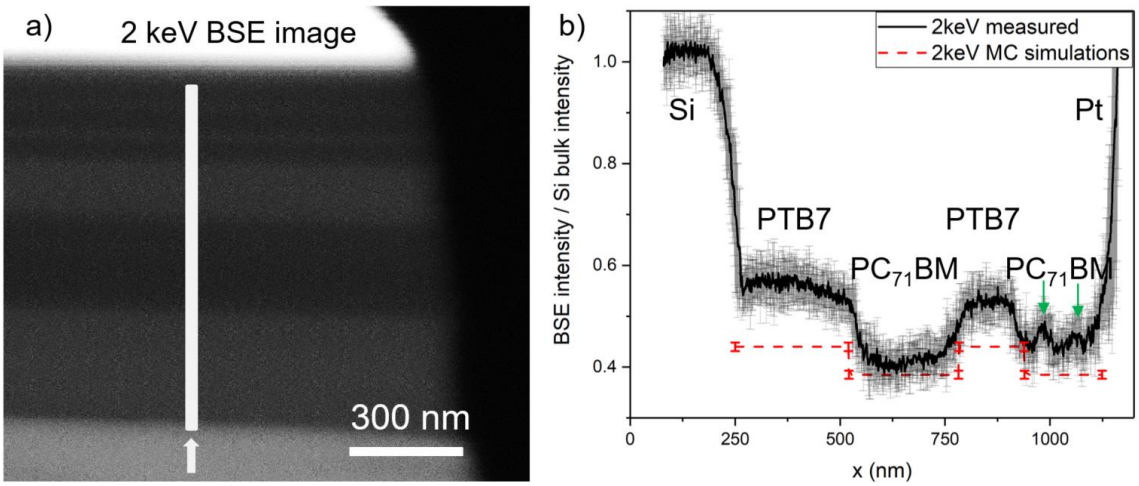

Figure 4.22 BSE-SEM intensity line scans perpendicular to the PTB7/$PC_{71}BM$-multilayer system. a) 2 keV BSE image showing the position of the BSE-intensity line scan across the PTB7/$PC_{71}BM$-multilayer system. The line scan is placed in the sample-thickness region where the bulk-BSE intensity is already reached. b) Normalised BSE-intensity line scan from a) (black curve) and corresponding MC simulated bulk intensities (dashed red line) for primary electron energy of 2 keV. The green arrows indicate the PEDOT:PSS layers visible in the measured BSE-intensity line scan.

One possible source for the discrepancies could be Ga^+ implantation as a wedge preparation artefact during FIB milling. Even though measures to reduce the Ga^+ implantation were considered (5 keV final polishing and grazing angles) during the wedge milling, Ga^+ could be present in the sample and thus increase the measured BSE intensities. However, this effect should be also present at the $PC_{71}BM$ layers causing a similar discrepancy. However, the discrepancy between the measurement and simulations is smaller for $PC_{71}BM$ compared to PTB7 layers (although the measured intensity is still higher than the simulated bulk intensity). The Ga^+ implantation was already discussed in section 3.3.2, where simulations were performed leading to the result that Ga^+ implantation occurs only in the upper few nm of the sample.

To examine the influence of the Ga^+ implantation on the BSE intensity the measured and simulated curves for Si were compared. The Ga^+ implantation should increase the slope of the measured curve compared to the simulations at small sample thicknesses. Figure 4.23 compares the measured (black) and MC-simulated (red) BSE intensities normalized to the Si-bulk intensity as a function of the specimen thickness (WD = 8 mm) for Si at 15 keV electron energy. The slope of the measured curve at the small sample thicknesses (encircled in blue) is only slightly higher compared to the slope of the simulated curve. This indicates that some Ga^+ might be present in the FIB-milled wedge specimen, however, the influence on the measured Si BSE intensity is not significant at higher sample thicknesses. For the PTB7 and $PC_{71}BM$ BSE intensities, the influence of the Ga^+ implantation is more pronounced (as PTB7 and $PC_{71}BM$ weakly scattering materials) and could explain the discrepancy between the measured and MC-simulated data for $PC_{71}BM$ (Figure 4.22). However, the discrepancy for PTB7 is too large to be assigned only to Ga^+ implantation.

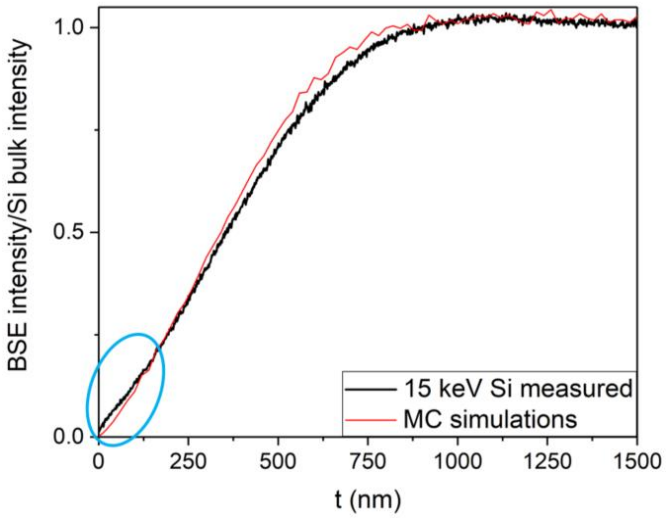

Figure 4.23 Check for Ga^+ implantation. Comparison of measured (black) and MC-simulated (red) BSE intensities normalized to the Si-bulk intensity as a function of the specimen thickness (WD = 8 mm) for Si at 15 keV electron energy. The circled thickness region indicates an influence of Ga+ implantation on the measured BSE intensity, as the slope of the measured curve is higher compared to the slope of the MC simulations.

Additionally, the measured BSE intensity could be influenced by the presence of surface contamination. This is not probable because the wedge was FIB milled and the BSE images were acquired directly afterwards without exposing the sample to ambient conditions. The surface contamination induced by the electron beam was examined by comparing the measured BSE intensities of the first and last BSE image within the measurement session. The dependence of the contamination on the measured BSE intensities was found to be insignificant.

Another possible source for the discrepancy between the measured and simulated BSE intensities could be the presence of additional PEDOT:PSS layers, which are not indicated in Figure 4.16a (PEDOT:PSS layers are marked by red lines). As already mentioned, the PEDOT:PSS in the PTB7/PC_{71}BM-multilayer system is an artefact of the preparation procedure. The PEDOT:PSS layers indicated in Figure 4.16a were recognized in the HAADF STEM image in Figure 4.13b. However, the real PTB7/PC_{71}BM-multilayer system can contain additional PEDOT:PSS layers (more than indicated in Figure 4.16a) or remaining parts of the PEDOT:PSS layers that are not visible in the HAADF STEM image nor in the BSE images. The presence of the PEDOT:PSS in the vicinity of the performed line scan in the BSE images increases the BSE intensity, as the average atomic number of the PEDOT:PSS is higher compared to PTB7 and PC_{71}BM (see Table 4.4). The increase of the measured intensity is visible in Figure 4.22b, where two PEDOT:PSS layers are present in the PC_{71}BM layer. As a result, two peaks (indicated by green arrows in Figure 4.22b) are visible in the measured BSE intensity. Unfortunately, mapping and localizing the presence of the PEDOT:PSS in the PTB7/PC_{71}BM multilayer system is not trivial.

Another possible source for the discrepancy could be incorrect material parameters assumed in the MC simulations for PTB7. To understand the influence of the material parameters on the measured BSE intensity, the material density of the PTB7

was changed in the MC simulations from $\rho = 1.12$ g/cm^3 to ρ_1 = 1.4 g/cm^3 and subsequently to ρ_2 = 1.8 g/cm^3. Interestingly, the calculated bulk BSE intensity for PTB7 at 2 keV for the three different material densities is the same and is 0.44% of the Si-bulk intensity. This result is surprising at the first glance, however, this phenomenon can be understood in analogy to BSE-intensity dependence on the sample thickness. The BSE intensity increases with increasing sample thickness because the interaction volume increases and more electrons are backscattered. With further increasing the sample thickness, the BSE intensity saturates because the penetration depth does not further increase and reaches its maximum value. By increasing the material density, the mean penetration depth is smaller and tends to saturation that is reached faster at smaller sample thicknesses while the bulk intensity remains the same for a particular electron energy.

As an alternative, the dependence of the simulated bulk-PTB7 intensity on the chemical composition can be studied. MC simulations at 2 keV were performed with 2 additional sulphur atoms ($C_{49}H_{57}FO_4S_6$) in the PTB7 molecule ($C_{49}H_{57}FO_4S_4$). The calculated bulk intensities normalized to the Si-bulk intensity yield 0.50 for $C_{49}H_{57}FO_4S_6$. The measured value is 0.55 and the MC-simulated intensity for the nominal chemical composition is 0.44, as shown in Figure 4.22b. This shows that adding 2 additional sulphur molecules to the nominal PTB7 composition leads to a simulated bulk intensity that improves the agreement with the measured bulk intensities at 2 keV. For 5 keV electron energy, the measured bulk intensity has a value of 0.4 and the MC-simulated BSE intensity based on the nominal chemical composition of PTB7 yields a value of 0.3. Adding 2 additional sulphur atoms to the nominal chemical composition of the PTB7 yields a bulk intensity value of 0.33 and thus improves the agreement to the measurement. It is likely that differences between the nominal and real chemical composition of PTB7 contribute to the discrepancy between the measured and MC-simulated BSE intensities (Figure 4.21 and Figure 4.22). This applies at least within the sample region that we have analysed. Another supporting argument to this statement is Figures 3.9 and 3.23, where the measured and MC-simulated HAADF-STEM intensities are compared. The MC simulations were performed using the nominal PTB7 chemical formula and show a similar discrepancy. The measured HAADF-STEM intensities at small sample thicknesses are higher compared to the MC simulations, which also indicates that the nominal chemical formula of PTB7 does not agree with the composition of the analyzed material. We note that the difference between the nominal and real chemical composition of PTB7 might be caused by electron/ion-beam-induced damage. Shrinkage and mass loss caused by electron beam irradiation has been reported for PTB7 [Roe2016, Lei2017]. $PC_{71}BM$ was found to be more stable under electron-beam irradiation [Lei2017], which agrees with our findings, as measured and MC-simulated data agree.

4.6 Summary

In this chapter, we describe a new procedure for quantitative analysis of BSE contrast in SEM. This method is based on relating the measured grey-values to the properties of the analysed materials (mean atomic number, mean atomic weight and

material density) based on the comparison of normalized measured BSE intensities with MC simulations. For realistic MC simulations, the selection of the differential scattering cross-section is essential together with consideration of the BSE-detector properties. Therefore, the threshold energy of the CBS detector was measured to be $E_{th} = 500\ \mathrm{V}$ and the detector collection angles were determined, which depend on the sample working distance. Furthermore, the influence of the different screening parameters on the BSE intensity was examined. For comparison of measured and simulated BSE intensities, the normalization of the data is necessary. We propose to normalize BSE intensities to the Si-bulk BSE intensity. Si is convenient to choose because it serves as a substrate for many sample systems. If Si is not present in the sample, we have shown that a Si wafer could be utilized for data normalization.

The proposed method was tested on two different challenging material systems. The first sample was a Si/ZnO/Zn(O_xS_{1-x})/ZnS-multilayer system, where the material parameters between sample layers vary only slightly and thus probe the sensitivity limits of the BSE analysis. The sample thickness was considered as an additional parameter and MC simulations before the BSE measurements suggest analyzing the sample at 15 keV electron energy in the 150 – 300 nm sample-thickness range because the contrast between the different layers is most pronounced. A FIB-milled wedge specimen of the Si/ZnO/Zn(O_xS_{1-x})/ZnS sample in cross-section geometry was analyzed by BSE SEM at 15 keV electron energy. The measured intensity line profile perpendicular to the Si/ZnO/Zn(O_xS_{1-x})/ZnS layers was normalized to the Si-bulk BSE intensity and compared with MC simulations. The results show that MC simulations with the Bishop screening parameter agree well with the measured data. A significant discrepancy was observed only for the ZnS layer where the measured intensities were influenced by the neighbouring Pt layer due to electron-beam broadening. The analysis of the Si/ZnO/Zn(O_xS_{1-x})/ZnS sample reveals that BSE imaging is capable of distinguishing materials as similar as Zn($O_{0.5}S_{0.5}$) and Zn($O_{0.7}S_{0.3}$), but smaller composition differences between Zn($O_{0.5}S_{0.5}$) and Zn($O_{0.4}S_{0.6}$) could not be distinguished.

The second test sample was a PTB7/$PC_{71}BM$-multilayer system as a representative of weakly scattering materials. A cross-section wedge-shaped specimen was prepared to study the sample-thickness dependence of the BSE contrast between these materials. MC simulations were used to predict the material contrast and optimize the imaging parameters. Based on the MC simulations, quantitative BSE analyses of the PTB7/$PC_{71}BM$-multilayer system are most promising in the bulk region at low electron energies $E_0 < 5\ \mathrm{keV}$, where the interaction volume is smaller than layer thicknesses. At higher electron energies, the interaction volume increases and information from the neighbouring layers in the multilayer system significantly contribute to the measured PTB7 (or $PC_{71}BM$) BSE intensity and complicates quantification. Moreover, MC simulations reveal that the escape probability of the BSEs plays an important role, particularly when a heavy scattering material (the Pt-protection layer of the FIB-milled specimen) is in the vicinity of the studied weakly scattering material. The measured BSE intensity vs. thickness curves at 2, 3, 5, 10 and 15 keV were normalized to Si-bulk BSE intensity and compared with MC simulations. It was found that the NIST screening

parameter in the screened Rutherford DSCS represents the measured data better compared to the Bishop screening parameter (Figure 4.20). However, the improvement was observed only for $PC_{71}BM$. Even at low electron energies (where the contribution of the surrounding layers to the measured intensity is minimized), significant discrepancies between the measured and MC-simulated data was observed for the PTB7 layers. The most probable origin of the discrepancy is the deviation of the nominal and real chemical composition of PTB7, possibly due to electron-beam damage.

This chapter demonstrates that quantification of BSE intensities using the proposed method is feasible. Materials with similar chemical composition can be distinguished with high sensitivity and the material composition can be quantified if pre-knowledge is available. For the analysis of multilayer samples, the layer thickness limits the applicable electron energy. For the bulk case, the BSE interaction volume increases with electron energy and leads to contributions of the neighbouring layers to the measured BSE intensity. Moreover, the escape probability of electrons influences the measured BSE intensity, particularly when a weakly scattering material is present in the vicinity of a strongly scattering material. Small electron energies are therefore preferable. For the case of electron-transparent specimens (which is not the standard situation for BSE-SEM), larger electron energies are favourable, because beam broadening is less pronounced and the beam diameter can be smaller than the layer thicknesses.

5. FIB-SEM tomography of porous polymers

This chapter deals with 3D imaging and the characterisation of porous polymer structures. The challenge in this work is the analysis of large sample volumes (10 x 10 x 10 μm^3) with the capability of resolving pores as small as 5 nm. A suitable technique for such investigations is focused-ion-beam-milling/scanning-electron-microscopy (FIB-SEM) tomography. The quantitative analysis of 3D structures by FIB-SEM tomography requires adequate image segmentation that is typically based on thresholding in the intensity histogram of SEM images. Recently machine learning (ML) segmentation algorithms have emerged with the opportunity to tune the segmentation algorithm based on prior knowledge of the SEM image contrast. This chapter discusses the FIB-SEM tomography of 3D-printed nanoporous polymer structures with a special focus on SEM image segmentation and pore-size determination.

Section 5.1 introduces the 3D quantitative analysis of porous polymers problematic. Prior FIB-SEM measurement the porous polymer sample preparation is presented. Next, the FIB-SEM process together with the most common issues originating from FIB-SEM is discussed. Section 5.1 closes with an introduction to SEM image segmentation algorithms. The experimental procedure of porous PETA structures fabrication, sample preparation and FIB-SEM data acquisition is presented in section 5.2. In section 5.3 Monte Carlo (MC) simulations were used to study the contrast of the pore/polymer interface and segmentation criteria for precise SEM image segmentation were derived. Moreover, section 5.4 evaluates the performance of several traditional segmentation algorithms on simulated SEM images and found erroneous results on pore sizes. It is shown that training the ML segmentation algorithm by the knowledge obtained from MC simulations yields more reliable segmentation results. Section 5.5 calculates 3D material properties of the porous PETA structures for different segmentation methods used. A strong dependence on the segmentation method is observed, which emphasizes the importance of the segmentation process in the 3D reconstruction of FIB-SEM data.

5.1 Introduction

Porous materials play an important role in many fields of modern material sciences, ranging from renewable energy storage (batteries [Bal2016], supercapacitors [Bor2017]) to water purification [Won2018] or gas separation [Ism2001]. Generally, the porous microstructure is strongly related to device performance and thus analysis and quantification of material properties (porosity, tortuosity, percolation, pore-size distribution, etc.) are essential for further development in many research fields. Three tomography methods are commonly used to reveal 3D material properties: 1. X-ray tomography [She2010], 2. Electron tomography [Küb2005], and 3. FIB-SEM tomography [Hol2004]. X-ray tomography is a non-destructive method capable to investigate large sample volumes. The drawback is its relatively low spatial resolution in the 0.1 µm range. The opposite situation prevails in electron tomography, where only small sample volumes can be analysed with sub-nm resolution. In FIB-SEM tomography, FIB milling and SEM imaging are alternately performed to obtain a stack of images that can be used

to reconstruct the 3D structure. The biggest advantage is the ability to investigate rather large sample volumes up to several 100 μm^3 at high (SEM) resolution in the 1 nm range. FIB-SEM tomography is an established technique, which has been recently used to investigate nanopores in coal [Fan2019], colloidal assemblies [Hoe2019], or a large number of carbon-based materials [Nan2019].

5.1.1 Sample preparation

Applying FIB-SEM tomography to porous materials usually requires gentle pore infiltration to stabilize the inner sample structure and to avoid shine-through artefacts (i.e. unwanted signal from the backside of the pore). The three most common ways to infiltrate the pores include: 1) Resin impregnation, 2) using the electron beam induced deposition, and 3) pore infiltration via atomic layer deposition (ALD). In the first case the sample is dipped into a resin and, depending on the resin viscosity and pore size, the pores are filled. In most FIB-SEM tomography investigations, Epon/Epoxy resin is preferred in vacuum impregnation due to its low viscosity [Hei2018, Wan2017]. For FIB-SEM tomography of carbon-based samples, Si-based resin [End2011] has to be used to distinguish the impregnated epoxy from the carbon structures present in the studied sample. However, the relatively high viscosity of the Si-based resin prevents satisfactory pore impregnation of structures with small pore sizes.

With respect to porous carbon-based materials, Eswara-Moorthy *et al.* [Esw2014] developed a pore infiltration approach that can be performed in-situ in a dual-beam FIB/SEM system based on Pt filling of pores from gaseous precursors. In this method, standard organometallic gaseous precursors were injected in the vicinity of the sample and by subsequent electron beam-induced dissociation pores were filled with Pt. Since the deposition depth is directly proportional to the primary electron energy, at 30 keV electron energy Pt deposition in the range of 10 µm is possible. The resulting contrast between the carbon structure and the Pt-filled pores is sufficient for trustworthy SEM image segmentation.

Another possibility to infiltrate pores and enhance the contrast between the infiltrated pores and sample material is atomic layer deposition (ALD). This technique allows to select a filling material to maximize the contrast with respect to the elements of the studied porous material. Vierrath *et al.* [Vie2015] demonstrated the use of ALD while filling the pores of a polymer catalyst layer with ZnO to enhance the contrast for more reliable FIB/SEM tomography analysis. The drawback of this approach is a low depth of infiltration (1.5 µm) requiring FIB-milling preparation before the ALD infiltration to enable access to the inner sections from at least four sides.

5.1.2 Issues originating from the FIB-SEM process

FIB-SEM tomography is a complex process where much care has to be taken during the data acquisition and data analysis to assure integrity and quality of the reconstructed 3D structure. In this section, we want to introduce all potential issues causing image artefacts and degrading the raw SEM images when they are directly obtained from FIB-SEM. The origin of these artefacts can be divided into two sources: 1) Geometrical distortions and 2) signal fidelity artefacts.

The dual-beam arrangement of the Helios G4 FX with an angle of 52° between the FIB and the electron beam (cf. Figure 5.1a) is convenient for its possibility to obtain serial images from any part of the sample surface. However, due to non-orthogonal SEM imaging of the milled surface, the SEM image is foreshortened resulting in a size reduction of 80 % in one direction [Kub2015]. In the User Interface (UI) it is usually possible to directly compensate for this foreshortening by applying a built-in geometrical transform, where the SEM image is rescaled by calculation using trigonometric functions to the original image size. The second issue is related to non-orthogonal SEM imaging, which will manifest itself after a few slices in the FIB-SEM measurement. To decrease the SEM imaging time, only a region of interest (ROI), the blue rectangle in Figure 5.1a, is defined in the FIB-SEM setup process. Due to the non-orthogonal SEM imaging, the so-called "Y-shift" correction has to be applied to the ROI to keep the ROI in the defined position while proceeding from section to section. The Y-shift correction can be carried out using beam shift (having only a limited range defined by the beam-shift range) or digitally by imaging a larger region than the defined ROI and subsequently "moving" the ROI accordingly to the calculated digital shift. A special geometrical solution of the FIB-SEM geometry with respect to both issues addressed above was established by Hitachi (MI-4000L; Hitachi, Japan) [Har2013], where the SEM is orthogonally arranged to the FIB. This solution allows to capture SEM images without any tilt, however, it allows to perform FIB-SEM measurements only at the margin of the block surface. Regardless of the FIB-SEM geometry, with proceeding from section to section, the imaged surface of the sample recedes from the focal point of the electron beam. For this reason, the electron beam has to be refocused after several FIB sections.

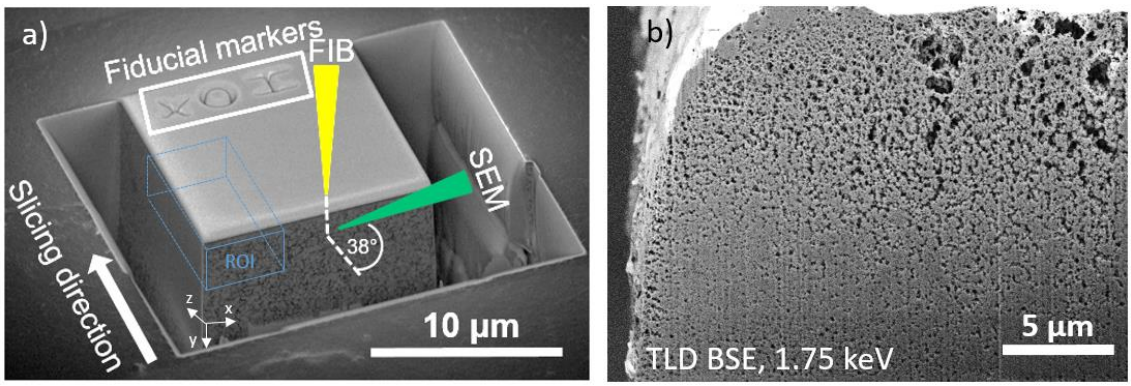

Figure 5.1 FIB-SEM tomography arrangement and related issues. a) FIB-SEM tomography arrangement, where the angle between the FIB and the electron beam is 52°. Adapted from a publication [Čal2021]. b) 1.75 keV BSE cross-section image of the porous polymer structure before infiltration showing curtaining and a non-uniform illumination image artefact.

Another issue that cannot be avoided during FIB-SEM measurement is sample drift. Thermal drift can be minimized by inserting the sample into the microscope chamber several hours before launching the FIB-SEM measurement. Even more severe drift is caused by charging. Sample charging can be efficiently reduced by coating the sample surface with Pt and amorphous C. Even though measures against sample drift are applied, the sample drift is only minimized and further compensation procedures have

to be applied. The FIB-SEM software usually comprises a possibility for sample drift compensation. Prior FIB-SEM measurement a fiducial marker is milled into the Pt-protection layer that serves as a reference point. Before every FIB milling, the drift compensation function scans the milled region, searches for the fiducial marker and calculates the actual position difference with respect to the reference. The stage is then moved accordingly to ensure that the FIB milling occurs at the correct position and keeps thus the slice thickness constant throughout the whole FIB-SEM measurement. For very thin thicknesses, keeping constant slice thickness is challenging. According to Jones *et al.* [Jon2014], the individual slice thickness can vary from the target value up to 20 %.

The second group of artefacts is related to signal fidelity and image quality corruption. A typical artefact of FIB milling is the curtaining effect (or streaking) [Mun2009] that is caused by the spreading of the ion beam. It results in inhomogeneous removal of material and leads to vertical streaking on the SEM images (Figure 5.1b). Several approaches exist to reduce this artefact, both hardware and software-based. Among the hardware-based approaches, the curtaining effect can be reduced by applying a thick and uniform protection layer [Gia2004] or using a rocking stage that adds a few degrees tilting in the plane of the cross-section [Loe2017]. Most of the software-based approaches are based on Fourier transforming the images [Kim2019]. Since the curtain artefacts are aligned in the vertical direction, displaying the given image in a frequency domain via Fourier transform the curtain verticals can be merged into a single bright horizontal band that is perpendicular to the direction of the patterns in the original image. Assuming that the original image does not contain any other distinct vertical features related to the material structure, the removal of the horizontal band will remove the curtain artefact from the image.

Another common artefact in SEM images acquired in the FIB-SEM configuration is nonuniform illumination (Figure 5.1b). This results due to the non-uniform distance between the detector and the sample, i.e., sample regions closer to the detector appear brighter (top of the SEM image) than those far from the detector because of the different number of collected electrons. This undesirable artefact must be compensated because most of the segmentation algorithms are based on global thresholding algorithms and thus require uniform illumination. Several methods for illumination correction have been developed [Kim2019, Tas2008] based on a least-squares method that neutralizes the illumination effect and restores the optimized signal. The non-uniform illumination artefact can be suppressed by sufficiently large pre-milled trenches along the ROI (Figure 5.1a) that enable the detection of electrons emitted from the bottom parts of the scanned region. Moreover, the large pre-milled trenches are beneficial not only with respect to the illumination artefact but prevent also redeposition (material that is deposited back onto the cross-section surface) during the FIB-milling process.

The quality of the SEM image is also limited by the ratio of the signal produced by the electron beam to the noise imparted by the electronics of the instrument. By increasing the number of electrons recorded per picture point, either by increasing the beam current or by increasing the dwell time, the signal-to-noise ratio and hence the

image quality is increased. However, a large beam current lowers the spatial resolution and an increased dwell time extends the image acquisition time, leading to image distortions caused by drift. Usually, a compromise is established and filtering of the SEM image after acquisition further reduces the noise and increases the SEM image quality. The main challenge of the noise reduction filters is preserving edges and structural details of the image. Facing these challenges, the Weighted local hysteresis smoothing filter [Maz2016], Adaptive Wien filter [Ara2017], or Anisotropic diffusion filter [Tsc2005] have been developed and are largely used.

5.1.3 Image segmentation algorithms for SEM images

Segmentation is the most crucial step in obtaining trustworthy quantitative information from FIB-SEM data of different phases in the SEM images. Image segmentation is a technique of dividing or partitioning an image into parts, called classes (e.g. pores and material or different material phases). The simplest and common way for assigning pixels to classes is based on global [Kim2019] and local [Sal2014] thresholding, taking into account only the intensity and spatial relationship of pixels in the SEM image. Reliable performance of thresholding algorithms can be expected for images having clearly separated peaks with different image intensities (corresponding to respective classes) in the image histogram. For such a case, the global thresholding method [Ots1978, Bez1981] iterate through all possible threshold values while calculating a measure of spread for all pixel levels on each side of the threshold, i.e. the pixels that either fall in foreground or background. The threshold value for which the sum of foreground and background spreads is at its minimum defines the global threshold.

Global thresholding segmentation algorithms are frequently used for their simplicity and reliable performance. However, segmentation of FIB-SEM images of highly porous materials is a challenging problem because the SEM images suffer from a shine-through artefact. In SEM images the hollow pore does not appear black as desired, but there is some signal coming from the backside of the pore that contributes to the pore intensity [Bal2013]. Filling the pores with a resin helps to reduce the shine-through artefact. However, a similar effect appears for filled pores that have similar or smaller dimensions as the interaction volume of the primary electrons. The interaction volume may considerably extend into the bulk of the sample depending on the primary electron energy and the sample properties. When the interaction volume exceeds the pore volume, the emitted BSEs will carry information from the pore and other phases that are present in the vicinity. As a result, a single pixel in the SEM image will contain an intermediate intensity that cannot be assigned to the pure pore (or material) phase. Therefore the grey-value itself is not sufficient as a segmentation criteria leading to a large number of incorrectly classified pixels by the global thresholding algorithms. In such a case, visual segmentation of complex SEM images by a human operator is often more reliable albeit much more time consuming because more information is inherently used for image segmentation.

In recent years, new segmentation methods have emerged based on machine learning (ML) algorithms, which have the potential to include more knowledge into the

segmentation procedure and reach visual segmentation performance [Aga2020, Ver2020]. As the name indicates, ML segmentation can be tuned according to the user knowledge and thus serves as automated human-operator segmentation. The ML algorithm working procedure can be divided into two steps. The first step comprises the ML software training procedure. The workflow in the training process is schematically shown in Figure 5.2. In the beginning, several regions in the training data (typically the first few images of the FIB-SEM image stack) are manually assigned to particular classes (phases) and the user selects several training features (i.e., functions that the software uses to extract features from the images and thus characterize the segmented data). In the ML training process, the training features are applied to the manually segmented regions, resulting in a vector for each manually segmented pixel containing information about the applied training features on this particular pixel. Based on this training vector set the ML software trains itself in assigning pixels to particular classes. The result of a training procedure is a file called "classifier" that contains all the gained knowledge in the training procedure. The training procedure can be performed iteratively (the user manually segments more regions in the training data or changes parameters in the training features) until satisfactory results of the classifier are obtained. In the second step, the obtained classifier is applied to unknown data (to the rest of the FIB-SEM data stack) [Arg2017].

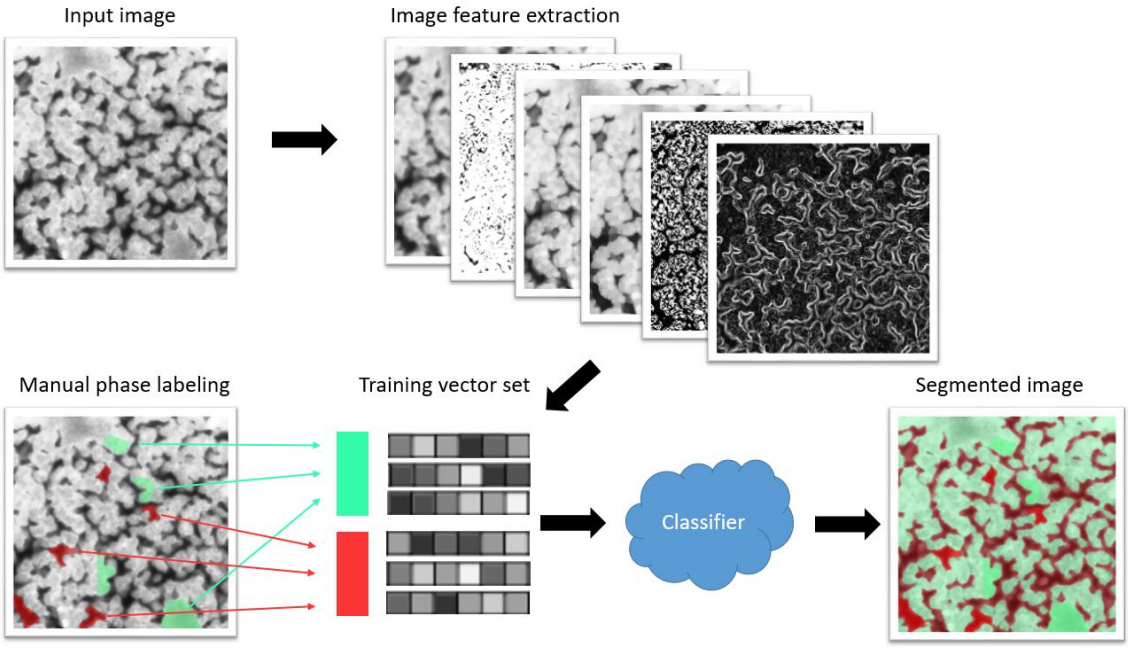

Figure 5.2 Schematic pathway of machine learning segmentation procedure. Parts of the input image are manually segmented. The training vector set is then obtained by extracting image features from the manually segmented image parts. Based on the training vector set the machine learning software creates a classifier, which contains all the knowledge of the pixel segmentation, and segments the rest of the input image.

In recent years the use of ML in the segmentation process has become increasingly popular and was successfully applied for microscopy image segmentation of rocks [Chu2016, Fan2019] and soil samples [Sch2018] or for ultrasound image segmentation in breast cancer research [Xu2019]. For the analysis of FIB-SEM

tomography data, ML has been used for the segmentation of high porosity membranes with shine-through artefacts [Tra2019] or ultrastructural changes of mitochondria upon disease onset [Ozt2017], enabling reliable and efficient data quantification. In the work of Andrew [And2018], the performance of three image segmentation algorithms was compared on a synthetic FIB-SEM dataset, which was created from measured data. ML segmentation algorithms result in a more accurate representation of the 3D structure in comparison with segmentation algorithms using global thresholding. ML segmentation also proved to be very noise tolerant and capable of correctly segmenting non-greyscale (textural based) contrast, where global thresholding algorithms completely failed. Röding *et al.* [Röd2020] developed a segmentation method for FIB-SEM data samples of ethylcellulose porous films based on ML and demonstrated good agreement with manual segmentation performed on parts of the data set. Moreover, the ML approach can be also used for resolution enhancement in the FIB-SEM data stack in the FIB-milling direction, as proposed by Hagita *et al.* [Hag2018].

The shine-through artefact in the SEM images challenges precise segmentation. Several ML-based approaches to reduce the error in the SEM image segmentation have been developed. Fager *et al.* [Fag220] used several times the Gaussian filter as a training feature in the training procedure and as a result claim to reliably segment SEM images with respect to the shine-through artefact. Another possibility to precisely train the ML algorithm is on simulated data. Prill *et al.* [Pri2013] used MC simulations to prepare a synthetic FIB-SEM data stack but did not test the simulation results on segmentation algorithms. Fend *et al.* [Fen2020] showed that the simulated data stack together with the stochastic geometrical model is ideal for training the ML segmentation algorithm and is able to correct the shine-through artefact in highly porous structures.

5.2 Experimental procedures

The experimental FIB-SEM tomography work begins with the fabrication of the porous PETA structures by a two-photon 3D micro-printing method. Prior the FIB-SEM tomography measurement the structures have to be stained with OsO_4 and infiltrated with Epon, in order to stabilize the inner sample structure and increase the contrast between the pore and PETA phase in the SEM images. For later Monte Carlo simulations the chemical composition of the PETA structures after the staining procedure is important. The quantified chemical composition of the stained PETA structures was determined via EDXS analysis.

5.2.1 Fabrication of porous PETA structures

The investigated nanoporous PETA samples were 3D printed by direct laser writing using a commercial 3D laser printer (Nanoscribe Professional GT). In this technique, a laser beam is focused on a droplet of polymer photoresist. Based on the two-photon absorption the region close to the laser focus is polymerized and becomes insoluble. By scanning with the photoresist droplet, almost arbitrary 3D objects can be printed. Subsequent washing-out of the unpolymerized photoresist reveals the fabricated 3D structure. Even though the two-photon absorption is a non-linear optical

phenomenon and occurs only at high laser intensities (which occur only at the focus of the laser) this technique is not capable of fabricating structures in the nanometre range.

As a novel photoresist system, which enables printing of inherently nanoporous structures by means of polymerization-induced phase separation was recently suggested by Mayer *et al.* [May2020]. The photoresist consists of (mass fractions): Pentaerythritol Triacrylate $52.94\,\%$ (Sigma-Aldrich); Irgacure 819 $2.12\,\%$; 2,2,6,6-tetramethylpiperidinyloxyl $0.07\,\%$ (TEMPO, Sigma-Aldrich), Dodecyl Acetate $22.43\,\%$ (Sigma-Aldrich), Octadecyl Acetate $22.43\,\%$ (TCI Chemicals). The samples were printed into cylinders with 350 µm diameter and 20 µm height (Figure 5.3a) on a polypropylene substrate, using a $25\times$ objective lens (Zeiss LCI Plan-Neofluar $25\times/0.8$) in dip-in mode. Prior to 3D printing, oxygen was removed from the photoresist by bubbling it with nitrogen gas. Furthermore, during the complete printing process, the sample was held under a nitrogen atmosphere. For printing, the laser power was set to 30 mW, at a scanning speed of 5 cm/s, a hatching distance of 0.5 µm and a slicing distance of 1 µm. Afterwards, the samples were immersed in acetone for 30 minutes to remove the unexposed photoresist. To preserve the pores from collapsing, subsequently, supercritical drying using carbon dioxide was employed.

An SEM image of one sample cylinder as fabricated is shown in Figure 5.3a. The sample appears homogeneous with a smooth surface and open pores. A FIB-milled trench, marked in Figure 5.3a by a white arrow, enables a cross-section (CS) view (Figure 5.3b) revealing the porous structure of the fabricated sample.

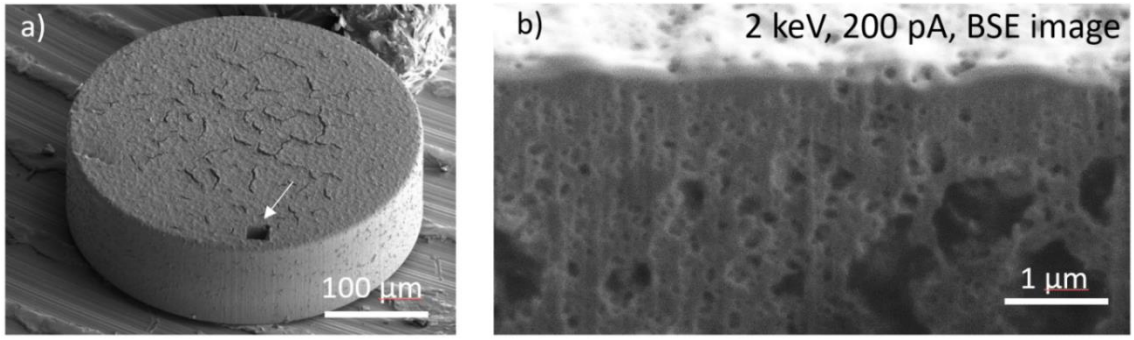

Figure 5.3 Fabricated porous PETA structures. a) Overview SEM image of the fabricated porous PETA structures. The SEM imaging parameters are included in the image. The samples were typically printed in a cylindrical shape with 300 µm diameter and 100 µm height. b) Cross-section backscattered (BSE) SEM image at the sample position marked by an arrow in a) revealing the porous structure of the studied sample.

5.2.2 Porous PETA staining and infiltration

In the following sample fabrication and preparation for FIB-SEM tomography is described (cf. schemes in Figure 5.4). In this work, we intended to investigate larger sample volumes (5 x 5 x 5 µm). For this reason, the only applicable infiltration technique (discussed in section 5.1.1) is resin impregnation. The expected smallest pore size of the porous PETA structure is in the range of 5 nm. To successfully infiltrate such small pores, low viscous Epon was used as a resin. Epon was fabricated by mixing 42.2 g Glycidether 100, 29.6 g Dodecenylsuccinic anhydrid, 18.4 g Methylacid anhydride, and 2.4 g

Tris(dimethylaminomethyl)phenol. Sample infiltration has to be carried out gently without applying any external force to preserve the inner sample structure. Epon infiltration stabilizes the inner pore structure, however, the contrast between the Epon infiltrated pore and PETA is very weak. The solution to distinguishing the PETA structure from the Epon-filled pores in SEM images is staining one of the phases. In the staining process atoms of heavy elements, which strongly scatter electrons, are implemented into the sample material and thus yield a contrast in BSE SEM or STEM-in-SEM images. Staining is a process widely used for biological samples, where as heavy elements Os or U are usually used [Odr2017]. Prior to Epon infiltration, the PETA structure was stained by the vapour of a 4 % solution of OsO_4 in H_2O for several days (cf. Figure 5.4b). The stained and infiltrated sample was trimmed, to reach the PETA cylinder within the Epon embedding (cf. Figure 5.4c). Finally, the sample is coated with 40 nm of amorphous C to ensure sufficient conductivity and minimize sample drift during measurement. In the SE SEM image in Figure 5.4e the bright region corresponds to the stained and infiltrated 20 µm high PETA cylinder in a cross-section. The white dashed box indicates a typical position for FIB-SEM tomography performed in direction of the arrow.

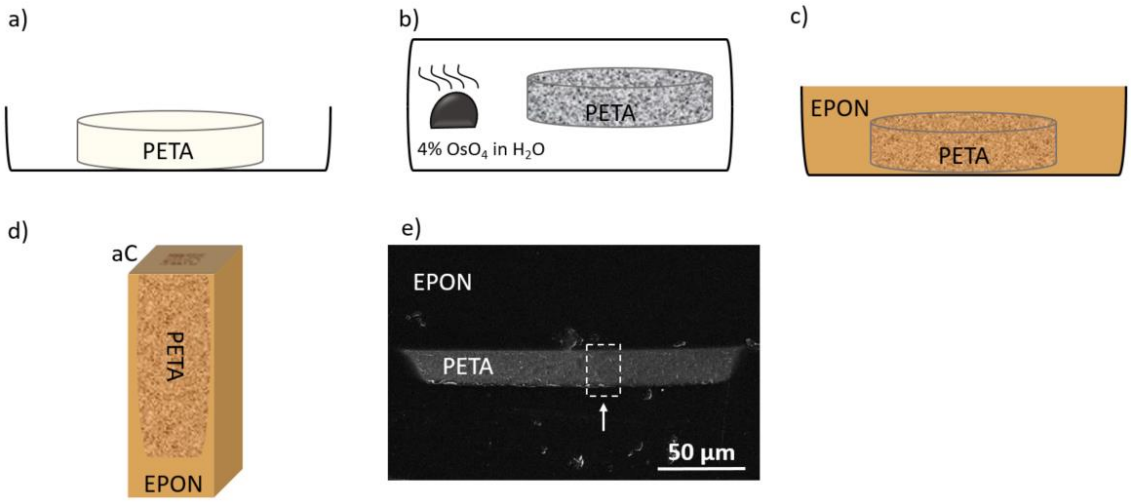

Figure 5.4 Sample preparation. a) Porous PETA structure after transfer from polypropylene substrate. b) Staining of the PETA structure by the vapour of 4 % OsO_4 in H_2O. c) Infiltration of the stained PETA structure with Epon. d) The stained and infiltrated PETA structure after trimming where the top surface was coated with 40 nm of amorphous carbon. e) 30 keV SE SEM image of the top surface of the prepared sample shown in d). The bright region corresponds to the stained and infiltrated PETA structure. FIB-SEM tomography was performed in the region marked by the white dashed box. Adapted from a publication [Čal2021].

Several PETA samples were stained by exposing the samples to OsO_4 vapour for different time periods (3 hours, 1, 1.5, 2, 2.5, 3 days) in order to determine the best parameters for the staining of PETA structures. In Figure 5.5a – e 1.75 keV SEM images acquired from samples stained for different time periods are shown. The stained PETA regions appear bright in SEM images and the Epon-infiltrated pores are dark. Because the staining process is governed by diffusion, increased staining times should increase the Os amount in PETA and improve the staining performance. Staining the PETA sample

for 3 hours (Figure 5.5a) and for 1 day (Figure 5.5b) yield similar results, where larger PETA structures are not fully stained in the centre as suggested by the reduction of the intensity. Increasing the staining time above 1.5 days (Figure 5.5c) leads to the formation of OsO_4 agglomerates inside the PETA structures, represented by dots with particular high intensity in the SEM images. PETA structures stained for 2.5 and 3 days are completely stained and provide sufficient contrast with respect to the Epon infiltrated pores. The OsO_4 agglomerates are considered to be staining artefacts, however, they are irrelevant with respect to SEM image segmentation because their pixel grey values are much higher than the grey values of stained PETA and can be easily distinguished in the image histogram. Similar agglomerates are visible in the work of Ghosh *et al.* [Gho2015] where a metalliferous epoxy polymer was used to fill the pores of a catalyst layer in a polymer electrolyte membrane fuel cell. Moreover, Ghosh *et al.* do not consider this issue to degrade the image segmentation procedure because they do not mention this issue nor explain the origin of the agglomerates.

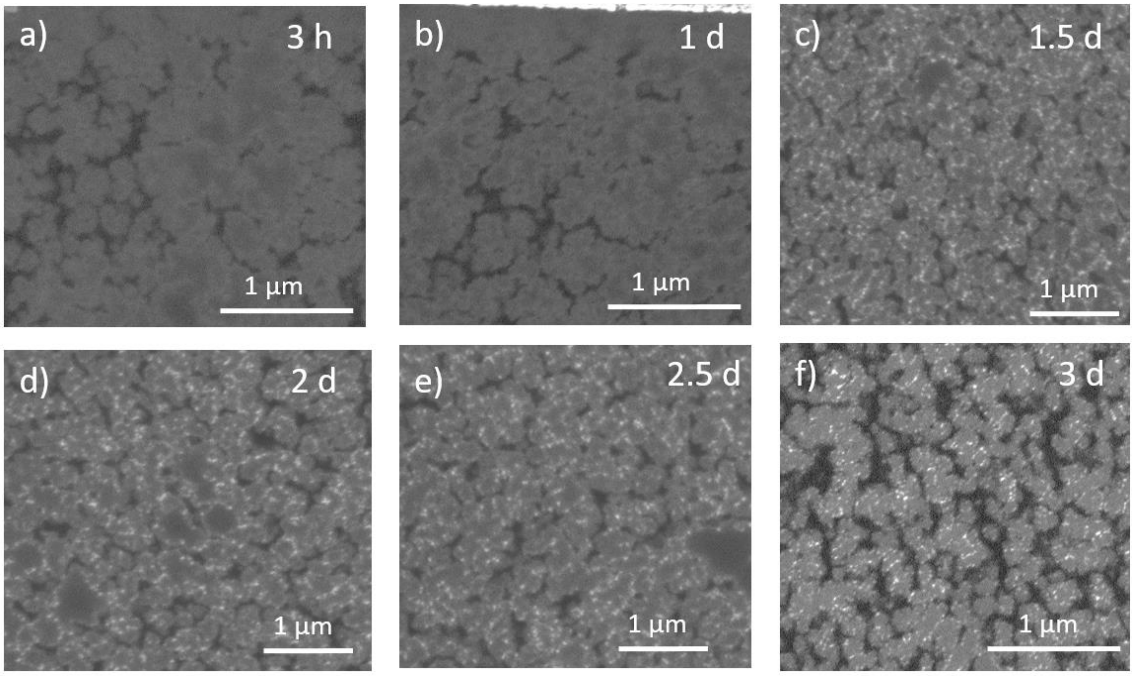

Figure 5.5 OsO_4 staining time series of the PETA structures. 1.75 keV BSE SEM images show the influence of various staining times, a) 3 hours, b) 1 day, c) 1.5 days, d) 2 days, e) 2.5 days, and f) 3 days, on the PETA structures. The very bright dots correspond to OsO_4 agglomerates that occur for staining times longer than 1 day.

For the Monte Carlo simulations presented in the following the chemical composition of the simulated data is essential and thus the content of Os in the PETA structures after staining has to be determined. Using a 5 keV electron beam, EDXS analyses were performed on a porous PETA sample stained for 3 days. EDXS spectra from 10 regions (shown in the SEM image in Figure 5.6a) were acquired and the chemical composition was quantified. A typical EDXS spectrum obtained for a stained PETA structure is shown in Figure 5.6b, where the carbon $K\alpha_1$, oxygen $K\alpha_1$, and the osmium $M\alpha_1$ peaks are present. Quantification results for each region separately are shown in

Table 5.1. Averaging the Os content from all 10 regions reveal the presence of 4.7 ± 0.3 % of Os in the PETA structure after a 3-day staining process.

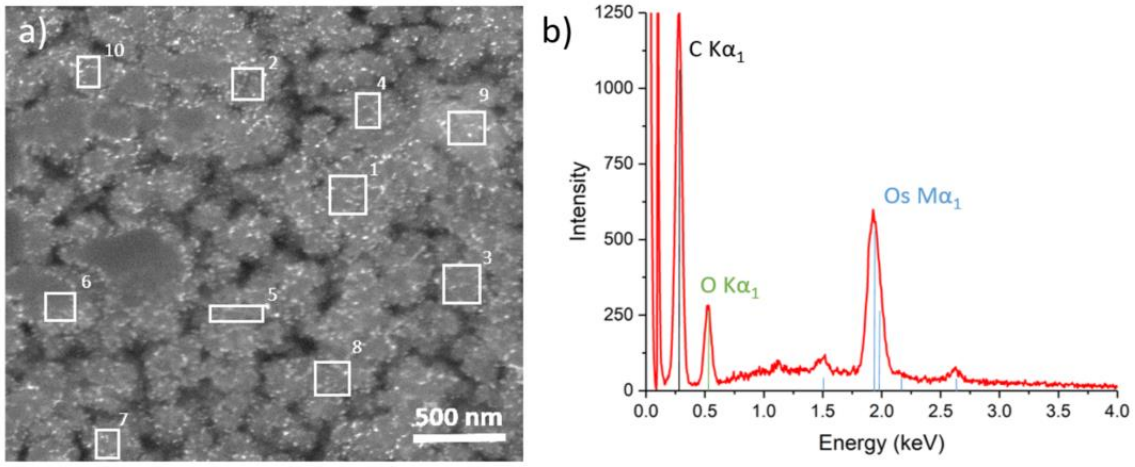

Figure 5.6 EDXS analysis of a 3-day stained porous PETA structure. a) SEM image with marked 10 regions where an EDXS analysis was performed. b) Typical EDXS spectrum revealing the carbon $K\alpha_1$, oxygen $K\alpha_1$, and osmium $M\alpha_1$ peaks.

Table 5.1 Quantification of EDXS spectra. The table gives results for the chemical composition of the 3 days stained porous PETA structures obtained by quantification of the measured EDXS spectra at 10 regions.

	Atomic concentration in %		
Inspected region	**Carbon**	**Oxygen**	**Osmium**
Region 1	79.6	16.0	4.4
Region 2	84.9	10.1	5.0
Region 3	79.7	15.6	4.7
Region 4	85.7	11.0	3.3
Region 5	86.8	7.7	5.5
Region 6	84.2	11.0	4.8
Region 7	82.4	12.4	5.2
Region 8	78.5	18.1	3.4
Region 9	82.9	11.8	5.3
Region 10	85.5	9.0	5.5
Summary	**83.0 ± 0.9**	**12.3 ± 1.0**	**4.7 ± 0.3**

5.2.3 FIB-SEM data acquisition

The FIB-SEM dual-beam Helios NanoLab G4 FX with the Auto Slice and View 4.0 software enabled guided preparation of region of interest (ROI) and automated acquisition of serial sectioning images. Firstly, a 2 µm Pt layer is deposited over the 10 x 10 µm (ROI), serving as a protection layer against damage induced by subsequent FIB imaging and milling. Pt has to be deposited with a maximal current of 90 pA because sputtering rather than Pt deposition occurs at higher ion-beam currents. Secondly, trenches along the sides and in front of the ROI are milled with a high ion-beam current

(20 nA), followed by cleaning of the front side cross-section with an ion-beam current of 90 pA. Sufficiently wide and deep trenches are necessary in order to enable detection of BSEs from deeper regions of the imaged cross-section as discussed in more detail in section 5.1.2. Lastly, two sets of fiducial markers are milled for the software to correct for sample drift. The prepared ROI is shown in Figure 5.1a.

FIB-SEM was performed under the following conditions: the specimen was milled with 30 keV Ga^+ ions at 30 keV acceleration voltage and a 90 pA beam current with a slice thickness of 10 nm. To achieve material contrast in the SEM images, the In Column Detector (ICD) and through-lens detector (TLD) in BSE mode were used simultaneously to collect the BSEs. The electron energy and current have to be chosen carefully. Low electron energies are preferred because the penetration depth is reduced. On the other hand, low electron energies reduce the resolution and signal-to-noise ratio (SNR). Another parameter related to the electron energy is the contrast between the stained PETA and Epon-infiltrated pores. The contrast between these two materials was measured as a function of the electron energy (shown in Figure 5.7b) yielding the highest contrast at 1.75 keV electron energy for the ICD detector. The contrast was calculated as $contrast = (I_{\mathrm{PETA}} - I_{\mathrm{pore}})/I_{\mathrm{Pt}}$, where I_{PETA} is the intensity of stained PETA (high intensity in Figure 5.7a), I_{pore} is the intensity of infiltrated pores (low intensity in Figure 5.7a), and I_{Pt} is the intensity of the Pt-protection layer, which serves as normalization of the contrast value, as pointed out in the BSE SEM image in Figure 5.7a. The electron current was set to 200 pA leading to SEM images with sufficient SNR.

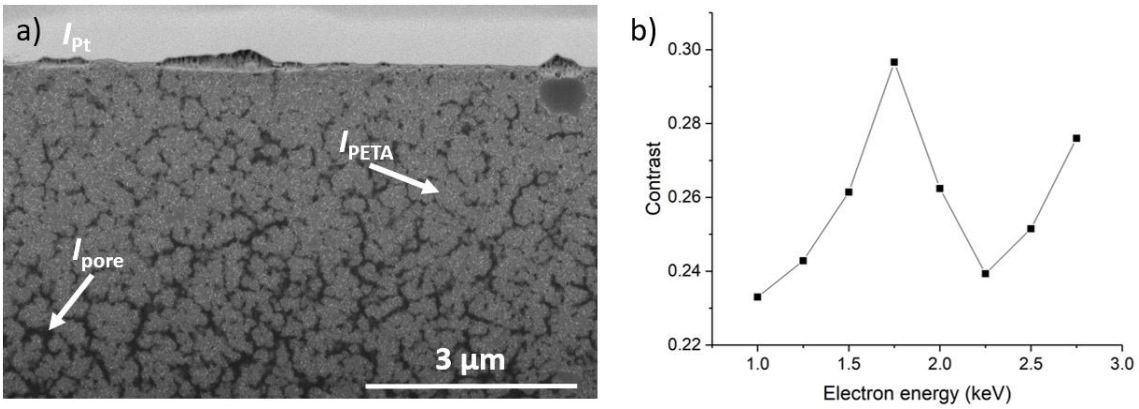

Figure 5.7 Contrast in SEM image. a) 1.75 keV BSE SEM image of an OsO_4-stained and Epon-infiltrated porous PETA structure taken with the ICD detector. b) Contrast between stained PETA and infiltrated pores calculated as $contrast = (I_{PETA} - I_{pore})/I_{Pt}$ (intensities marked a)) as a function of the primary electron energy revealing a maximum at 1.75 keV, which is the most suitable for SEM imaging and image segmentation. Adapted from a publication [Čal2021].

Figure 5.8 compares SEM images acquired simultaneously (with the same imaging conditions: E_0 = 1.75 keV, I = 200 pA) with the ICD (Figure 5.8a) and TLD-BSE (Figure 5.8b) detectors. Both detectors provide the same contrast, stained PETA is brighter than Epon infiltrated pores. Images acquired with the ICD detector have better SNR and the ICD detector is less sensitive to the shadowing artefact as compared with

the TLD detector. Moreover, the ICD detector has a smaller detection-angle range (0-85 mrad) as compared to the TLD detector and thus detects more electrons that have experienced only a few scattering events. As a result, the information depth of the ICD image is lower as compared to the TLD image, which is preferred in the FIB-SEM tomography. This can be seen in the insets of the images showing the same area with an infiltrated pore. The pore in the ICD image (Figure 5.8a) is larger as compared to the same pore in the TLD image, demonstrating a smaller information depth in the ICD image. For the reasons discussed above, the ICD detector is better suited and was used for electron detection in the following measurements.

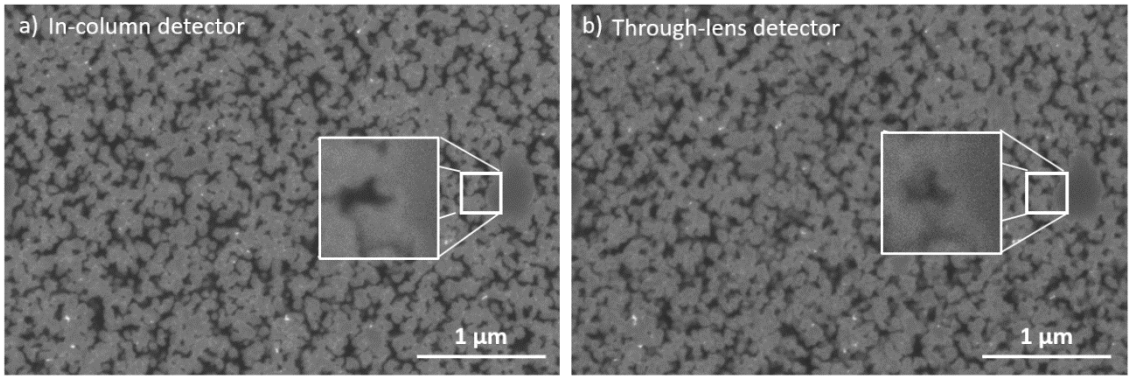

Figure 5.8 Comparison of BSE detectors. a) SEM image acquired with an in-column BSE detector (ICD). b) The same image is simultaneously acquired with a through-lens detector in backscattered mode (TLD-BSE). Comparison of the insets of the images demonstrate a smaller information depth in the ICD image a).

The Auto Slice & View 4.0 software was developed by Thermo Fischer Scientific and serves as a tool for automatized FIB-SEM tomography. Within setting up the software, many parameters have to be chosen carefully to avoid failure in the FIB-SEM tomography process. In the first step, FIB-milling properties are defined. In the milling settings, the drift correction can be chosen. From experience, to successfully compensate for the sample drift, the fiducial marker score (a score that evaluates the quality of milled fiducial markers) has to be at least 90 %. This can be usually achieved by milling the fiducial markers with the shape shown in Figure 5.1a using a 30 keV and 1.2 nA ion current and setting the FIB-image resolution to 1536 x 1024 pixels with 300 ns dwell time. In the imaging settings, the ICD detector was selected to acquire the SEM images. The image acquisition time needs to be kept below 90 s, otherwise the drift within one image prevents further precise image alignment. Thus possible settings are 10 µs dwell time with 1536 x 1024 image resolution, or 3 µs dwell time with 3072 x 2048 image resolution, giving a pixel resolution in a range of 2 nm while imaging a 6 x 4 µm area of interest. The section alignment and Y-shift correction must be activated since the electron beam is not perpendicularly impinging on the imaged surface and thus the ROI within the SEM images shifts (as discussed in section 5.1.2). Finally, the Auto focus function was enabled, performing auto-focus after the acquisition of 7 images.

By alternating FIB milling and SEM imaging, the FIB-SEM data stack is acquired. The obtained stack consists of several 100 SEM (692 images for the example shown in

the following) with 1536 x 1024 image resolution giving a 2.8 nm pixel size while imaging a 4.3 x 2.9 μm^2 area of interest. The raw data stack was further processed using the Avizo software. The slices were aligned using the least-square alignment method. Although compensation algorithms for sample drift were applied, the ROI slightly shifts during the acquisition of the whole image stack and thus cropping is necessary. After alignment and cropping of the SEM images, the data set has a total array of 1482 × 494 × 692 voxels, representing a volume of 4.2 × 1.4 × 6.9 μm^3. The SNR of the images was improved by applying the anisotropic diffusion 2D filter [Tsc2005], which is a plug-in the ImageJ software. The use of this filter is convenient because it preserves the sharpness of the edges between phases. An example of a cropped, filtered, and contrast-enhanced SEM image from the data stack is shown in Figure 5.9a.

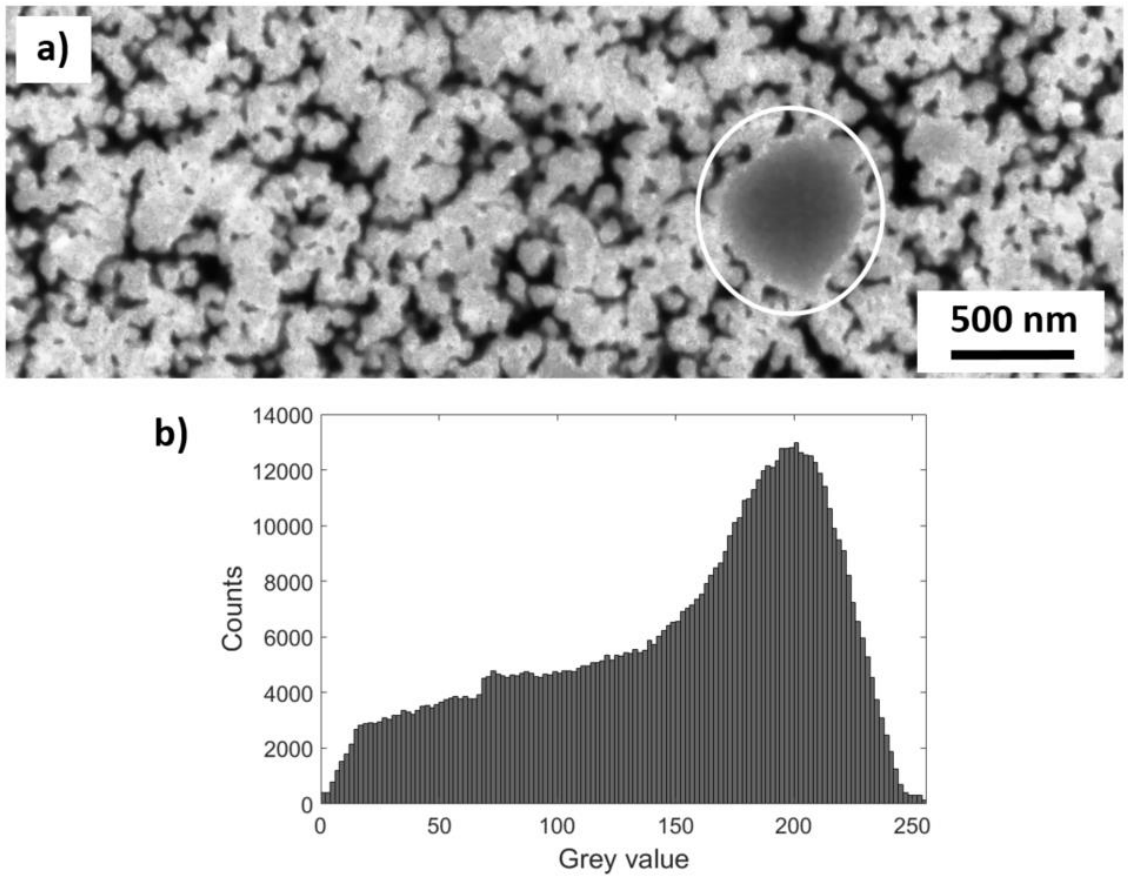

Figure 5.9 Processed SEM image. a) 1.75 keV cropped, filtered, and contrast-enhanced BSE SEM image of Epon-infiltrated pores in an Os-stained PETA structure. The encircled region is an unstained "blob" of PETA originating from the fabrication process as an artefact. B) Image histogram obtained from the image in a).

In Figure 5.9a so-called PETA "blob" can be seen (circled). These PETA blobs are large PETA structures that result as a fabrication artefact. In SEM images the PETA blobs appear darker in the middle because the staining molecules are not capable of diffusing through the whole structure. For ideal image segmentation, two peaks should be present in the image histogram, one representing the stained PETA phase and the other representing the Epon-infiltrated pores. Figure 5.9b shows an image intensity histogram of the image in Figure 5.9a, where only one peak for the PETA phase with a broad

shoulder at lower grey values representing pores is observed. The intermediate grey values originate from the finite penetration depth of the primary electrons leading to image information not only from the surface but also from the electron-interaction volume below. The second source of the intermediate grey values is the PETA blobs.

In the image histogram shown in Figure 5.9b, it is not clear where the threshold separating the two phases should be set. As a result, imprecise SEM image segmentation using the global thresholding segmentation algorithms can be expected leading to incorrectly derived 3D material properties of the porous PETA structures. To facilitate precise SEM-image segmentation, deeper insight into the SEM-image formation (especially at the pore/PETA interface) is necessary. Monte Carlo (MC) simulations are well established to simulate the interaction of electrons with matter to model and understand the contrast formation of SEM images. MC simulations were therefore used in this work to derive criteria for precise segmentation of SEM images of porous PETA structures.

5.3 SEM-image interpretation supported by Monte Carlo simulations

Understanding contrast formation at the interface between PETA and Epon-infiltrated pores is mandatory for correct segmentation. Interface contrast depends on the proportion of the Epon-infiltrated pore and PETA in the interaction volume of the primary electron beam. In this work, the NISTMonte simulation package [Rit2005] was used with implemented screened Rutherford differential scattering cross-sections and the continuous-slowing-down approximation for energy-loss calculations [Joy1989] to understand contrast formation at the pore/PETA interface and to derive criteria for subsequent SEM image segmentation.

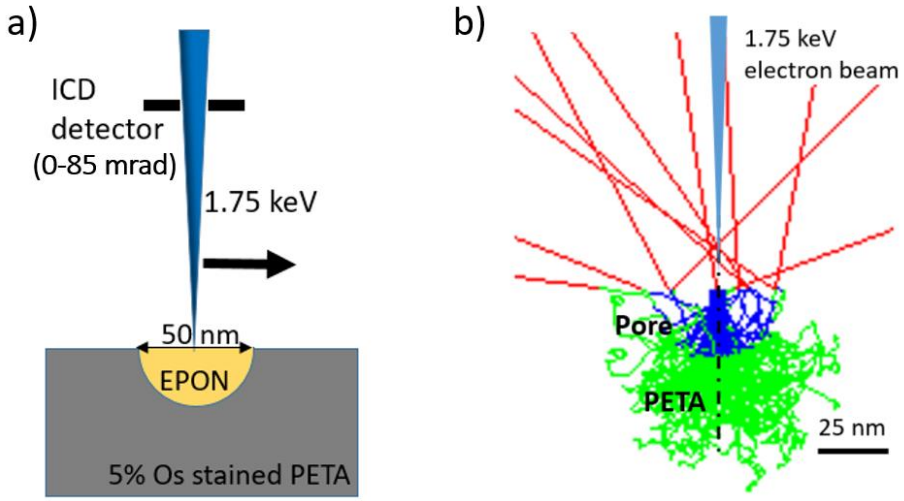

Figure 5.10: Monte Carlo simulation model of pore in PETA. a) Model of Epon-infiltrated half-pore with a radius of 25 nm in Os-stained PETA for MC simulations. b) Electron trajectories from MC calculations for 1.75 keV primary electrons interacting with an Epon-infiltrated half-pore in Os-stained PETA. Electron trajectories in the Epon-infiltrated pores are marked by blue lines, trajectories in PETA by green lines. Red lines indicate emitted BSEs. Adapted from a publication [Čal2021].

For MC simulations, a model of an Epon-infiltrated spherical half-pore (and full-pore) embedded in Os-stained PETA was defined (cf. Figure 5.10a for a half-pore). Simulations were performed for Epon with a chemical composition $H_{20}C_{12}O_6$, average atomic number $\bar{Z} = 4.6$ and material density $\rho = 1.15\ \mathrm{g/cm^3}$. Os-stained PETA was estimated to have a chemical composition of pure PETA ($H_{18}C_{14}O_7$) with an additional 5 % of Os (determined by EDXS, section 5.2.2) leading to an average atomic number $\bar{Z} =$ 17.5 and a density of $\rho = 1.2\ \mathrm{g/cm^3}$. To achieve sufficient accuracy 10^7 electron trajectories were simulated. A trajectory image of the modelled half-pore in the PETA structure interacting with 1.75 keV primary electrons is shown in Figure 5.10b. The electron trajectories in Epon-infiltrated pores are marked by blue lines, trajectories in PETA are green, and emitted BSEs are described by red lines. From the trajectory image, the penetration depth of 1.75 keV electrons in Os-stained PETA can be estimated. The distance from the surface to the deepest electron trajectory indicates a penetration depth of $P \cong 70\ \mathrm{nm}$. This results in an information depth of $P/2 \cong 35\ \mathrm{nm}$ [Rei1998] from which BSEs can escape from the material and be detected.

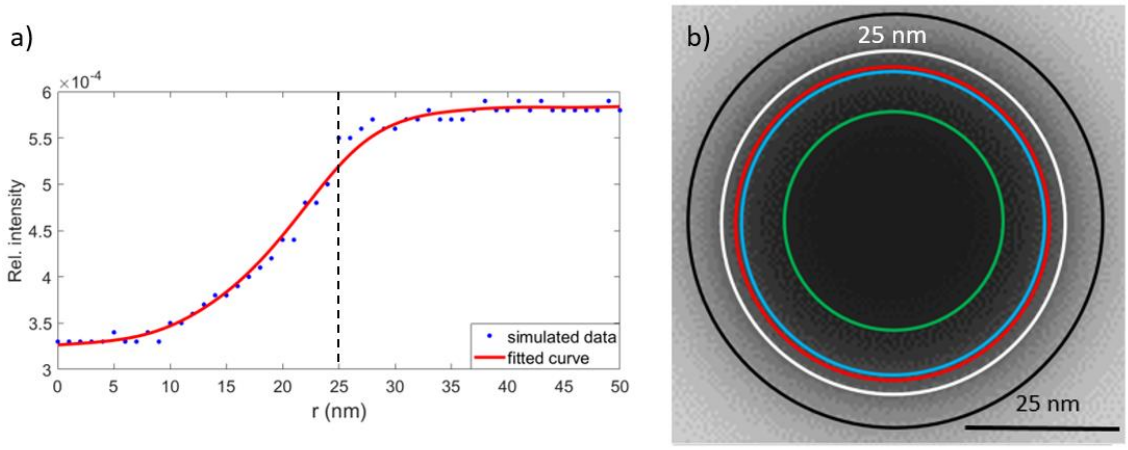

Figure 5.11 Segmentation algorithm test on simulated SEM image. a) Line profile of the simulated normalized BSE intensity across the PETA/pore interface obtained by moving the electron beam in the direction of the arrow (cf. Figure 5.10a) and by detection of BSEs with the ICD detector as indicated in Figure 5.10a. c) Simulated image of the pore/PETA interface (white circle), which was subjected to different segmentation algorithms. The resulting pore radii are marked with colours: 22.4 nm (red circle) for the Otsu, DPSO and HSO algorithms, 22.0 nm (blue circle) for fuzzy c-means clustering, 15.8 nm (green circle) for fuzzy Tsallis entropy and 29.4 nm (black circle) for EMO. Adapted from a publication [Čal2021].

The simulated normalized intensity of BSEs is given by the sum of all electrons scattered into the detection-angle range of the ICD detector (0 – 85 mrad) and their energies. The detected charge of the silicon ICD detector is determined by the individual energy E_i of each BSE according to Eq. 2.23, as discussed in more detail previously. The intensities are normalized with respect to the total number of simulated electrons. In order to obtain a simulated intensity line profile through the pore/PETA interface, the

beam was moved in direction of the arrow in Figure 5.10a. A simulated intensity line profile for a pore with a radius of 25 nm is plotted in Figure 5.11a where *r* describes the distance from the centre of the pore. The dashed vertical line in Figure 5.11a positioned at *r = 25 nm* indicates the real position of the pore/PETA interface and enables the determination of the intensity corresponding to the pore/PETA interface.

Fitting a curve to the simulated data points and rotating the line profile around its origin, a simulated SEM image of the 25 nm pore in PETA is obtained (Figure 5.11b). This simulated SEM image can serve as a test image for the performance evaluation of established segmentation algorithms. Several commonly used segmentation algorithms, Otsus thresholding method [Ots1978], fuzzy c-means clustering [Bez1981], fuzzy-Tsallis entropy thresholding [Sar2014], Darwin particle swarm optimization (DPSO) [Gha2012], Harmony search optimization (HSO) [Oli2013], and electromagnetism optimization (EMO) [Oli2014] were applied to the simulated test image. All listed segmentation algorithms are implemented using MATLAB 2017b built-in functions or the MATLAB user file exchange website[1]. The segmentation results are summarized in Figure 5.11b, where coloured circles represent the position of the pore/PETA interface determined from the above-mentioned segmentation algorithms. The white circle has a radius of 25 nm and thus marks the position of the true pore/PETA interface. The Otsu, DPSO, and HSO segmentation algorithms yield the same radius of 22.4 nm (red circle). Only a slightly lower value (22.0 nm, blue circle) is obtained by fuzzy c-means clustering. The pore radius is strongly underestimated by the fuzzy-Tsallis entropy algorithm with a radius of only 15.8 nm (green circle). Only the EMO algorithm overestimates the pore radius (29.4 nm, black circle). Overall, the simulations demonstrate that pore radii tend to be underestimated by the majority of traditional segmentation algorithms.

In order to obtain more general insight into the position of the pore/PETA interface, line scans with the same parameters as in Figure 5.11a were simulated for spherical full pores (Figure 5.12a) and half-pores (Figure 5.12b) with different radii. The true pore radius is marked by the colour-coded vertical lines. The intersection with the line profile determines the intensity corresponding to the pore/PETA interface. For all simulated pore radii (full and half-pores), the pore/PETA interface is located at an intensity slightly below I_{PETA} and not at an average intensity given by I_{PETA} and I_{pore} as could be intuitively anticipated. This knowledge of the pore/PETA interface is decisive for reliable segmentation of FIB-SEM tomography data. A small shift towards lower intensities is observed for full pores with a smaller radius and for half-pores with increasing radius. This shift is related to the interaction volume of the primary electrons. For spherical full pores, the volume fraction of the infiltrated pore within the information depth of the primary electrons decreases with increasing the pore size, resulting in a shift of the pore/PETA interface to higher intensities. For spherical half-pores the volume fraction of the infiltrated pore increases with increasing pore radius, resulting in a shift of the pore/PETA interface towards lower intensities. The slight shift of the interface position with pore size was not taken into account in the segmentation

[1] https://mathworks.com/matlabcentral/fileexchange/

of real data because it only leads to a minor correction and the distinction between half and full pores is not straightforward in experimental images.

Because the chemical composition of Epon and PETA was only estimated, the validity of the derived segmentation criteria has to be checked for slightly different chemical compositions. Additional MC simulations were performed with the same material parameters (Epon $H_{20}C_{12}O_6$, $\rho = 1.15\ \mathrm{g/cm^3}$; PETA $H_{18}C_{14}O_7$, $\rho = 1.2\ \mathrm{g/cm^3}$.), however, only 2% Os staining of the PETA was considered. The simulated line profiles with modified composition are shown in Figure 5.13. The behaviour of the pore/PETA interface position with respect to the intensity of PETA, I_{PETA}, is very similar to the results obtained for PETA structures stained with 5% Os (Figure 5.12). For larger full-sphere pores the pore/PETA interface lies already in the I_{PETA}. Contrary, for larger half-sphere pores the pore/PETA interface shifts to slightly lower intensities. Overall, the segmentation criteria derived from the plots in Figure 5.12 did not show significant changes when changing the Os content in the PETA structures to 2% Os.

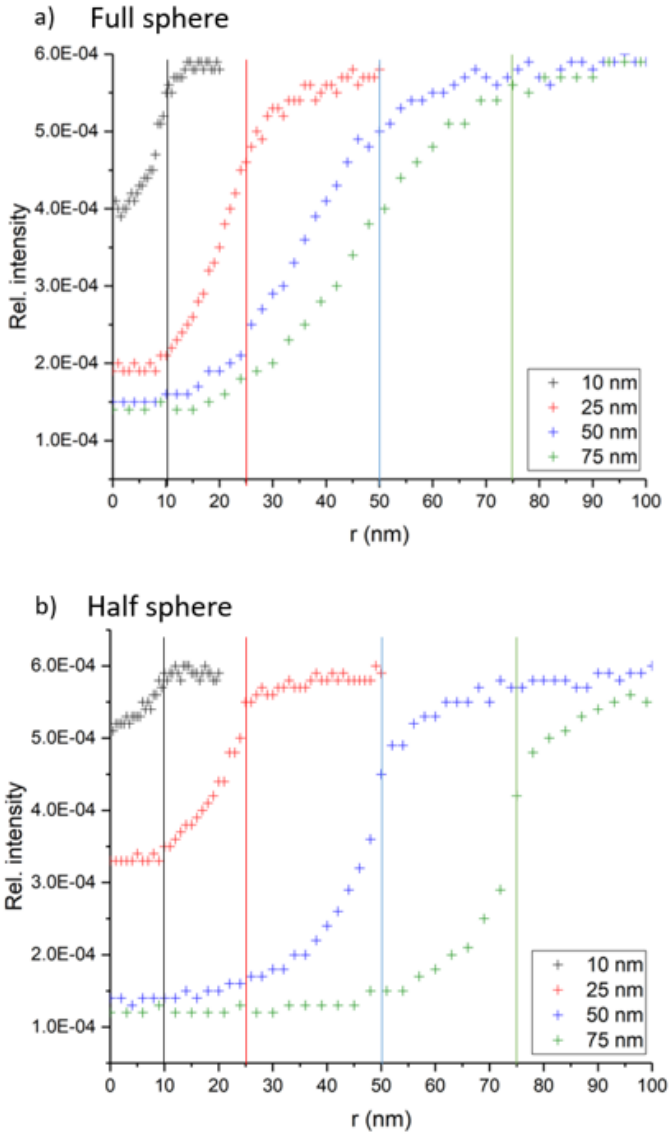

Figure 5.12 Derivation of segmentation criteria. Simulated line profiles of the normalized BSE intensity for a) Epon-infiltrated spherical full pores embedded in 5 % Os-

stained PETA and b) half-pores with different radii and the same parameters as in Figure 5.11a. Colour-coded vertical lines indicate the simulated pore radius.

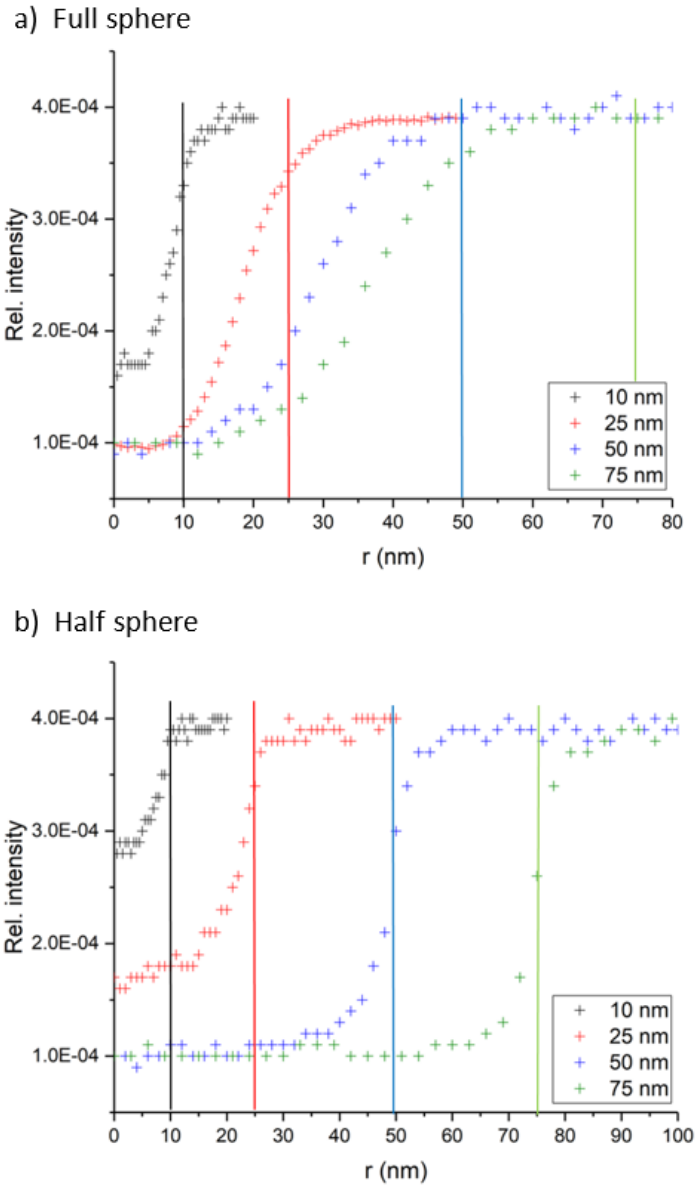

Figure 5.13 MC simulations of PETA with 2% Os content. Simulated intensity line profiles of the normalized BSE intensity for a) spherical full pores and b) half-pores with different radii and the same parameters as in Figure 5.12. Only the Os content in PETA was reduced to 2%. Colour-coded vertical lines indicate the simulated pore radius.

5.4 Comparison of image segmentation algorithms

Segmentation of the whole data stack was performed using two traditional segmentation methods (Otsu, fuzzy c-means clustering (fcm)) and ML segmentation, using the trainable WEKA segmentation (TWS) algorithm [Arg2017] that is part of the Fiji image processing distribution of ImageJ[2]. Applying the Otsu and fcm algorithms to the whole data stack is straightforward using particular built-in functions in Matlab. The

[2] http://imagej.net/Trainable_Weka_Segmentation

performance of the TWS algorithm strongly depends on the training procedure and therefore training the TWS algorithm has to be done with special care.

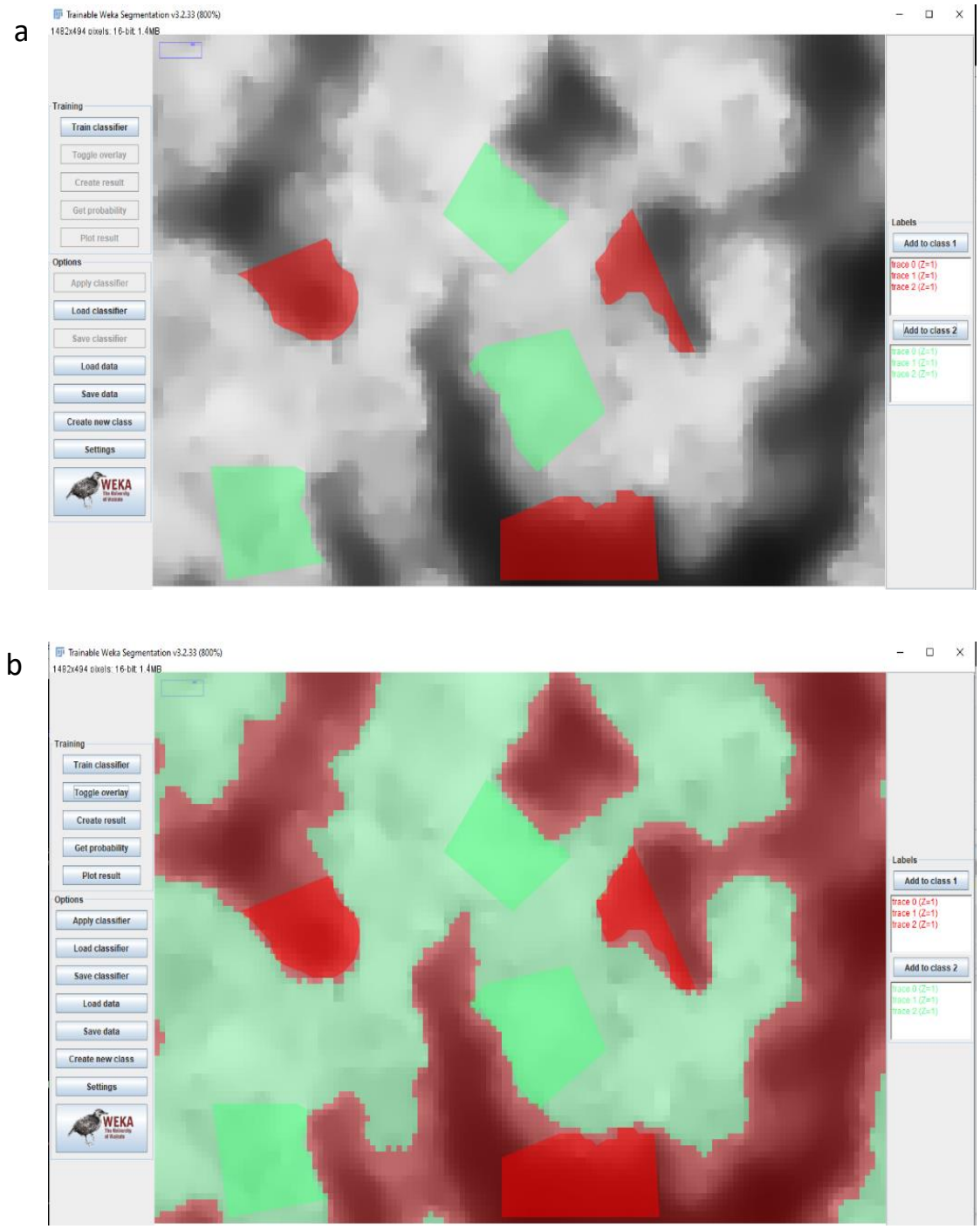

Figure 14.14 Trainable WEKA segmentation algorithm in a training procedure. a) Manually segmented regions based on the knowledge obtained from MC simulations. The red regions correspond to pores, green regions to PETA. b) Result of the training procedure, where the remaining pixels are assigned to particular phases.

The knowledge obtained from the MC simulations was passed to the TWS algorithm by manually segmenting 10 regions in one SEM image of the FIB-SEM data stack by carefully marking the pore/PETA interface. The pore/PETA interface was set to an intensity close to the intensity of stained PETA, as suggested by the MC simulations. Figure 5.14a shows the TWS user interface in the training procedure with several manually segmented regions. The red regions correspond to pores and the green regions to the PETA structure. Training the TWS algorithm on such manually segmented regions based on preselected training features results in assigning the remaining pixels of the SEM image to particular phases and the creation of a classifier. The result of the training procedure is shown in Figure 5.14b. The best performance of the TWS algorithm for the segmentation of stained PETA structures was found for the following training features: Sobel filter, Gaussian blur, Difference of Gaussian, Variance, Neighbors, Entropy, and Membrane projections.

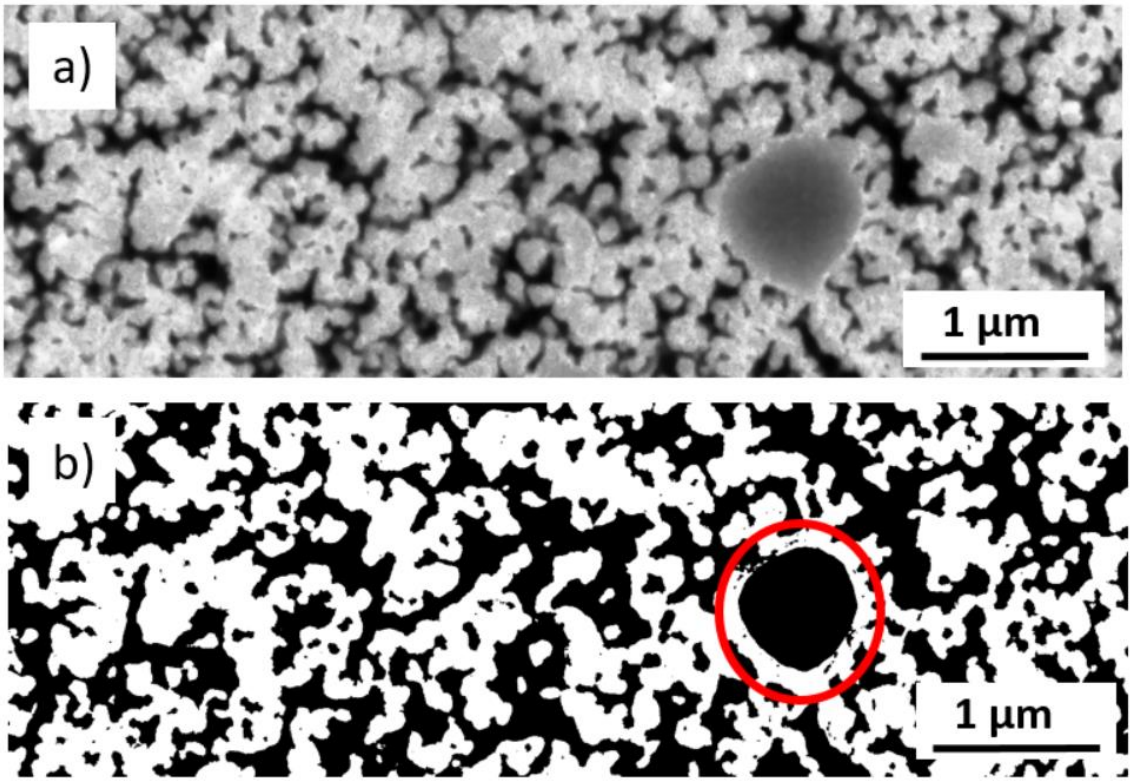

Figure 5.15 TWS segmented SEM image. a) 1.75 keV BSE SEM image (one of the SEM images from the FIB-SEM data stack) of Epon-infiltrated pores in an Os-stained PETA structure. b) TWS segmentation of a) showing a false-segmented PETA “blob” marked by a red circle.

An example of a TWS-segmented image belonging to an SEM image in Figure 5.15a is presented in Figure 5.15b. The red circle in Figure 5.15b reveals that the trained TWS algorithm is not capable of segmenting large PETA “blobs”. Changing segmentation settings and applying other filters in the training procedure did not improve the segmentation of the PETA blobs and manual correction of the TWS segmented data has to be applied to correctly segment large PETA blobs. The manual correction was performed in the Avizo software. Figure 5.16 shows the rendered 3D

model of the porous PETA structure obtained from the TWS-segmented image stack, revealing a homogeneous pore distribution in the analysed sample volume.

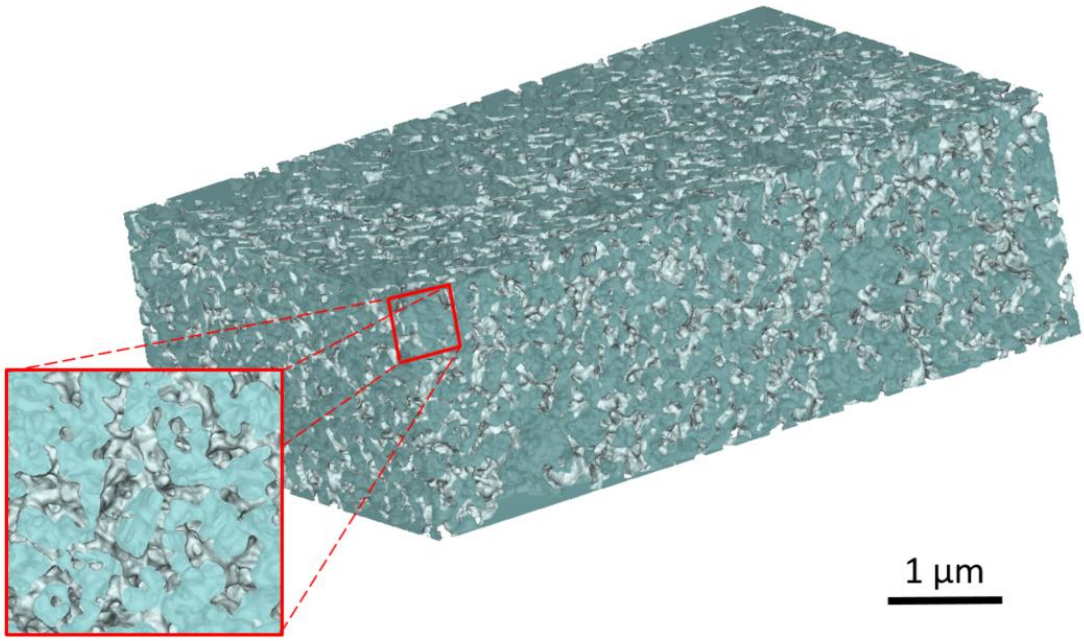

Figure 5.16 3D model of the reconstructed PETA structure obtained from the TWS-segmented image stack. Adapted from a publication [Čal2021].

An enlarged selection of the SEM image in Figure 5.15a showing the gradual intensity transition between pore and PETA is shown in Figure 5.17a. The white line represents the pore/PETA interface that would be manually set in the training procedure by visual inspection considering the information from the MC simulations. The same enlarged region was subjected to several segmentation algorithms to evaluate their performance on real SEM images. The results (Figure 5.17b) of the Otsu (red), fcm clustering (yellow), and TWS (blue) algorithms are overlaid upon Figure 5.17a for direct comparison. Comparing the three segmentation algorithms in Figure 5.17b with visual segmentation in Figure 5.17a (covering 127 pixels) demonstrates the obvious underestimation of the pore phase from the Otsu (54 pixels) and fcm (56 pixels) thresholding algorithms. The TWS algorithm significantly improves segmentation by yielding only 34 erroneously classified pixels as compared to 89 incorrectly classified pixels for the Otsu algorithm. These findings are consistent with the results obtained on the artificial MC-simulated SEM image, where the Otsu and fcm clustering algorithm yield similar segmentation results and underestimate the real pore sizes. These conclusions are confirmed by Figure 5.17d where another region (Figure 5.17c) of the SEM image was inspected in the same manner. The black line in Figure 5.17c highlights the pore/PETA interface defined by the TWS in Figure 5.17d. The pixels assignment to the pore phase by the TWS algorithm is performed not only by the pixel grey value but also based on the pixel relationship to surrounding pixels. This can be observed in Figure 5.17c, where two pixels with similar grey values (marked by an arrow in Figure 5.17c) are assigned to different phases.

The discrepancy between the results obtained by visual segmentation and the TWS algorithm is caused by the contribution of pores in deeper sample regions to the

measured intensity, which affects the gradual intensity transition between pore and PETA. The TWS algorithm will inaccurately segment regions where the subsurface contribution is stronger. Reducing the information depth of the BSEs would lead to more straightforward SEM image interpretation regarding surface structures followed by improved segmentation performance. One way of reducing the information depth of the BSEs is a further reduction of the primary electron energy. MC simulations suggest that decreasing the primary electron energy to 1 keV or 500 V results in an information depth of 17 nm and 7 nm, respectively. However, maintaining sufficient resolution and SNR is not straightforward at these low electron energies. Alternatively, the information depth can be reduced by filtering the BSEs prior to detection according to their energy. Detecting only the BSEs with an energy close to the primary electron energy reduces the information depth because these BSEs are scattered close to the sample surface. Unfortunately, BSE energy filtering is not possible with conventional BSE detectors and a special detector for this purpose is required.

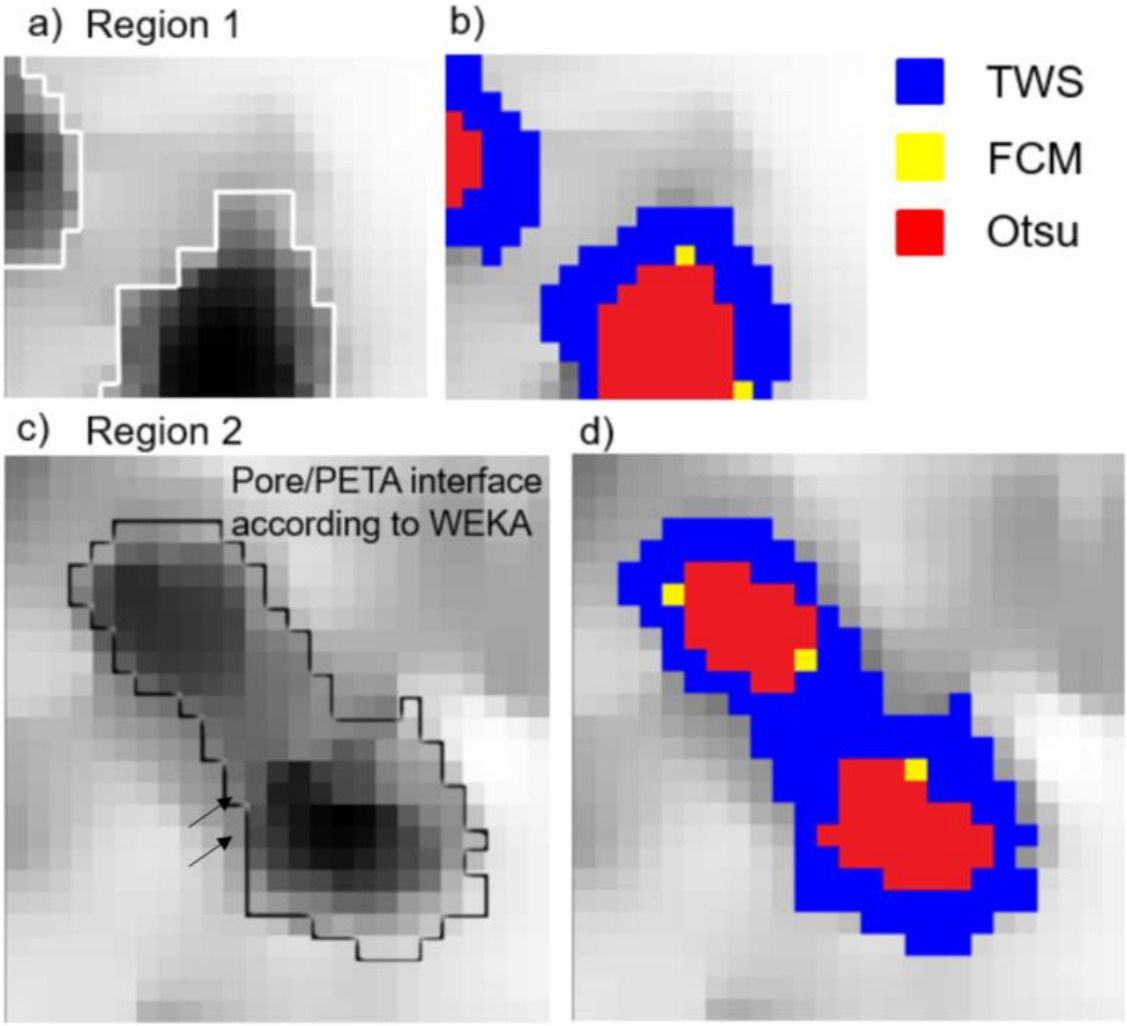

Figure 5.17 Comparison of segmentation algorithms on real SEM images. a) An enlarged section of Figure 5.15a with a gradual intensity transition at the pore/PETA interface. The white line represents the pore/PETA interface that is determined by a visual inspection. b) The enlarged section in a) is overlaid by results of different segmentation algorithms using the Otsu (red), fuzzy c-means (yellow) and TWS (blue)

algorithms. c) Analysis of another enlarged region of Figure 5.15a. The black line represents the pore/PETA interface that is determined by the TWS algorithm. d) Enlarged selection in c) overlaid by results of different segmentation algorithms in the same manner as in b).

5.5 Influence of the segmentation algorithm on 3D material properties

Credible segmentation of SEM images is essential for the trustworthy determination of the 3D material properties of the studied structures. The discrepancies between the segmentation algorithms discussed in the previous section will lead to differences in the derived 3D material properties. This section presents the determination of several material properties (porosity, tortuosity, pore-size distribution, and average pore size) of the PETA structures and the evaluation of the obtained results with respect to the used segmentation algorithm.

5.5.1 Porosity and tortuosity

Basic 3D material properties of porous structures are porosity and tortuosity. The porosity is given by the fraction of voxels assigned to pores over the total number of voxels. The tortuosity factors give the increase of path length through pores as compared to the straight-line distance between two points in the 3D structure. Most of the software calculating 3D material properties require isotropic voxels. The voxel size of the FIB-SEM data set is 2.8 x 2.8 x 10 nm^3, making it difficult to transform voxels to isotropic voxels without losing information. However, the open-source MATLAB 2017b application Tau Factor [Coo2016] is capable of handling anisotropic voxel data, enabling the calculation of the porosity and tortuosity factors of the PETA structures.

Table 5.2 Comparison of 3D material properties based on different segmentation algorithms. The porosity and tortuosity factors are calculated from the reconstructed 3D structure using the Tau Factor application. Average pore sizes were determined from 5 segmented SEM images.

	Porosity [%]	Tortuosity factor			Average pore size [nm]
		x	y	Z	
Otsu	32.6	2.89	2.68	2.6	49.3 ± 2.5
fuzzy c-means	32.6	2.88	2.67	2.59	49.5 ± 2.4
TWS	45.9	2.14	2.02	1.99	58.6 ± 6.7

The results on the porosity and tortuosity factors based on different segmentation algorithms are summarized in Table 5.2. For porosity, the results follow the trend seen in Figures 5.17b and 5.17d. The porosity is larger for the TWS-segmented data stack (45.9 %) compared to the Otsu (32.6 %) and fuzzy c-means (32.6 %)

segmented data. The tortuosity factors for the Otsu and fuzzy c-means segmented data are almost identical and slightly higher than for TWS segmented data. Overall, the tortuosity factor results indicate isotropy of pore sizes in the PETA structure because their values are similar in the *x*-, *y*- and *z*-directions.

5.5.2 Pore-size distribution and average pore sizes

The determination of pore sizes and the pore-size distribution of porous PETA structures is not straightforward because most of the pores are connected and cannot easily be subdivided into individual pores. The pore-size distribution problem reduces to a problem of finding a method that correctly splits the connected pores. However, due to the artificial introduction of pore boundaries, artefacts and simplifications of the resulting pore-size distributions are inevitable. The two most common approaches in the literature, which aim to extract the pore sizes, are the maximal inscribed sphere (Bubble analysis) method [Jon2006, Mün2013] and the watershed algorithm [Rab2014]. Both approaches need a segmented data stack and in the first step use the common distance transform [End2012, Ket2001]. The segmented data stack is transformed into a 3D distance map, whose elements are assigned to a value representing their distance from the nearest pore-solid interface. An artificial example in 2D is shown in Figure 5.18. Figure 5.18a shows a segmented image of a connected pore in black. Figure 5.18b is the distance transform of the image in Figure 5.18a where the brightness of the pixels increases with increasing distance from the pore-solid interface. Local maxima of the distance map define centres of the pores and are further used in both approaches. In the Bubble method, the centre of the pore represents the centre of a sphere with a maximum size that can be inscribed into the pore (Figure 5.18d). The radius of the sphere with maximum size defines the pore size. For the Watershed approach, the centres of the pores serve as an origin of a basin for water flow (source). The first contact line, that the water from two pores create, defines the pore-solid interface (Figure 5.18c).

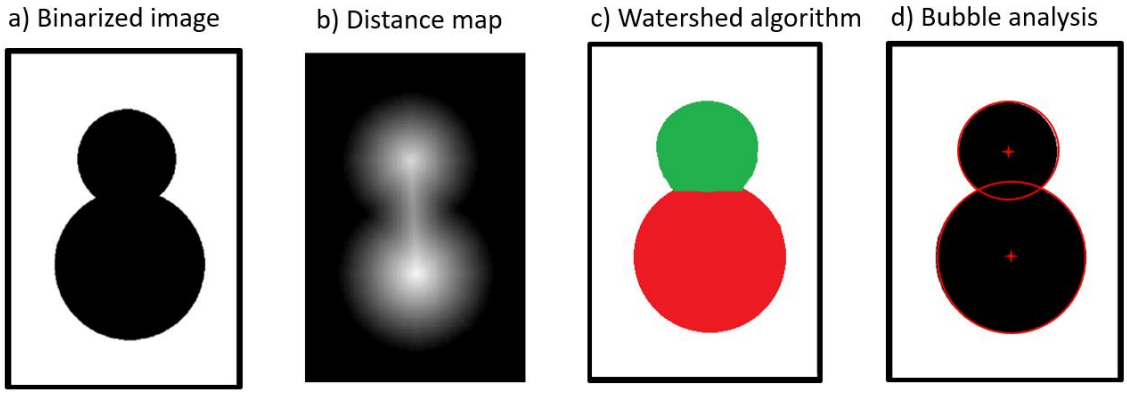

Figure 5.18 Approaches for pore-size determination. a) Segmented image showing connected pores. b) The distance map obtained by the distance transform of the image in a). c) Resulting pore separation from the watershed algorithm. d) Resulting pore separation from the Bubble analysis method. Adopted from [Rab2014]

Watershed and Bubble analysis performed on real segmented SEM images is presented in Figure 5.19. Figure 5.19a shows the segmented SEM image from

Figure 5.15 with manually corrected segmentation of PETA blobs. Local maxima in the corresponding calculated distance map (Figure 5.19b) reveal the centres of the pores. The result of the Watershed algorithm is shown in Figure 5.19c and in Figure 5.19d for the Bubble analysis. From a qualitative analysis of the presented results, a difference in the pore-size distribution based on the method used can be expected. In the case of the Bubble analysis, the pore size is equal to the radius of the inscribed sphere. In order to derive pore sizes (radii) of individual pores defined by the Watershed algorithm, it has been assumed that the radius of the pore is equal to the radius of a sphere with the same volume as the pore. This allows us to directly compare the pore-size distributions obtained from both approaches of the same data. The pore-size distributions are plotted in Figure 5.20. A clear difference is observed, the Bubble analysis tends to partition the connected pores into smaller individual pores as compared to the Watershed algorithm. This tendency has to be considered when comparing pore-size distributions obtained from different approaches.

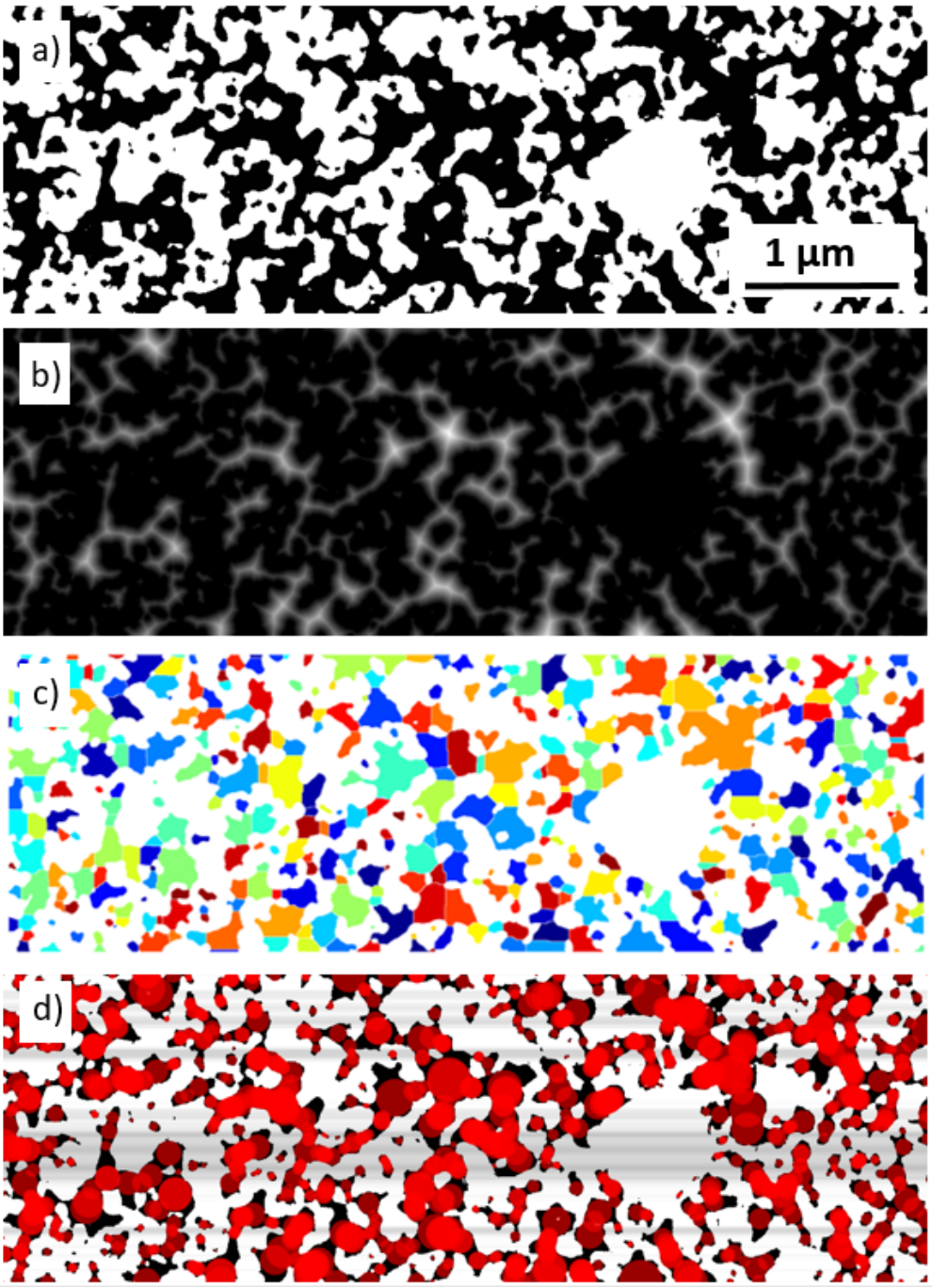

Figure 5.19 Pore-network partition. a) Segmented SEM image from Figure 5.15 with manually corrected segmentation of PETA blobs. b) Distance map obtained from a) using the distance transform. Based on the distance map the pores were partitioned using c) the Watershed algorithm and d) the Bubble analysis.

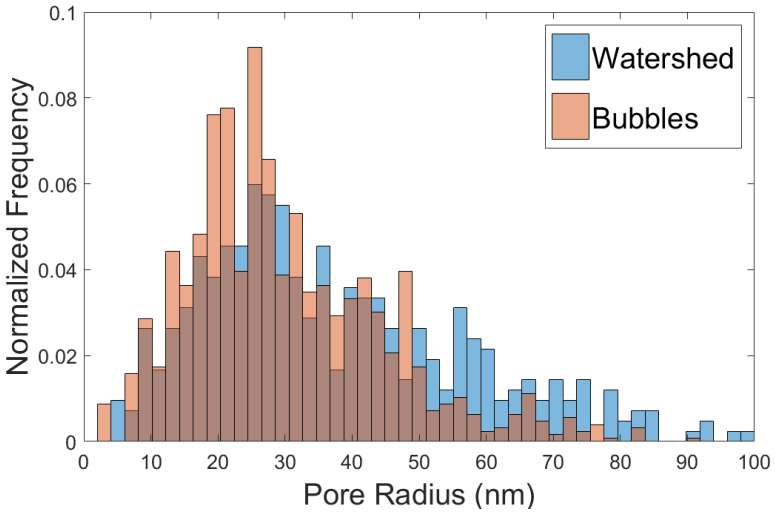

Figure 5.20 Comparison of pore-size distributions obtained from the Watershed (Figure 5.19c) and the Bubble analysis (Figure 5.19d) algorithms.

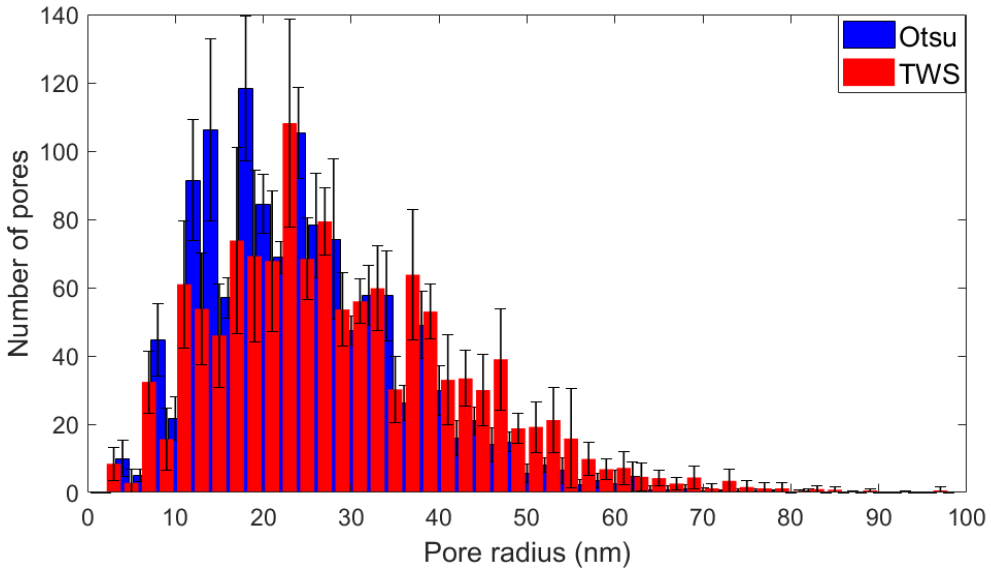

Figure 5.21 Comparison of pore-size distributions calculated from 5 TWS (red) and Otsu (blue) segmented 2D SEM images. Adapted from a publication [Čal2021].

Since pores in the PETA structure are isotropic, the pore-size distribution of the porous PETA structures was extracted from segmented 2D SEM images using the Bubble analysis. The Bubble analysis was preferred over the Watershed algorithm because is more common in literature. The average pore size and the pore-size distribution was determined for the different tested segmentation algorithms using the same five SEM images that were selected from different positions of the FIB-SEM image stack. The pore-size distributions with appropriate error bars from TWS (red) and Otsu (blue) segmentation are compared in Figure 5.21. Distributions corresponding to the Otsu and fuzzy c-means segmentation algorithm do not differ significantly with average pore sizes of 49.3 ± 2.5 nm and 49.5 ± 2.4 nm, respectively. Therefore, only the results for the Otsu and TWS algorithms are shown in Figure 5.21. The pore-size distribution belonging to

the TWS segmentation shows a larger spread towards larger pore radii, resulting in average pore size of 58.6 ± 6.7 nm (see Table 5.2).

5.6 Summary

This chapter presents focused-ion-beam/scanning-electron-microscopy (FIB/SEM) tomography of a nanoporous PETA polymer structure with a focus on the SEM image segmentation and quantification of the 3D material properties. The porous polymer PETA structures were infiltrated with Epon and stained with OsO_4 to enhance the contrast in SEM images. For reliable segmentation of the SEM images, precise location of the pore/PETA interface is essential. In order to understand SEM image contrast at the pore/PETA interface, Monte Carlo (MC) simulations were performed using models of infiltrated spherical full- and half-pores. As a result, criteria for selecting the intensity threshold at the pore/polymer interface were derived (Figure 5.12 and 5.13). Moreover, a simulated SEM image was subjected to several segmentation algorithms (Otsu, DPSO, HSO, and fuzzy c-means thresholding) showing that these traditional segmentation algorithms slightly underestimate the real pore sizes, which lead to errors in quantitative analysis of the reconstructed 3D structures. To overcome this problem and correctly segment the SEM images, the machine learning (ML) segmentation algorithm (TWS) was trained using the derived criteria for the selection of the intensity threshold at the pore/polymer interface. Segmentation results of the TWS, Otsu, and fuzzy c-means algorithms were compared with a visually segmented image, showing clear supremacy of the ML algorithm in the segmentation procedure over the traditional global thresholding methods. Moreover, the calculated properties of the reconstructed 3D structure show a significant discrepancy between TWS-segmented (porosity 45.9%, average pore size 58.6 ± 6.7 nm) and Otsu-segmented (porosity 32.6%, average pore size 49.3 ± 2.5 nm) data. This emphasizes the importance of the segmentation procedure in the quantification of 3D structures. Therefore, segmentation algorithms have to be carefully chosen with deeper insight into the SEM image formation. Further improvements require the reduction of shine-through effects by reducing the primary electron energy without loss of resolution and maintaining signal-to-noise levels. Another approach is energy-filtered electron detection because high-energy backscattered electrons are mainly emitted from the surface of the imaged structure.

6. Summary

Material contrast in electron microscopy images enables the distinction of different materials within a single image with high spatial resolution. The measured image intensity is, however, determined by a complex interplay of imaging and material parameters. Therefore, extracting quantitative information on, e.g., the composition of the imaged materials is not straightforward and relies on the comparison of experimental and simulated image intensities. Simulations are often performed by Monte Carlo (MC) simulations under conditions, where Bragg contrast is negligible, and provide valuable insight into the measured intensities. High-angle annular dark-field scanning transmission electron microscopy (HAADF-STEM) and backscattered-electron scanning electron microscopy (BSE-SEM) imaging, performed in scanning electron microscopes at energies of 30 keV and below, are recognised to reveal strong material contrast. Therefore, this thesis is focused on the development of quantification methods of material contrast in HAADF-STEM and BSE-SEM imaging under various experimental conditions.

Quantification of the measured intensities requires MC simulations that reliably represent the measured data. Therefore, MC simulations must be first demonstrated to accurately describe the experimental data on samples with well-known material properties (atomic number, atomic mass and material density) and sample thickness. Wedge-shaped specimens prepared by focused-ion-beam (FIB) milling from a range of (known) materials were used in this work as test samples because they meet all the requirements. The use of the parameter specimen thickness is uncommon in BSE-SEM imaging, but it provides additional information that can be exploited to improve the understanding of BSE-SEM intensities. It is also essential to consider the detector properties in the MC simulations to achieve agreement with the measurements. The MC simulations in this work (and in many other studies) were performed by using screened Rutherford differential scattering cross-sections (DSCSs), where the choice of the screening parameter in the DSCSs significantly influences the calculated result. Based on the comparison of MC-simulated and experimental data from known test samples, the proper screening parameter is selected. Realistic MC simulations are a valuable addition to the measurements and can be utilized to optimize the imaging parameters, explain the origin of an unexpected contrast or is used for the determination of material parameters of the studied material based on the image intensity. Therefore this thesis is particularly concerned with the verification of MC simulations to realistically describe experimental image intensities.

In Chapter 3, a method for the quantitative analysis of low-keV HAADF-STEM intensities at electron energies between 10 and 30 keV is presented that relies on the comparison of measured and MC-simulated data. It focuses on the importance of the screening parameter in screened Rutherford DSCSs and its suitability for MC simulations. Several screening parameters from the literature were implemented into the NISTMonte simulation package [Ric2005] and the MC-simulated HAADF-STEM intensities were compared with experimental data obtained from test specimens with well-known properties. For this purpose, a set of wedge-shaped test samples was

prepared with known thickness profiles and compositions that cover a wide range of atomic numbers Z from polymers to tungsten. From the experimental images, the HAADF-STEM intensity as a function of the specimen thickness $I_{\mathrm{HAADF}}(t)$ was extracted and normalized to the intensity of the incident electron beam. The comparison of measured and MC-simulated $I_{\mathrm{HAADF}}(t)$ curves for all nine investigated materials (cf. Figures 3.9-3.17) demonstrate that none of the tested screening parameters is suited to consistently describe the measured data. A new procedure was developed to overcome this problem. The screening parameter in the screened Rutherford DSCS is a function of a screening radius R according to Eq.3.2. The screening radius was treated as a fit parameter in the MC simulations. For each studied single-element material (C, Si, Ge, Pd, W), the value of the screening parameter was determined from the best fit between the measured and simulated HAADF-STEM intensities (Figure 3.18). Fitting the adjusted screening radii by a power-law function (Figure 3.19) yields a new expression for the screening radius $R = 1.28a_0Z^{-0.44}$. This new expression was validated by comparing the measured and MC simulated data for compounds (PTB7, ZnO, MgO, $SrTiO_3$). The use of the new expression for the screening radius in the Bishop screening parameter yields good agreement with the measured data (Figure 3.20), demonstrating the validity of the new screening radii. Additionally, the Z dependence of the I_{HAADF} in the low-energy HAADF STEM regime was estimated by integrating the DSCS over the detection range of the HAADF-STEM detector segment (65-272 mrad). For the newly derived screening parameter, the Z dependence was found to be proportional to $Z^{1.58}$ and only weakly dependent on the detection-angle range. The $Z^{1.58}$ dependence is only slightly smaller compared to the $Z^{1.64}$ dependence derived by Krivanek *et al.* [Kri2012] by analysing a monolayer of BN with 60 keV electrons, where the contrast is governed purely by Z. The new expression for the screening radius was derived based on experimental data obtained with the Thermo Fisher Helios G4 FX microscope. The comparison of MC-simulated and measured data performed with another microscope (FEI DualBeam Strata 400S) with a larger HAADF-STEM detection-angle range (58-610 mrad) using the newly derived screening radius in the Bishop screening parameter shows also good agreement but some discrepancies between experiments and simulations were observed, especially for low-Z materials. To eliminate the discrepancies, the screening radius should be again readjusted to the detection-angle range of the FEI DualBeam Strata 400S microscope. Therefore, we do not claim that the new screening radius is valid for all experimental setups, but rather recommend the introduced procedure to determine screening radii for other microscopes with different experimental setups.

Chapter 4 presents a new method for the quantitative analysis of the BSE contrast in SEM. Based on the comparison with MC simulations, the measured BSE intensity is related to the material parameters (average atomic number, material density) of the studied materials. To enable comparison of the measured and simulated data, simulations and experimental data must be normalized. Contrary to HAADF-STEM, normalization with the intensity of the primary electron beam by direct illumination of the detector is not possible in the BSE-SEM configuration. To overcome this problem, we propose the normalization of the BSE intensity by using the Si-bulk BSE intensity, because silicon serves as a substrate for many thin-film samples. Alternatively, a

separate Si wafer can be utilized for data normalization. In addition, the detector properties must be accurately known and taken into account in the MC simulations. The threshold energy of the circular backscattered-electron semiconductor detector (CBS) was measured to be $500\,\mathrm{eV}$ and the detection-angle range was determined as a function of the working distance between the sample and the detector. Furthermore, it was shown (Figure 5.7) that the choice of the screening parameter in screened Rutherford DSCSs influences the MC-simulated BSE intensity. The proposed quantitative BSE analysis was tested on two challenging material systems. The first test sample was a Si/ZnO/Zn(O_xS_{1-x})/ZnS-multilayer system with only slightly different O and S concentrations and layer thicknesses of only 100 nm, which probes the sensitivity of the BSE analysis. BSE-SEM measurements were performed on a wedge-shaped electron-transparent specimen prepared by FIB milling because it introduces sample thickness as an additional parameter. Distinguishing the individual layers within the Si/ZnO/Zn(O_xS_{1-x})/ZnS-multilayer system is possible at small sample thicknesses for 15 keV and above, where the beam broadening does not exceed the particular layer thickness. The comparison of the normalized intensities of the materials in the Si/ZnO/Zn(O_xS_{1-x})/ZnS-multilayer system with MC simulations (Figure 5.12) reveals that MC simulations with the Bishop screening parameter represent the measured BSE intensities well. The quantitative BSE analysis of the Si/ZnO/Zn(O_xS_{1-x})/ZnS sample revealed that materials as similar as Zn($O_{0.5}S_{0.5}$) and Zn($O_{0.7}S_{0.3}$) can be distinguished in a BSE image, as suggested by the MC simulations. However, the Zn($O_{0.5}S_{0.5}$) and Zn($O_{0.4}S_{0.6}$) layers could not be distinguished because the chemical compositions and scattering properties are too similar. The second test sample was a PTB7/$PC_{71}BM$-multilayer system as a representative for weakly scattering materials. Before BSE measurements, MC simulations were performed to optimize the imaging parameters to achieve the best possible contrast between the PTB7 and $PC_{71}BM$ layers. According to the MC simulations, quantitative BSE analyses of the PTB7/$PC_{71}BM$-multilayer system under bulk conditions should be performed at low electron energies $E_0 < 5\,\mathrm{keV}$, where the interaction volume is smaller than layer thicknesses. At higher electron energies, the interaction volume increases and information from neighbouring layers in the PTB7/$PC_{71}BM$-multilayer system significantly contributes to the measured PTB7 (or $PC_{71}BM$) BSE intensity and complicates quantification. The measured normalized BSE intensity as a function of the specimen thickness at 2, 3, 5, 10 and 15 keV enables the comparison with MC simulations. The comparison reveals that the measured $PC_{71}BM$ intensities can be reliably simulated by using the NIST screening parameter in the screened Rutherford DSCS. Even at low electron energies (where the contribution of the neighbouring layers to the measured intensity is minimized), significant discrepancies between the measured and MC-simulated data was observed for the PTB7 layers. Possible origins of the discrepancy (Ga^+ implantation, surface contamination, presence of additional PEDOT:PSS layers in the structure) were discussed. However, the most probable origin of the discrepancy is the deviation of the nominal and real chemical composition of PTB7, which may have been modified by electron-beam induced damage.

The methodological developments show that quantitative analysis of the HAADF-STEM and BSE-SEM intensities are feasible. MC simulations are a valuable addition to the experimental images, which enable a deeper understanding of image formation as a function of imaging and material parameters. Furthermore, they can be used to optimize the imaging parameters (electron energy, detection-angle range) in advance to avoid tedious experimental trial and error optimization. The use of the screened Rutherford DSCS in the MC simulations enables the calibration of the MC-simulation software by the adaption of the screening parameter, as shown in Chapter 3, to precisely simulate the measured intensities. Under optimal imaging conditions pre-determined by MC simulations HAADF STEM as well as BSE SEM techniques are capable of distinguishing materials with small composition differences. In general, quantification of the measured image intensities is a valuable source of additional information and is an integral part of modern electron microscopy.

Chapter 5 is concerned with the analysis of nanoporous polymer (PETA) structures. The goals of this study were the three-dimensional (3D) reconstruction of the porous material and the quantitative measurement of the pore sizes of the fabricated porous PETA structures. This task was addressed by FIB/SEM tomography, which is capable of analyzing comparatively large volumes (10x10x10 μm^3) with SEM resolution. In the FIB/SEM tomography, FIB milling of thin material slices is alternated with BSE imaging resulting in a BSE-image data stack. The images in the data stack are segmented into pore and polymer phases and reconstructed to reveal the 3D structure. The main challenge is to find optimal contrast for the pore and polymer phase to facilitate reliable segmentation of the BSE images. Moreover, the shine-though effect (i.e. unwanted signal from regions within a slice) must be considered in the BSE-image segmentation of porous materials. To address these challenges MC simulations and a machine learning (ML) segmentation algorithm were employed. The porous polymer PETA structures were infiltrated with Epon, a weakly scattering epoxy material, and stained with OsO_4 to enhance the contrast in SEM images. For reliable segmentation of the SEM images, the precise location of the pore/PETA interface is essential. To understand the SEM-image contrast at the pore/PETA interface, MC simulations were performed using models of infiltrated spherical full- and half-pores. As a result, criteria for selecting the intensity threshold at the pore/polymer interface were derived (Figure 4.12 and 4.13). A simulated SEM image was then subjected to several different segmentation algorithms (Otsu, DPSO, HSO, and fuzzy c-means thresholding) showing that these traditional segmentation algorithms underestimate the real pore sizes, which lead to errors in the quantitative analysis of reconstructed 3D structures and pore-size distributions. To overcome this problem and to correctly segment the SEM images, an ML segmentation algorithm (TWS) was trained by applying the criteria for the selection of the intensity threshold at the pore/polymer interface derived from MC simulations. Segmentation results of the TWS, Otsu, and fuzzy c-means algorithms were compared with a visually segmented image and show clear supremacy of the ML algorithm in the segmentation procedure. Moreover, the calculated properties of the reconstructed 3D structure show a significant discrepancy between TWS-segmented and Otsu-segmented data. This emphasizes the importance of the segmentation procedure in the

quantification of 3D structures. Therefore, segmentation algorithms have to be carefully chosen based on a deeper insight into the SEM-image formation. Further improvements require the reduction of shine-through effects by reducing the primary electron energy without loss of resolution and maintaining high signal-to-noise levels. Another approach is energy-filtered electron detection because high-energy backscattered electrons are mainly emitted from the surface of the imaged structure.

Bibliography

[Aga2020] S. Agarwal, S. Verma, and D.P. Agarwal: Machine Intelligence and Signal Processing. *Springer Nature Singapore Pte Ltd.* (2020). ISBN 978-981-15-1365-7.

[And2018] M. Andrew, A quantified study of segmentation techniques on synthetic geological XRM and FIB-SEM images, *Computat. Geosci.* 22 (2018) 1503-1512.

[Aoy2015] T. Aoyama, M. Nagoshi and K. Sato: Quantitative analysis of angle-selective backscattering electron image of iron oxide and steel. Microscopy 64 (2015) p. 319-325.

[Ara2017] N. Arazm, A. Sahab and M. F. Kazemi, "Noise reduction of SEM images using adaptive Wiener filter," *2017 IEEE International Conference on Cybernetics and Computational Intelligence (CyberneticsCom)*, Phuket, 2017, pp. 50-55

[Arg2017] I. Arganda-Carreras, V. Kaynig, C. Rueden, K.W. Eliceiri, J. Schindelin, A. Cardona, and H.S. Seumg, Trainable Weka Segmentation: a machine learning tool for microscopy pixel classification, *Bioinformatics* 33 (2017) 2424-2426.

[Aro2007] M.A. Aronova, Y.C. Kim, G. Zhang, and R.D. Leapman: Quantification and thickness correction of EFTEM phosphorous maps. Ultramicroscopy 107 (2007) p. 232-244.

[Ass2018] A.M.D. Assa'd: Monte Carlo calculation of the backscattered coefficient of thin films of low on high atomic number materials and the reverse as a function of the incident electron energy and film thickness. Appl. Phys. A 124 (2018) p.699-675.

[Ass2019] A.M.D. Assa'd: Monte Carlo computation of the influence of carbon contamination layer on the energy distribution of backscattered electrons emerging from Al and Au. J. J. Phys. 12 (2019) p. 37-44.

[Bal2013] J. Balach, F. Soldera, D.E. Acevedo, F. Mücklich, and C.A. Barbero, A Direct and QuantitativeThree-Dimunsional Reconstruction of the Internal Structure of Disordered Mesoporous Carbon with Tailored Pore Size. *Microsc. Microanal.* 19 (2013) p. 745-750.

[Bal2016] M. S. Balogun, Y. Luo, W. Qiu, P. Liu, and Y. Tong: A review of carbon materials and theri composites with allsy metals for sodium ion battery anodes. *Carbon* 98 (2016) p 162-178.

[Bas2011] N.D. Bassim, B.T. de Gregorio, A.L.D. Kilcoyne, K. Scott, T. Chou, S. Wirick, G. Cody, and R.M. Stroud, Minimizing damage during FIB sample preparation of soft materials, J. Microsc. 245 (2011) 288-301.

[Bel2014] D.C. Bell, M. Mankin, R.W. Day, and N. Erdman: Successful application of low voltage electron microscopy to practical materials problems. Ultramicroscopy 145 (2014) p. 56-65.

[Bet1930] H. Bethe: Zur Theorie des Durchgangs schneller Korpuskularstrahlen durch Materie. Annalen der Physik 397 (1930) p. 325-400.

[Bez1981] J. C. Bezdec, Pattern Recognition with Fuzzy Objective Function Algorithms, *Plenum Press*, New York (1981).

[Boh1948] N. Bohr, The Penetration of Atomic Particles Through Matter, Mat. Fys. Medd. Dan. Vid. Selsk (1948), p. 19-34.

[Bor2017] A. Borenstein, O. Hanna, R. Attias, S. Luski, T. Brousse, and D. Aurbach: Carbon-based composite materials for super-capacitor electrodes: a review. *J. Matter. Chem. A* 5 (2017) pp. 12653-12672.

[Bra1999] R. Bracewell, The Fourier Transform and Its Applications, McGraw-Hill Book Company (1999) p. 6-24.

[Bro1994] R. Browning, T.Z. Li, B. Chui, J. Ye, R.F.W. Pease, Z. Czyżewski, D.C. Joy, Empirical forms for the electron/atom elastic scattering cross sections from 0.1 to 30 keV, J. Appl. Phys. 76 (1994) 2016–2022.

[Caz2012] J. Cazaux: Electron back-scattering coefficient below 5keV: Analytical expression and surface-barrier effects. J. Appl. Phys 113 (2012) 084905.

[Chu2016] S. Chuahan, W. Rühaak, F. Khan, F. Enzmann, P. Mielke, M. Kersten, and I. Sass. Processing of rock core microtomography images: Using seven different machine learning algorithms, *Comput. Geosci.* 86 (2016) 120-128.

[Cid2018] A. Garitagoitia Cid, R. Rosenkranz, M. Löffler, A. Clausner, Y. Standke and E. Zschech. Quantitative analysis of backscattered electron (BSE) contrast using low voltage scanning electron microscopy (LVSEM) and its application to $Al_{0.22}Ga_{0.78}N$/GaN layers. Ultramicroscopy 195 (2018) p. 47-52.

[Coo2016] S.J. Cooper, A. Bertei, P.R. Shearing, J.A. Kilner, and N.P. Brandon, TauFactor: An open-source application for calculating tortuosity factors from tomographic data, *SoftwareX* 5 (2016) 203-210.

[Cox1967] H.L. Cox and R.A. Bonham, Elastic electron scattering amplitudes for neutral atoms calculated using the partial wave method at 10, 40, 70 and 100 kV for Z=1 to Z=54. J. Chem. Phys. 47 (1967) 2599.

[Cro2008] F. Croccolo and C. Riccardi: Passive mirror imaging through a solid-state back-scattered electron detector. Microscopy Today 16 (2008) p. 40-43.

[Czy1990] Z. Czyżewski, D.O.N. MacCallum, A. Romig, D.C. Joy, Calculations of Mott scattering cross section, J. Appl. Phys. 68 (1990) 3066–3072.

[Čal2019] M. Čalkovský, E. Müller, M. Hugenschmidt and D. Gerthsen: Differential electron scattering cross-sections at low electron energies: The influence of screening parameter. Ultramicroscopy 207 (2019) 112843

[Čal2021] M. Čalkovský, E. Müller, M. Meffert, N. Firman, F. Mayer, M. Wegener and D. Gerthsen: Comparison of segmentation algorithms for FIB-SEM

tomography of porous polymers: Importance of image contrast for machine learning segmentation. Mater. Charact. 171 (2021) 110806.

[Dap2013] M. Dapor, N. Bazzanella, L. Toniutti, A. Miotello, M. Crivellari and S. Gialanella: Backscattered electrons from gold surface films deposited on silicon substrates: a joint experimental and computational investigation to add new potentiality to electron microscopy. Surf. Interface Anal. 45 (2013) p. 677-681.

[Del2013] A.T. DeLaRiva, T.W. Hansen, S.R. Challa, A.K. Datye: *In situ* Transmission electron microscopy of catalyst sintering. *J. Catal.* 308 (2013) p. 291-305.

[Dil1974] D. Dill and J.L. Dehmer, Electron-molecule scattering and molecular photoionization using the multiple-scattering method, J. Chem. Phys. 61 (1974) p.692-699.

[Dre2017] H. Drees, E. Müller, M. Dries and D. Gerthsen, Electron-beam broadening in amorphous carbon films in low-energy scanning transmission electron microscopy, Ultramicroscopy 185 (2017) p.65-71.

[Dru2014] L.F. Drummy: Electron microscopy of organic-inorganic interfaces: Advantages of low voltage. Ultramicroscopy 145 (2014) p. 74-79.

[Dyc2015] O. Dyck, S. Hu, S. Das, J. Keum, K. Xiao, B. Khomami and G. Duscher: Quantitative phase fraction detection in organic photovoltaic materials through EELS imaging. Polymers 7 (2015) p. 2446-2460.

[Ege2004] R.F. Egerton, P. Li, and M. Malac: Radiation damage in the TEM and SEM. Micron 35 (2004) p. 399-409.

[Ege2012] R.F. Egerton: Mechanisms of radiation damage in beam-sensitive specimens, for TEM accelerating voltages between 10 and 300 kV. Microsc. Res. Tech. 75 (2012) p. 1550-1556.

[Ege2019] R.F. Egerton: Radiation damage to organic and inorganic specimens in the TEM. Micron 119 (2019) p. 72-87.

[End2011] M. Ender, J. Joos, T. Carraro and E. Ivers-Tiffee: Three dimensional reconstruction of a composite cathode for lithium-ion cell. *Electrochem Comm* 13 (2011) p. 166-168.

[End2012] M. Ender, J. Joos, T. Carraro, and E. Ivers-Tiffée, Quantitative Characterization of $LiFePO_4$ Cathodes Reconstructed by FIB/SEM Tomography, *J. Electrochem. Soc.* 159 (2012) A972-A980.

[Esw2014] S.K. Eswara-Moorthy, P. Balasubramanian, W. van Mierlo, J. Bernhard, M. Marinaro, M. Wohlfahrt-Mehrens, L. Jörissen and U. Kaiser: An *In Situ* SEM-FIB-Based Method for Contrast Enhancement and Tomographic Reconstruction for Structural Quantification of Porous Carbon Electrodes. *Microsc. Microanal.* 20, (2014) p. 1576-1580.

[Eve1955] E. Everhart, G. Stone and R.J. Carbone, Classical Calculation of Differential Cross Section for Scattering from a Coulomb Potential with Exponential Screening, Phys. Rev. 99 (1955) p. 1287-1290.

[Eve1960] T.E. Everhart and R.F.M. Thornley: Wideband detector for micro-microampere low-energy electron currents. J. Sci. Instr. 37 (1960) p. 246-249.

[Fag2020] C. Fager, M. Röding, A. Olsson, N. Loren, Ch. Corswant, A. Särkkä, and E. Olsson, Optimization of FIB-SEM Tomography and Reconstruction for Soft, Porous, and Poorly Conducting Materials. *Microsc. Microanal.* 26 (2020) p. 837-845.

[Fan2019] H. Fang, S. Sang, S. Liu, and Y. Du: Methodology of three-dimensional visualisation and quantitative characterization of nanopores in coal by using FIB-SEM and its application with anthracite in Qinshui basin. *J. Petrol. Sci. Eng.* 182 (2019) 106285.

[Fen2020] Ch. Fend, A- Moghiseh, C. Redenbach, and K. Schladitz, Reconstruction of highly porous structures from FIB-SEEM using a deep neural network trained on synthetic images. (2020) Journal of Microscopy. doi:10.1111/jmi.12944

[Fit1985] H.-J. Fitting, J. Reinhardt, Monte-Carlo simulation of keV-electron scattering in solid targets, phys. stat. sol. (a) 88 (1985) 245–259.

[Ful2008] B. Fultz and J.M. Howe, Transmission Electron Microscopy and Diffractometry of Materials. Springer Berlin (2008) p. 163-221.

[Gau2016] R. Gauvin and S. Rudinsky, A universal equation for computing the beam broadening of incident electrons in thin films, Ultramicroscopy 167 (2016) p.21-30.

[Gen1976] P. Gentsch, H. Gilde, and L. Reimer: Measurement of the top bottom effect in scanning transmission electron microscopy of thick amorphous specimens. *J. Microsc.* 100 (1976) p. 81-92.

[Gha2012] P. Ghamisi, M.S. Couceiro, J.S. Benediktsson and N.M. Ferreira: An efficient method for segmentation of images based on fractional calculus and natural selection. *Expert Syst Appl*, 39(16) (2012), pp. 12407-12417

[Gho2015] S. Ghosh, H. Ohashi, H. Tabata, Y. Hashimasa, T. Yamaguchi: Microstructural pore analysis of the catalyst layer in a polymer electrolyte membrane fuel cell: A combination of resin pore-filling and FIB/SEM. *Int. J. Hydrog. Energy* 40 (2015) p. 15663-15671.

[Gia1999] L.A. Giannuzzi and F.A. Stevie: A review of focused ion beam milling techniques for TEM specimen preparation. Micron 30 (1999) p. 197-204.

[Gia2004] L.A. Giannuzzi: Introduction to Focused Ion Beams: Instrumentation, Theory, Techniques and Practice. Heidelberg, Germany: Springer Sciences & Business media (2004).

[Giu2020] W. Giurlani, E. Berretti, M. Innocenti and A. Lavacchi: Measuring the thickness of metal films: A selection guide to the most suitable techniques. Matter. Proc. 2 (2020) p. 1-30.

[Gol1977] J.I. Goldstein, J.L. Costley, G.W. Lorimer and S.J.B. Reed, Quantitative X-ray analysis in the electron microscope, Scan. Electron Microsc. 1 (1977) p.315-324.

[Gol1992] J. Goldstein, D. Newbury, P. Echlin, D. Joy, A. Romig, C. Lyman, C. Fiori and E. Lifshin: Scanning electron microscopy and X-ray Microanalysis: A Text for Biologists, Materials scientists and Geologists. (1992) p. 69-147 New York: Plenum Press.

[Gou1940] S. Goudsmit and J.L. Saunderson, Multiple scattering of electrons, Phys. Rev. 57 (1940) p.24-29.

[Gua2020] K. Guanira, T.M. Valente, C.A. Rios, O.M. Castellanos, L. Salazar, D. Lattanzi and P. Jaime: Methodological approach for mineralogical characterization of tailings from a Cu(Au,Ag) skarn type deposit using QEMSCAN (quantitative evaluation of minerals by scanning electron microscopy). J. Geochem. Explor. 209 (2020) 106439.

[Hag2018] K. Hagita, T. Higuchi, and H. Jinnai, Super-resolution for asymmetric resolution of FIB-SEM 3D imaging using AI with deep learning, *Sci. Rep.* 8 (2018) 1-8.

[Hai1996] J. Haimovich, K. Leibold and G. Staudt: Estimating and measuring thickness of thin layers by Monte Carlo simulation and backscattered electorn image analysis. J. Technol. 5 (1996) p. 65-78.

[Ham2018] Ul-Hamid, A. (2018). *A Beginners' Guide to Scanning Electron Microscopy* (1st ed. 2018.). Cham: Springer International Publishing.

[Han2014] M. Hannachi, Z. Rouabah, C. Champion and N. Bouarissa: Electron backscattering from solid targets: Elastic scattering calculations. J. Electron Spectrosc. Relat. Phenom. 195 (2014) p. 155-159.

[Har1996] P. Hartel, H. Rose and C. Dinges, Conditions and reasons for incoherent imaging in STEM, *Ultramicroscopy* 63 (1996) 93-114.

[Har2013] T. Hara, K. Tsuchiya, K. Tsuzaki, X. Man, T. Asahata, and A. Uemoto: Application of orthogonally arranged FIB-SEM for precise microstructure analysis of materials. *J. Alloy. Compd.* 577 (2013) p. 717-721.

[Hay2011] M.W. Haynes: CRC Handbook of Chemistry and Physics. (2011) 92nd ed. CRC Press.

[Hee2014] A.J. Heeger: 25th anniversary article: bulk heterojunction solar cells: understanding the mechanism of operation. Adv. Mater. 26 (2014) p. 10-28.

[Hei2018] A. Heiss, D. Park and A.Ch. Joel: The Calamistrum of the Feather-Legged Spider Uloborus plumipes Investigated by Focus Ion Beam and Scanning

Electron Microscopy (FIB-SEM) Tomography. *Microsc. Microanal.* 24 (2018) pp. 139-146.

[Hil1995] S. Hillyard, J. Silcox, Detector geometry, thermal diffuse scattering and strain effects in ADF STEM imaging, Ultramicroscopy 58 (1995) 6–17.

[Hoe2019] J.E.S Van der Hoeven, *et al.*: Bridging the gap: 3D real-space characretization of colloidal assemblies *via* FIB-SEM tomography. *Nanoscale* 11 (2019) pp. 5304-5316.

[Hol2004] L. Holzer, F. Indutnyi, P.H. Gasser, B. Münch, and W. Wegmann: Three-dimensional analysis of porous $BaTiO_3$ ceramics using FIB nanotomography. *J. Microsc.* 216 (2004), pp. 84-95.

[Hol2018] J. Holm, Scattering intensity distribution dependence on collection angles in annular dark-field STEM-in-SEM images, Ultramicroscopy 195 (2018) p. 12-20.

[Hug2019] M. Hugenschmidt, E. Müller and D. Gerthsen, Electron beam broadening in electron-transparent samples at low electron energies, J. Microsc. 274 (2019) p.150-157.

[Huh2013] Y. Huh, K.J. Hong, and K.S. Shin: Amorphization induced by focused ion beam milling in metallic and electronic materials. Microsc. Microanal. 19 (2013) p. 33-37.

[Ism2001] A. F. Ismail and L.I.B. David: A review on the latest development of carbon membranes for gas separation. *J. Membr. Sci.* 193 (2001) pp. 1-18.

[Jab2004] A. Jablonski, F. Salvat, C.J. Powell, Comparison of electron elastic-scattering cross sections calculated from two commonly used atomic potentials, J. Phys. Chem. Ref. Data 33 (2004) 409–451.

[Jac1973] J.H. Jacob, Multiple Electron Scattering through a Slab, Phys. Rev. A 8 (1973) p.226-235.

[Jin2019] X. Jin, R. Popescu, A. Pasha, R. Schneider, D. Hariskos, W. Witte, M. Powalla and D. Gerthsen: Structural and microchemical characterization of $Cu(In,Ga)Se_2$ solar cells with solution-grown CdS, Zn(O,S), and $In_x(O,S)_y$ buffers. Thin Solid Films 671 (2019) p. 133-138.

[Jon2006] M.W. Jones, J.A. Baerentzen, and M. Sramer, 3D distance fields: a survey of techniques and application. *Vis. Comput. Graph. IEEE Trans.*, 12 (2006) p. 581-599.

[Jon2014] H.G. Jones, K.P. Mingard, and D.C. Cox: Investigation of slice thickness and shape milled by a focused ion beam for three-dimensional reconstruction of microstructures. *Ultramicroscopy* 139 (2014) p. 20-28.

[Joy1989] D.C. Joy and S. Luo, An empirical stopping power relationship for low-energy electrons, *Scanning* 11 (1989) 176–180.

[Joy1991] D.C. Joy: An introduction to Monte Carlo simulations. Scanning Microsc. 5 (1991) p.329-337.

[Joy1995] D. C. Joy, Monte Carlo Modeling for Electron Microscopy and Microanalysis, Oxford University Press Inc, New York (1995)

[Kai2011] U. Kaiser, J. Biskupek, J.C. Meyer, J. Leschner, L. Lechner, H. Rose, M. Stöger-Pollach, A.N. Khlobystov, P. Hartel, H. Müller, M. Haider, S. Eyhusen, G. Benner, Transmission electron microscopy at 20 kV for imaging and spectroscopy, Ultramicroscopy 111 (2011) 1239–1246.

[Kai2014] U. Kaiser and M. Stöger-Pollach: Foreword to the special issue low-voltage electron microscopy. Uötramicroscopy 145 (2014) p. 1-2.

[Kan1972] K. Kanaya and S. Okayama: *Penetration and energy-loss theory of electrons in solid targets.* J. Phys. D-Appl. Phys., 1972. **5**: p. 43-58.

[Kar2016] I. Karbovnyk, I. Olenych, O. Aksimentyeva, H. Klym, O. Dzendzelyuk, Y. Olenych and O. Hrushetska: Effect of radiation on the electrical properties of PEDOT-based nanocomposites. Nanoscale Res. Lett. 11 (2016) 84.

[Kaz2004] H. Kazumori, K. Honda, M. Matsuya, M. Date, and C. Nielsen. Field emission SEM with a spherical and chromatic aberration corrector. Microscopy and Microanalysis, 10, 1370{1371 (2004).

[Kel2013] R. Kelley, K. Song, B. Van Leer, D. Wall, and L. Kwakman: Xe^+ FIB milling and measurement of amorphous silicon damage. Microsc. Microanal. 19 (2013) p. 862-863.

[Ket2001] R.A. Ketcham and W.D. Carlson, Acquisition, optimization and interpretation of X-ray computed tomographic imagery: applications to the geosciences. *Comput. Geosci.* 27 (2001) p. 381-400.

[Kim2010] H. Kim, T. Negishi, M. Kudo, H. Takei and K. Yasuda: Quantitative backscattered electron imaging of field emission scanning electron microscopy for discrimination of nano-scale elements with nm-order spatial resolution. J. Electron Microsc. 59 (2010) p. 379-385.

[Kim2019] D. Kim, S. Lee, W. Hong, H. Lee, S. Jeon, S. Han and J. Nam: Image Segmentation for FIB-SEM Serial Sectioning of Si/C-Graphite Composite Anode Microstructure Based on Preprocessing and Global Thresholding. *Micros. Microanal.* 25 (2019) pp. 1139-1154.

[Kir1987] E.J. Kirkland, R.F. Loane, J. Silcox, Simulation of annular dark field stem images using a modified multislice method, Ultramicroscopy 23 (1987) 77–96.

[Kno1932] M. Knoll and E. Ruska: Beitrag zur geometrichen elektronenoptik. I. Annalen der Physik 12 (1932) p. 607-640.

[Koh2008] H. Kohl and L. Reimer, Transmission Electron Microscopy, vol. 36. Springer New York, New York (2008).

[Kow2017] T. Kowoll, E. Müller, S. Fritsch-Decker, S. Hettler, H. Störmer, C. Weiss and D. Gerthsen: Contrast of backscattered electron SEM images of

nanoparticles on substrates with complex structure. Scanning (2017) p. 1-12.

[Kri2012] O.L. Krivanek, M.F. Chisholm, V. Nicolosi, T.J. Pennycook, G.J. Corbin, N. Dellby, M.F. Murfitt, C.S. Own, Z.S. Szilagyi, M.P. Oxley, S.T. Pantelides, S.J. Pennycook, Atom-by-atom structural and chemical analysis by annular dark-field electron microscopy, Nature 464 (2010) 571–574.

[Küb2005] Ch. Kübel, A. Voigt, R. Schoenmakers, M. Otten, D. Su, T.Ch. Lee, A. Carlsson, and J. Bradley. Recent Advances in Electron Tomography: TEM and HAADF-STEM Tomography for Materials Science and Semiconductor Applications. *Microsc. Microanal.* 11 (2005) pp. 378-400.

[Kub2015] Y. Kubota: New developments in electron microscopy for serial image acquisition of neuronal profiles. *Microscopy* 63 (2015) p. 1-10.

[Kuh1999] J.Ch. Kuhr and H.J. Fitting: Monte-Carlo simulation of low energy electron scattering in solids. Phys. Stat. sol 172 (1999) p. 433-449.

[Kur2007] O. Kurniawan, V.K.S. Ong: *Investigation of range-energy relationships for low-energy electron beams in silicon and gallium nitride.* Scanning, 2007. **29**(6): p. 280-286.

[Kyr2013] I. Kyriakou, D. Emfietzoglou, A. Nojeh, M. Moscovitch, Monte Carlo study of electron-beam penetration and backscattering in multi-walled carbon nanotube materials: The effect of different scattering models, J. Appl. Phys. 113 (2013) 84303.

[Kys1976] D.F. Kyser and K. Murata, Application of Monte Carlo simulation to electron microprobe analysis of thin films on substrates, U.S. Dep. Of Commerce, Washington, DC (1976) p.129

[Lak1997] H. Lakner, C. Mendorf, B. Bollig, W. Prost and F.-J. Tegude, Determination of interface composition in III-V heterojunction devices (HBT and RTD) with atomic resolution using STEM techniques, *Mater. Sci. Eng.* B44 (1997) 52-56.

[Lea1984] R.D. Leapman, C.E. Fiori, and C.R. Swyt: Mass thickness determination by electron energy loss for quantitative X-ray microanalysis in biology. J. Microsc. 133 (1984) p. 239-253.

[Lei2017] Z.J.W.A. Leijten, A.D.A. Keizer, G. de With and H. Friedrich: Quantitative Analysis of Electron Beam Damage in Organic Thin Films. J. Phys. Chem. C 121 (2017) p. 10552-10561.

[Len1954] F. Lenz, Zur Streuung mittelschneller Elektronen in kleinste Winkel, Z. Naturforschg. 9a, (1954) 185.

[Len2011] A. Lenz, H. Kariis, A. Pohl, P. Persson and L. Ojamäe: The electronic structure and reflectivity of PEDOT:PSS from density functional theory. Chem. Phys. 384 (2011) p. 44-51.

[Lew1956] R. R. Lewis, Potential Scattering of High-Energy Electrons in Second Born Approximation, Phys. Rev. 102 (1956) p. 537-543.

[Li2020] Y. Li, E. Müller, Ch. Sprau, A. Colsmann and D. Gerthsen: Imaging of polymer:fullerene bulk-heterojunctions in a scanning electron microscope: methodology aspects and nanomorphology by correlative SEM and STEM. Adv. Struct. Chem. Imag. 6 (2020) p. 1-12.

[Li2021] Y. Li, M. Calkovsky, E. Müller, Ch. Sprau, A. Colsmann and D. Gerthsen: Highly selective Cu staining if sulphur-containing polymers facilitates 3D nanomorphology reconstruction of polymer:fullerene blends in organic solar cells by FIB-SEM tomography. ACS Appl. Mater. Interfaces 13 (2021) p. 53252-53261.

[Lia2012] B.Y. Liang, Z. Xu, J. Xia, S.T. Tsai, Y. Wu, G. Li, C. Ray and L. Yu: For the bright future – bulk heterojunction polymer solar cells with power conversion efficiency of 7.4%. Adv. Mater. 22 (2010) p. 135-138.

[Lid1998] D. R. Lide: CRC Handbook of Chemistry and Physics, 79th Edition, CRC Press, Boca Raton, FL, 1998

[Liu2001] Ch.-P. Liu, R.D. Twesten and J.M. Gibson, High-angle annular dark-field imaging of self-assembled Ge islands on Si(001), *Ultramicroscopy* 87 (2001) 79-88.

[Loe2017] T.H. Loeber, B. Laegel, S. Wolff, S. Schuff, F. Balle, T. Beck, D. Eitler, J.H. Fitschen, and G. Steidl: Reducing curtaining effects in FIB/SEM applications by a goniometer stage and an image processing method. *J. Van. Sci. Technol. B* 35 (2017) 06GK01.

[Mat2015] W.R. Mateker, T. Heumueller, R. Cheacharoen, I.T. Sachs-Quintana, M.D. McGehee, J. Warnan, P.M. Beaujuge, X. Liu and G.C. Bazan: Molecular packing and arrangement govern the photo-oxidative stability of organic photovoltaic materials. Chem. Mater. 27 (2015) p. 6345-6353.

[May2007] J. Mayer, L.A. Giannuzzi, T. Kamino, and J. Michael, TEM sample preparation and FIB-induced damage, MRS bulletin 32 (2007) p. 400-407.

[May2020] F. Mayer, D. Ryklin, I. Wacker R. Curticean, M. Čalkovský, A. Niemeyer, Z. Dong, P.A. Levkin, D. Gerthsen, R.R. Schröder, and M. Wegener. 3D Two –Photon Microprinting of Nanoporous Architectures. *Adv. Mater.* (2020).

[Maz2016] M. Mazhari and R.P.R. Hasanzadeh: Suppression of Noise in SEM Images Using Weighted Local Hysteresis Smoothing Filter. *Scanning* 38 (2016) p. 634-643.

[Mer2005] P.G. Merli and V. Morandi: Low-energy STEM of multilayers and dopant profiles. Microsc Microanal. 11 (2005) p. 97-104.

[Mic1987] J.R. Michael and D.B. Williams, A consistent definition of probe size and spatial resolution in the analytical electron microscope, J. Microsc. 147 (1987) p.289-303.

[Mic2003] M. Michaud, A. Wen and L. Sanche, Cross Sections for Low-Energy (1-100 eV) Electron Elastic and Inelastic Scattering in Amorphous Ice, Radiat. Res. 159 (2003) p. 3-22.

[Mol1947] G. Moliere, Theorie der Streuung schneller geladener Teilchen I. Einzelstreuung am abgeschirmten Coulomb-Feld, Z. Naturforsch. A 2 (1947) 133–145.

[Mor2007] V. Morandi and P.G. Merli: Contrast and resolution versus specimen thickness in low energy scanning transmission electron microscopy. J. Appl. Phys. 101 (2007) p. 1-8.

[Mot1987] N.F. Mott, H.S.W. Massey, The theory of atomic collisions, 3rd ed., Clarendon Press, Oxford, 1987.

[Mül2017] E. Müller and D. Gerthsen: Composition quantification of electron-transparent samples by backscattered electron imaging in scanning electron microscopy. Ultramicroscopy 173 (2017) p. 71-75.

[Mun2009] P.R. Munroe: The application of focused ion beam microscopy in the material sciences. *Mater. Character.* 60 (2009) p. 2-13.

[Mün2013] S. Münster and B. Fabry, A Simplified Implementation of the Bubble Analysis of Biopolymer Network Pores. *Biophys J.* 104 (2013) p. 2774-2775.

[Mur1971] K. Murata, T. Matsukawa, and R. Shimizu: Monte Carlo calculations on electron scattering in a solid target. Jpn. J. Appl. Phys. 10 (1971) p.678-686.

[Nan2013] L.K. Nanver, T.L.M. Scholtes, A. Šakíč, C.S. Kooijman and G.N.A. van Veen: Radiation detector. US patent 8,450,820 B2, issued May 28, 2013.

[Nan2019] N. Nan and J. Wang: FIB-SEM Three-Dimensional Tomography for Characterization of Carbon-Based Materials. *Adv. Mater. Sci. Eng.* (2019), Artice ID 8680715.

[Neg2005] C. Negreanu, X. Llovet, R. Chawla and F. Saůvat, Calculation of multiplescattering angular distribution of electrons and positron, Radiat. Phys. Chem. 74 (2005) p.264-281.

[Nig1959] B.P. Nigam, M.K. Sundaresan, and T.Y. Wu, Theory of Multiple scattering; Second Born Approximation and Corrections to Moliere's Work, Phys. Rev. 115 (1959) p. 491-502.

[Odr2017] A. Odriozola, J. Llodra, J. Radecke, C. Ruegsegger, S. Tschanz, S. Saxena: (2017). High contrast staining for serial block face scanning electron microscopy without uranyl acetate. *bioRxiv 207472*. doi: 10.1101/207472

[Oli2013] D. Oliva, E. Cuevas, G. Pajares, D. Zaldivar and M. Perez-Cisneros: Multilevel tresholding segmentation based on harmony search optimization. *J. Appl. Math* (2013), pp. 1-24.

[Oli2014] D. Oliva, E. Cuevas, G. Pajares, D. Zaldivar and V. Osuna: A Multilevel Tresholding algorithm using electromagnetism optimization. *Neurocomputing*, 139 (2014), pp. 357-381.

[Ots1978] N. Otsu, A Treshold Selection Method from Gray-Level Histograms, *IEEE Transactions on Systems, Man. and Cybernetics* 9 (1978) 62-66.

[Ozt2017] I. Oztel, G. Yolcu, I. Ersoy, T. White, and F. Bunyak, Mitochondria segmentation in electron microscopy volumes using deep convolutional neural network, *2017 IEEE International Conference on Bioinformatics and Biomedicine* (2017) 1195-1200.

[Pen1988] S. Pennycook and L. Boatner: Chemically sensitive structure-imaging with a scanning transmission electron microscope. Nature 336 (1988) p. 565-567.

[Pen2000] S.J. Pennycook, B. Rafferty and P.D. Nellist, Z-contrast Imaging in an Aberration-corrected Scanning Transmisison Electron Microscope, *Microsc. Microanal.* 6 (2000) 343-352.

[Pfa2011] M. Pfaff, E. Müller, M.F.G. Klein, A. Colsmann, U. Lemmer, V Krzyzanek, R. Reichelt, and D. Gerthsen, Low-energy electron scattering in carbon-based materials analyzed by scanning transmission electron microscopy and ist application to sample thickness determination, J. Mircosc. 243 (2011) p. 31-39.

[Pfa2012] M. Pfaff, M.F.G. Klein, E. Müller, P. Müller, A. Colsmann, U. Lemmer, and D. Gerthsen, Nanomorphology of P3HT:PCBM-based absorber layers of organic solar cells after different processing conditions analyzed by low-energy scanning transmission electron microscopy, Microsc. Microanal. 18 (2012) p. 1380-1388.

[Pri2013] T. Prill and K. Schladitz, Simulation of FIB-SEM Images for Analysis of Porous Microstructures, *Scanning* 35 (2013) 189-195.

[Rab2014] A. Rabbani, S. Jashidi, and S. Salehi, An automated simple algorithm for realistic pore network extraction from micro-tomography images. *J. Petrol. Sci. Eng.* 123 (2014) p. 164-171.

[Raj2002] S. Rajsiri, B.W. Kempshall, S.M. Schwarz, and L.A. Giannuzzi: FIB damage in silicon: Amorphization or redeposition. Microsc. Microanal. 8, (2002) S02.

[Rei1984] R. Reichelt and A. Engel: Monte Carlo calculations of elastic and inelastic electron scattering in biological and plastic materials. *Ultramicroscopy* 13 (1984) p. 279-294.

[Rei1998] L. Reimer, Scanning Electron Microscopy: Physics of Image Formation and Microanalysis, second ed., Springer, Berlin, London, 1998.

[Rey2001] S. Reyntjens and R. Puers: A review of focused ion beam applications in microsystem technology. J. Micromech. Microeng. 11 (2001) p. 287-300.

[Rhi2011] D. Rhinow, M. Büenfeld, N.E. Weber, A. Beyer, A. Gölzhäuser, W. Kühlbrandt, N. Hampp, and A. Turchanin: Energy-filtered transmission electron microscopy of biological samples on highly transparent carbon nanomembranes. Ultramicroscopy 111 (2011) p. 342-349.

[Rit2005] N.W.M. Ritchie, A new Monte Carlo application for complex sample geometries, Surf. Interface Anal. 37 (2005) p. 1006-1011.

[Röd2020] M. Röding, C. Fager, A. Olsson, C.V. Corswant, E. Olsson and N. Loren, Three-dimensional reconstruction of porous polymer films from FIB-SEM nanotomography data using random forests. Journal of Microscopy. (2020) Accepted Author Manuscript. doi:10.1111/jmi.12950

[Roe2016] J.D. Roehling, D. Baran, J. Sit, T. Kassar, T. Ameri, T. Unruh, Ch. J. Brabec and A.J. Moule: Nanoscale Morphology of PTB7 Based Organic Photovoltaics as a Function of Fullerene Size. Sci. Rep. 6 (2016) 30915.

[Ros1995] P. Roschger, H. Plenk Jr., K. Klaushofer and J. Exchberger: A new scanning electron microscopy approach to the quantification of bone mineral distribution: Backscattered electron image grey-levels correlated to Calcium Kα-line intensities. Scanning Microsc. 9 (1995) p. 75-88.

[Rus1984] J.C. Russ: Fundamentals of energy dispersive X-ray analysis. (1984) Butterworth-Heinemann ISBN 978-0-408-11031-0.

[Rut1911] E. Rutherford, The scattering of α and β particles by matter and the structure of the atom, Phylos. Mag. 6 (1911) p. 669-688.

[Sal2014] M. Salzer, S. Thiele, R. Zengerle and V. Schmidt: On the importance of FIB-SEM specific segmentation algorithms for porous media. *Mater. Charact.* 95 (2014) pp. 36-43.

[San2012] E. Sánchez, M. Torres Deluigi and G. Castellano: Mean atomic number quantitative assessment in backscattered electron imaging. Microsc. Microanal. 18 (2012) p. 1355-1361.

[Sar2014] S. Sarkar, S. Paul, R. Burman, S. Das, S.S. Chaudhuri, A Fuzzy Entropy Based Multi-Level Image Thresholding Using Differential Evolution, *International Conference on Swarm, Evolutionary, and Memetic Computing* 8947 (2014) 386-395. https://doi.org/10.1007/978-3-319-20294-5_34.

[Sas2014] T. Sasaki, H. Sawada, F. Hosokawa, Y. Sato, and K. Suenaga: Aberration-corrected STEM/TEM imaging at 15 keV. Ultramicroscopy 145 (2014) p. 50-55.

[Sat2015] K. Sato, H. Sueyoshi and K. Yamada: Characterization of complex phase steel using backscattering electron images with controlled collection angles. Microscopy 64 (2015) p. 297-304.

[Sch1992] P. Schauer, R. Autrata: Light transport in a single-crystal scintillation detectors in SEM. Scanning 14 (1992) p. 325-330.

[Sch2018] S.A. Schweizer, C. Hoeschen, S. Schlüter, I. Kögel-Knabner, and C.W. Mueller, Rapid soil formation after glacial retreat shaped by spatial patterns of organic matter accrual in microaggregates, *Glob. Change Biol.* 24 (2018) 1637-1650.

[Sel1991] S.M. Seltzer, Electron-Photon Monte Carlo Calculations: The ETRAN Code, Appl. Radiat. Isot. 42 (1991) 917-941

[She2010] P.R. Shearing, D.J.L. Brett, and N.P. Brandon: Towards intelligent engineering of SOFC electrodes: a review of advanced microstructural characterisation techniques. *Int. Mater. Rev.* 55 (2010) pp. 347-363.

[Shi1992] R. Shimizu and D. Ze-Jun, Monte Carlo modelling of electron-solid interactions. Reports on Progress in Physics, 55 (4), 487 (1992).

[Shi2002] D. Shindo and T. Oikawa: Energy dispersive X-ray spectroscopy. (2002) Analytical electron microscopy for materials science, Springer, Tokyo. ISBN 978-4-431-66988-3.

[Sin2020] A. Sinigalia, Scattering of low-energy electrons in scanning transmission electron microscopy (2020). Bachelor thesis, Karlsruhe Institute of Technology, Karlsruhe, Germany.

[Sun2016] T. Sunaoshi, K. Kaji, Y. Orai, C.T. Schamp, and E. Voelkl: STEM/SEM, chemical analysis, atomic resolution and surface imaging at ≤ 30 kV with no aberration correction for nanomaterials on graphene support. Microsc. Microanal. 22 Suppl 3 (2016) p. 604-605.

[Sun2018] Ch. Sun, E. Müller, M. Meffert, and D. Gerthsen: On the progress of scanning transmission electron microscopy (STEM) imaging in a scanning electron microscope. Microsc. Microanal. 24 (2018) p. 99-106.

[Tak2004] M. Takeguchi, M.R. McCartney and D.J. Smith, Mapping In concentration, strain, and internal electric field in InGaN/GaN quantum well structure, *Appl. Phys. Lett.* 84 (2004) 2103-2105.

[Tas2008] T. Tasdizen, E. Jurrus, and R.T. Whitaker: Non-uniform illumination correction in transmission electron microscopy. *MICCAI Workshop on Microscopy Image Analysis with Applications in Biology,* New York, (September 2008).

[Tia2018] J. Tian, J. Wu, and Y.L. Chiu: Monte carlo simulation and theoretical calculation of SEM image intensity and its application in thickness measurement. Ultramicroscopy 187 (2018) p. 19-19.

[Tra2019] J. Tracey, S. Lin, J. Jankovic, A. Zhu, and S. Zhang, Iterative Machine Learning Method for Pore-Back Artifact Mitigation in High Porosity Membrane FIB-SEM Image Segmentation, *Microsc. Microanal.* 25 (2019) 186-187.

[Tsc2005] D. Tschumperle and R. Deriche, Vector-valued image regularization with PDEs: a common framework for different applications, *IEEE Transactions on Pattern Analysis and Machine Intelligence* 27 (2005) 506-517.

[Utk2012] I. Utke, S. Moshkalev and P. Russell: Nanofabrication using focused ion and electron beams: Principles and applications. (2012) Oxford university Press p. 410-435.

[Ver2004] J. Verbeeck, D. Van Dyck, and G. Van Tendeloo: Energy-filtered transmission electron microscopy: an overview. Spectrochimica Acta Part B 59 (2004) p. 1529-1534.

[Ver2020] O.P. Verma, S. Roy, S.Ch. Pandey, and M. Mittal: Advancement of Machine Intelligence in Interactive Medical Image Analysis, *Springer Nature Singapore Pte Ltd.* (2020). ISBN 978-981-15-1099-1.

[Vie2015] S. Vierrath, F. Güder, A. Menzel, M. Hagner, R. Zengerle, M. Zacharias and S. Thiele: Enhancing the quality of the tomography of nanoporous materials for better understanding of polymer electrolyte fuel cell materials. *J. Power Sources* 285 (2015) pp. 413-417.

[Vol2010] T. Volkenandt, E. Müller, D.Z. Hu, D.M. Schaadt, and D. Gerthsen, Quantification of sample thickness and In-concentration of InGaAs quantum wells by transmission measurements in a scanning electron microscope, Micros. Microanal. 16 (2010) p. 604-613.

[Vol2014] T. Volkenandt, E. Müller, and D. Gerthsen, Sample thickness determination by scanning transmission electron microscopy at low electron energies, Microsc. Microanal. 20 (2014) p. 111-123.

[Voy2003] P.M. Voyles, J.L. Grazul and D.A. Muller, Imaging individual atoms inside crystals with ADF-STEM, *Ultramicroscopy* 96 (2003) 251-273.

[Vys2017] T. Vystavěl, L. Tůma, P. Stejskal, M. Unčovský, J. Skalický, and R. Young: Expanding capabilities of low-kV STEM imaging and transmission electron diffraction in FIB/SEM systems. Mircosc. Miroanal. 23 Suppl 1 (2017) p. 554-555.

[Wal2018] C.G.H. Walker, I. Konvalina, F. Mika, L. Frank and I Müllerova: Quantitative comparison of simulated and measures signals in the STEM mode of a SEM. Nuclear Inst. and Methods in Physics Research B 415 (2018) p. 17-24.

[Wan2015] Q. Wan, R.A. Plenderleith, M. Dapor, S. Rimmer, F. Claeyssens and C. Rodenburg: Separating topographical and chemical analysis of nano-structure of polymer composite in low voltage SEM. J. Phys. Conf. Ser. 644 (2015) 012018.

[Wan2016] Q. Wan R.C. Masters, D. Lidzey, K.J. Abrams, M. Dapor, R.A. Plenderleith, S. Rimmer, F. Claeyssens and C. Rodenburg: Angle selective backscattered electron contrast in the low-voltage scanning electron microscope: Simulation and experiment for polymers. Ultramicroscopy 171 (2016) p. 126-138.

[Wan2017] F. Wankmüller, J. Joos, M. Meffert, D. Gerthsen, and E. Ivers-Tiffée: Quantitatite Study of LSCF and LSM-YSZ Cathode Microstructure by FIB/SEM Tomography. *ECS Transactions* 78 (2017) pp. 861-867.

[Wil2009] D.B. Williams and C.B. Carter, *Transmission electron microscopy: a textbook for materials science*. 2009, Springer. p. 23-479.

[Won2018] S. Wong, N. Ngadi, I.M. Inuwa, and O. Hassan: Recent advances in application of activated carbon from biowaste for wastewater treatment: a short review. *J. Clean. Prod.* 175 (2018) pp. 361-375.

[Xia2018] J. Xiao, G. Foray and K. Masenelli-Varlot: Analysis of liquid suspensions using scanning electron microscopy in transmission: estimation of the water film thickness using Monte-Carlo simulations. J. Microsc. 269 (2018) p. 151-160.

[Xu1989] M.L. Xu, J.J. Barton and M.A. Van Hove, Electron scattering by atomic chains: Multiple-scattering effects, Phys. Rev. B 39 (1989) p. 8275-8283.

[Xu2019] Y. Xu, Y. Wang, J. Yuan, Q. Cheng, X. Wang, and P.L. Carlson, Medical breast ultrasound image segmentation by machine learning, *Ultrasonics* 91 (2019) 1-9.

[Zau1992] R. Zauter, F. Petry, M. Bayerlein, C. Sommer, H.J. Christ and H. Mughrabi: Electron channelling contrast as a supplementary method for microstcructural investigations in deformed metals. Phylos. Mag. A 66 (1992) p. 425-436.

[Zie2010] J. F. Ziegler, M.D. Ziegler, and J.P. Biersack, SRIM – The stopping and range of ions in matter, Nucl. Instrum. Methods Phys. Res., B 268 (2010) p. 1818-1823.

Publications and Conference Contributions

Reviewed publications

M. Čalkovský, E. Müller, M. Meffert, N. Firman, F. Mayer, M. Wegener and D. Gerthsen: Comparison of segmentation algorithms for FIB-SEM tomography of porous polymers: Importance of image contrast for machine learning segmentation. Mater. Charact. 171 (2021) 110806.

Y. Li, **M. Čalkovský**, E. Müller, Ch. Sprau, A. Colsmann, D. Gerthsen: Highly Selective Cu Staining of Sulfur-Containing Polymers facilitates 3D Nanomorphology Reconstruction of Polymer:Fullerene Blends in Organic Solar Cells by FIB-SEM Tomography. ACS Appl. Mater. Interfaces 13 (2021) 53252-53261.

F. Mayer, D. Ryklin, I. Wacker, R. Curticean, **M. Čalkovský**, A. Niemeyer, Z. Dong, P.A. Levkin, D. Gerthsen, R.R. Schröder and M. Wegener: 3D Two-Photon Microprinting of Nanoporous Architectures. Adv. Mater. 32 (2020) 2002044.

M. Čalkovský, E. Müller, M. Hugenschmidt and D. Gerthsen: Differential electron scattering cross-sections at low electron energies: The influence of screening parameter. Ultramicroscopy 207 (2019) 112843.

Conference contributions

M. Čalkovský, E. Müller, M. Meffert, N. Firman, F. Mayer, M. Wegener and D. Gerthsen: Comparison of segmentation algorithms for FIB-SEM tomography of porous polymers: Importance of image contrast for machine learning segmentation, Microscopy & Microanalysis, 1.-5.8.2021, Pittsburgh, USA (online)

M. Čalkovský, E. Müller, M. Meffert, N. Firman, F. Mayer, M. Wegener and D. Gerthsen: Comparison of segmentation algorithms for FIB-SEM tomography of porous polymers: Importance of image contrast for machine learning segmentation, European Microscopy Congress 2020, 24.-26.11.2020 (online)

M. Čalkovský, E. Müller, M. Hugenschmidt and D. Gerthsen: Differential electron scattering cross-sections at low electron energies: The influence of screening parameter, Microscopy Conference 2019, 1.-5.9.2019, Berlin, Germany

M. Čalkovský, E. Müller, M. Hugenschmidt and D. Gerthsen: Differential electron scattering cross-sections at low electron energies: The influence of screening parameter. Microscopy & Microanalysis, 4.-8.8.2019, Portland, OR, USA

Acknowledgements

First of all, I would like to express my deep gratitude to Prof. Dagmar Gerthsen for giving me the chance to spend several years at KIT-LEM and supervise work on my PhD thesis. I have benefited greatly from your wealth of knowledge, meticulous and patient guidance, and support in solving many research challenges.

I would like to thank Prof. Christian Kübel from KIT-INT for being the co-referee of this PhD thesis and for valuable comments and suggestions from other research perspectives.

Special thank you to Dr. Erich Müller for the many answered ‘‘short‘‘ questions, many advice and encouragement with a perfect blend of insight and humor.

Special thank you to Dr. Milena Hugenschmidt, Dr. Cheng Sun and Dr. Yonghe Li for being very nice office neighbors creating a great working environment enhanced by an always positive atmosphere.

Special thank you to Dr. Frederik Mayer for the nice collaboration in the cluster of excellence 3DMM2O and the extensive discussions regarding many research topics.

Many thanks to all the LEM members for creating a nice, friendly and inspiring atmosphere, where I really enjoyed working in.

Finally, I would like to thank my entire family for their love and endless support in my studies.